Computer Simulations of Phase Transitions in Confined Fluids

Héctor Domínguez-Castro

H. H. Wills Physics Laboratory,
University of Bristol

A thesis submitted to the University of Bristol
in accordance with the requirements of the degree of
Doctor of Philosophy
in the Faculty of Science

June 1997

Abstract

A series of Monte Carlo and Molecular Dynamics simulations have been performed to investigate freezing of a Lennard Jones fluid, modelling argon, confined between two parallel walls (a slit-pore). Structural investigations of the confined fluids show that they stratify in layers and, when they freeze, each layer forms in the (111) plane of the fcc crystal. Studies have been performed for several wall-fluid potentials. The freezing transition in slit-pores was determined using a variation of the NPT ensemble, which I term the NP_zT ensemble. In these simulations the pressure P_z normal to the walls is fixed and the mean separation of the walls is determined by this pressure. The location of the equilibrium transition is found using a novel method to evaluate free energies for the inhomogeneous fluid. A complete phase diagram for the confined fluid is presented for different numbers of particles and for fluids interacting with different wall potentials (purely repulsive and weakly attractive). We observe that the liquid-gas and liquid-solid coexistence lines are shifted from those in bulk as a result of confinement. The location of the triple point of the confined fluid is also presented. In an attempt to mimic experimental conditions another simulation was carried out. The slit pore is immersed in a thermal bath, keeping the pressure of the pore and the reservoir fluid constant. Freezing, melting, and the accompanying hysteresis was investigated for several pore widths under different thermodynamic conditions. The freezing temperature, defined as the limit of metastability, is always at a lower temperature than the equilibrium freezing bulk temperature. The diffusion coefficients of confined fluids are measured and the behaviour of these near the freezing is discussed.

Acknowledgements

Firstly I wish to thank my advisors Prof. R. Evans and Dr. M. P. Allen for their advice, patience, teaching and encouragement throughout these years.

I should also like to acknowledge the financial support received from the National Council of Science and Technology, "Consejo Nacional de Ciencia y Tecnología (CONACyT)", México, through a Postgraduate Scholarship over the last 4 years.

I also acknowledge the staff of the Maria Mercer Physics Library for their help, and J.-P. Melot for keeping the computing facilities in good conditions.

I would also like to thank the other member of the group for their advice and scientific discussions, Mark, Julian, Philip, Jeroen and Marjolein.

For all the time I was away from my family and they still love me, my thanks and gratitude go to them: Angelina, Tlemilko, Gustavo, and especially Mum and Dad (thanks for your love and support).

Finally the biggest thanks go to my wife, Margarita, and son, Alberto, who shared the happiness and sadness over the last 4 years: words are not enough. This work is as much yours as mine.

Para mi chiquita y mi chiquito.

Author's Declaration

I declare that no part of this thesis has been submitted for a higher degree in this, or any other, university. The research reported herein is the result of my own investigation except where reference is made to the work of others. All research was carried out under the supervision of Prof. R. Evans and Dr. M. P. Allen at the University of Bristol, between October 1993 and June 1997.

Héctor Domínguez-Castro

June 1997

The views expressed in this thesis are those of the author and not necessarily those of the University of Bristol.

Contents

1 INTRODUCTION 1

1.1 Interfaces 3

1.2 Wetting 4

1.3 Confined fluids: Experiments. 6

1.4 Models for Confined Fluids 9

2 CONFINED FLUIDS 14

2.1 Liquid-Gas Transition 14

2.1.1 Thermodynamics 14

2.1.2 Computer Simulations: Liquid-Gas Transition 20

2.1.3 Experimental and Theoretical work 25

2.2 Liquid-Solid Transition 26

2.2.1 Computer Simulations of the Liquid-Solid Transition in Bulk Systems 26

2.2.2 Computer Simulations of the Liquid-Solid Transition in Confined Fluids 28

2.2.3 Experimental background 33

3 COMPUTATIONAL TECHNIQUES AND MODELS FOR PORE SYSTEMS 39

3.1 Introduction 39

3.2 Molecular Dynamics. 42

3.3 Monte Carlo Method. 44
3.4 Models for Pore Systems. 48
3.4.1 Potential Functions. 48
3.4.2 Simulations in the NP_zT ensemble 51
3.4.3 Simulations in the NPT ensemble using a reservoir. 52

4 Freezing in the NP_zT ensemble **56**
4.1 Equivalence between the NP_zT and μVT ensemble 56
4.2 Simulations in the NP_zT ensemble. 57
4.3 Structure of the confined fluid. 59
4.4 Temperature dependence 72
4.5 The influence of the wall-fluid interaction 73
4.5.1 Strong and weak walls 73
4.5.2 Purely Repulsive walls 77
4.5.3 Structured walls 79
4.5.4 Bulk crystal structure versus that in the pore 80
4.6 Hysteresis 82
4.7 Conclusions. 85

5 Phase Diagram **88**
5.1 Introduction 88
5.2 Thermodynamics for the slit-pore ensemble 88
5.3 Free Energy Calculations 93
5.4 Gibbs-Duhem Integration 99
5.5 Results and discussion 101
5.5.1 Bulk Phase Diagram 101
5.5.2 Phase Diagram of confined fluids 102

6 A slit-pore in contact with a reservoir **132**
6.1 Introduction 132

6.2 Molecular Dynamic Simulations 133
6.2.1 Freezing of the pore and reservoir fluid 133
6.2.1.1 Structure of the solid 137
6.2.1.2 Diffusion Coefficients 146
6.2.2 Melting of the pore and reservoir system 155
6.2.2.1 Structure of the fluid at melting 156
6.3 Monte Carlo simulations 159
6.3.1 Structure of the confined fluid: Strongly attractive walls . . . 164
6.4 Conclusion 166

7 Summary and conclusion **169**

List of Figures

1.1 Schematic phase diagram for a simple fluid. The full lines show the phase boundaries in the bulk. The dashed lines are the conjectured shifted phase boundaries arising from confinement (see section 1.3). . 3

1.2 The contact angle θ of a liquid drop at a substrate surrounded by a gas phase. 5

1.3 Transmission electron micrograph of a slice of Vycor Glass.. The white region indicates the pore space. Picture taken from [19] 8

2.1 Picture of two adsorbing walls of area A, immersed in a thermal bath at constant (μ, T, V), repelling with force Af and separated by a distance l. 16

2.2 The in-plane pair correlation function for the contact layer for methane confined by structured and structureless graphite walls. The figure was taken from reference [96]. 31

2.3 Freezing of oxygen in sol-gel glass (using a picosecond optical technique). Note the depression in the temperature as a function of the inverse of the mean pore radius. Figure reproduced from reference [23]. 34

2.4 Phase diagram for CO_2. The (+) symbols and the solid curves refer to the bulk fluid. The solid symbols are for CO_2 confined in Vycor glass. The dashed lines are to guide the eye. PC means pore condensation and PF pore freezing. PT is the quasi triple point of the confined system. The figure was taken from reference [72]. Note that all the positron data were taken on cooling the samples at fixed pressure. Because of hysteresis different PC and PF lines would be obtained using data taken on heating. 38

3.1 A two-dimensional example of a periodic system 41

3.2 The two different single wall-fluid potentials described in this chapter. The LJ pair potential is shown for comparison. The plots are given with the same parameters, $\epsilon' = 1.2771\epsilon$, $\sigma' = 1.0946\sigma$ and $\rho\sigma^3 = \sqrt{2}$. ϵ and σ are the Lennard Jones parameters. For the 10-4-3 potential we also have $\Delta l = \sigma/\sqrt{2}$ and $\alpha = 1.0$. 51

3.3 Sketch of the slit-pore model used in the NP_zT simulation 53

3.4 Sketch of the slit-pore model which is located in the middle of a reservoir 54

4.1 The density profiles for a fluid in a slit- pore at T=1.15. In a) normal pressure, $P_z = 6.0$ and the fluid is liquid-like and in b) where $P_z = 8.0$ it is totally frozen. The first layer remains frozen for all pressures. The left wall is located at z=0 and the dashed lines indicate the positions of the right wall. In each case $N = 300$ 61

4.2 The in-plane correlation function (ICF) of each layer shown in figure 4.1 a) P_z=6.0. The first layer is solid- like but the rest are liquid-like. b) $P_z = 8.0$. All the ICF's show crystalline structure (see text). $N = 300$ 63

4.3 The corresponding Fourier Transform (FT) of the in-plane correlation function of each layer shown in figure 4.1 and figure 4.2. a) $P_z = 6.0$ and b) $P_z = 8.0$. $N = 300$. 64

4.4 Snapshots of the particle-configurations corresponding to figure 4.1. a) A liquid-like behaviour can be seen in the middle of the pore at $P_z = 6$ whereas b) a layered, solid-like structure is observed at $P_z = 8$. 65

4.5 In plane snapshots of layer 1 (adjoining the wall) and layer 4 (near the middle of the slit). a) and b) refer to $P_z = 8$ and c) and d) to $P_z = 6$. In both cases layer 1 is solid-like. 66

4.6 Density profiles and snapshots for a 600-particle system. The thermodynamic conditions are the same as for the 300-particle system. a) $P_z = 6$ and b) $P_z = 8$. 68

4.7 The $g(r)$ (ICF) and its $S(k)$ for the layers shown in figure 4.6. a) and b) are for the liquid, $P_z = 6.0$ and c) and d) are for the solid $P_z = 8.0$. $N = 600$. 69

4.8 Height of main peak in the structure factor versus number of Monte Carlo sweeps. The value 2.85 is the empirical (Hansen-Verlet) value for the onset of bulk freezing. $P_z = 8.0$, $T = 1.15$ and $N = 300$. . . . 70

4.9 Density profiles at different Monte Carlo steps for a state where the 600-particle system should freeze, $P_z = 8.0$ and $T = 1.15$. Observe how the layers in the fluid start freezing from the walls to the centre. The dashed line represents the position of the second wall. 71

4.10 The density profiles for a 300-particle system for different thermodynamic conditions. The dashed line represents the position of the second wall. 74

4.11 The density profiles for a 300-particle system for different values of ϵ^* the parameter which measures the strength of the attractive wall-fluid potential. The main effect is in the first contact layer. $T = 1.15$. The dashed line represents the position of the second wall. 75

4.12 The $g(r)$ for the layers shown in figure 4.11. For ϵ^*=1.0 and 3.0 all layers in the solid have almost identical $g(r)$ (ICF). 76

4.13 The density profile $\rho(z)$ and the $g(r)$ of each layer for a fluid confined by purely repulsive walls. $\epsilon^* = 1.2771$, $\alpha = 0.0$, $T = 1.15$ and $N = 300$. Note the lack of crystalline structure in the first layer when the system is in the liquid-like state. When the system freezes all layers have similar density profile and $g(r)$ (ICF). The dashed line represents the position of the second wall. 78

4.14 The density profile $\rho(z)$ and the $g(r)$ for a fluid confined by structured walls. The results refer to $P_z = 8.0$, $T = 1.15$ and $N = 300$ where the system is solid-like. Here, once the fluid freezes all the layers are in registry with the particles forming the structured walls, i.e. they take the structure of the (100) face of a fcc crystal. 81

4.15 The 3 dimensional pair correlation function $g(r)$ and the structure factor $S(k)$ for bulk and confined solids for several pore conditions. All the confined fluids are at $T = 1.15$. $P_z(N = 600) = P_z(N = 300) = P_z(\text{struc.Walls}) = 8.0$, $P_z(\text{Rep.Walls}) = 12.3$, $P_z(\text{9-3 Walls}) = 9.0$. The bulk was simulated at $P(\text{Bulk}) = 5.68$ and $T = 0.5$ with $N = 300$. 83

4.16 Mean density ρ (in reduced units) versus P_z for various wall-fluid potentials. The upper curve in each figure refers to solid and the lower to liquid. There is pronounced hysteresis in all cases. Note the different pressure scales. $N = 300$ for all figures except figure f) where $N = 600$. Error bars are of the size of the symbols. 86

5.1 Different single wall-fluid potentials and the fluid-fluid (LJ) potential used in this work. The LJ (12-6) and the 10-4-3 potentials are given by equations (3.26) and (3.28). In all cases $\sigma' = 1.0946\sigma, \epsilon' = 1.2771\epsilon, \rho\sigma^3 = \sqrt{2}$ and $\Delta l = \sigma/\sqrt{2}$ with σ and ϵ the fluid-fluid LJ parameters. These parameters with $\alpha = 1$ mimic Argon fluid with CO_2 walls. 98

5.2 Liquid and solid density profiles at coexistence for purely repulsive walls $\alpha = 0.0$. The graphs are for temperature $T = 1.15$ and the coexistence pressure $P_z = 8.52$. The IFC, $g(r)$, of each layer is also plotted. Note that $\langle l \rangle$ is larger for the liquid than for the solid. $\langle l \rangle = 11.41$ for the liquid and $\langle l \rangle = 10.68$ for the solid. 104

5.3 Plots of the mean density ρ and Gibbs free energy per particle (G/N) as a function of normal pressure P_z for the 300-particle system with repulsive walls ($\alpha = 0.0$). The equilibrium transition is shown by the dashed vertical line in the top figure. $T = 1.15$. Error bars associated with the data are of the size of the symbols. 106

5.4 Liquid and solid density profiles at coexistence for purely repulsive walls $\alpha = 0.0$. for the 600-particle system. The graphs are for temperature $T = 1.15$ and coexistence pressure $P_z = 7.48$. The ICF, $g(r)$, of each layer is also plotted. $\langle l \rangle = 21.51$ for the liquid and $\langle l \rangle = 19.88$ for the solid. 107

5.5 Plots of the mean density ρ and Gibbs free energy per particle (G/N) as a function of normal pressure P_z for the 600 particle system with repulsive walls ($\alpha = 0.0$). The equilibrium transition is shown by the dashed vertical line in the top figure. $T = 1.15$. Error bars associated with the data are of the size of the symbols. 108

5.6 Liquid and solid density profiles at coexistence for weakly attractive walls $\alpha = 0.5$ for the 300-particle system. The graphs are for $T = 1.15$ and the coexistence pressure $P_z = 5.56$. The ICF, $g(r)$ of each layer is also plotted. Note that the first layer, for the liquid branch, is more highly structured than those in the middle but it is still liquid-like. 110

5.7 Plots of the mean density ρ and Gibbs free energy per particle (G/N) as a function of normal pressure P_z for the 300 particle system with weakly attractive walls ($\alpha = 0.5$). The equilibrium transition (at $T = 1.15$) is indicated by the dashed vertical line in the top figure. Error bars associated with the data are of the size of the symbols. 111

5.8 The phase boundaries for the confined fluids compared with those of bulk. Note that for the bulk system, P is the bulk pressure whereas for the confined fluid P is P_z, the normal pressure. TP means triple point. Error bars are indicated when they are bigger than the size of the symbols. 113

5.9 The phase boundaries for the confined fluids compared with those of bulk. The figure is plotted in normal scale for values of temperature and pressure close to the triple point. Compare this figure with figure 5.8. Note that for the bulk system, P is the bulk pressure whereas for the confined fluid P is P_z, the normal pressure. TP means triple point. 114

5.10 Density profiles for the liquid coexisting with the solid at different points on the coexistence line for the 300-particle system. The normal pressure P_z and the temperature are indicated. We can see how the fluid loses its oscillatory behaviour as the pressure decreases. Here the fluid is confined by purely repulsive walls ($\alpha = 0.0$). The dashed line indicates the position of the right hand wall. 116

5.11 Density profiles for the liquid coexisting with the solid at different points on the coexistence line for the 600-particle system. The normal pressure P_z and the temperature are indicated. We can see how the fluid loses its oscillatory behaviour as the pressure decreases. Here the fluid is confined by purely repulsive walls ($\alpha = 0.0$). The dashed line indicates the position of the right hand wall. 117

5.12 Density profiles for the confined fluid with repulsive walls ($\alpha = 0.0$) approaching the liquid-gas transition. $N = 600$. The system exhibits capillary evaporation. The graphs refer to a fixed temperature of T =0.95. For this temperature coexistence occurs for $P_z = 0.050$. The bulk coexistence pressure at this temperature is $P \approx 0.045$. Note that the results for P=0.04 and 0.03 refer to metastable states (see text). For P=0.01 we have a gas state. 122

5.13 Plots of the mean density ρ and Gibbs free energy per particle (G/N) as a function of normal pressure P_z for the 600-particle system with purely repulsive walls ($\alpha = 0.0$). The temperature is fixed at $T = 0.95$ This plot is for the liquid-gas transition. The equilibrium transition is indicated by the dashed vertical line in the top figure. Error bars are indicated when they are bigger than the size of the symbols. . . . 124

5.14 Liquid and solid density profiles ($\rho(z)$) at coexistence for a WCA fluid confined by purely repulsive walls. The figures refer to temperature $T = 1.0$ and pressure of $P_z = 11.51$ The ICF, $g(r)$ of each layer is also plotted. $N = 300$. 126

5.15 Plots of the mean density ρ and Gibbs free energy per particle (G/N) as a function of normal pressure P_z for the 300 particle repulsive system (the WCA fluid) confined by purely repulsive walls ($\alpha = 0.0$). $T = 1.0$. The equilibrium transition is indicated by the dashed vertical line in the upper figure. Error bars associated with the data are of the size of the symbols. 127

5.16 The freezing lines for the repulsive WCA fluid (with $N = 300$) confined by purely repulsive walls ($\alpha = 0.0$) compared with the bulk one (de Kuiper et al. [134]). The lines joining the points are drawn to guide the eye. For the confined fluid $P = P_z$ while for the bulk P is the bulk pressure. 129

5.17 This figure shows the differences in entropy (top) and enthalpy (bottom) between the liquid and the solid at coexistence. 131

6.1 Internal energy of the system per particle as a function of the temperature. $P = 0.05$, pore width $l = 12.5$ and $N = 2000$ particles. Note the large hysteresis between heating and cooling. The bulk freezing transition, for the same pressure, occurs around $T \approx 0.6$ (indicated by the dashed line). Error bars are of the size of the symbols. 135

6.2 Snapshots of particles for a slit-pore in contact with a reservoir ($l = 12.5$ $N = 2000$) at temperatures slightly above and below the freezing transition. a) For $T = 0.427$ the pore and the reservoir fluid are liquid-like. b) For $T = 0.425$ both fluids, the pore and the reservoir, simultaneously freeze showing the same ordering of the particles. The black circles represent the particles in the pore whereas the open circles are the particles in the reservoir. 136

6.3 The density profile of the confined fluid at different temperatures T for two pore widths. a) $l = 7.5$ and b) $l = 12.5$. For both cases $P = 0.05$ and $N = 2000$. We observe, once the freezing temperature is reached, the formation of layers parallel to the walls. 139

6.4 The internal energy as a function of the temperature for a slit-pore of width a) $l = 8.0$ and b) $l = 10.0$. The jumps at the left and the right of the curves indicate the freezing and the melting temperature respectively. $P = 0.05$ and $N = 2000$. The bulk transition temperature is indicated by the dashed line ($T \approx 0.6$). Error bars are of the size of the symbols. 140

6.5 Density profiles for several of the temperatures in figure 6.4. a) $l = 8.0$ and b) $l = 10.0$. Note that at the temperature where the freezing transition occurs (the jumps in figure 6.4 at $T = 0.454$ and $T = 0.447$ for the pore of $l = 8.0$ and $l = 10.0$ respectively) the pore fluid does not form well-defined layers throughout the pore. The layering does not appear even for temperatures ($T = 0.325$ for $l = 8.0$) which are far below the freezing temperature ($T \approx 0.6$ for this pressure $P = 0.05$), see inset in figure a). 141

6.6 Snapshots of particle configurations for the pore system investigated in figures 6.4 b) and 6.5 b), i.e. $l = 10.0$ and $P = 0.05$. a) Prior to the jump (in the internal energy) both the pore and reservoir fluids are liquid-like. b) At the temperature where the jump occurs, $T = 0.447$, the pore and the reservoir fluid freeze simultaneously. Apart from the first (contact) layer next to the walls, the pore and the reservoir solid appear to adopt the same ordering. The black circles represent the particles in the pore whereas the open circles are the particles in the reservoir. 142

6.7 Snapshots of particles configurations for the pore system investigated in figures 6.4 a) and 6.5 a), i.e. $l = 8.0$ and $P = 0.05$. a) At temperature $T = 0.456$, both the pore and reservoir fluid are liquid-like. b) Once the freezing temperature is reached ($T = 0.454$) both fluids freeze simultaneously. The black circles represent the particles in the pore whereas the open circles are the particles in the reservoir. 143

6.8 The bulk and the pore particle configuration for a Yukawa fluid confined by repulsive Yukawa walls. $l = 6.0$, the pressure $P = 0.016$, is well below the bulk freezing pressure ($P_{bulk} = 0.024$). The figure was taken from [95]. Note the formation of horizontal layers inside the slit parallel to the pore walls and of vertical layers at the end of the bulk fluid. The latter arise from interactions with the plates which are imposed at the ends of the simulation box. 145

6.9 Mean square displacement, perpendicular to the walls, for different layers for a slit pore with $l = 12.5$, at pressure of $P = 0.05$ and $N = 2000$ and at temperature before freezing (T=0.427). The effective diffusion coefficient is obtained from the slope of each curve in the range of t=8-20. The number 1 refers to the first layer closest to the walls, 2 to the second inner layer, etc. 150

6.10 The self-diffusion coefficient (in each layer) as a function of the temperature for a slit-pore with $l = 12.5$, at pressure of $P = 0.05$ and with $N = 2000$. The diffusion coefficients b) parallel and c) transverse to the walls are smaller for the first contact layers than in the middle. The self-diffusion coefficient in the reservoir is also measured (plot a) for the same temperatures. These values are always much higher than those in the pore -note different scales. Note that at temperature $T = 0.425$ where the system freezes, both the pore and the bulk diffusion coefficients drop simultaneously. The number 1 refers to the first layer closest to the walls, 2 to the second inner layer, etc. 152

6.11 The self-diffusion coefficient (in each layer) as a function of the temperature for a small slit-pore, $l = 7.5$, at pressure of $P = 0.05$ and with $N = 2000$. Once again, we observe that the reservoir diffusion coefficient (plot in figure a)) is always much higher than those in the pore. However, all drop simultaneously at the freezing temperature (see text). The number 1 refers to the first layers closest to the walls, 2 to the second inner layer, etc. 153

6.12 The self-diffusion coefficient for a pore width of $l = 10.0$ at pressure $P = 0.05$ and $N = 2000$. Because the layers are not well-developed parallel to the pore walls when the fluid freezes (see figures 6.5 b and 6.6), I plot the diffusion coefficient for the first and second layer and for the "middle" of the pore. The "middle" means the average of the diffusion coefficients in the inner layers. The reservoir diffusion coefficient is also plotted (figure a). Note once more, that the pore and reservoir diffusion coefficients drop simultaneously at the freezing temperature ($T = 0.447$.) 154

6.13 The internal energy as a function of the temperature for a pore of width $l = 11.0$. $P = 0.05$ and $N = 2000$. The freezing temperature occurs at $T = 0.437$ and the melting at $T = 0.625$ (jumps at the left and right respectively). Note that the hysteresis extends much further below the bulk freezing temperature ($T_{bulk} \approx 0.6$, dashed line) than it does above. 156

6.14 The internal energy as a function of temperature for a bulk system; $N = 2000$, $P = 0.05$. The equilibrium freezing transition occurs at $T \approx 0.60$. Compare this plot with those for the pore systems (figures 6.1, 6.4, 6.13). Error bars are of the size of the symbols. 157

6.15 Snapshots of particles for a pore with $l = 9.0$, $P = 0.05$, $N = 2000$. a) At $T = 0.530$, both the pore and reservoir are solid-like. The OP are 0.715 and 0.751 respectively. b) Close to the melting temperature $T = 0.610$ the reservoir seems to be solid-like ($OP = 0.662$) whereas the pore fluid starts losing its solid structure ($OP = 0.348$). c) Finally at temperature $T = 0.615$, both the pore and reservoir fluid are liquid-like. The OP for the pore fluid is 0.313 and for the reservoir is 0.332. The black circles represent the particles in the pore whereas the open circles are the particles in the reservoir. 160

6.16 Snapshots of particles for a pore width with $l = 10.0$, $P = 0.05$, $N = 2000$. a) At $T = 0.585$, both the pore and reservoir are solid-like. The OP are 0.696 and 0.650 respectively. b) Close to the melting temperature $T = 0.625$ the reservoir seems to be solid-like ($OP = 0.590$) whereas the pore fluid starts losing its structure ($OP = 0.413$). c) Finally at temperature $T = 0.635$, both the pore and reservoir fluid are liquid-like. The OP for the pore fluid is 0.301 and for the reservoir is 0.282. The black circles represent the particles in the pore whereas the open circles are the particles in the reservoir. 161

6.17 Snapshots of particles for a pore width with $l = 12.0$, $P = 0.05$, $N = 2000$. a) At $T = 0.595$, both the pore and reservoir are solid-like. The OP are 0.750 and 0.702 respectively. b) Close to the melting temperature $T = 0.635$ the reservoir seems to be solid-like ($OP = 0.736$) whereas the pore fluid starts losing its structure ($OP = 0.5320$). c) Finally at temperature $T = 0.640$, both the pore and reservoir are liquid-like. The order parameter for the pore fluid is 0.360 and for the reservoir one is 0.332. The black circles represent the particles in the pore whereas the open circles are the particles in the reservoir. . . 162

6.18 Snapshots of particles for a pore width with $l = 12.5$, $P = 0.05$, $N = 2000$. a) At $T = 0.565$, both the pore and reservoir are solid-like. The OP are 0.711 and 0.701 respectively. b) Close to the melting temperature $T = 0.700$, both the reservoir and the pore are solid-like. The OP are 0.698 and 0.689 respectively. c) Finally, at temperature $T = 0.705$, both the pore and reservoir are liquid-like. The OP for the pore fluid is 0.389 and for the bulk one is 0.387. The black circles represent the particles in the pore whereas the open circles are the particles in the reservoir. 163

6.19 Results of Monte Carlo simulations for a pore of width $l = 10.0$ at a high pressure, $P = 6.0$. Here the wall area is $A = (7.5)^2$. The density profiles $\rho(z)$ and the corresponding in-plane correlation function $g(r)$ in each layer are plotted. The top figures refer to above the freezing temperature and the bottom ones are just below the freezing temperature. The wall fluid interaction mimics argon confined by graphite walls, $\epsilon' = 7.2375\epsilon$ and $\sigma' = 0.7823\sigma$. We observe two crystalline-like layers close to the walls for all temperatures (even when the fluid is liquid-like in the middle). Note that the bulk equilibrium freezing temperature is $T_{bulk} \approx 1.05$. 165

6.20 The internal energy per atom as a function of the temperature for a slit pore of width $l = 10.0$. Each plot refers to a different pressure, P. In all cases, most of the hysteresis lies to the left of the corresponding bulk equilibrium transition, T_{bulk}. The bulk transition temperature is indicated by the vertical dashed line in figures a) and b). These results refer to weak wall-fluid potential: $\epsilon' = 1.2771\epsilon$ and $\sigma' = 1.0946\sigma$.167

List of Tables

4.1 Thermodynamic properties for a slit-pore using different ensembles showing the equivalence between them, $T = 1.2$. In reference [32] the wall-fluid and fluid-fluid potential energy are given separately. In this table both terms are included in the results for $\langle U/N \rangle$. 58

5.1 Values of pressures and temperatures at coexistence for the bulk liquid-solid boundary, $N = 400$. The numbers in parentheses denote the mean error estimated in the last decimal place, e.g. 6.90(5) $= 6.90 \pm 0.05$. Errors in T or P depend on which Clapeyron equation was used (equation (5.33) or (5.34)). 103

5.2 Values of pressures and temperatures at coexistence for the bulk liquid-gas boundary. Data were taken from reference [106]. 105

5.3 Values of pressures and temperatures at coexistence for the liquid-solid boundary. Data are for the 300-particle system confined by purely repulsive walls (α=0.0). The numbers in parentheses denote the mean error estimated in the last decimal place, e.g. 8.52(9) = 8.52 $\pm$ 0.09. Errors in T or P_z depend on which Clapeyron equation was used (equation (5.33) or (5.34)). 115

5.4 Values of pressures and temperatures at coexistence for the liquid-solid boundary. Data are for the 600-particle system confined by purely repulsive walls (α=0.0). The numbers in parentheses denote the mean error estimated in the last decimal place, e.g. 0.709(5) = 0.709 $\pm$ 0.005. Errors in T or P_z depend on which Clapeyron equation was used (equation (5.33) or (5.34)). 118

5.5 Values of pressures and temperatures at coexistence for the liquid-solid boundary. Data are for the 300-particle system confined by weakly attractive walls (α=0.5). The numbers in parentheses denote the mean error estimated in the last decimal place, e.g. 5.56(5) = 5.56 $\pm$ 0.05. Errors in T or P_z depend on which Clapeyron equation was used (equation (5.33) or (5.34)). 119

5.6 Values of pressures and temperatures at coexistence for the liquid-gas boundary. Data are for the 300-particle system confined by purely repulsive walls (α=0.0). The numbers in parentheses denote the mean error estimated in the last decimal place, e.g. 1.041(13) = 1.041 $\pm$ 0.013. 120

5.7 Values of pressures and temperatures at coexistence for the liquid-gas boundary. Data are for the 600-particle system confined by purely repulsive walls (α=0.0). The numbers in parentheses denote the mean error estimated in the last decimal place, e.g. 0.993(10) = 0.993 $\pm$ 0.010. 121

5.8 Values of pressures and temperatures at coexistence for the liquid-gas boundary. Data are for the 300-particle system confined by weakly attractive walls (α=0.5). The numbers in parentheses denote the mean error estimated in the last decimal place, e.g. 0.769(5) = 0.769 $\pm$ 0.005. Errors in T or P_z depend on which Clapeyron equation was used (equation (5.33) or (5.34)). 123

5.9 Values of pressures and temperatures at coexistence for the liquid-solid boundary. Data are for the 300-particle system (WCA fluid) confined by purely repulsive walls (α=0.0). The numbers in parentheses denote the mean error estimated in the last decimal place, e.g. 11.51(13) = 11.51 ± 0.13. Errors in T or P_z depend on which Clapeyron equation was used (equation (5.33) or (5.34)). 128

5.10 Values of pressures and temperatures at coexistence for the bulk liquid-solid boundary for the WCA system. Data were taken from reference [134]. 130

6.1 The freezing temperature for a slit pore with $l = 10.0$ at various pressures. 137

6.2 The freezing temperature for different pore widths, l, for pressure $P = 0.05$ and $N = 2000$. 144

Chapter 1

INTRODUCTION

Although we are surrounded by fluids it is probably safe to argue that we still do not understand much about them. For instance we would like to understand and to predict their behaviour under all conditions. After all that is our job, as (future) researchers, to describe accurately the phenomena occurring in nature.

We distinguish between homogeneous (where the average density is uniform) and inhomogeneous (where the average density is spatially varying) fluids and between simple and complex fluids.

Simple fluids are those composed of atoms which are electrically neutral and whose electron density exhibits spherical symmetry. We note that such fluids can have translational (positional) ordering only, i.e. we exclude systems with rotational or vibrational degrees of freedom and which can exhibit orientational correlations, such as liquid-crystals, plastic crystals, etc. We exclude even simple molecular systems (with chemical bonds) where the intermolecular forces are highly anisotropic. Since strong hydrogen bonds exist in water, we also exclude this important fluid. Moreover, we do not consider electrolytic solutions or molten salts, where the Coulomb forces play an important role. In this thesis, I specialize to simple atomic fluids.

It is often stated that nowadays we understand homogeneous simple fluids rather well. In particular, these fluids can be investigated either from a macroscopic or a

microscopic viewpoint. Classical thermodynamics is a phenomenological science, independent of any microscopic model of the system, which can describe the three states of matter, gas, liquid and solid from a few postulates [1].

However, we know matter is made of particles, atoms, molecules, etc. which obey the laws of quantum mechanics. How can we relate this information to the macroscopic world? The answer is given by Statistical Mechanics. Given the Hamiltonian for any particular physical system (the total energy as a function of all the positions and momenta of the molecules) it is possible to write the partition function of that system, i.e. the number of accessible states available to the system [2]. Once this partition function is determined, all the thermodynamic properties can be calculated. Of course, the partition function cannot usually be calculated analytically. There are only a few problems in statistical mechanics which are exactly soluble [3] (apart from the trivial problems such as the perfect gas or the Einstein crystal). The best known example is the two-dimensional Ising model. A less well-known example is the case of hard rods in one dimension where the thermodynamics and correlation functions are known exactly for an inhomogeneous system [4,5].

Both thermodynamics and statistical mechanics assume that the fluid under consideration is in equilibrium (they do not care how the equilibrium was reached). Separate theories are used to investigate fluids away from equilibrium [6]. For instance, if the fluid is a dilute gas, kinetic theories are often suitable [7]. I do not discuss non-equilibrium aspects in this thesis.

A typical phase diagram, for a simple one-component fluid, is shown in figure 1.1. The solid lines show the phase boundaries of the bulk system.

But what about inhomogeneous fluids? Unfortunately in this case we know less, even for simple fluids. Theories are generally not as well developed and there are more questions, often rather subtle, to answer. The inhomogeneity, in a fluid phase, can be produced by an external field such as the gravitational, magnetic or electric fields or by the presence of an interface.

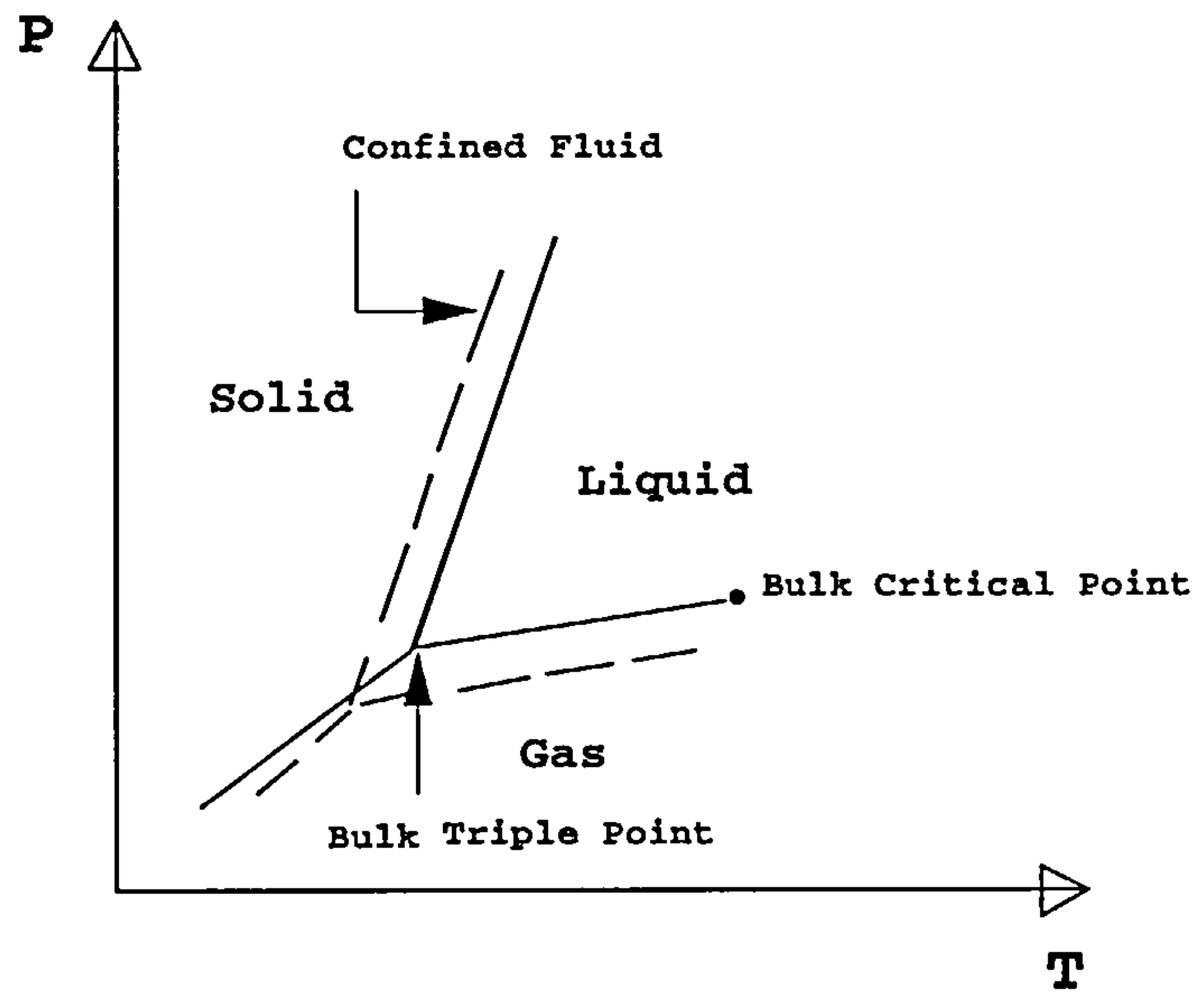

Figure 1.1: Schematic phase diagram for a simple fluid. The full lines show the phase boundaries in the bulk. The dashed lines are the conjectured shifted phase boundaries arising from confinement (see section 1.3).

1.1 Interfaces

Within the physics of interfaces new effects emerge which do not appear in bulk and which make the physics richer and more interesting. But what is an interface? The interface can be seen as the boundary between two bulk coexisting phases, e.g. liquid-gas or solid-liquid, which are in thermodynamic equilibrium. As a first attempt this interface can be treated as a mathematical discontinuity and one can consider quantities such as the Laplace pressure difference (the relation between the pressure inside and outside a spherical drop of radius R) [8]. Of course, a more realistic model is to think in terms of a transition region of non-zero width where the

fluid density can be a continuous function of the position but where we expect the local properties of the fluid to change rapidly in the neighbourhood of this interface. New physical concepts appear such as the surface tension, which can be regarded either as the force per unit length of boundary which acts to minimise the area of the interface or as the work necessary (at constant temperature) to increase the surface area, A, by a quantity dA.

Whilst the interface can be seen as the frontier between two coexisting fluid phases (liquid and gas), or between the solid and the liquid or the solid and the vapour phase, it can also be the boundary between a fluid and a solid spectator phase (i.e. a substrate). The spectator phase can be regarded as a rigid wall that exerts an external potential on the fluid atoms and confines them in a fixed volume which is finite in one or more dimension. This wall can adsorb atoms of the fluid.

1.2 Wetting

The study of fluids near a wall has been the subject of many investigations [9,10] in the last few years. Of special interest is the question of whether a fluid wets a wall or not. Consider a liquid drop that rests on a wall and is surrounded by a saturated vapor (gas). The liquid-vapor and the wall-liquid interface make a define angle θ which is called the contact angle (figure 1.2). Whether the wall is wet or not by the liquid is determined by the value of this contact angle which is related to the surface tensions (surface excess free energy) by the Young-Dupré equation,

$$\sigma_{wg} = \sigma_{wl} + \sigma_{lg} \cos\theta \tag{1.1}$$

where σ_{lg} is the liquid-gas surface tension, σ_{wl} is the wall-liquid surface tension and σ_{wg} is the wall-gas surface tension.

According to the different values that θ can take, we refer to different wetting

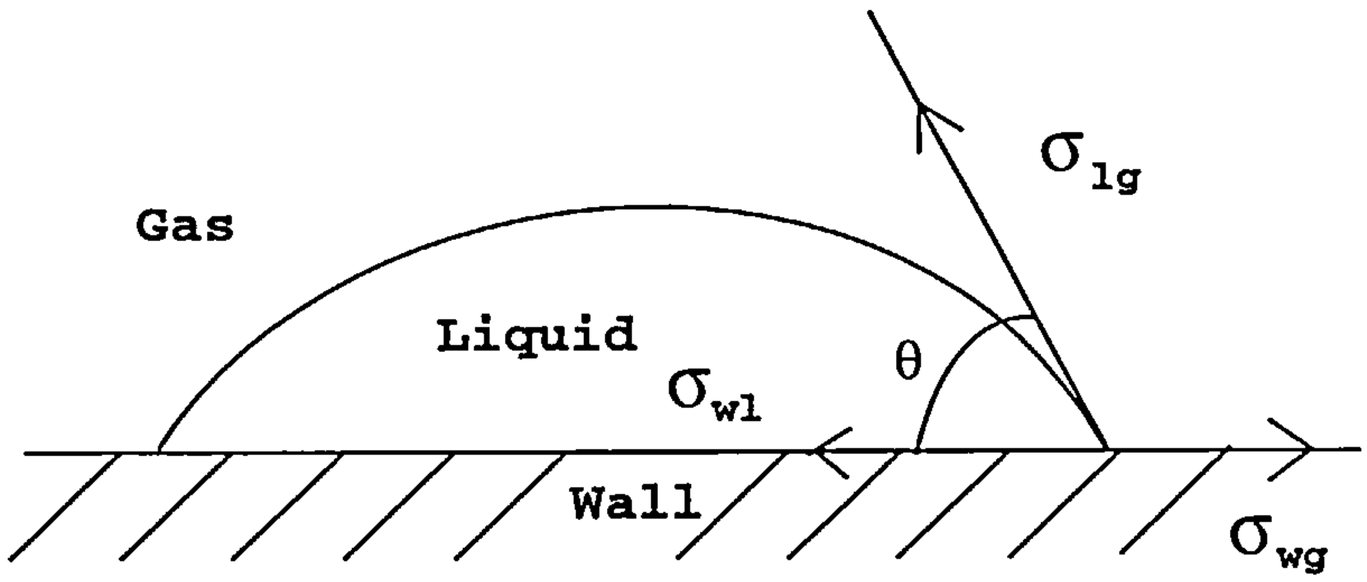

Figure 1.2: The contact angle θ of a liquid drop at a substrate surrounded by a gas phase.

situations. If $0 < \theta < \pi/2$ we say the walls are partially wet; if $\theta = 0$ the walls are completely wet by liquid. However, if $\pi/2 < \theta < \pi$ we term this partially dry and if $\theta = \pi$ we have a completely dry state. A dry state is when a thick film of gas develops between the liquid and the walls [10]; then

$$\sigma_{wl} = \sigma_{wg} + \sigma_{lg} \tag{1.2}$$

and this is wetting of the wall-liquid interface by gas.

In order to clarify wetting phenomena we can also think in terms of a simple adsorption experiment. Imagine we have a gas in equilibrium with the walls of a container. The thermodynamic parameters are known (the temperature and pressure are fixed by a reservoir). Suppose that a film of liquid is formed on the walls. If the pressure is increased at constant temperature to the value where the gas coexists with the liquid, two possibilities can occur; either the liquid film becomes thick or it does not. If the liquid film is macroscopically thick at coexistence we say the walls

are wet completely by liquid. If the liquid film remains thin in this limit we say the walls are not wet. The transition by which the system goes from non-wet to wet can be effected in two different ways. If it is from non-wet off-coexistence to wet at coexistence, it is called complete wetting. If it goes from non-wet at coexistence to wet at coexistence, by increasing the temperature, it can do so either as a continuous (critical wetting) or a discontinuous (first order wetting transition) [10].

1.3 Confined fluids: Experiments.

When fluids are confined by physical geometries (e.g. walls), especially when the size of these geometries are comparable with the dimension of the fluid molecular-diameter, the physics becomes even richer and more complex. The wall-geometry (finite size) and the interactions between the fluid and the wall play an important role.

Since the invention of the Surface Force Apparatus (SFA) [11–13], the experimental study of fluids confined between two substrates has progressed significantly. These experiments involve two mica surfaces in crossed cylinder configuration. The crossed cylinders (with macroscopic radii) are immersed in a reservoir of bulk fluid. Molecules can flow from the bulk and the surfaces until equilibrium is reached. Using the Derjaguin approximation [14], the crossed cylinder configuration can be translated locally into a two-spheres arrangement. Thus, the contact area of these spheres can be considered approximately flat on a microscopic scale. In this approximation the interfacial energy W per unit area between the two flat surfaces and the force F as a function of the distance (measured between the mica surfaces) is related by:

$$W = \frac{F}{2\pi R} \tag{1.3}$$

where R is the radius of the sphere.

In a typical experiment in the SFA the force between two mica surfaces is measured for a reservoir of liquid held at constant temperature and chemical potential. These measurements yield information about the solvation force, the excess pressure arising from confinement (see chapter 2). One of the new and interesting features which is observed in these experiments (at very small separations) is the presence of decaying oscillations in the (solvation) force measured as a function of the separation of the surfaces. A sort of order is induced in the confined fluid (layer structure) by confinement. Such oscillatory forces have a mainly geometric origin and can be explained in terms of the packing of particles in the free space between the surfaces. The oscillations have periodicity of approximately one molecular diameter. At large separations, the oscillations disappear and the force goes to zero [13]. Examples of these experiments can be found in [15–17].

Other kinds of experiment refer to fluids in porous solids where the geometry is much more complex. These have been conducted for fluids such as argon, hydrogen, oxygen and carbon dioxide confined in porous glasses (e.g. Vycor and silica xerogel). The porous glasses, in this case, a form of porous silica, are characterized by a series of interconnected pores which fill the glass space in a complex way [18]. Typical values for the average pore diameters are 40-200 Å. The characterization of the glasses has three basic aspects, a) the connectivity of the pore network b) the morphology of the pore volume and c) the mesoscopic (and microscopic) structure of the pore. A section through Vycor glass is shown in figure 1.3.

A variety of experiments have shown how the fluid properties change dramatically from those in bulk [20–26]. The phase diagram is strongly modified by the pore size and by the interaction of the fluid with the pore surfaces. The coexistence lines of the confined fluid appear to be shifted from those in bulk as a result of the confinement (figure 1.1) [see e.g. ref. [21]]. Although it is often difficult to interpret the results from these experiments (because of the complex nature of the pores), there is strong evidence to indicate that at constant pressure the gas-liquid coexistence line is shifted towards higher temperatures. For the the liquid-solid transition

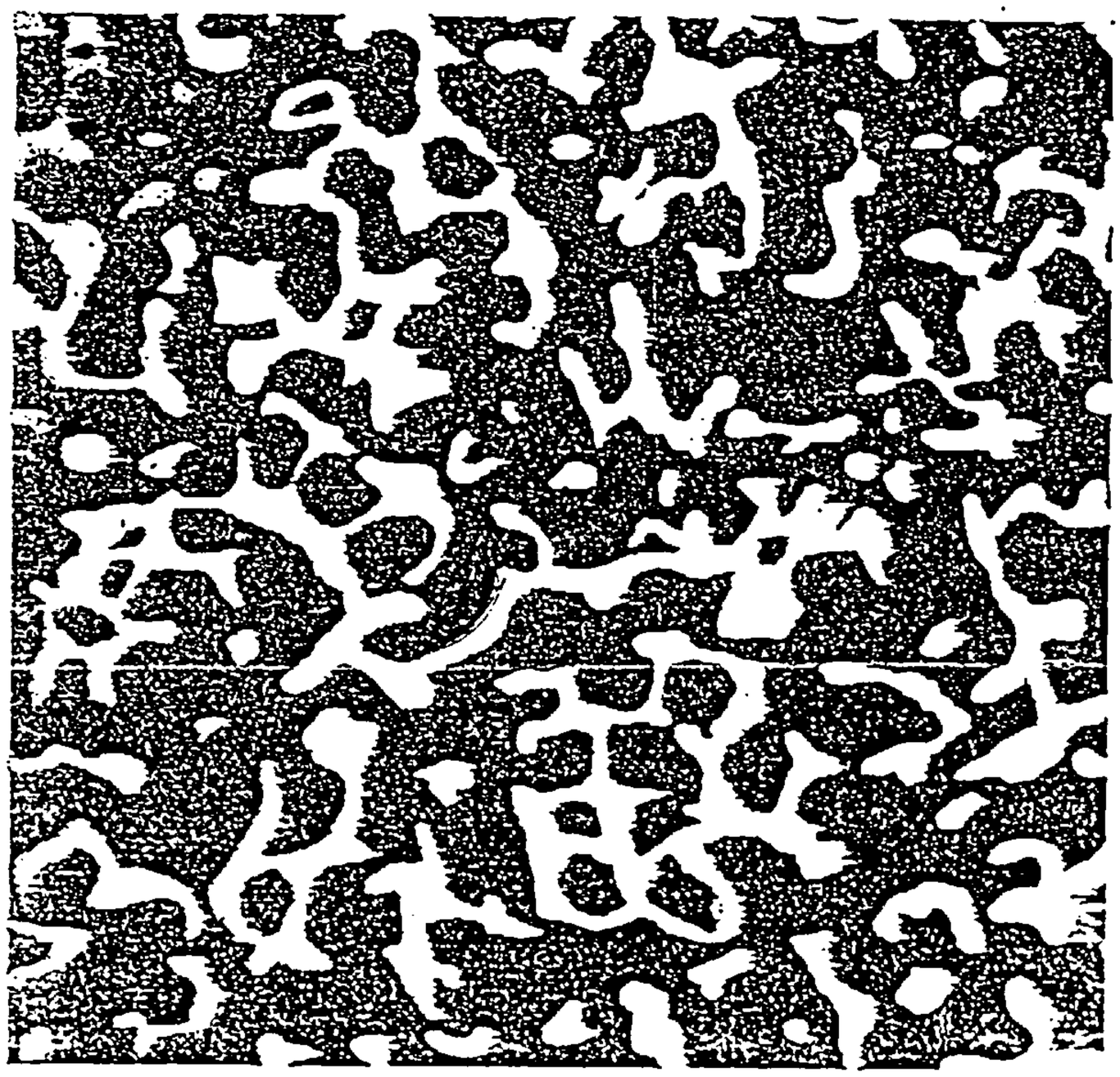

Figure 1.3: Transmission electron micrograph of a slice of Vycor Glass. The white region indicates the pore space. Picture taken from [19]

there are no systematic conclusions yet. However, it seems that the transition line is shifted towards lower temperatures. I will come back to discuss more of these experiments in the next chapter.

What physical features are responsible for the observed shifts in the phase diagram?. There are many other interesting questions to ask (and also to answer), for example: i) What is the nature of the new phase transitions?, ii) Are there well defined triple or critical points in these systems?, iii) Is the structure of the confined fluid the same as in bulk? iv) How are the transport properties of the fluid affected by confinement (i.e. diffusion coefficients, viscosity, etc.)?. Of course these studies are not restricted to experiments in porous solids. In order to answer these questions, it should be easier to start the investigations in simple geometries (single

pores), such as the work on freezing by Christenson [27] or the study of shear viscosity by Klein and Kumacheva [28]. Again I will come back to these experiments in the next chapter.

However, Since these questions can even be difficult to answer directly from any experiment it is not surprising that researchers have also been investigating these phenomena by theory and computer simulations.

1.4 Models for Confined Fluids

In order to describe confined fluids, we must specify the fluid-fluid interaction potentials and the wall-fluid interaction. First I describe the fluid models.

As is usual, we are excluding quantum effects. All the calculations are in the classical limit. Thus, we are assuming that the de Broglie wavelength ($\Lambda = (h^2/2\pi m k_B T)^{1/2}$) is much smaller than the average interatomic separation.

Both theoreticians and computer simulators work with two basic fluid models. Perhaps the simplest and most used model is that of hard spheres. In this model, hard particles interact via repulsive forces only; there are no attractive interactions:

$$\phi_{HS}(r) = \begin{cases} \infty & r < d \\ 0 & r > d. \end{cases} \tag{1.4}$$

d is the hard core diameter.

For a fluid at high density and high temperature this model captures several features of the structure of real atomic liquids. In particular, it accounts for the main features of the liquid structure factor [29].

A slightly more realistic model which includes the repulsive and attractive interactions between particles is the well-known Lennard Jones (LJ) potential. For a simple atomic fluid of N particles (atoms), we assume that the main interactions are described by a pairwise potential. We ignore contributions from 3-body, 4-body

etc. interactions, so the total potential energy is

$$\Phi(\mathbf{r}_1, ..., \mathbf{r}_N) = \frac{1}{2} \sum_{j \neq i} \sum_{i=1}^{N} \phi(\mid \mathbf{r}_i - \mathbf{r}_j \mid) \tag{1.5}$$

where the ϕ is modelled by the Lennard Jones potential (LJ):

$$\phi_{LJ}(r) = 4\epsilon \left[\left(\frac{\sigma}{r} \right)^{12} - \left(\frac{\sigma}{r} \right)^{6} \right]. \tag{1.6}$$

The r^{-6} is due to the Van der Waals (dispersion) forces while the r^{-12} models the Pauli repulsion of electrons in their outer shells. ϵ is the well depth of the potential and σ is a parameter which measures the atomic diameter. These can be chosen to mimic the fluid of interest. For rare gases such as Argon, Krypton, etc. the LJ potential describes many thermodynamic properties and the liquid structure reasonably accurately.

Sometimes it is useful to separate the attractive and repulsive components of the potential. We follow the prescription of Weeks, Chandler and Anderson [30] who split the potential at the minimum. For a Lennard Jones fluid we have;

$$\phi^{RLJ}(r) = \begin{cases} \phi_{LJ} + \epsilon & r < r_{min} \\ 0 & r_{min} \leq r \end{cases} \tag{1.7}$$

$$\phi^{ALJ}(r) = \begin{cases} -\epsilon & r < r_{min} \\ \phi_{LJ} & r_{min} \leq r \end{cases} \tag{1.8}$$

where $r_{min} = 2^{1/6}\sigma$. In perturbation theory [29] ϕ^{RLJ} is the repulsive force part of the potential and a fluid with this potential is treated as the reference system. ϕ^{ALJ} is the attractive part of the potential and this is treated as a perturbation.

We turn now to the pore model. Again, from the viewpoint of theoreticians or computer simulators it is convenient to start working with simple geometries (these can be far from realistic) which mimic the effects of confinement in the real (complex) pore structure. A typical pore geometry, used by many authors, is the slit-pore [31–35]. There are also many simulations working with cylindrical or spherical pores [36–39].

In Chapter 3, I shall describe the pore-model used in the present work in detail. Here, I mention briefly what the idealised model is for slit-pores.

Two identical parallel plates, separated by a distance l, are placed in a reservoir of fluid at fixed temperature and bulk pressure (or chemical potential). Any increase in the chemical potential is reflected in the number of atoms adsorbed by the walls. These walls can be structured or structureless with purely repulsive or with both attractive and repulsive interactions with the fluid. In the case of structureless walls (assumed of infinite area) the total wall-fluid interaction is given by the contributions of both walls acting in the z-direction only (the direction normal to the walls),

$$\phi(z) = \phi_s(z) + \phi_s(l - z) \tag{1.9}$$

where ϕ_s is the wall-fluid potential due to a single wall.

In order to characterize a phase transition it is useful to define an order - parameter. As we know, all phase transitions are signalled by a jump or the vanishing of an order parameter. For first order phase transitions, the magnitude of the jump is given in terms of the shapes of the coexistence curves by the appropriate Clapeyron equation [1].

For bulk fluids (i.e. liquid-gas transitions) the order-parameter is the difference in density between the two coexisting states. For confined fluids one useful order parameter is the adsorption, defined as follows:

$$\Gamma = \frac{1}{A}\int(\rho(\mathbf{r}) - \rho_b)d\mathbf{r}. \tag{1.10}$$

$\rho(\mathbf{r})$ is the density profile of the inhomogeneous fluid, ρ_b is the bulk density of the reservoir and A is the area of the plates. If the external potential is a function of z only then $\rho(\mathbf{r}) \equiv \rho(z)$ in a fluid state.

Several investigations of the liquid-gas transition of the confined fluid have been performed and this is rather well understood now. For instance, it is well known that depending on the strength of the attractive wall-fluid interaction compared to that of the fluid-fluid attraction, capillary condensation or evaporation appears. For a LJ fluid with reasonably attractive walls we observe capillary condensation [40,41], the phenomenon where a gas condenses in the pore at pressures below that at saturation while the fluid in the reservoir remains gas. If the walls are purely repulsive or very weakly attractive we observe capillary evaporation, i.e. a low density gas occupies the slit at pressures greater than that at saturation.

For the freezing transition there are no systematic studies, and many questions remain open or not satisfactorily answered. For instance, as was mentioned above, the phase diagram for this transition is not well defined yet. The main subject of this thesis is to investigate the freezing transitions of confined fluids. However, I present a brief review of work on the liquid-gas transition and, when necessary, some comparison will be made between these two types of transitions.

Before finishing this introduction let me remark that the study of confined fluids is not only interesting from the fundamental scientific viewpoint but is also relevant in applied fields such as clay swelling, protein folding, nanotribology [42,43] etc.

The structure of this thesis is as follows:

In chapter two, I will describe in more detail the physics of confined fluids. I will say more about the various experiments which motivated these studies, review earlier studies of the gas-liquid and liquid-solid transition and describe more generally the

behaviour of confined fluids.

In Chapter three I will outline the computer simulation methods used in this work. These are the Monte Carlo and Molecular Dynamics techniques. The pore model (a slit pore model) that has been used to simulate the confined fluid is also described in detail.

In Chapter four I describe studies of the confined fluid using one particular Monte Carlo simulation method, a modification of the Isothermal-Isobaric ensemble. Structural properties such as typical configurations and the ordering of the confined fluid-particles are presented. Hysteresis effects and the effects of different wall-fluid interactions are discussed.

In Chapter five the results of calculations to determine the location of the equilibrium transition for situations described in chapter four are discussed. Calculations of free energies of the inhomogeneous system are carried out to map out the phase diagram for the confined fluid for the particular Isothermal-Isobaric ensemble. A novel method to calculate free energies for the inhomogeneous liquid is presented. These calculations are performed for different pore sizes and for different wall-fluid interactions.

In Chapter six I present results for confined fluids using another simulation method. The slit-pore now is immersed in a reservoir which controls the pressure and chemical potential in the system. Simulations using Monte Carlo and Molecular Dynamics techniques are presented. Structural investigations of freezing and melting of the confined fluid are also discussed in this chapter.

Chapter 2

CONFINED FLUIDS

2.1 Liquid-Gas Transition

In this first section I focus on the liquid-gas transition. For several years researchers have studied the liquid-gas transition of confined fluids (capillary condensation) and we can assume that this phenomenon is well known. Although the study of this transition is not the main purpose of this thesis, I mention some relevant results and discuss this phenomenon. This serves as a prelude to studies of other phase transitions.

2.1.1 Thermodynamics

In this section I outline some of the thermodynamics required in the description of a slit-pore system. The results are, in principle, valid for any phase and they are not restricted to the liquid-gas transition. As stated at the end of chapter one, from the viewpoint of theoreticians or computer simulators, it is convenient to work with simple geometries. Probably one of the most common geometries used to study confined fluids is the slit-pore; two parallel walls (adsorbing on their inner surfaces) separated by a distance l are placed in a thermal bath which fixes the temperature and the chemical potential μ (figure 2.1). An external force Af is applied to the

walls in order to keep the separation constant. The change in the internal energy is given by

$$dU = -PdV + TdS + \mu dN + 2\sigma dA - Afdl. \tag{2.1}$$

The first three terms are analogues of the bulk contributions and $2\sigma dA$ is the work required to increase the wall area A by an amount dA. The term $Afdl$ is due to the force applied externally on the walls. N is the total number of atoms, V is the total volume available to the fluid and $P = P(\mu, T)$ is the pressure of the reservoir.

However, for an open system (the slit in a reservoir) it is more natural to work with the grand potential which is defined as $\Omega = U - TS - \mu N$. Thus, a change in the grand potential is given by [44];

$$d\Omega = -PdV - SdT - Nd\mu + 2\sigma dA - Afdl. \tag{2.2}$$

Here, the surface tension is defined as

$$\sigma = \frac{1}{2}\left(\frac{\partial \Omega}{\partial A}\right)_{V,T,\mu,l}. \tag{2.3}$$

From equation (2.2) we can define the force per unit area acting on the walls (f) as, $f = \tilde{p} - P$ where $\tilde{p} = -A^{-1}(\partial\Omega/\partial l)_{\mu,T,A}$. If the direct intermolecular interaction between the molecules forming the two walls is excluded, f is termed the solvation force. In the limit when $l \to \infty$ we have $\tilde{p} \to P$, then $f \to 0$. f is clearly an excess (over the bulk) arising from confinement. This force can be measured with the Surface Force Apparatus (see chapter 1).

For this particular system it is useful to introduce dividing surfaces at each wall and define excess quantities with respect to the bulk (with the same volume and

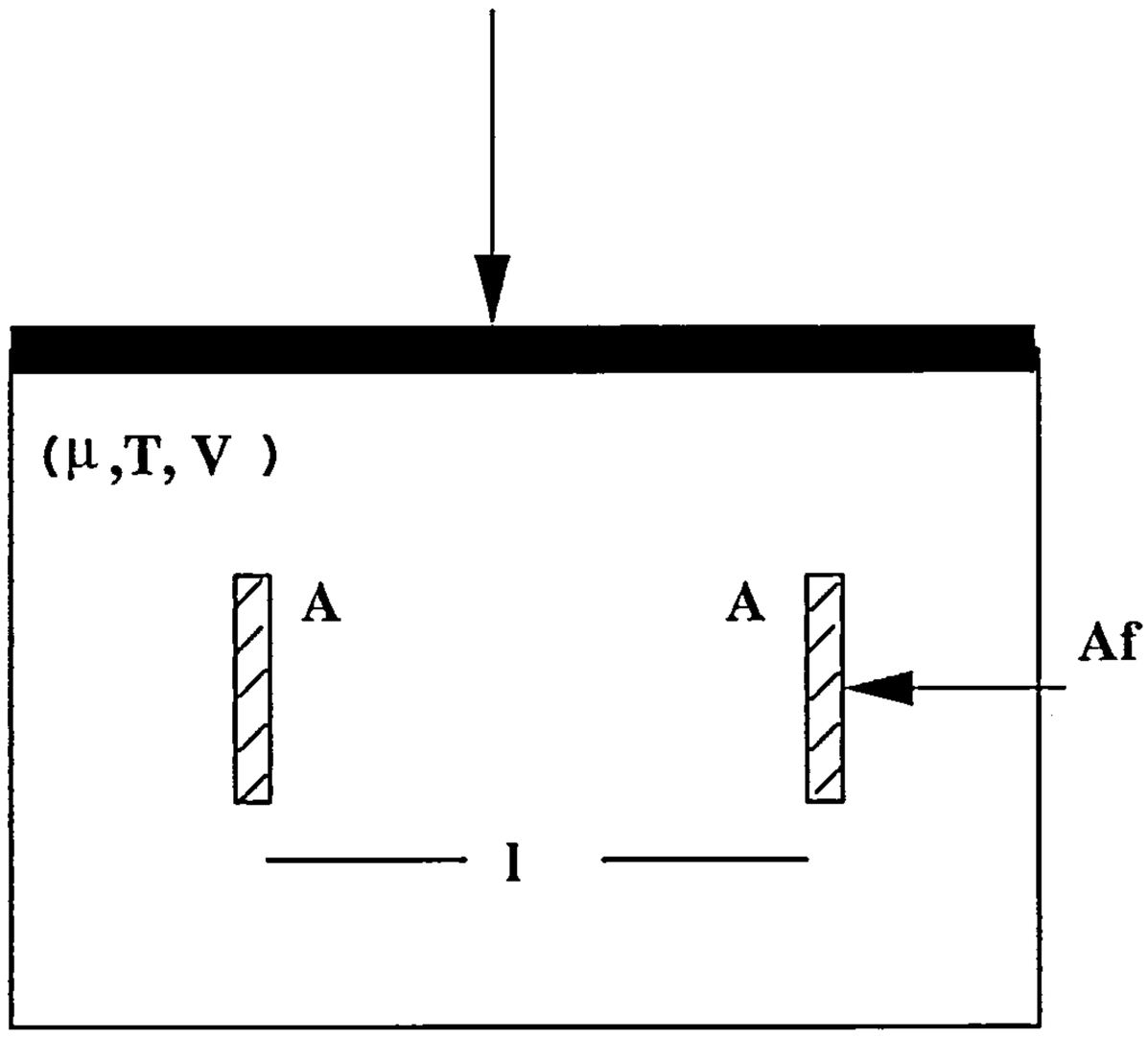

Figure 2.1: Picture of two adsorbing walls of area A, immersed in a thermal bath at constant (μ, T, V), repelling with force Af and separated by a distance l.

chemical potential):

$$\Omega_{ex} = \Omega - \Omega_b, S_{ex} \equiv S - S_b = 2As, N_{ex} \equiv N - N_b = A\Gamma. \tag{2.4}$$

Γ is the Gibbs adsorption and s is the excess entropy per unit area. Then, equation (2.2) can be expressed as

$$d\Omega_{ex} = -2(As)dT - (A\Gamma)d\mu + 2\sigma dA - (Af)dl. \tag{2.5}$$

From equation (2.1) we have that the interfacial tension (at fixed area) is a function of the intensive variables, T, P, μ and the separation between the walls l. Thus if we integrate equation (2.1) at T, P, μ and l fixed we have:

$$U = -PV + TS + \mu N + 2\sigma \dot{A} \tag{2.6}$$

Then, using $\Omega = U - TS - \mu N$ we have

$$\Omega = -PV + 2\sigma A \tag{2.7}$$

Since, $\Omega_b = -PV$ (bulk) we can write

$$\Omega_{ex} = \Omega - \Omega_b = 2\sigma A \tag{2.8}$$

or

$$d\Omega_{ex} = 2Ad\sigma + 2\sigma dA \tag{2.9}$$

Now, combining equations (2.5) and (2.9) one can obtain [44] the Gibbs adsorption equation for the confined fluid,

$$2d\sigma + 2sdT + \Gamma d\mu + fdl = 0. \tag{2.10}$$

The phase equilibrium between two states, α and β, occurs when the grand potentials of the phases are equal, i.e. $\Omega_{ex}^{\alpha} = \Omega_{ex}^{\beta}$ or equivalently $\sigma^{\alpha} = \sigma^{\beta}$, since

we showed that $\Omega_{ex} = 2\sigma A$ [44]. At constant wall area we perform an infinitesimal change in (μ, T, l) so that the phases remain in equilibrium, then we have,

$$2(s^\alpha - s^\beta)dT + (\Gamma^\alpha - \Gamma^\beta)d\mu + (f^\alpha - f^\beta)dl = 0. \tag{2.11}$$

From this equation we can determine the following Clapeyron relations:

$$\left(\frac{\partial \mu}{\partial T}\right)_l = -\frac{2(s^\alpha - s^\beta)}{(\Gamma^\alpha - \Gamma^\beta)} \tag{2.12}$$

$$\left(\frac{\partial l}{\partial \mu}\right)_T = -\frac{(\Gamma^\alpha - \Gamma^\beta)}{(f^\alpha - f^\beta)} \tag{2.13}$$

$$\left(\frac{\partial l}{\partial T}\right)_\mu = -\frac{2(s^\alpha - s^\beta)}{(f^\alpha - f^\beta)} \tag{2.14}$$

This set of equations determines the shape of different projections of the coexistence surface. They suggest that useful order parameters to characterize the phase transition can be either the difference in the solvation force $\Delta f = f^\alpha - f^\beta$ or in the adsorption $\Delta\Gamma = \Gamma^\alpha - \Gamma^\beta$.

For large pore separations, i.e. in the limit when l goes to infinity, it is possible to approximate the grand potentials of each confined phase by [44,45]

$$\Omega^\beta \approx -PAl + 2\sigma_{w\beta}A \tag{2.15}$$

and

$$\Omega^\alpha \approx -P_\alpha^+ Al + 2\sigma_{w\alpha}A. \tag{2.16}$$

The phase β corresponds to the phase in the reservoir while α corresponds to the capillary condensing phase. $P = P(\mu)$ is the pressure in the reservoir while P_α^+ is

the pressure of the α phase at the same chemical potential μ. $\sigma_{w\beta}$ and $\sigma_{w\alpha}$ are the wall-β and the wall-α interfacial tension, respectively, taken at bulk coexistence. Thus capillary coexistence occurs when $\Omega^{\alpha} = \Omega^{\beta}$, i.e.

$$P - P_{\alpha}^{+} = (2/l)(\sigma_{w\beta} - \sigma_{w\alpha}) = (2/l)\sigma_{\alpha\beta}\cos\theta. \tag{2.17}$$

Here I used Young's equation for the contact angle at a single wall (equation 1.1 of chapter 1). If we expand $P(\mu)$ about P_{sat} to first order in $\Delta\mu$, $P - P_{\alpha}^{+} = \Delta\mu(\rho_{\alpha} - \rho_{\beta})$, we have;

$$\mu_{sat} - \mu = \frac{2(\sigma_{\alpha\beta})}{l(\rho_{\alpha} - \rho_{\beta})}\cos\theta = \frac{2(\sigma_{w\beta} - \sigma_{w\alpha})}{l(\rho_{\alpha} - \rho_{\beta})} \tag{2.18}$$

μ_{sat} is the saturation chemical potential. ρ_{α} and ρ_{β} are the densities of the α and β coexisting bulk phases, respectively.

Equation 2.18 is a form of the Kelvin equation [46]. If we fixed the pressure rather than the temperature, then we obtain the following expression [44],

$$T - T_b = 2T_b(\sigma_{w\beta} - \sigma_{w\alpha})/lh\rho_b. \tag{2.19}$$

h is the latent heat per mole, T_b is the temperature of the bulk transition and ρ_b is the density of the bulk phase with the lower wall interfacial tension.

For instance if we have the gas-liquid transition, β corresponds to the gas phase and α to the liquid phase. If the wall-fluid interaction is such that walls favour liquid, capillary condensation occurs, i.e. we have $\sigma_{wg} > \sigma_{wl}$ in equation (2.18) and a transition at $\mu < \mu_{sat}$. On the other hand, if walls favour gas, capillary evaporation occurs, $\sigma_{wg} < \sigma_{wl}$ and a transition at $\mu > \mu_{sat}$ [41,47]. It is known that for a fluid in contact with purely repulsive walls a gas layer develops between the

liquid and the wall when $\mu \to \mu_{sat}$. Evidence of such a phenomenon can be found in simulations of a Lennard-Jones fluid [48] and for a square-well fluid [49] in contact with a single planar hard wall. This implies the repulsive walls are completely wet by vapour i.e. $\sigma_{wg} < \sigma_{wl}$ and we expect to observe capillary evaporation for such systems. Capillary condensation and evaporation are examples of shifted bulk phase transitions in confined fluids, with the shift in μ or in T arising from the effects of confinement. In addition there are surface transitions [50], e.g. prewetting and layering, which can also occur in confined (slit) geometry [41]

2.1.2 Computer Simulations: Liquid-Gas Transition

The most commonly used technique in these systems has been Grand Canonical Monte Carlo, where the chemical potential, the temperature and the volume are fixed. This kind of simulation has been carried out by several authors. Lane and Spurling pioneered simulation studies for slit pores. They showed [33], for a slit-pore model of fluid argon adsorbed by weak (carbon dioxide) walls (modelled by a 9-3 potential), how the solvation force oscillates with a period of approximately one molecular diameter (for small separations between the pore-walls, 1-5 molecular diameters). The weak wall interaction was chosen because of its relevance in studies of wetting transition. For large wall separations, the solvation force loses its oscillatory behaviour and eventually it goes to zero. The same authors in later papers [51, 52] observed a first order transition, calculating the solvation force (f) as a function of the wall separation (l). For a Lennard-Jones fluid confined by two identical walls, they observed an abrupt change from a gas-like state to a liquid-like state when l was reduced at fixed temperature and chemical potential. The oscillatory behaviour of the solvation force has also been observed in fluids between two structured walls [53], indicating that the oscillatory character of the confined fluid seems not to be dependent on the nature of the walls, at least for intermediate to large separations. Curry et al. [54] also observed oscillations in the interfacial

tension as a function of the pore size and the registry for a Lennard Jones fluid confined by two structured plates.

Schoen and co-workers conducted Grand Canonical Monte Carlo simulations to investigate the influence of the solid wall on the fluid. They performed simulations in small pores using structured and structureless walls. They found that planar walls induce order normal to the walls whereas structured walls not only produce the same transverse order but they also produce order parallel to the walls [32]. However, Peterson et al. [37], also in Grand Canonical Monte Carlo simulations, showed for a Lennard-Jones fluid within cylindrical pores (with strong wall-fluid attraction) that the first adsorbed layer can take solid-like ordering for a continuous unstructured wall, provided the bulk phase is a dense liquid.

An interesting subject, that has been intensively studied for the gas-liquid transition in confined fluids, is the nature of adsorption at the transition. Several papers have investigated adsorption isotherms and the hysteresis which can accompany these; that is when the adsorption branch of the isotherm does not coincide with the desorption one.

Early work [55, 56], in the Grand Canonical ensemble, of adsorption isotherms of Lennard Jones fluids confined between two continuous walls did not report any manifestations of hysteresis. However, later, Quirke [57] reported hysteresis for a model of N_2 in a graphite slit-pore. Peterson and Gubbins [58] also reported hysteresis in the Grand Canonical ensemble, for a Lennard Jones fluid confined in a cylindrical pore.

Papadopoulou and co-workers [38] studied adsorption hysteresis in cylindrical and slit pores using the Grand Canonical ensemble. For slits, they work with a lattice gas model (only nearest-neighbour interactions were considered) between two walls (using a 9-3 potential to model these) and for cylinders, a Lennard Jones fluid within "carbon-dioxide walls". They concluded that the effects of the pore ends have significant influence on the hysteresis. They performed two kinds of simulation. In the first they imposed periodic boundary conditions in the simulation

box, containing the whole pore, and in the second they used a type of bulk fluid reservoir attached to the pore ends. They observed that the use of periodic boundary conditions extends the desorption branch. The adsorption branch is practically unaffected. Periodic boundary conditions also influence shape of the hysteresis loop, since rounded knees appear in the curves when these are employed.

Jiang et al. [34] in their studies of adsorption isotherms showed that for low temperatures the hysteresis is large but as the temperature increases the hysteresis loop becomes smaller and it disappears at high temperatures. They performed a combination of Grand Canonical Monte Carlo and Molecular Dynamic simulations for a Lennard Jones fluid with the parameters appropriate to mimic fluid methane. For the wall- fluid interaction the walls were modelled by a 10-4-3 potential with parameters modelling graphite. On the other hand, Schoen et al. [59], in a study of a Lennard Jones fluid confined by two structured walls, claimed that the hysteresis observed in molecular simulations is due to the time limitation (the length of the Markov chain). They argued that the hysteresis can be diminished by increasing the surface area and the length of the Markov chain.

Using a variation of the isobaric-isothermal ensemble, Finn and Monson [60] conducted adsorption studies for slit pores. For hard spheres between hard walls in one and three dimensions they calculated density profiles, showing that their results agreed well with the exact analytical ones in D=1 [61]. In a comparison between the Grand Canonical and their isobaric-isothermal ensemble they also investigated the multilayer adsorption of a 3D Lennard Jones system confined by planar walls which interact with the fluid via a 9-3 potential, mimicking the argon/graphite interface. Since the isobaric-isothermal ensemble has no difficulties sampling high density regions, they found there was less uncertainty in their results using this ensemble.

Capillary condensation has been studied by several authors [40, 51, 52, 55]. Peterson and co-workers [37], in series of Grand Canonical Monte Carlo simulations, observed a series of layering transitions at temperatures below the bulk triple point.

Starting from an empty pore they observed distinct layering transitions prior to capillary condensation (when the pore is totally filled by liquid) as the chemical potential was increased.

In a similar study, Jiang et al. [34] performed simulations in slit-pores for a model of methane confined between graphite walls for several pore widths. They found various layering transitions in the adsorption isotherms. The first transition is due to the creation of the first adsorption plane, the 2D fluid-solid transition of the contact layer. Increasing the chemical potential (at constant temperature) the isotherm undergoes a discontinuous jump, at the formation of the second adsorbed layer. The process finally ends when the pore is completely filled, i.e. capillary condensation occurs. They repeated the same procedure for several temperatures and they observed that the discontinuous jump at the layering transition, for low temperatures, becomes continuous at high temperatures, i.e. there is a layering critical point. Since they also found hysteresis they calculated the free energies necessary to locate the equilibrium phase transition. Thus, they could present a detailed phase diagram for one particular pore size. The grand potential was calculated by integration of the adsorption. They integrated the adsorption (and desorption) curve for one particular isotherm, using the equation

$$\left(\frac{\partial \Omega}{\partial \mu}\right)_{T,V,A} = -N \tag{2.20}$$

where N is the average number of atoms (see e.g. equation 2.2). For the gas branch the reference system is:

$$\Omega^{id}(\mu) = -k_B T N^{id}(\mu) \tag{2.21}$$

for a low density. For the liquid branch the reference system can be calculated using equation 2.20 and 2.21 along a continuous and reversible isotherm (above the

layering or condensation critical temperature), then integrating between isotherms using the equation:

$$\left(\frac{\partial(\Omega/T)}{\partial(1/T)}\right)_{V,A} = U - N\left(\frac{\partial(\mu/T)}{\partial(1/T)}\right)_{V,A}. \tag{2.22}$$

One of the disadvantages of the Grand Canonical ensemble is that it does not allow the direct observation of two phases present in the same box. Thus, some authors have tried simulations using Molecular Dynamics techniques [62,63] to study adsorption phenomenon.

Heffelfinger et al. in a series of Molecular Dynamics simulations of Lennard Jones fluids in cylindrical pores investigated adsorption isotherms calculating free energies (as in reference [34], explained above) to locate the onset of capillary condensation [64]. One of the most significant results given by these authors is that they are able to determine the capillary critical point (predicted on general theoretical grounds [41]). The capillary critical point seems to be shifted below that of the bulk as result of confinement (see e.g. figure 1.1). However, probably the most detailed study of capillary condensation was performed by Binder and Landau [65]. In their Monte Carlo simulations for a three-dimensional lattice gas model, with nearest-neighbour attractive interaction, confined by parallel walls which exerted local surface fields on the neighbouring atoms they accurately located a capillary condensation critical point.

Dynamical properties of the confined fluid, such as the diffusion coefficient of the layers, are discussed by Schoen et al. [66,67] for a Lennard-Jones fluid confined by both structured and structureless walls. From this work and that of others [31], one can observe how the diffusion coefficient oscillates as a function of the pore size and what effects the walls have on the self-diffusion of a particle in the pore.

The study of confined fluids is not restricted to standard simulations, such as the Canonical, Isothermal-Isobaric and Grand Canonical ensemble. For instance, other

ensembles have been used to investigate the structure of the fluid [68]. Svensson and Woodward used another ensemble as an alternative to the Grand Canonical, keeping the chemical potential constant in the isotension ensemble [69]. If comparison with results from Surface Force Apparatus measurements is required, the Grand Isostress ensemble probably gives more direct information [70].

2.1.3 Experimental and Theoretical work

Capillary condensation has been observed experimentally, e.g. in adsorption experiments for Oxygen and Krypton in sol-gel glasses [71] (for a brief description of these glasses see section 1.3 of chapter 1). There are also many studies of mass and volumetric adsorption isotherms which show capillary condensation (see e.g. [41] and references therein). More recently, a Positronium Annihilation technique has been used to investigate capillary condensation of N_2 gas and CO_2 in Vycor glass [20, 21, 72]. Moreover, these authors mapped out a phase diagram for the CO_2 system, indicating the shifts in the coexistence lines of the confined fluid with respect to the bulk ones.

Capillary condensation (or capillary evaporation) has also been described in many theoretical papers. Density functional theories [40, 41, 44, 45, 73–75] which are based on minimization of an approximate Grand potential functional (which is a functional of the local density [76]) have given much insight, and interesting predictions of competitions between different phase transitions, e.g. prewetting and condensation [41].

In the light of the vast amount work done by experimentalists, theoreticians and computer simulators, we can probably assume that the key features of capillary condensation are now well understood.

2.2 Liquid-Solid Transition

The liquid-solid transition of confined fluids has not been studied in as much detail as the liquid-gas transition. For instance, we do not know systematically the shift of the boundary lines in the phase diagram. From the Kelvin equation (equation 2.18) we have now that the β and α phase can be identified with the liquid and the the solid respectively. However, in this case it is not clear (for a given model) which of the interfacial tensions is smaller, σ_{ws} or σ_{wl}. There is also a practical feature to consider if the bulk fluid in the reservoir freezes first. In this case there are no particles flowing from the thermal bath to the pore. Thus, the freezing temperature in the pore may depend on this effect and these may much more extended hysteresis. Here I review some relevant results for this transition.

2.2.1 Computer Simulations of the Liquid-Solid Transition in Bulk Systems

Before any discussion of the liquid-solid transition in confined fluids a brief summary of results for the bulk transition is presented. Investigations have been performed for hard and soft particle potentials and for two and three dimensions. The first Monte Carlo simulations of hard disks were performed many years ago [77]. Alder and Wainwright [78] showed the existence of two different phases in this system, the fluid at low densities and the solid at high densities. Hoover and Ree [79], using a single-occupancy cell method (in Monte Carlo simulations), evaluated the entropy in the solid phase for the two dimensional hard disk system. Using this method they calculated the chemical potential of the liquid and the solid phase to find the equilibrium state of the system. However, the transition can be quite different in two and three dimensions. While in three dimension the transition is a first-order transition, in two dimensions it is not necessarily first order. It may be a continuous transition. For a detailed study of two dimensional systems the reader should see reference [80].

Alder and Wainwright [78], using the cell method, investigated the melting transition for a hard sphere system (a three dimensional system) . They found the equilibrium parameters for the transition to be a pressure of $P = 8.27Nk_BT/V_0$, where V_0 is the volume at close packing and densities equal to 0.736 and 0.667 of that at close packing for the solid and the liquid respectively. The solid-liquid transition has also been studied for Lennard Jones systems using conventional simulations in the NVT ensemble by Hansen and Verlet [81] and by Ladd and Woodcock [82,83]. Hansen and Verlet determined several equilibrium pressures for different values of temperatures. As they also performed simulations for the gas-liquid transition they could estimate the location of the triple point. Ladd and Woodcock carried out simulations for a large system with all three phases in coexistence and the properties of interest were measured directly by observing regions in each phase. Their results showed fairly good agreement with those of Hansen and Verlet. The complete liquid-solid coexistence line was studied in more detail recently by Agrawal and Kofke [84]. The melting line was computed by performing a thermodynamic integration along the coexistence line using the appropriate Clapeyron equation (see chapter 5). A further review of this topic (solid-liquid transition in 3D) may be found, e.g. in reference [85].

In order to determine the onset of freezing, in bulk systems, several empirical criteria have been tested. For three-dimensional systems we have, e.g. the Hansen-Verlet criterion [81], which states that when the first peak of the structure factor reaches the value 2.85 the liquid freezes. Another criterion is that given by Wendt and Abraham [86], which measures the ratio of the first minimum to the first maximum of the pair correlation function. Freezing occurs when the ratio is approximately equal to 0.14. Probably the oldest melting criterion is that due to Lindemann [87], which focuses on the ratio between the root mean square displacement of an atom from its equilibrium position in the solid and the nearest neighbour distance. For Argon at melting this value is approximately 0.13. These criteria are valid for soft and hard systems and are quite well-obeyed by real atomic

liquids, including liquid metals. For two dimensional systems the criteria are different. Caillol et al. [88] in a study of hard disks found that freezing occurs when the first maximum in the structure factor is approximately 4.4. For simulations in two dimensional fluids interacting with purely repulsive potentials, Broughton et al. [89] showed that the peak of the structure factor is about 5.0 near freezing. Ranganathan and Pathak [90], in Molecular Dynamics simulations of a two-dimensional Lennard Jones fluid, found that freezing transition occurs when the first peak in the structure factor reaches the value of 4.6 and the ratio between the first minimum and maximum in the pair correlation function is approximately 0.07.

2.2.2 Computer Simulations of the Liquid-Solid Transition in Confined Fluids

Since it is more difficult to simulate a solid phase (or a liquid at very high density), using the Grand Canonical ensemble, less research has appeared in the literature for the liquid-solid transition of confined fluids. For high density systems the probability of particle creation and destruction becomes very low (i.e. poor convergence of the Monte Carlo averages). Although some attempts have been made, none of them (in my opinion) have carried out a comprehensive analysis for the freezing transition. Many questions remain unanswered.

Several years ago, Cape studied the structure and dynamics of a repulsive fluid. He conducted Molecular Dynamics simulations of 4000 particles for a r^{-12} fluid interacting with a hard wall, at conditions close to the bulk freezing transition [91]. Although he found pronounced layer structure parallel to the wall, he did not see evidence of any crystallization for the first contact layer i.e. no evidence of heterogeneous nucleation of the crystal prior to the bulk freezing.

Later, however, Courtemanche and van Swol observed the growth of a crystalline layer for hard spheres near a planar hard wall, i.e. they observed prefreezing, in normal Molecular Dynamics simulations [92] and subsequently in Molecular Dynamics

in the NP_zT ensemble [93]. They showed that the hard wall is wetted by a hard sphere crystal.

Earlier in testing their new method, Molecular Dynamic simulations in the NP_zT ensemble, Lupkowski and van Swol performed simulations which investigated the crystallization of a fluid confined by two parallel walls -a slit-pore with 180 fluid-particles. In their brief investigation they observed a type of capillary freezing for a system of hard spheres between two hard walls [94], i.e. solid formed as the pressure P_z was increased. However they were not able to determine the chemical potential and confirm that freezing occurred at a lower value than for the bulk transition.

Ma and Banavar [35] carried out studies for Lennard Jones particles (at high density, $\rho = 0.95$) confined in a slit pore with structured walls using Molecular Dynamics simulations. The fluid interacted with either purely repulsive or Lennard Jones wall particles and the pore sizes were reasonably large (l= 13.3, 12.92 and 17.76). They found that for Lennard Jones walls the layers seem to freeze from the walls towards the centre while for purely repulsive walls all the layers appear to freeze simultaneously. This suggests that the layer-by-layer growth is due the attractive part of the Lennard Jones wall-fluid potential. When the system is warming up, the Lennard Jones walls ensure that the solid goes back to the same original state (liquid-like), i.e. the layered structure disappears. The repulsive walls do not produce the same effect, however. Here it seems that the system reaches a metastable state with layered structure. These authors also investigated the layer structure in some detail. Their calculations of the diffusion coefficients indicated that the first layer remains liquid-like for repulsive walls, in contrast to the layers near a Lennard-Jones wall. Finally their results, for the Lennard-Jones walls, suggest a depression in the freezing temperature, since no solidification was found in the centre of the pore for $T > 0.8$ (bulk freezing is approximately 1.1). However, no calculations of free energies were reported to corroborate that result.

Recently, Hug et al. [95] simulated a repulsive Yukawa fluid between repulsive Yukawa walls to investigate colloidal systems. In order to mimic experimental situ-

ations they performed simulations in the NPT ensemble for slit pores surrounded by a reservoir of bulk fluid. In this way, they have the pore fluid in contact with the bulk at controlled bulk pressure (chemical potential). They showed, from their results, that at pressures below bulk freezing the particles in the pore seem to form a crystal whereas the bulk remains liquid-like, indicating capillary freezing. Then they sketched a phase diagram based on their observations of the structure of the confined fluid only. However, Hug et al. did not report any hysteresis loop or any calculations of free energies that would allow them to locate the equilibrium transitions.

Very, recently, Miyahara and Gubbins [96] performed simulations in slit pores for Lennard Jones methane interacting with different types of walls. What is surprising in this paper is the successful use of the Grand Canonical Monte Carlo method for a solid and for the high density liquid.

In their studies of freezing they found rather interesting results. If the fluid is confined by hard walls the freezing transition occurs at lower temperatures that in bulk (at fixed chemical potential or pressure). On the other hand, if the fluid is confined by strongly attractive walls (graphite) the freezing temperature is raised to a higher value than that in the bulk. If methane walls are employed, i.e. the wall-particle/fluid-particle interaction is the same as fluid-fluid, there is no significant temperature change. The graphite and methane walls were modelled by the continuous 10-4-3 potential. For simulations in very small pores they found that the freezing transition disappears. The change in the freezing temperature in the pore with respect of that in bulk was explained in terms of the form of the wall-fluid potential using a simple model. They obtain a relation between the potential and the elevation in the temperature, a strongly attractive wall-fluid potential giving a higher freezing temperature. In their model the change in the temperature is proportional to the change in the potential (between a particle in the liquid which feels the wall potential and a particle in the solid phase which feels the potential due to its own solid molecules instead of the wall potential, i.e. assuming that the structure

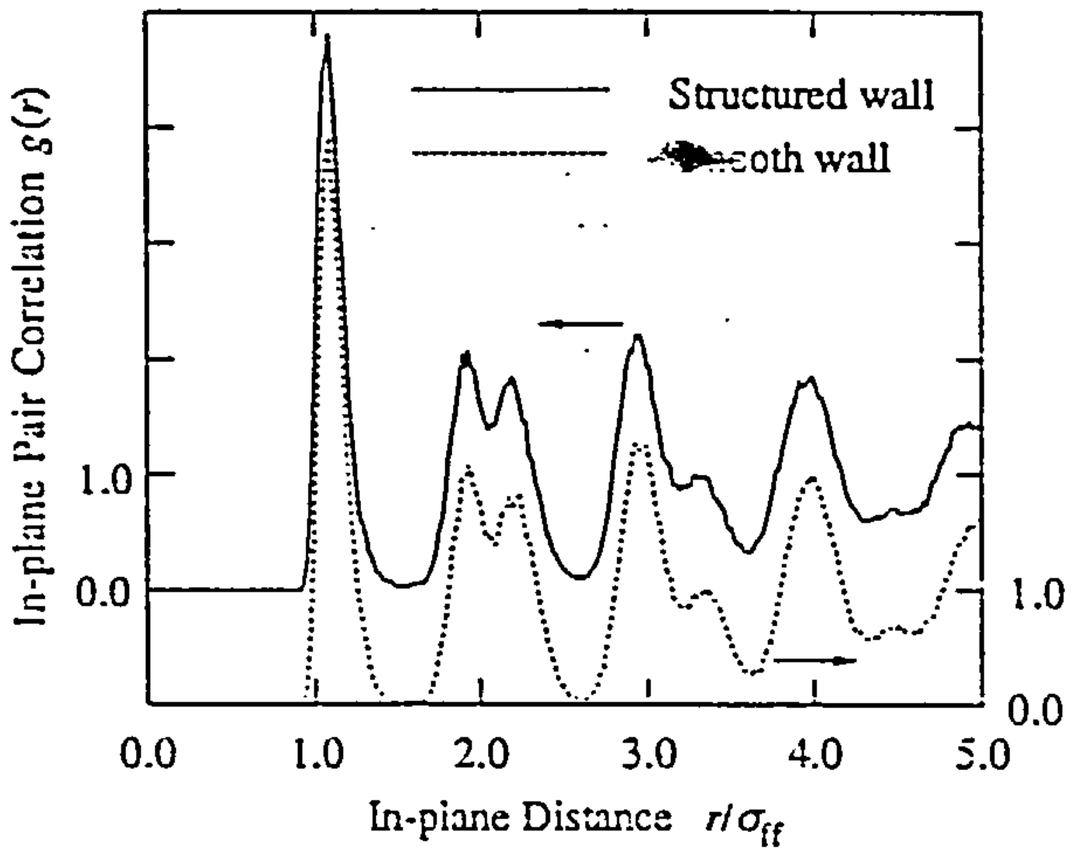

Figure 2.2: The in-plane pair correlation function for the contact layer for methane confined by structured and structureless graphite walls. The figure was taken from reference [96].

of the bulk solid is negligibly perturbed due to the confinement)

They also investigated the structure of the confined fluid employing both smooth and corrugated walls. However, surprisingly, they did not find any significant difference in the structure of the fluid, even for the first contact layer (see figure 2.2). The in-plane pair correlation functions for the contact layer in both are similar, indicating that corrugated and smooth walls produce the same type structure in the confined fluid.

When the temperature was raised they observed hysteresis in their mean density versus temperature graphs. Although the extent of the hysteresis was very dependent on the pore width, they did not calculate any free energies in order to

locate the equilibrium phase transition. They claimed that for certain pore widths the hysteresis is very narrow, i.e. the difference between the freezing and melting temperature is not large. Thus, the transition should be somewhere between these values. Using this argument and assuming that the creation and deletion of particles is more successful on cooling they assumed that the equilibrium transition lies closer to the freezing temperature than the melting temperature.

For very small pores, the behaviour of confined fluids can be rather different. Then the effects of the reduced dimensionality may be more important. Using Monte Carlo simulations Diestler et al. [68, 70, 97] simulated Lennard Jones fluids in very small pores (up to four layers) between two structured walls (constructed from particles in the face (100) of the fcc crystal). They studied the shear melting of the confined fluid as function of the shear stress, temperature and a registry parameter which measures registry between the top and bottom structured walls. They found that shear melting can be either continuous or discontinuous according to the particular choice of the parameters.

Schmidt and Löwen [98] performed studies of phase transitions of hard spheres confined between two hard walls. They carried out Monte Carlo Simulations in very narrow pores. The wall separation, (l), was from one to two sphere diameters, l equal to one molecular diameter corresponds to the two dimensional limit. They mapped out the phase diagram for this system and they found not only a liquid-solid transition but also solid-solid transitions (between buckled, layered and rhombic crystals). While the liquid-solid transition is always strong, the solid-solid transition can be both strong and weak.

In summary, many of these papers provide strong indications of the direction of the shift of the transition temperature (or pressure) with respect to the bulk, but none of them have attempted to calculate free energies in order to confirm these indications. Moreover, the most detailed studies have focused on repulsive fluids e.g. hard sphere fluids confined within hard walls. More realistic fluids or walls (e.g. Lennard-Jones interactions) have not been investigated systematically. Thus, the

main motivations for the present investigation are to ascertain the location of the shifted phase boundaries, characterize the nature of the fluid-solid phase transition in confined systems and, study the role of different wall-fluid interactions for the structure of the confined solid.

2.2.3 Experimental background

Many experimental studies, using a variety of different techniques, have investigated the freezing of confined fluids. Here I mention some of the relevant results; this is by no means a comprehensive survey of this large subject.

The shift in the freezing temperature of fluids confined in mesoporous solids has been studied by several authors. Awschalom and Warnock [23] used a pico second optical technique to monitor the freezing of oxygen confined in controlled pore (sol-gel) glasses with radii in the range 10-250 Å, and in vycor glass with radii up to 22 Å. They showed that the freezing temperature is strongly affected by the pore size and that freezing occurs at lower temperatures than in bulk. They found pronounced hysteresis in the freezing and the melting behaviour and speculated that the hysteresis could be produced by an amorphous layer formed at the pore walls. After the liquid in the centre freezes, the freezing may propagate partially through the amorphous wall layer, changing the effective surface tension. Using a simple geometrical model, and equating the free energies of the two phases in the system, they estimated that the depression in the temperature should vary with the inverse of the pore radius (figure 2.3). This is equivalent to the Kelvin result discussed earlier.

Ultrasonic velocity and attenuation experiments for ethanol in the same type of sol-gel glasses by the same group [26] found clear evidence for depression of the freezing temperature. For small pores, this could be as large as 20% of the bulk value. They also observed that the melting occurred at lower temperatures than in bulk but was at higher temperatures than the freezing. This investigation

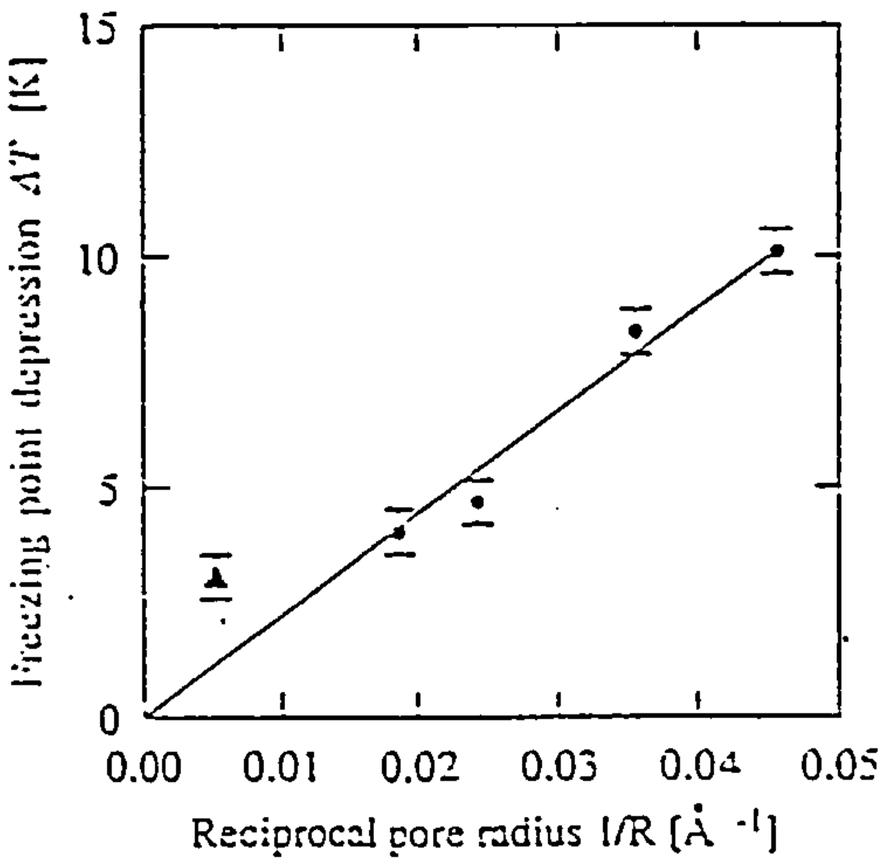

Figure 2.3: Freezing of oxygen in sol-gel glass (using a picosecond optical technique). Note the depression in the temperature as a function of the inverse of the mean pore radius. Figure reproduced from reference [23].

did not find evidence that the fluid freezes from the wall, since their velocity and attenuation data remained unchanged until the fluid completely froze. This would not be expected if the liquid were partially converted into a solid.

A study of liquid Indium metal in silica glasses [99] using differential scanning calorimetry technique showed similar effects, i.e. depression of the freezing (and melting) temperature.

Torii et al. [25] performed heat capacity and torsional oscillator experiments for para-hydrogen in Vycor glasses. They conducted two series of experiments corresponding to different pore sizes. For very small pores they did not observe a freezing transition (pore radius < 12 Å). For large pores (pore radius > 15 Å), they found

two different freezing transition temperatures, both at values below the bulk one. They attributed these two transition temperatures to the two different radii which characterize the pore size distribution measured for their glass. One interesting point in their investigations for large pores is that they did not observe the freezing transition until a critical filling of the pore was reached. This suggests that the freezing process depends not only on the pore size but also on the degree of pore filling.

In neutron scattering measurements, Sokol and co-workers [100] investigated the freezing of O_2 and D_2 in Vycor glass with average pore diameter of 70 Å. As in earlier work, they found a depression in the freezing temperature. However, when they compared the Bragg peaks of the confined solid with those in bulk they found that for confined O_2 these are in good agreement with those of the bulk, but for confined D_2 the solid structure does not take the bulk crystalline form, indicating that confinement brings about more than just a shift of the bulk transition in this particular case. A different type of study of the structure of confined fluids can be found in the paper of Grier and Murray [101]. They investigated a colloidal system confined between two parallel, optically smooth glass plates using time-resolved digital video microscopy techniques. In their studies they found that freezing proceeds through the gradual formation of a layered fluid near the wall, and finally crystallization of the whole liquid.

Recent studies [22] of several cryogenic fluids (hydrogen, neon, oxygen and argon) in vycor and silica xerogel glasses (see chapter 1) using heat-capacity and high ultrasonic techniques found a liquid-solid phase transition, with the freezing occurring at lower temperatures than melting, but both lying below the bulk melting point. In a detailed analysis of argon the authors found that the freezing process is highly irreversible in contrast with melting, which is nearly reversible (if the solid is partially melted by heating, it refreezes when the fluid is recooled).

Investigations of water in thin quartz capillaries (of radius $\approx 1\mu$m) showed that the viscosity (measured on the basis of shift rates of ice columns) is greater than the

bulk value at the same temperature [102, 103]. Ramsey and Poinsignon [104] conducted neutron quasi-elastic and inelastic scattering experiments for water in silica gels (pore radius $\approx$ 20 Å). They observed a depression in the freezing temperature and in the translational diffusion, below those values in bulk, when the pore size is reduced.

Although several authors have seen a lowering of the freezing temperature for confined fluids, the majority of the results are for a single pressure only (usually atmospheric) and data for different thermodynamic states (e.g. pressures) is not presented. The determination of a complete phase diagram for the confined fluid has been attempted by few researchers.

More than ten years ago, Beamish et al. [24] investigated ^{4}He in Vycor, with pore radius of approximately 34 Å. Using a transverse sound velocity technique they observed an increase of up to 30 bar in the freezing pressure with respect to bulk when ^4He is confined and they mapped out freezing lines in the (P, T) diagram. They also reported hysteresis in their experiments.

Duffy et al. [21,72], using a Positron Annihilation technique (measuring the ratio between the emission of 3γ and 2γ photons by the annihilation of the ortho and para-positronium formed from positrons) investigated not only the liquid-solid but also the liquid-vapour transition (capillary condensation). They found that for CO_2 in Vycor (average pore radius of 20 Å) that the hysteresis at the liquid-solid transition is larger than that at the liquid-vapour one, and in keeping with other authors, that the freezing (melting) transition occurs at lower temperatures than in bulk, with the freezing occurring at a lower temperature than melting. They made some effort to map out the liquid-vapour and liquid-solid coexistence lines, for confined CO_2, in order to make a comparison with the bulk phase diagram. Finally, from the merging of the coexistence lines they located what they called the quasi triple-point of the confined fluid (Figure 2.4).

Due to the complex geometry of the porous solid, a glass with a network of interconnected pores of amorphous shapes, it is often rather difficult to interpret the

experimental results. Comparison between theory and experiment is not straightforward. Thus, the observed shift in the phase boundaries or changes in the structure of the fluid can be associated with special topological features of the confining space. Dynamicals of the confined fluid may also depend on the interconnectivity. Whether the depression of the freezing temperature of liquids in these materials is a result of the finite-size effect or whether the porous solid brings abut some (non-equilibrium) supercooling below the bulk temperature is still a matter for discussions.

Thus, in order to understand better the actual behaviour of a confined fluid (and to observe the finite-size effects more directly), some authors have performed experiments in simpler geometries. Christenson, in a detailed experiment on alcohols between mica surfaces [27], investigated freezing temperature depression and showed this is inversely proportional to the distance between the surfaces.

Klein and Kumacheva [28] conducted experiments in the Surface Force Apparatus (two atomically smooth mica surfaces, see chapter one for a brief description of the SFA) for the organic liquid octamethylcyclotetrasiloxane (OMCTS). In this investigation the liquid to solid transition, as a function of the surface separation, was studied by monitoring the effective viscosity. For large surface separations the system exhibits a liquid-like shear viscosity. When the separation is reduced the rigidity of the confined system increases by several orders of magnitude, indicating that the system undergoes a transition to a solid phase.

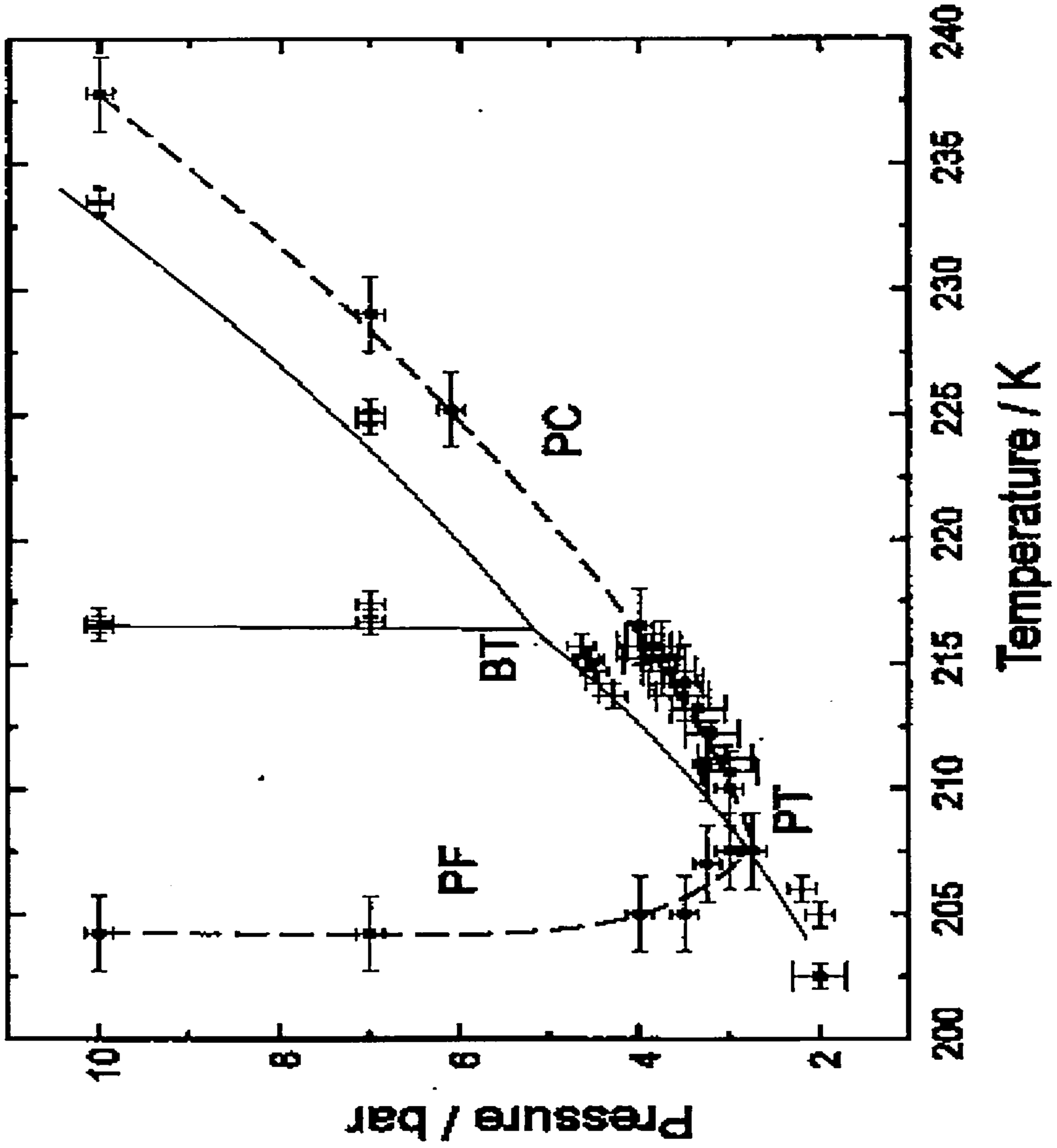

Figure 2.4: Phase diagram for CO_2. The (+) symbols and the solid curves refer to the bulk fluid. The solid symbols are for CO_2 confined in Vycor glass. The dashed lines are to guide the eye. PC means pore condensation and PF pore freezing. PT is the quasi triple point of the confined system. The figure was taken from reference [72]. Note that all the positron data were taken on cooling the samples at fixed pressure. Because of hysteresis different PC and PF lines would be obtained using data taken on heating.

Chapter 3

COMPUTATIONAL TECHNIQUES AND MODELS FOR PORE SYSTEMS

3.1 Introduction

Until relatively recently, experiment or pure theoretical physics were the only tools we had to tackle the fundamental problems of nature. With the invention of computers a new branch of science came about, namely computer simulations [77]. This is a different tool that is neither experimental nor theory; it can be considered as something in between. From the theory viewpoint this new tool allows us to examine the predictions of theories which relate to well-defined models and which can be difficult to test with real experiments. From the experimental viewpoint it can be used to measure properties that could be difficult to obtain directly from experiments. Even though simulations can help theoreticians and experimentalists to predict physical phenomena, they do have some limitations. For instance the size of the simulations (the number of particles) is always limited. Typical simulations consider hundreds of particles or in some cases thousands (depending on the power

of the computer and details of the model). Because of this finite size, surface effects can be significant and doing simulations which mimic real infinite systems is not always straightforward. To avoid (and minimize) this finite size effect, it is usual to work with what are called periodic boundary conditions. This means that the system is composed of a central box (we usually envisage a cubic box, however this is not necessary and other geometries can be used [105]) surrounded by identical replicas of this box in all directions (see figure 3.1 for a two-dimensional example). When a particle enters or leaves the central box its image will leave or enter through the opposite face keeping the number of particles in the system fixed. Since the main interactions, for a given particle, come from the neighbouring particles (assuming pairwise interactions) it is convenient to work with truncated potentials in order to save CPU time. This means that one particle interacts only with those within a sphere of radius r_c (the cut-off radius) centered on this particle. For particles outside the sphere all interactions are zero:

$$\phi^T(r) = \begin{cases} \phi(r) & r \leq r_c \\ 0 & r > r_c \end{cases} \tag{3.1}$$

Obviously the values of the thermodynamic properties, such as the pressure, chemical potential and internal energy, need to be corrected due to the missing interactions [105], if the results are to be appropriate to systems with a power law potential such as the Lennard Jones potential. In bulk these corrections are usually calculated assuming that the pair correlation function $g(r) \approx 1$ for $r > r_c$.

Since the discontinuity in the potential can produce problems in evaluating quantities such as the force between particles, some authors avoid the difficulty by subtracting the value of $\phi_c = \phi(r_c)$ to the potential. Now the potential is shifted and truncated:

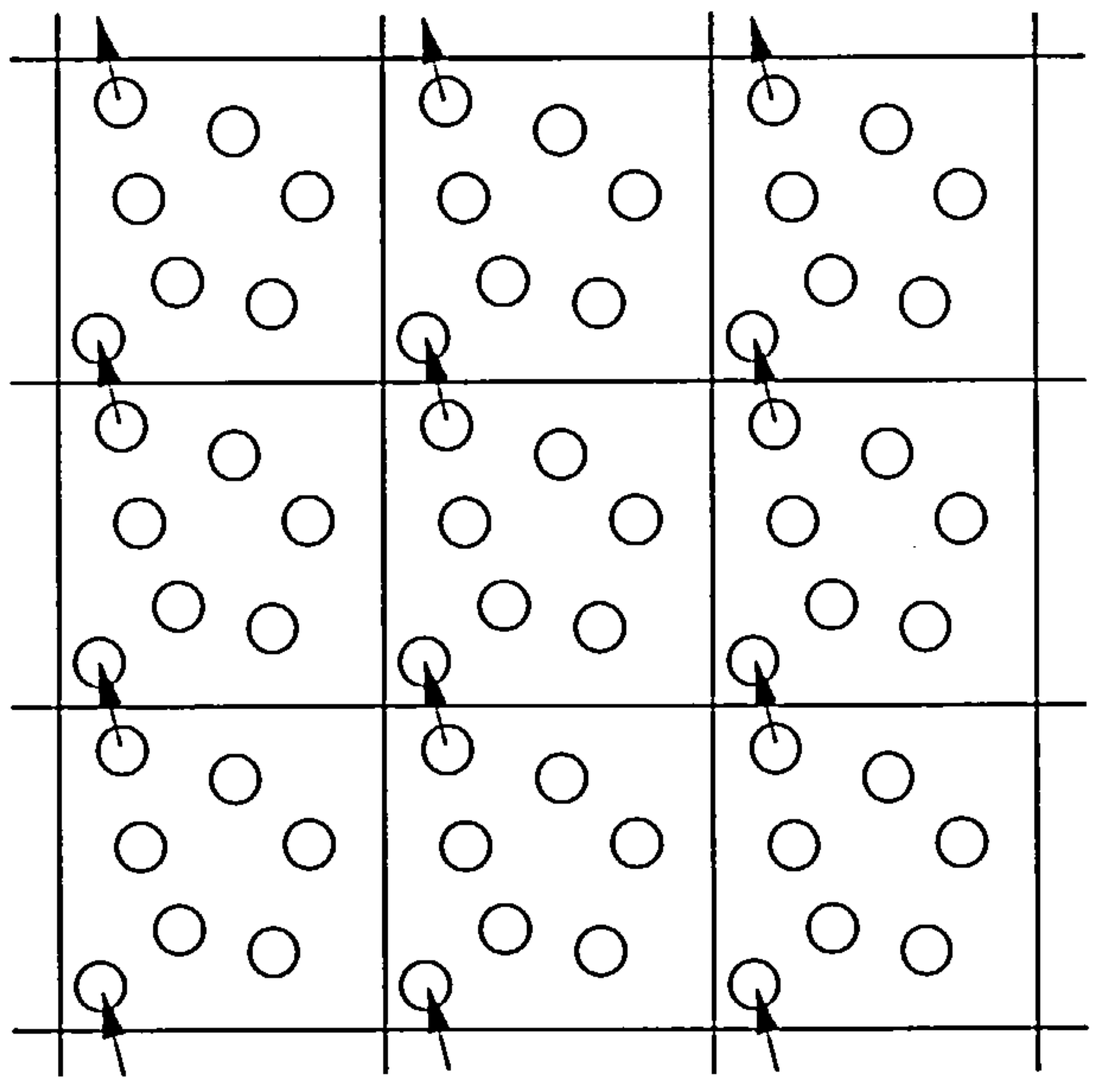

Figure 3.1: A two-dimensional example of a periodic system

$$\phi^{ST}(r) = \begin{cases} \phi(r) - \phi_c & r \leq r_c \\ 0 & r > r_c \end{cases} \tag{3.2}$$

Again, the thermodynamic properties should be corrected, especially if we are interested in comparisons of results from this fluid model with those of real experiments [106].

There are two main techniques used in computer simulations. I discuss them in the following sections.

3.2 Molecular Dynamics.

Molecular dynamics, as its name suggests, solves the equations of motions of the particles which constitute any physical system. For instance, if we have a system with N particles interacting with each other through a known potential, their trajectories can be determined by solving the classical equations of motion. These equations can be obtained using standard techniques such as the Lagrangian method [107]; they are equivalent to the traditional Newton equations. In cartesian coordinates we have:

$$m_i \ddot{\mathbf{r}}_i = \mathbf{f}(i) \tag{3.3}$$

where m_i is the mass of atom i and $\mathbf{f}(i)$ is the total force exerted on the particle i. This is a set of $3N$ (for a system of N particles) coupled, second-order differential equations which governs the trajectories of the particles. Obviously it is not possible to solve the equations analytically, therefore they are usually solved by finite difference methods. The idea is the following: if we know all the positions and momenta of the particles at any time t then we attempt to predict the positions and momenta for a time $t + \delta t$. Here we will assume that all interactions among the particles are described by a continuous potential (for discontinuous potentials such as hard spheres the method is rather different [105, 108]). Hence we can make a Taylor expansion about the position $\mathbf{r}_i(t)$.

$$\mathbf{r}_i(t \pm \delta t) = \mathbf{r}_i(t) \pm \mathbf{v}_i(t)\delta t + (1/2)\mathbf{a}_i(t)\delta t^2 + ... \tag{3.4}$$

a is the particle acceleration. Adding the resulting two equations we get an expression for the position

$$\mathbf{r}_i(t+\delta t) + \mathbf{r}_i(t-\delta t) = 2\mathbf{r}_i(t) + \mathbf{a}_i(t)\delta t^2 \tag{3.5}$$

which rearranges to

$$\mathbf{r}_i(t+\delta t) = 2\mathbf{r}_i(t) - \mathbf{r}_i(t-\delta t) + \mathbf{a}_i(t)\delta t^2 \tag{3.6}$$

and if we subtract them we get another expression for the velocity

$$\mathbf{v}_i(t) = \frac{\mathbf{r}_i(t+\delta t) - \mathbf{r}_i(t-\delta t)}{2\delta t}. \tag{3.7}$$

This algorithm is the well known Verlet algorithm [109] which is probably the most common method used to solve these equations. There are also other methods to solve them, e.g. the predictor-corrector method or modifications of the Verlet algorithm such as the 'leap-frog' method (see e.g. reference [105] and references therein). All the properties of the fluid, such as the pressure, temperature, etc, are given as time averages.

Since we are treating conservative systems, an important quantity which should be monitored is the energy. Thus, to maintain the conservation of energy and accuracy in the particle-trajectories the time step δt should be chosen to be not too large.

Sometimes it is useful to have control over the temperature and the pressure in a Molecular Dynamics simulation. This is the case in several simulations of confined fluids. In these simulations, one approach is to make the instantaneous pressure and temperature constants of the motion. This can be done by introducing appropriate Lagrange multipliers to the equations of motions. Then, one proceeds to solve these modified equations [110] (using one of the standard methods mentioned above):

$$\dot{\mathbf{r}} = \frac{\mathbf{p}}{m} + \chi(\mathbf{r},\mathbf{p})\mathbf{r} \tag{3.8}$$

$$\dot{\mathbf{p}} = \mathbf{f} - \chi(\mathbf{r},\mathbf{p})\mathbf{p} - \xi(\mathbf{r},\mathbf{p})\mathbf{p} \tag{3.9}$$

$$\dot{V} = 3V\chi(\mathbf{r},\mathbf{p}). \tag{3.10}$$

V is the volume of the simulation box, $\mathbf{p}$ is the momentum, χ and ξ are the Lagrange multipliers which can be viewed as the rate of dilation of the system and a type of friction coefficient, respectively. Explicit expressions for χ and ξ follow from the conservation conditions [105,110].

3.3 Monte Carlo Method.

In statistical mechanics we are used to working in terms of the partition function or configurational integral [2]. For instance, if we know this partition function we define the average of any observable $A = A(\mathbf{r})$, which depends on the positions only, (e.g. for the canonical ensemble) as:

$$\langle A \rangle_{NVT} = \frac{\int d\mathbf{r} A \exp(-\beta\Phi)}{Z} \tag{3.11}$$

where we defined the configurational integral Z as;

$$Z = \int d\mathbf{r} \exp(-\beta\Phi) \tag{3.12}$$

Here $\mathbf{r}$ is a shorthand for the positions of the N particles and Φ is the total potential energy.

What the Monte Carlo method does essentially is to estimate the integral in equation (3.11), in such a intelligent way, by generating (sampling) a large number of random configurations from a chosen distribution, in this case $\rho = \exp(-\beta\phi)/Z$.

This method was developed by Metropolis at al. [77] and it is usually known as the Metropolis Monte Carlo Method.

The way to generate these configurations is by performing a Markov chain. Let us define two different states, m and n with distributions ρ_m and ρ_n respectively. These two states are connected by a transition probability π_{mn}, the probability of going from state m to state n. The limiting distribution $\rho \equiv (\rho_1 ... \rho_m ... \rho_n ...)$ must satisfy the eigenvalue relationship

$$\rho\pi = \rho \tag{3.13}$$

which is short for

$$\sum_m \rho_m \pi_{mn} = \rho_n \tag{3.14}$$

and expresses the stationary nature of the equilibrium probabilities. π is a stochastic matrix which satisfies the conditions

$$\sum_n \pi_{mn} = 1 \tag{3.15}$$

$$0 \leq \pi_{mn} \leq 1 \tag{3.16}$$

There is a lot of freedom in the choice of solutions for π. One way is to define the elements of π so that they satisfy the microscopic reversibility condition

$$\rho_m \pi_{mn} = \rho_n \pi_{nm} \tag{3.17}$$

In this case equation (3.13) is satisfied automatically, as may be seen by summing both sides over m and using the equivalent of equation (3.15), namely $\sum_m \pi_{nm} = 1$.

The first solution of equations, satisfying the condition (3.15)-(3.17) was given by Metropolis [77]

$$\pi_{mn} = \alpha_{mn} \qquad \rho_n \geq \rho_m \qquad m \neq n \tag{3.18}$$

$$\pi_{mn} = \alpha_{mn}(\rho_n/\rho_m) \qquad \rho_n < \rho_m \qquad m \neq n \tag{3.19}$$

The condition that the system remains in the same state (which is also a possible state) is given by

$$\pi_{mm} = 1 - \sum_{n \neq m} \pi_{mn} \tag{3.20}$$

α is a symmetrical stochastic matrix ($\alpha_{mn} = \alpha_{nm}$) which defines the probability of attempting a move from any state m to any n. The equal probability of selecting forward and reverse Monte Carlo moves is an essential part of the Metropolis prescription. Then this attempt is accepted or rejected with probability $\min(1, \rho_n/\rho_m)$, and the product of this factor with α_{mn} gives the overall values of π_{mn} reported above.

The distribution ρ depends on the ensemble we are using. For the canonical ensemble where the volume, temperature and number of particles are fixed, the particle movements are accepted with a probability

$$\rho_n/\rho_m = \exp(-\beta\delta\phi_{nm}) \tag{3.21}$$

where $\delta\phi_{nm} = \phi_n - \phi_m$, the difference in the configurational energies of the states n and m respectively. $\beta = 1/k_B T$ where k_B is the Boltzmann constant.

For the Isothermal-Isobaric ensemble the temperature, the pressure and the number of particles are fixed. Here, apart from the particle displacement described by equation (3.21), there is also a volume change with acceptance probability;

$$\rho_n/\rho_m = \exp(-\beta(PV_{nm} + \delta\phi_{nm}) + N\ln(V_n/V_m)) \tag{3.22}$$

$V_{nm} = V_n - V_m$, is the difference in volumes, N is the number of particles and P is the pressure.

In the Grand Canonical ensemble where the volume, the temperature and the chemical potential μ are fixed, it is usual to define three kinds of moves in the system:

a) displacement of a particle.

b) creation of a particle.

c) destruction of a particle.

The first move is executed with the same probability as in the normal canonical ensemble. For creation the probability is given by

$$\rho_n/\rho_m = \exp(-\beta\delta\phi_{nm} + \ln(zV/N + 1)) \tag{3.23}$$

and for destruction the probability is given by

$$\rho_n/\rho_m = \exp(-\beta\delta\phi_{nm} + \ln(N/zV)) \tag{3.24}$$

where z is the activity, defined as

$$z = \exp(\beta\mu)/\Lambda^3. \tag{3.25}$$

V is the volume of the simulation box and Λ is the thermal de Broglie wavelength.

There are also other ensembles with different transition probabilities. The interested reader can find useful information in reference [111] and references therein.

3.4 Models for Pore Systems.

The most common simulation technique used to study pore systems has been the Grand Ensemble Monte Carlo (GEMC) method, where the chemical potential, temperature and volume are fixed [105]. Since real experiments are performed with the bulk fluid in thermodynamic equilibrium with the pore fluid, i.e. at constant chemical potential and temperature, this approach is particularly useful to study these systems. Unfortunately, at high densities, where the freezing transition occurs (which is the primary interest in this work), GEMC becomes more difficult to perform successfully. Nevertheless, some authors seem to be able to employ it, apparently without any problems (see chapter 2 for presentation of Miyahara and Gubbins work [96]). Since the probability of inserting and removing particles is low it is difficult to get accurate data. Hence an alternative ensemble should be used. For much of this work I did computer simulations in the Isothermal-Isobaric ensemble (NPT). Although my simulation follows the main structure of a normal NPT simulation there are some changes appropriate for this particular study (the slit pore) [60,68,94].

3.4.1 Potential Functions.

The simulation consists of a fluid confined between two structureless or structured, rectangular parallel walls separated by a distance l in the z direction. The side-lengths of the walls are S_x and S_y and they lie in the x and y directions. Between the walls, particles are initially placed in a random initial configuration. The total energy of the system is due to the particle-particle fluid interaction and the particle-wall interaction. The interaction among fluid particles is via the Lennard-Jones potential described in chapter 1:

$$\phi_{LJ}(r) = 4\epsilon\left[\left(\frac{\sigma}{r}\right)^{12} - \left(\frac{\sigma}{r}\right)^{6}\right]. \tag{3.26}$$

All calculations were performed using a cut and shifted potential, where the value of 2.5σ was chosen for the cut-off, r_c. For the wall-fluid interaction three potentials were used.

In a simple model we can consider the wall as a continuum of atoms of uniform number density. Thus, if the wall particle-fluid particle interaction is given by the Lennard-Jones potential, and we integrate uniformly over the x, y plane, we get the 9-3 potential,

$$\phi(z) = \frac{2}{3}\pi\rho\sigma'^3\epsilon' \left[\frac{2}{15}\left(\frac{\sigma'}{z}\right)^9 - \left(\frac{\sigma'}{z}\right)^3\right] \tag{3.27}$$

ϵ' and σ' are the parameters describing the wall particle-fluid particle and ρ is the wall density.

This is now a function of the z-coordinate of the fluid particle only. A better model is to consider that the wall-atoms are in a parallel layer structure of uniform density (e.g. for the case of a graphite structure). Then, if we integrate the interaction (Lennard Jones) between one fluid particle and atoms in the first uniform layer of the solid and sum over all the layers, we obtain the 10-4-3 potential. With $\alpha = 1$ this is usually referred to as the Steele potential [112,113]:

$$\phi(z) = 2\rho\pi\sigma'^2\epsilon'\Delta l \left[\frac{2}{5}\left(\frac{\sigma'}{z}\right)^{10} - \alpha\left(\frac{\sigma'}{z}\right)^4 - \alpha\frac{\sigma'^4}{3\Delta l(z+0.61\Delta l)^3}\right] \tag{3.28}$$

Δl is the separation between the solid layers. Once more, this depends on the z-coordinate of the fluid particle only.

I will say more about the parameter α in chapter 5. For now simply note that by changing this parameter from 0 to 1 one changes from a purely repulsive wall ($\alpha = 0$) to weakly attractive walls ($0 < \alpha \ll 1$), to fully attractive walls (α=1). For these cases, neither shifted nor cut-off potentials were employed for the single

wall-fluid interaction

A more realistic model takes into account explicitly the atomic corrugations in the wall. The walls are made by fixing particles at the sites of a face centered cubic lattice (fcc). Each wall has N_s particles and they are aligned in the x and y plane. The first layer coincides with the $z = 0$ plane and the other with the $z = l$ plane. These layers can be in registry with each other or not. Additional layers can be used to accurately represent the solid further from the interface. In any case, the potential will depend on the x, y, and z coordinates of the fluid atom. For this particular simulation, all the interactions, fluid particle-fluid particle and even the wall particle-fluid particle are via the same truncated and shifted Lennard-Jones potential, and the total configurational (potential) energy of the N fluid particles in the system is:

$$\phi = \phi_{ff} + \phi_{fw}^{(1)} + \phi_{fw}^{(2)} \tag{3.29}$$

where

$$\phi_{ff} = \sum_{i=1}^{N-1} \sum_{j>i}^{N} \phi_{LJ}(r_{ij}) \tag{3.30}$$

and

$$\phi_{fw}^{k} = \sum_{i=1}^{N} \sum_{j=1}^{N_s} \phi_{LJ}(r_{ij}), \qquad k = 1, 2 \tag{3.31}$$

ff refers to fluid-fluid interaction, fw refers to fluid-wall interaction and k refers to wall 1 or 2 (solid layers).

A plot of the different potentials as a function of z/σ is shown in figure 3.2; the 9-3 and 10-4-3 potentials are plotted with the same wall-fluid parameters.

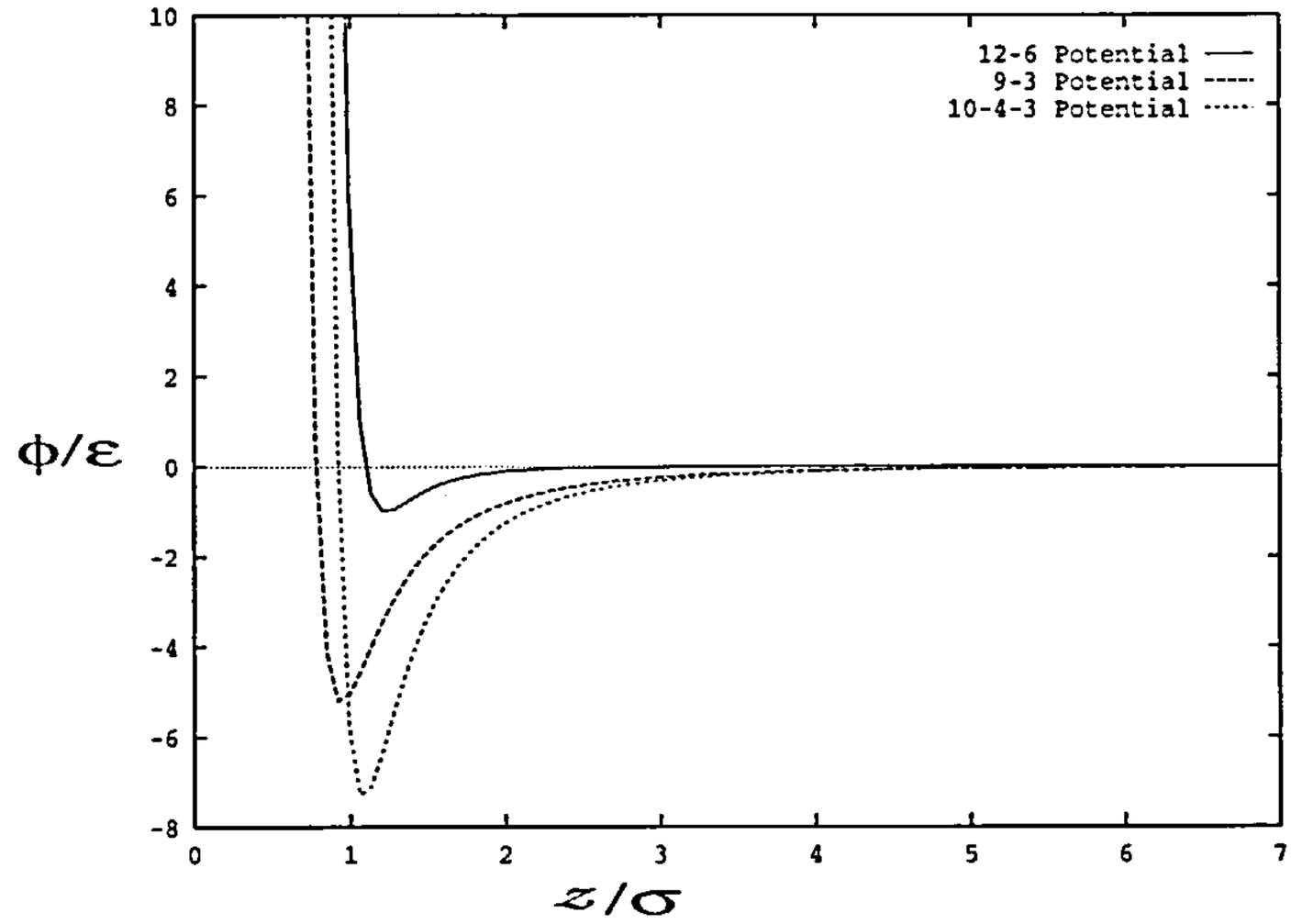

Figure 3.2: The two different single wall-fluid potentials described in this chapter. The LJ pair potential is shown for comparison. The plots are given with the same parameters, $\epsilon' = 1.2771\epsilon$, $\sigma' = 1.0946\sigma$ and $\rho\sigma^3 = \sqrt{2}$. ϵ and σ are the Lennard Jones parameters. For the 10-4-3 potential we also have $\Delta l = \sigma/\sqrt{2}$ and $\alpha = 1.0$.

3.4.2 Simulations in the NP_zT ensemble

This simulation method contrasts with that for the bulk NPT ensemble in which the volume changes are both homogeneous and isotropic, i.e. the same in all directions. The present simulation fixes the normal component of the pressure in the walls, which controls volume fluctuations through homogeneous changes in the z-direction. The system reaches its equilibrium configuration and its equilibrium value of l [60, 68,94]. When the separation between the walls (l) goes to infinity a bulk liquid forms in the middle of the pore, with a bulk density determined by the input pressure.

Here, the pressure is the same as that in the bulk. In the x and y directions periodic boundary conditions are imposed. A sketch of the system is shown in figure 3.3.

The correct simulation of this ensemble requires that the transition probabilities be written differently from those given in equation (3.22). For the particle displacement the transition probability remains equal to that defined in equation (3.21). However for the volume changes, the wall area $A = S_x S_y$ is fixed and l is changing so that equation (3.22) (for a bulk system) is replaced by [60,68,94];

$$\rho_n/\rho_m = \exp(-\beta(P_z A l_{nm} + \delta\phi_{nm}) + N\ln(l_n/l_m)) \tag{3.32}$$

where $l_{nm} = l_n - l_m$ (the difference in the pore width of the states n and m). P_z is again the pressure normal to the walls.

3.4.3 Simulations in the NPT ensemble using a reservoir.

Although the NP_zT simulation is a good option to use for work on confined fluids, it has disadvantages when l is small. Since the fixed quantity is the pressure normal to the walls (i.e. the normal component of the stress tensor) it is not easy to relate results in this ensemble to those of the bulk. This can be problematic when one is attempting to determine the shift of a phase transition due to confinement, relative to that in bulk ($l = \infty$). Moreover, since l is varying one does not have control over the pore size.

Because of these considerations, a second simulation in the NPT ensemble was performed, similar to that in reference [95]. The model is basically the same. However, the slit-pore now has a fixed size and is immersed in a thermal bath where the pressure and temperature are fixed (see figure 3.4). The number of particles (of the whole system), the temperature and the pressure are the input parameters. Now, particles can go from the reservoir into the pore and vice-versa, maintaining equilibrium between the pore and the bulk. The pressure of the whole system is controlled

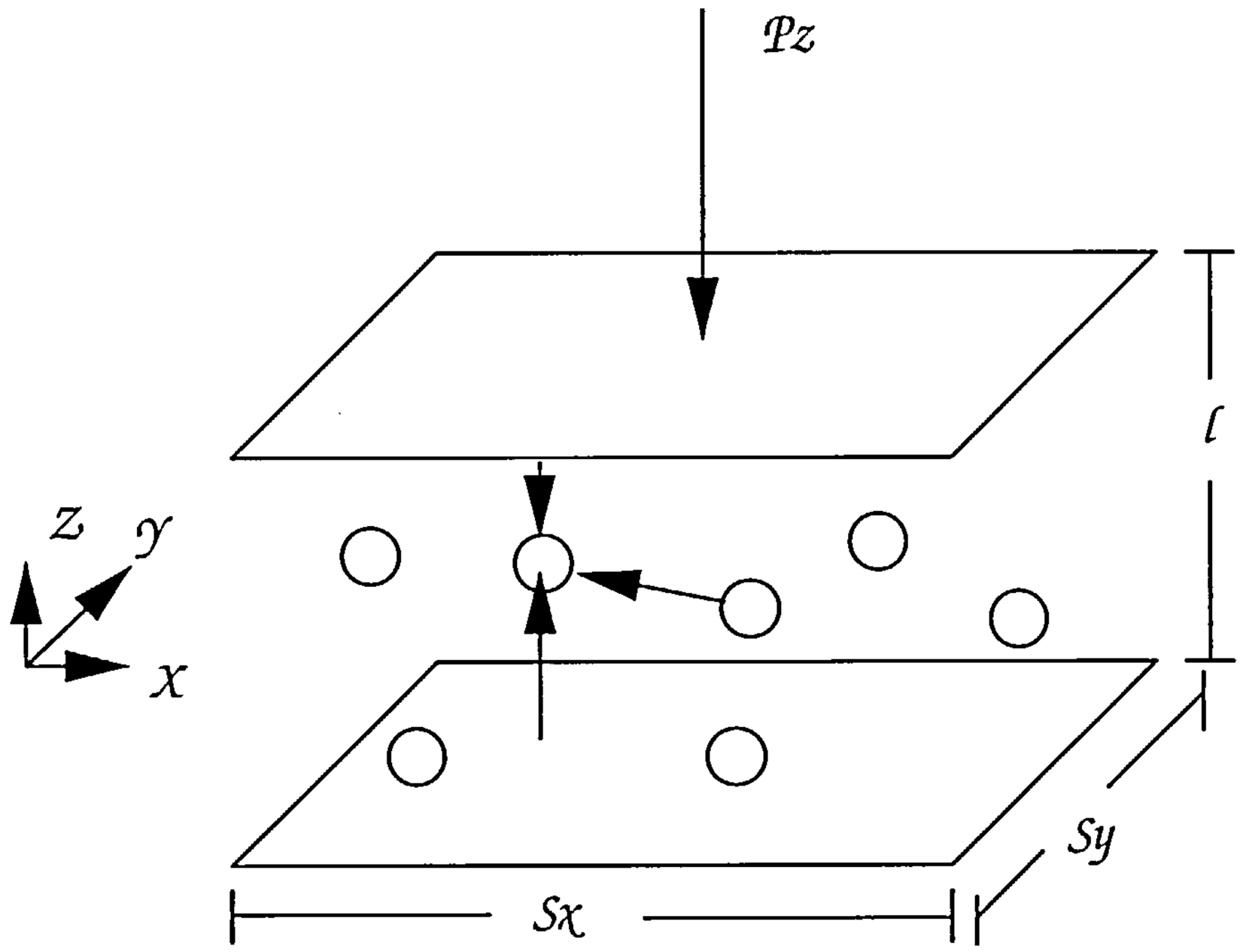

Figure 3.3: Sketch of the slit-pore model used in the NP_zT simulation

by homogeneous changes (fluctuations) in the size of the reservoir box, in x and y directions only. Periodic boundary conditions were imposed in x and y directions, and in the z-direction, outside the pore region. In this way the input pressure should be the same in the reservoir as in the pore and the chemical potential is constant through the system. This simulation is closer than the last one to real experiments where the pore is usually in contact with a reservoir at fixed chemical potential.

Working in this ensemble it is necessary to take into account some extra conditions. Now, the wall-fluid interaction has two separate contributions which are included in the total energy. The first one is the same as described above (in the first NP_zT ensemble) and the second is that due to interactions of the edges of the

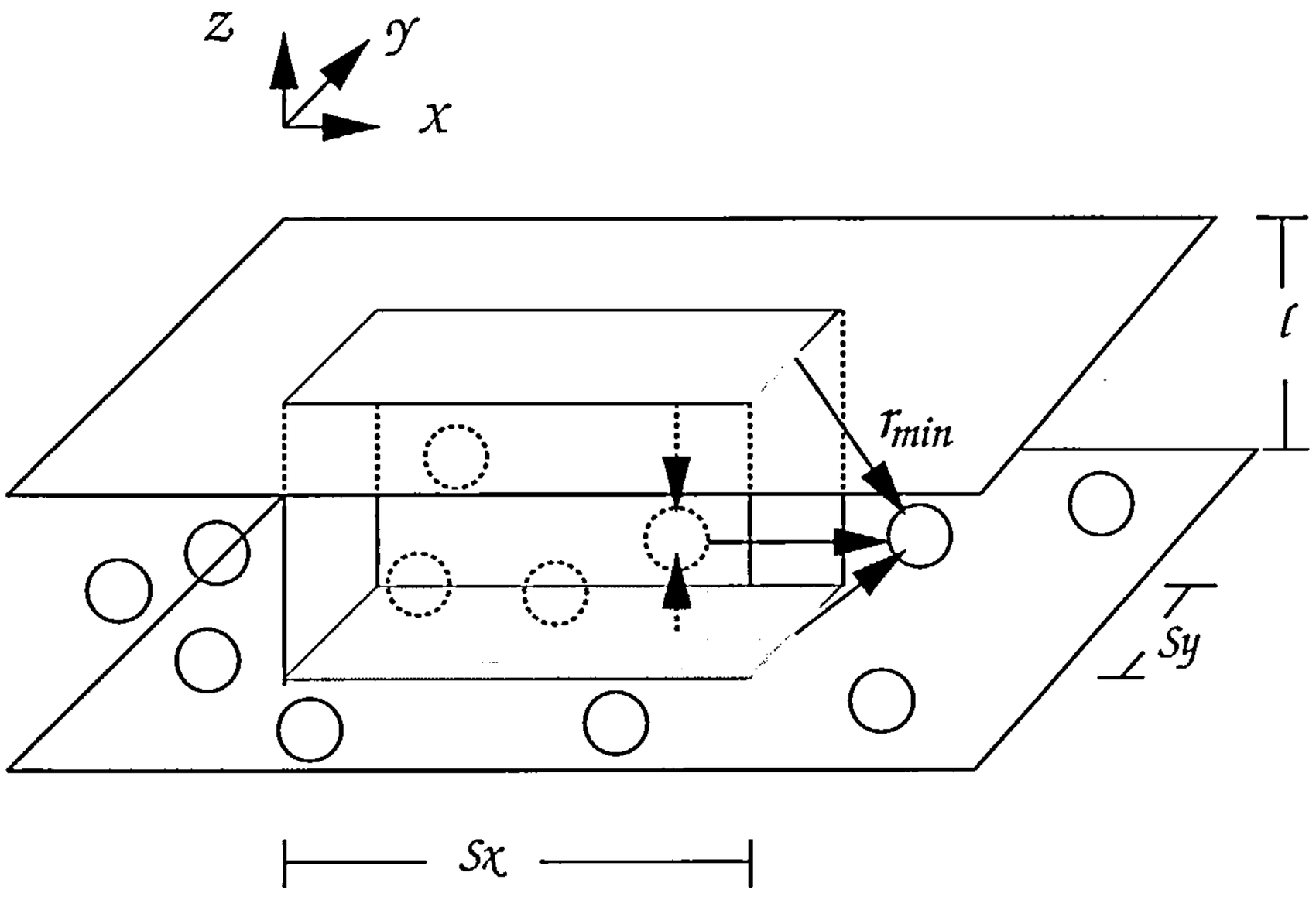

Figure 3.4: Sketch of the slit-pore model which is located in the middle of a reservoir

walls with the particles. This last contribution makes the particles experience a continuous potential when they either go out of or into the pore. For this purpose I calculate the minimum distance (r_{min}) of the fluid particle to the nearest edge of the walls and I write a full Lennard Jones interaction (equation (3.26)) as a function of this distance (see figure 3.4). However, in equation (3.26) I used σ' and ϵ' (the wall-fluid parameters) instead of σ and ϵ. I should say that this last interaction, of the particles with the edges of the walls, was imposed to make the particles feel a continuous wall-interaction only, and it does not pretend to simulate the real effects of the edges of the walls. Thus, I do not expect this interaction to have much contribution neither in the freezing process nor in the structure of the particles (inside or outside of the pore). The advantage of this ensemble is that studies of the bulk and

the pore fluid can be carried out at the same time. The disadvantage is that a large number of atoms are necessary. The fluid-fluid and fluid-(wall)edges interactions were Lennard-Jones using the same shifted and cut-off potential mentioned before.

This simulation differs from that in reference [95] in one detail. Hug and van Swol attached additional planes at opposite ends of their simulation box; nevertheless the purpose of these planes is not clear. They were used possibly, to assist nucleation of the solid from fluid. However, in my opinion, this leads to a problem in interpreting correctly their particle configurations due to mis-matching between the crystal layers forming in the pore walls and in these planes (I discuss this point in more detail in chapter 6). In this work I decided not to use such planes

Finally, as is common in all computer simulations of fluids, I work in reduced units [105]. The reduced units are defined as follows: $T^*=k_BT/\epsilon$ (temperature), $r^*=r/\sigma$ (distance), $P^*=P\sigma^3/\epsilon$ (pressure) and $t^* = (\epsilon/m\sigma^2)^{1/2}t$ (time). Here ϵ and σ refer to the fluid-fluid Lennard Jones pair potential.

For simplicity, in subsequent chapters these quantities will be written without the asterisk, i.e. all results will refer to reduced units.

Chapter 4

Freezing in the NP_zT ensemble

4.1 Equivalence between the NP_zT and μVT ensemble

When I began my study of confined fluids, using Monte Carlo simulations, before performing any calculations in the system of interest, the consistency of results from the NP_zT ensemble was tested. It is known that a bulk system can be characterized using different ensembles, e.g. the (NVT), the (NPT) or the (μVT) [29]. There is no particular preference to choose one and in the thermodynamic limit all of them are equivalent. For inhomogeneous systems (e.g. a fluid in a slit pore) one expects to have the same equivalence. For instance in the Grand Ensemble the natural variables are the chemical potential, the slit-pore width (assuming fixed area) and the temperature (μlT). Then quantities such as the average normal pressure $(\langle P_z \rangle)$ on the walls and the average number of particles $(\langle N \rangle)$ can be calculated [32,33,114]. Hence, using these parameters in the (NP_zT) ensemble we should obtain the same results as for the thermodynamic state described by the (μlT) ensemble. To show this equivalence, a few simulations were performed for both ensembles. The calculations were for a slit-pore system of square plates at reduced temperature of $T = 1.2$ and reduced chemical potential $\mu = -12.80$ (the thermodynamic state lies in

a two-phase gas-liquid region of the Lennard Jones phase diagram). The fluid-fluid interaction is the shifted and truncated LJ potential (argon fluid) given by equation (3.26) and the wall-fluid potential is given by equation (3.28). For comparison of these test simulations with other authors I used a cut-off of $r_c = 3.5$ and the factor (in reduced units) $\rho\sigma'^2\epsilon'\Delta l = 1.0$ (as in reference [32]) ($\Delta l = \sigma/\sqrt{2}$ with $\alpha = 1.0$). The results are shown in table 4.1. Firstly, simulations were performed in the Grand ensemble (GEMC) using the pore width (l), the wall length (S) (the area $A = S^2$) and the temperature as the input parameters. Thus the (total) potential energy per particle ($\langle U/N \rangle$), the pressure ($\langle P_z \rangle$) and the average number of particles $\langle N \rangle$ are calculated. $\langle N \rangle$ is the nearest integer to that of the ensemble average over the number of particles in the simulation box. The normal pressure, $\langle P_z \rangle$, is calculated using the expression:

$$\begin{aligned} \langle P_z \rangle V &= \langle N \rangle k_B T - \langle \sum_{i=1}^{N} z_i \frac{d\phi_s(z_i)}{dz_i} \\ &\quad - \sum_{i=1}^{N} (l - z_i) \frac{d\phi_s(l - z_i)}{d(l - z_i)} - \sum_{i=1}^{N-1} \sum_{j=i+1}^{N} (z_i - z_j)^2 \frac{d\phi_{LJ}(r_{ij})/dr_{ij}}{r_{ij}} \rangle. \quad (4.1) \end{aligned}$$

Here ϕ_s is the wall-fluid potential of a single wall and ϕ_{LJ} is the fluid-fluid potential. V is the volume of the simulation box.

The results are close to those of Schoen et al [32]. I then took the results for $\langle P_z \rangle$ and $\langle N \rangle$ from my own simulations as the input for the (NP_zT) simulation. Now, the potential energy per particle ($\langle U/N \rangle$), the pore width ($\langle l \rangle$) and the chemical potential $\langle \mu \rangle$ are calculated. The chemical potential was calculated using the Widom test-particle insertion method [115]. As we can observe from the table the values calculated in both ensembles are in good agreement.

4.2 Simulations in the NP_zT ensemble.

The subsequent simulations were carried out as follows. For a certain number of particles (placed initially in a random configuration) at fixed temperature and pressure,

Sim.	l	S	$\langle U/N \rangle$	P_z	$\langle N \rangle$	-μ	Ref.
GEMC	3.75	14.0	7.035	1.52	378	12.80	Ref. [32]
GEMC	3.75	14.0	6.998	1.529	376	12.80	This work
NP_zT	3.761	14.0	7.031	1.529	376	12.889	This work
GEMC	2.90	7.0	8.371	2.16	70	12.80	Ref. [32]
GEMC	2.90	7.0	8.363	2.182	70	12.80	This work
NP_zT	2.903	7.0	8.350	2.182	70	12.745	This work
GEMC	2.75	7.0	8.185	4.71	62	12.80	Ref. [32]
GEMC	2.75	7.0	8.239	4.849	63	12.80	This work
NP_zT	2.751	7.0	8.195	4.849	63	12.792	This work

Table 4.1: Thermodynamic properties for a slit-pore using different ensembles showing the equivalence between them, $T = 1.2$. In reference [32] the wall-fluid and fluid-fluid potential energy are given separately. In this table both terms are included in the results for $\langle U/N \rangle$.

P_z, the system was initially equilibrated in a liquid-like state. Then the pressure was increased until the fluid seemed to freeze. The first investigation was performed for a system of 300 particles at temperature $T = 1.15$, confined by a rectangular box with planar walls of lengths $S_x = S_y = S = 5.66139$. The fluid-fluid and the wall-fluid potential interaction were those described in chapter three by equations (3.26) and (3.28), respectively. The reduced fluid parameters were selected to model an argon-like fluid, $\epsilon/k_B = 119.8K$ and $\sigma = 3.405$ x 10^{-10} m. The wall density was $\rho^* = \rho\sigma^3 = \sqrt{2}$ and $\Delta l^* = \Delta l = \sigma/\sqrt{2}$. The parameters $\epsilon^* = \epsilon'/\epsilon = 7.2375$ (with the parameter $\alpha = 1$) and $\sigma^* = \sigma'/\sigma = 0.7823$ were chosen to mimic argon on a strongly attractive substrate. These parameters are even stronger than the

parameters of a graphite substrate. Literature values for the argon-graphite interactions, using the same units as reference [60] are $2\pi\sqrt{10}\sigma' 3\rho\epsilon'/(9\epsilon) = 9.24$ (whereas in this work $2\pi\sqrt{10}\sigma' 3\rho\epsilon'/(9\epsilon) = 22.5964$) and $\sigma'/\sigma = 0.7863$ [60] (we should say that the 9-3 potential in reference [60] is written in a different form of that in equation (3.27). However, equation (3.27) can be written as in reference [60] using the factors $2\pi\sqrt{10}\sigma' 3\rho/9$ and $1/1.39908$ for the ϵ' and σ' parameters respectively). In a typical simulation, for this system, data accumulation over 30000-50000 steps began after an equilibration of 10000 Monte Carlo steps.

4.3 Structure of the confined fluid.

A quantity that is straightforward to analyze is $\rho(z)$, the density profile of the fluid as a function of z. This is obtained in simulation from the formula:

$$\rho(z) = \frac{\langle N(z) \rangle}{S_x S_y \Delta z}. \tag{4.2}$$

$N(z)$ is the number of particles in a layer of thickness Δz and $\langle\rangle$ brackets denote ensemble averages over configurations.

From figure 4.1 we can observe how the walls induce local order in the fluid. This is evident from the oscillations in the density profile along the width of the pore. At pressure $P_1 = P_z = 6$, although the fluid develops sharply defined maxima i.e. layers, near the walls, the density profile is liquid-like in the middle of the pore. The pore width $\langle l \rangle$ is approximately 10 σ. We shall see there is no evidence of any solid-like structure in the central region. When the pressure is increased to $P_2 = P_z$=8, ten well-defined layers, separated by approximately one molecular diameter, are formed parallel to the walls. The width of the pore $\langle l \rangle$ is now approximately 9.5 σ. This pronounced layering allows us to make a quasi two-dimensional study by layer. The in-plane pair correlation function (ICF) per layer is defined to be a function

of the z coordinate and the separation vector between atoms. Thus, in cylindrical coordinates, the pair correlation function is a function of the reference atom 1, z_1, and the relative coordinates of particle 1 and 2, r_{12} and z_{12} [32]:

$$g^{(2)}(z_1, z_{12}, r_{12}) = \frac{\langle N(z_1, z_{12}, r_{12}) \rangle}{2\pi r_{12} \Delta z_{12} \Delta r_{12} \bar{\rho}(z_2)} \tag{4.3}$$

$N(z_1, z_{12}, r_{12})$ is the number of particles 2 in a cylindrical annulus of radius r_{12}, of width Δr_{12} and height Δz_{12} centered on reference particle 1. $\bar{\rho}(z_2)$ is the average density over the layer of thickness Δz_{12}. Δz_{12} is taken as the distance between two adjacent minima in the density profile.

If $g^{(2)}$ is restricted to the in-plane $z_1 = z_2$ we have

$$g(r) = g^{(2)}(z_1, 0, r_{12}) = \frac{\langle N(z_1, 0, r_{12}) \rangle}{2\pi r_{12} \Delta z_{12} \Delta r_{12} \bar{\rho}(z_1)} \tag{4.4}$$

Simulations were performed at a series of different (increasing) pressures before the fluid completely froze. No matter what the value of the pressure was, the fluid always seemed to form crystal layers adjacent to the walls, even when it was liquid-like in the middle. The second inner layer also seems to be crystalline, and for large pores even the third one is strongly ordered although these do not seem to develop a well defined crystal structure. This is illustrated by the ICF (figure 4.2) and by the snapshots of the layers (figure 4.4). The walls not only induce order perpendicular to the walls but also induce order parallel to them. At pressure P_1, the ICF for the middle layers is a typical of the pair correlation function of a bulk liquid, however peaks which are characteristics of a solid structure appear at P_2 for the same middle layers. Analysis of the structure factor $S(k)$, i.e. the Fourier Transform (FT) of the ICF's, shows behavior characteristic of a liquid at P_1 and of a solid at P_2 (figure 4.3). To be consistent a two-dimensional definition for the FT was used:

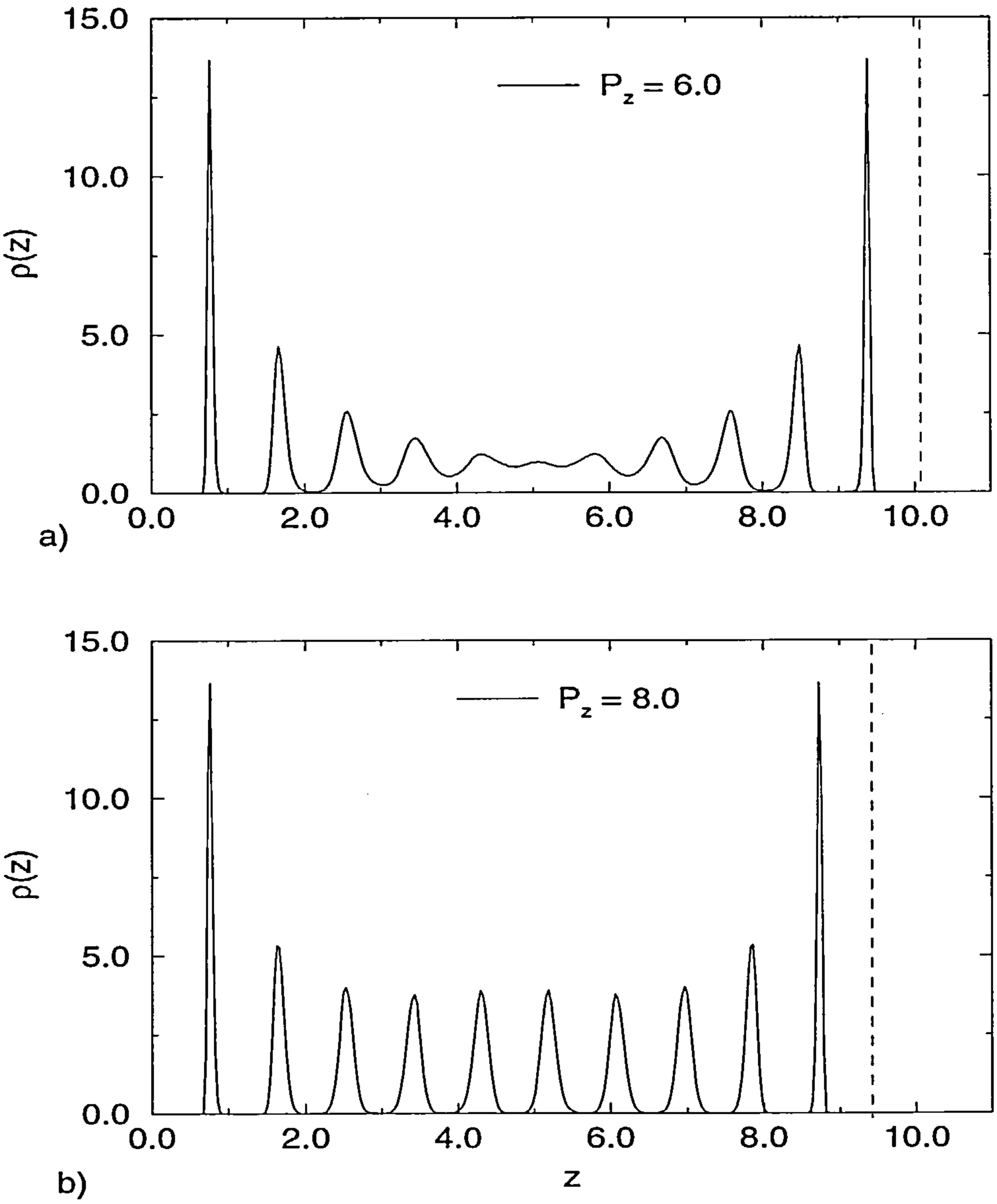

Figure 4.1: The density profiles for a fluid in a slit- pore at T=1.15. In a) normal pressure, $P_z = 6.0$ and the fluid is liquid-like and in b) where $P_z = 8.0$ it is totally frozen. The first layer remains frozen for all pressures. The left wall is located at z=0 and the dashed lines indicate the positions of the right wall. In each case $N = 300$

$$S(k) = 1 + 2\rho\pi \int r J_0(kr)(g(r) - 1)dr \tag{4.5}$$

where J_0 is the Bessel function of order 0 and ρ is the mean density, i.e. $N/\langle V \rangle$, where $\langle V \rangle$ $(= S_x S_y \langle l \rangle)$ is the total volume of the slit-pore.

In figure 4.3 we observe rapid oscillations in the structure factor for $k \leq 5$ (and for all further $S(k)$ curves). However, these oscillations have no physical meaning. Such behaviour results from for the use of the truncated pair correlation function, arising from the finite size of my simulations (finite area).

These two structure functions, the ICF and its FT (the structure factor), suggest that the fluid suffers a freezing transition. Crystalline layers form parallel to the walls. Each layer appears to be a two-dimensional hexagonal lattice (face (111) of the face centred cubic crystal, fcc). This is confirmed by the peak separations in $g(r)$ and $S(k)$. The peaks in $g(r)$ are located at the distances of the first, second, etc. nearest neighbours of a hexagonal crystal structure, i.e. the (111) plane of the fcc crystal (see also figures 4.4 and 4.5). This structure has been reported by previous authors [35, 95, 96].

For bulk systems the Hansen-Verlet criterion [81] predicts that freezing occurs when the first maximum of the structure factor (FT) reaches the value 2.85 (for a bulk 2-dimensional system this value is higher [90]). In these simulations we observe that the layers freeze when the first peak in the structure factor reaches the value of about 2.85. It seems that the Hansen-Verlet criterion is approximately obeyed for these quasi two-dimensional systems.

Considering the number of particles per layer (once the fluid freezes), it is observed that all layers do not have the same number. Since the wall-fluid interaction is strongly attractive, the first layers have more particles than those in the middle, therefore the separation of the first (second, etc.) nearest neighbours is less in the contact layers than for the centre layers (figure 4.2 and 4.5). This makes

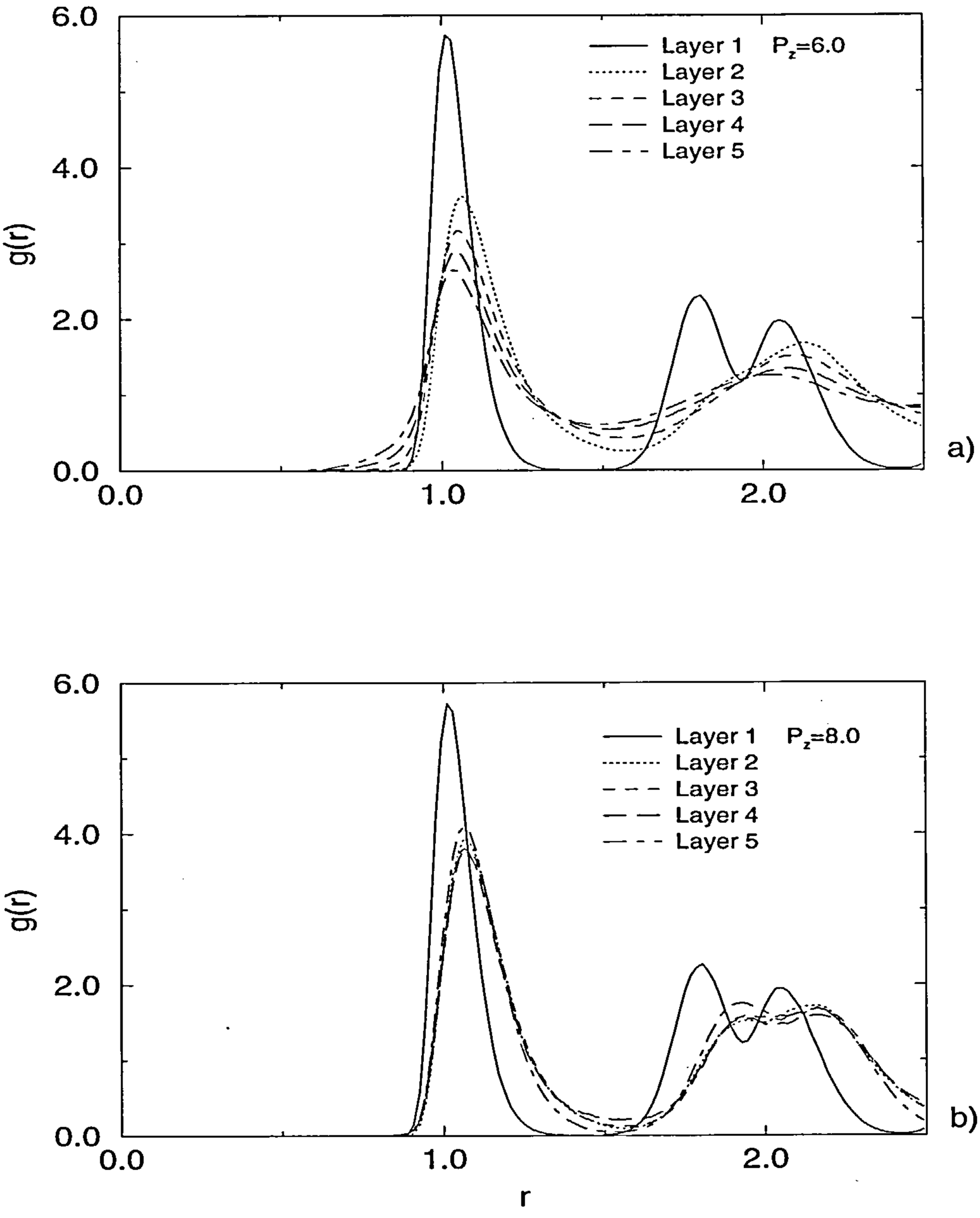

Figure 4.2: The in-plane correlation function (ICF) of each layer shown in figure 4.1 a) P_z=6.0. The first layer is solid- like but the rest are liquid-like. b) $P_z = 8.0$. All the ICF's show crystalline structure (see text). $N = 300$

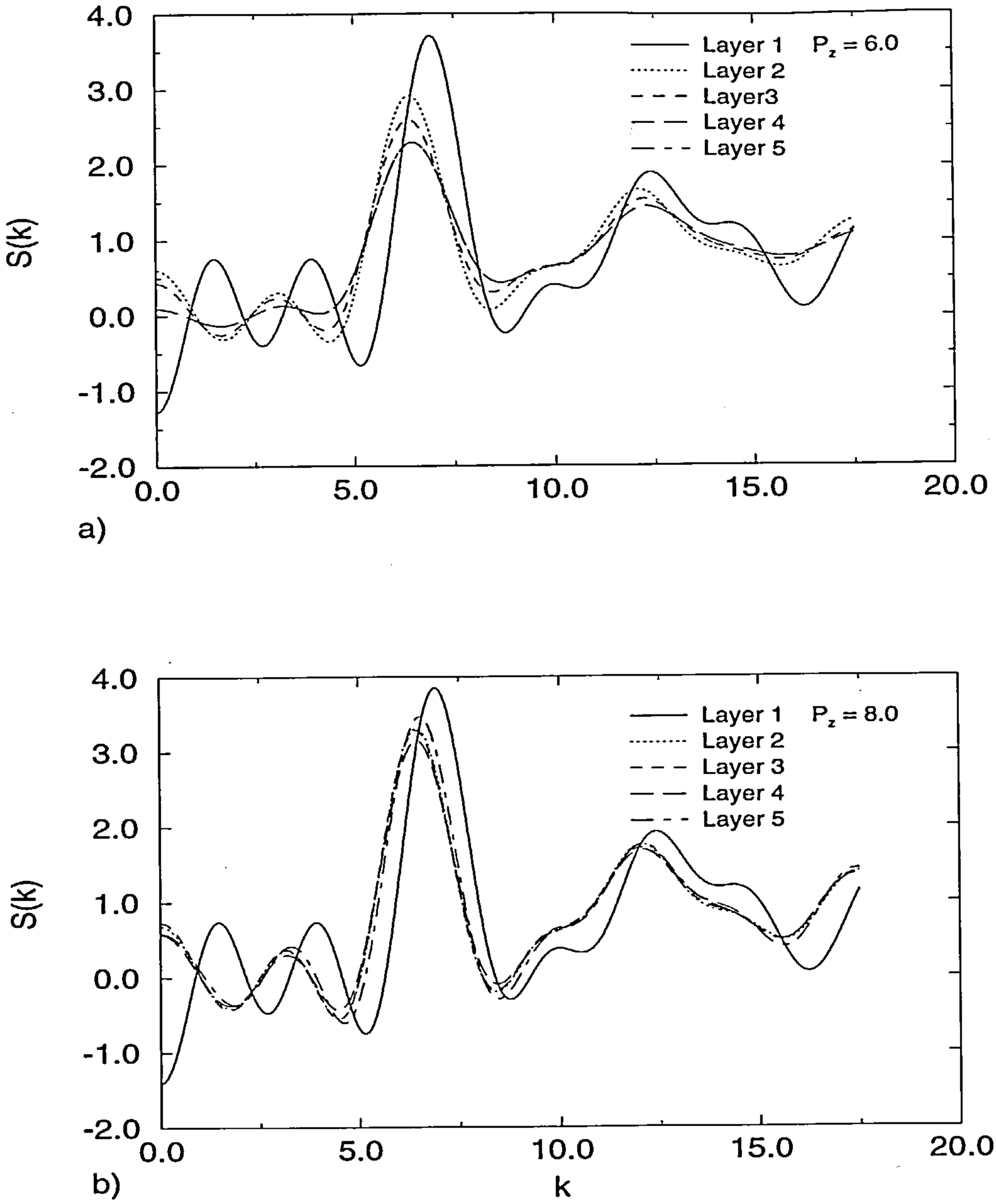

Figure 4.3: The corresponding Fourier Transform (FT) of the in-plane correlation function of each layer shown in figure 4.1 and figure 4.2. a) $P_z = 6.0$ and b) $P_z = 8.0$. $N = 300$.

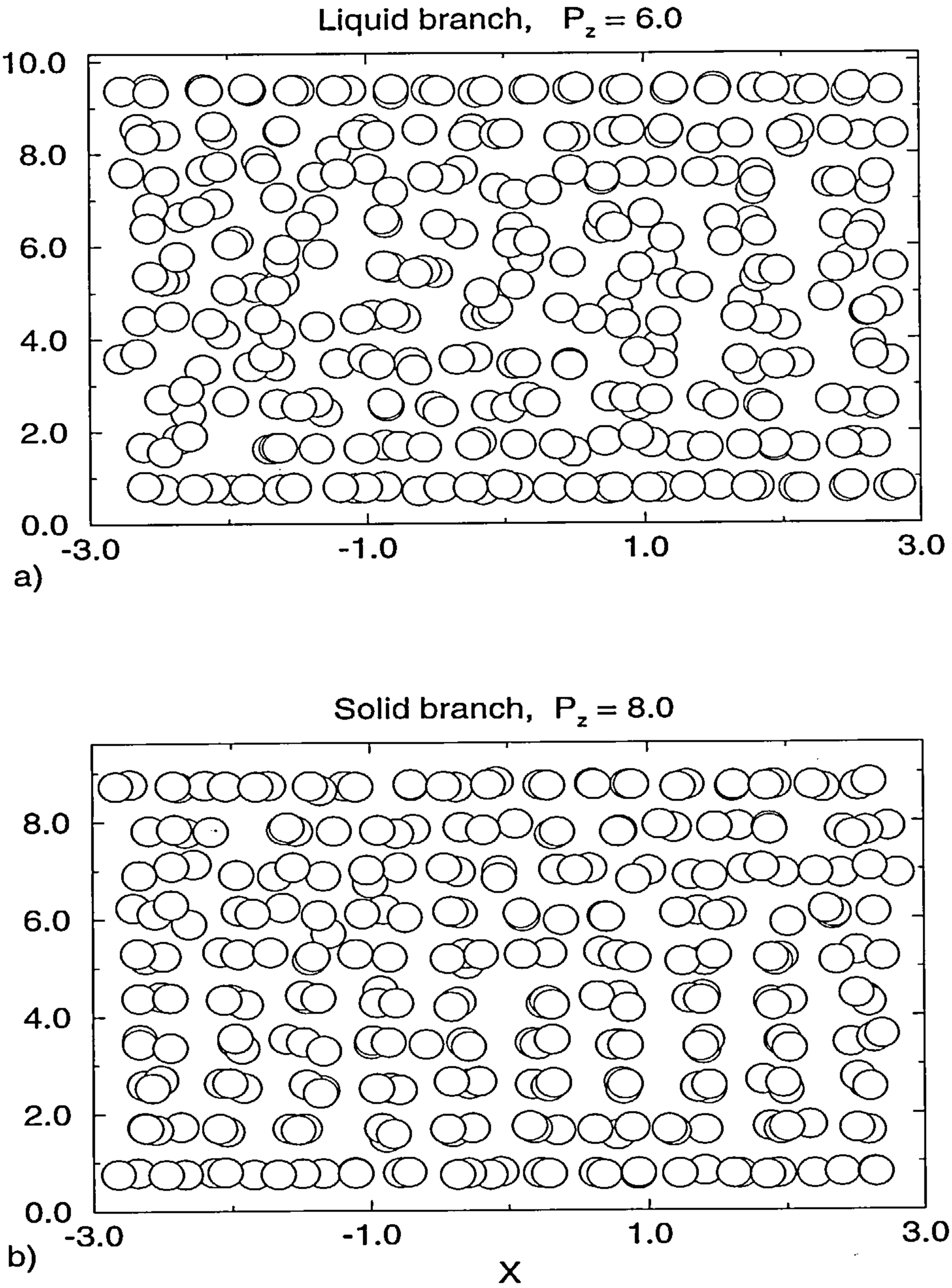

Figure 4.4: Snapshots of the particle-configurations corresponding to figure 4.1. a) A liquid-like behaviour can be seen in the middle of the pore at $P_z = 6$ whereas b) a layered, solid-like structure is observed at $P_z = 8$.

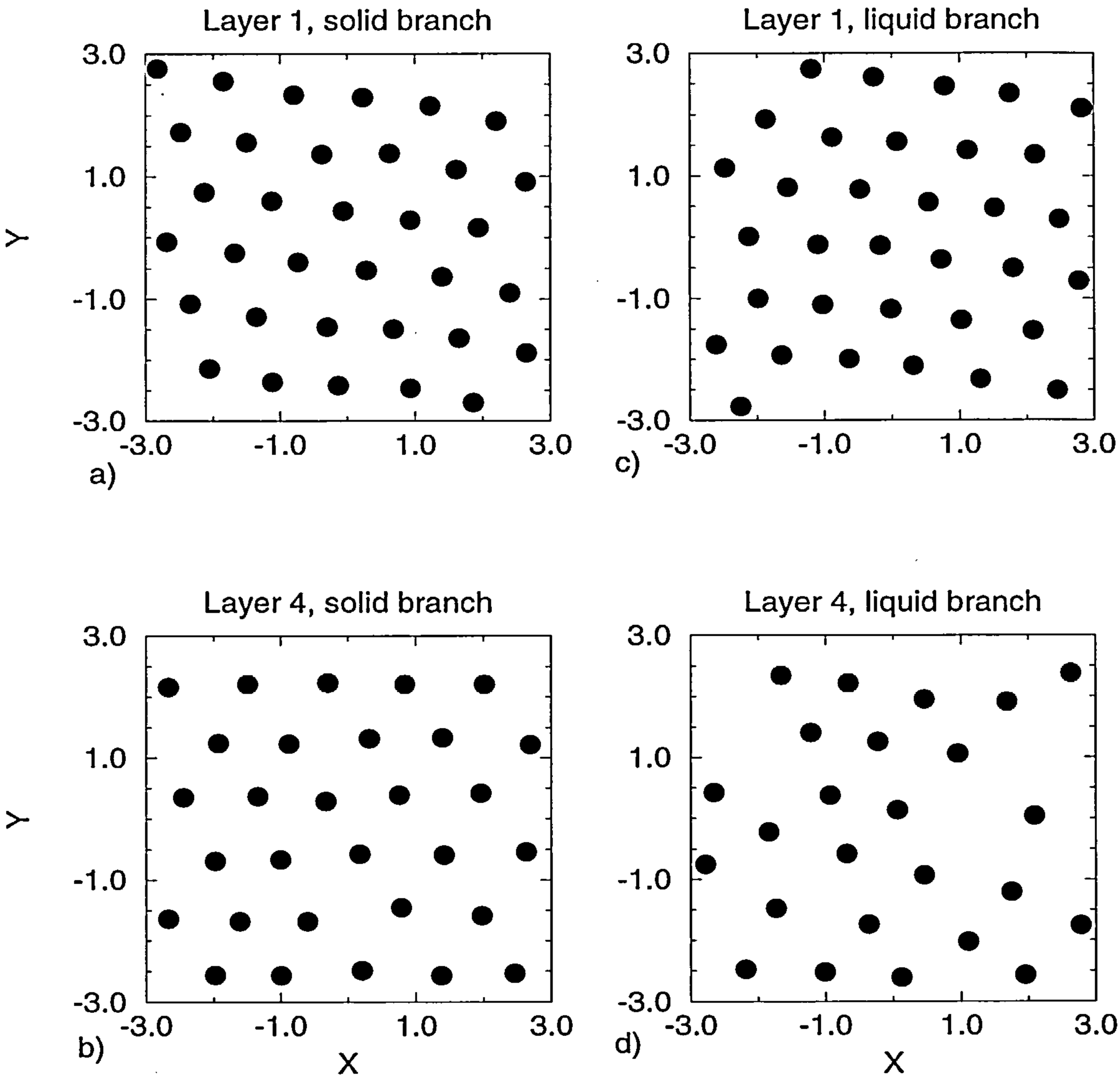

Figure 4.5: In plane snapshots of layer 1 (adjoining the wall) and layer 4 (near the middle of the slit). a) and b) refer to $P_z = 8$ and c) and d) to $P_z = 6$. In both cases layer 1 is solid-like.

the first crystal-plane different from those in the middle. If the total number of particles in the fluid is constant and each layer has a different number of particles we would expect to have some crystal layers with defects. Moreover, if a stacking analysis of the layers is done, it is observed that they are placed in a disordered arrangement [116]. There is not a perfect sequence of the planes such as abcabc...(fcc crystal) or abab...(hexagonal close packed crystal, hcp). They do not even have the same in-plane direction; some of them align to the (01) direction while others align to the (10). Because of these considerations, we do not expect to have a well defined (perfect) three dimensional crystal as in bulk.

For a larger pore (600 particles), with the same wall area $S^2 = (5.66139)^2$, under the same conditions, the pore width is almost twice as large as for a 300-particle system and we see that when this is liquid-like (the first two contact layers remain crystalline) the oscillations in $\rho(z)$ in the middle of the pore are much weaker than in the small pore and when it freezes it forms 20 crystal layers (figure 4.6 and 4.7). It is expected that for very large pores ($l \to \infty$) the fluid in the centre will be a true bulk fluid. We observe that two well developed solid layers appear close to the walls instead of one as occurred for the 300-particle system. This obvious from the $g(r)$ and $S(k)$ (figure 4.7). Once the fluid freezes, apart from the first contact layer near to the walls, all the solid layers are alike (compare $g(r)$ and $S(k)$ for this system with those for the 300-particle system). We also observe that when the fluid is solid-like the peaks in the density profile seem to form a well defined modulation (figure 4.6 b). However, this has not physical meaning and it probably tells us the way in how the layers are packed (i.e. the width of the layers). Since I observed other similar features in the density profile at different wall-fluid conditions (see further section of this chapter) I discus more about this point (and possible explanations) in the next sections and in the next chapter. Apart from these differences the process of freezing appears to be the same as for the 300-particle system. But we cannot establish at precisely which value of P_z freezing occurs and how this depends on the pore width (see next chapter)

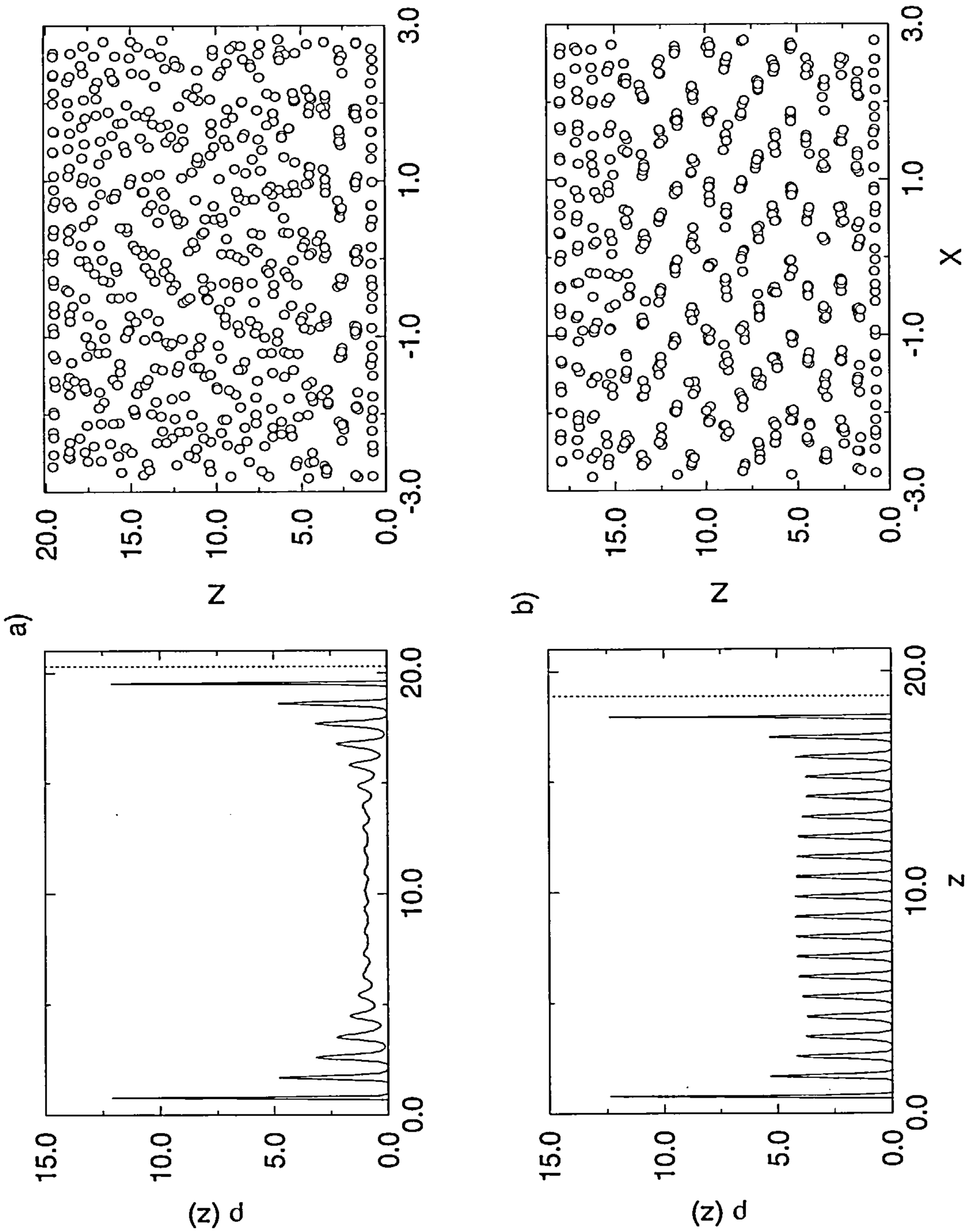

Figure 4.6: Density profiles and snapshots for a 600-particle system. The thermodynamic conditions are the same as for the 300-particle system. a) $P_z = 6$ and b) $P_z = 8$.

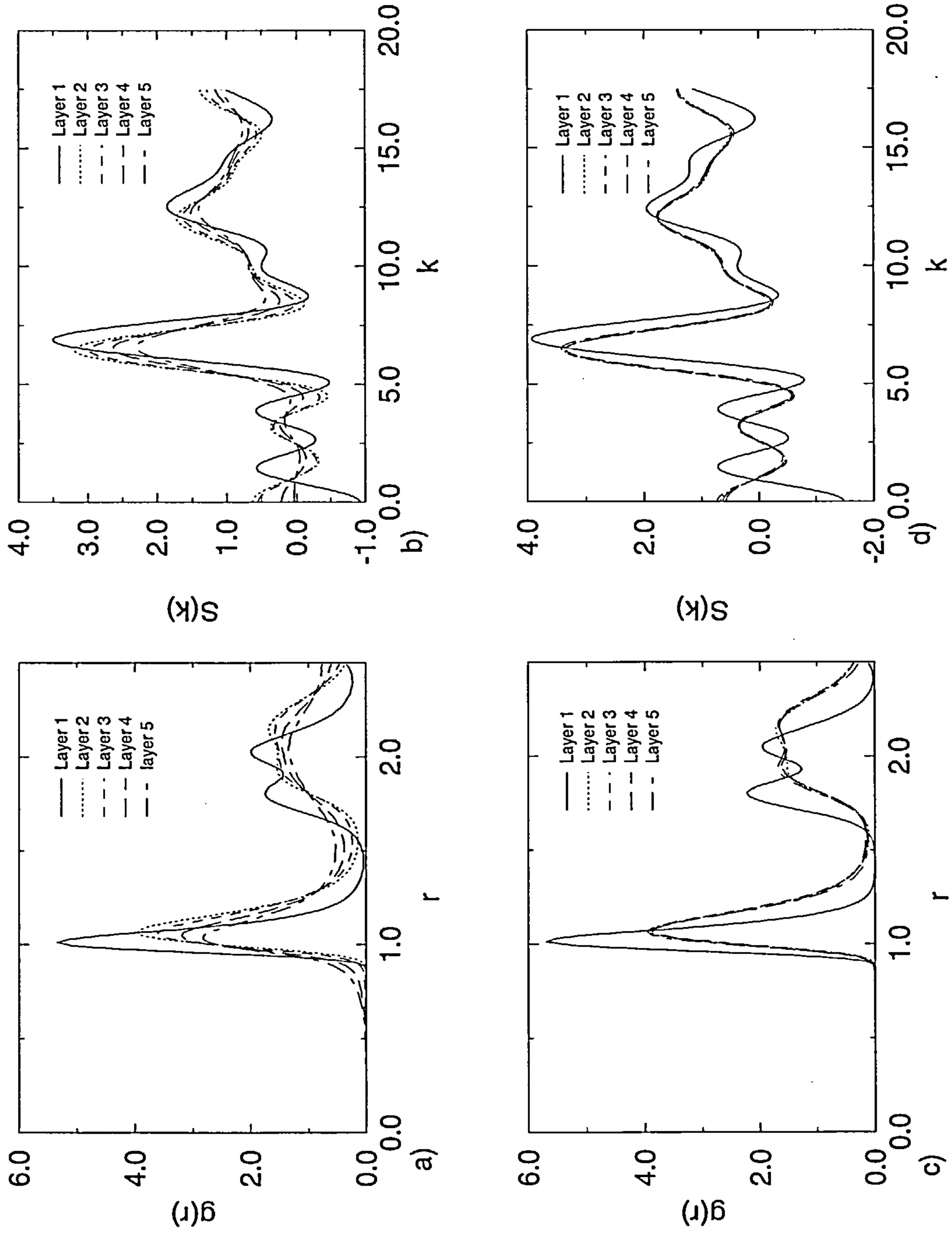

Figure 4.7: The $g(r)$ (ICF) and its $S(k)$ for the layers shown in figure 4.6. a) and b) are for the liquid, $P_z = 6.0$ and c) and d) are for the solid $P_z = 8.0$. $N = 600$.

To see how the freezing begins, a plot of the height of the first peak in the structure factor was made (criterion for freezing) against the number of Monte Carlo computer steps for the 300-particle system. This analysis was carried out at conditions where the fluid freezes ($P_z = 8.0$). The layer next to the wall first reaches the value of 2.85, then the second one does and the process is propagated towards the centre of the pore. The subsequent layers reach the value 2.85 at almost the same time (figure 4.8). Similar results have been obtained by other authors using Molecular Dynamics simulations [35] and different potential functions. Additional confirmation of this scenario was obtained for the 600-particle system by following the density profiles over Monte Carlo sweeps (figure 4.9). Starting from a liquid-like configuration the input parameters (pressure $P_z = 8.0$) were fixed at conditions where the fluid should freeze. Initially (10000 sweeps), apart from the 2 or 3 layers close to the walls, the fluid is liquid-like through the slit. At 20000 sweeps, although the fluid is not totally frozen, further layers start freezing (they develop well defined crystal structure) but the system is still liquid-like in the middle. At 30000 sweeps, the middle layers are strongly ordered but the fluid is still not completely frozen until after 40000 sweeps when all the layers freeze. These remain frozen (as is seen for 50000 sweeps). This represents the equilibrium configuration for this thermodynamic state point.

4.4 Temperature dependence

The next study was performed in order to investigate the temperature dependence. Three different temperatures were studied ($T = 1.35, 1.15, 0.95$) for the 300- particle system. The wall area and all the potential functions were the same as described above. It is observed that changing the temperature does not modify the freezing process described previously. The only obvious difference on increasing or decreasing the temperature is the change in the freezing pressure. As is expected, from bulk behaviour, the higher the temperature, the higher is the freezing pressure, and

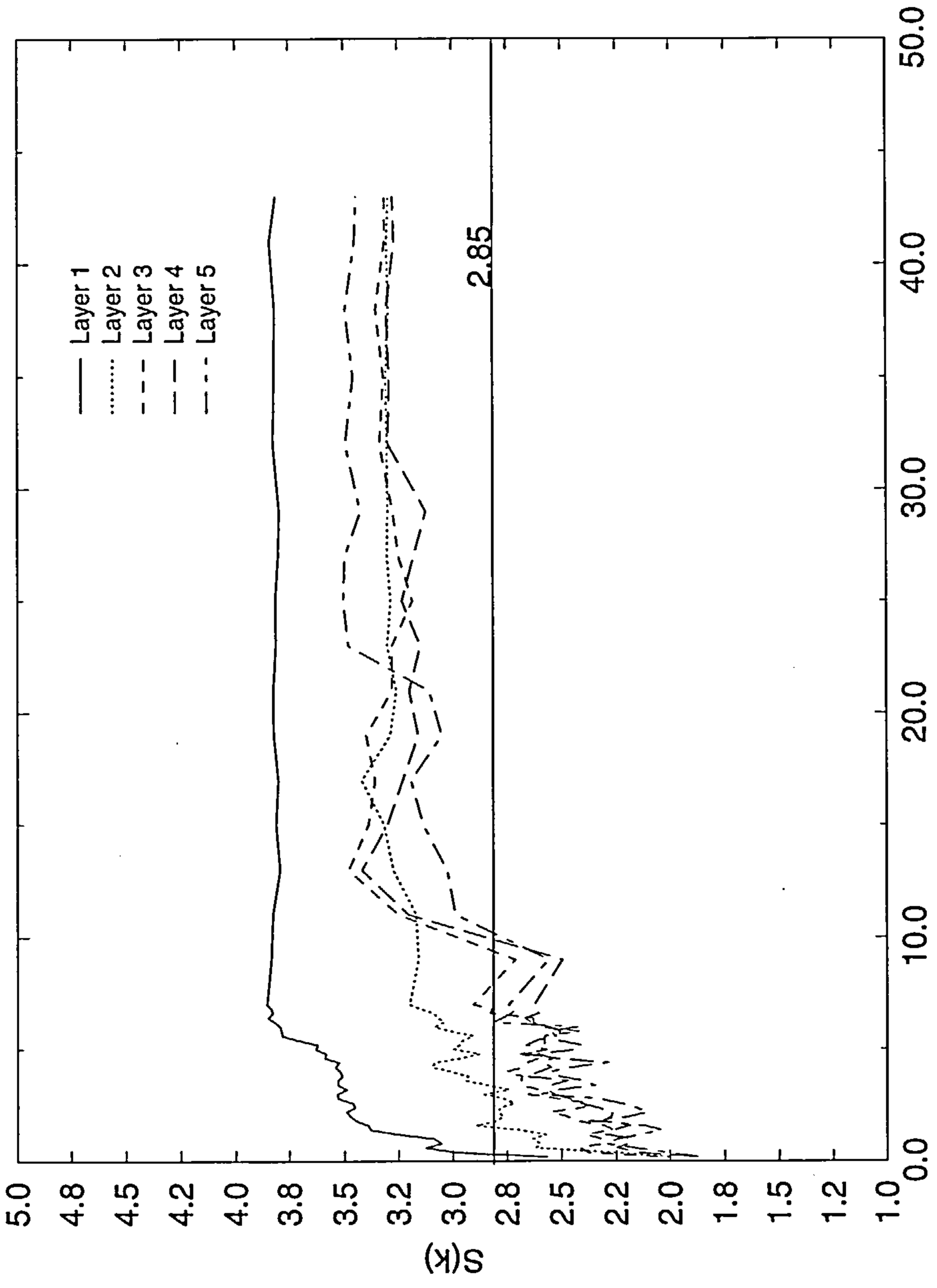

Figure 4.8: Height of main peak in the structure factor versus number of Monte Carlo sweeps. The value 2.85 is the empirical (Hansen-Verlet) value for the onset of bulk freezing. $P_z = 8.0$, $T = 1.15$ and $N = 300$.

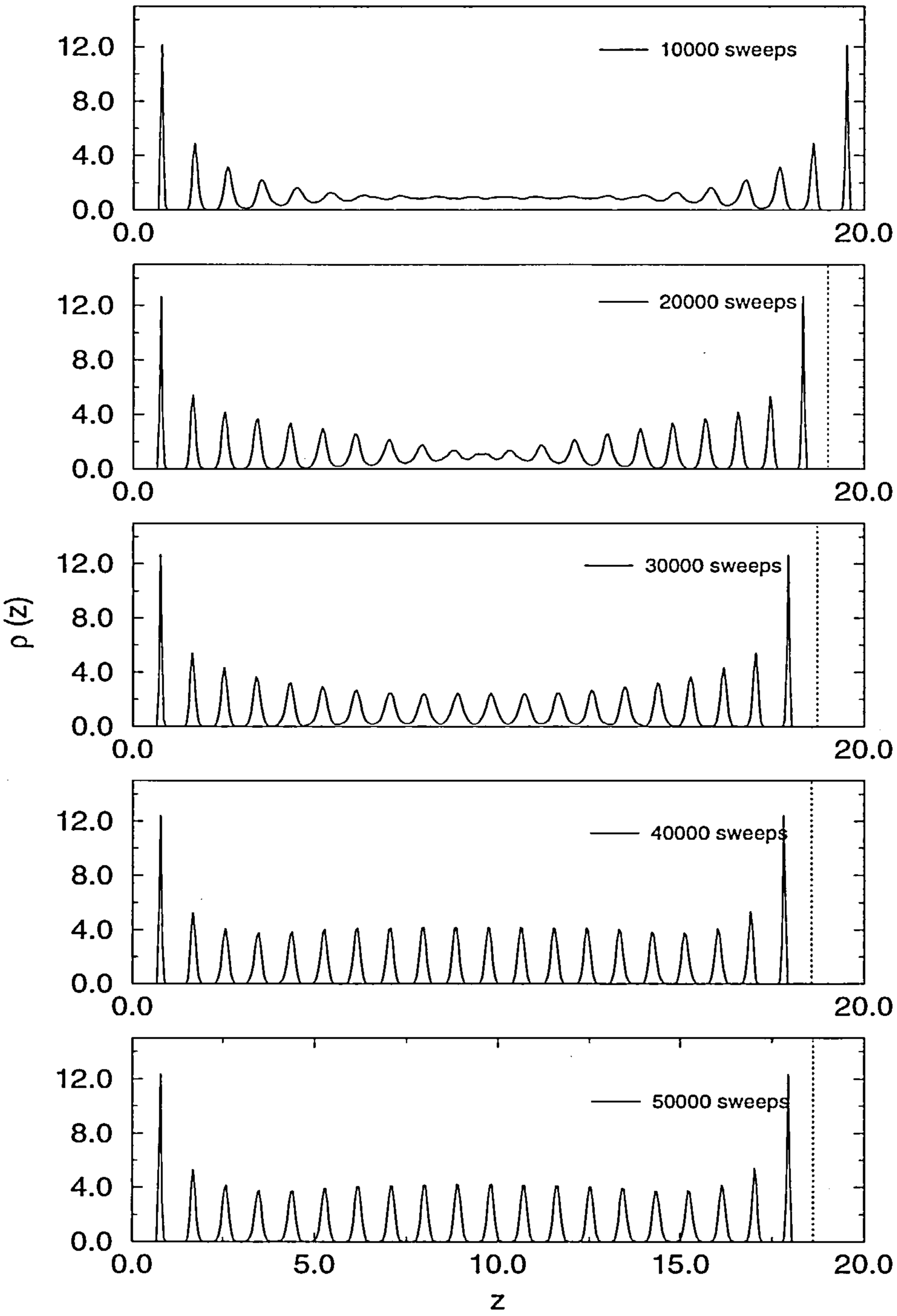

Figure 4.9: Density profiles at different Monte Carlo steps for a state where the 600-particle system should freeze, $P_z = 8.0$ and $T = 1.15$. Observe how the layers in the fluid start freezing from the walls to the centre. The dashed line represents the position of the second wall.

consequently the equilibrium width of the pore is modified. For example, at the pressure where the fluid is liquid-like (P_z= 8.0) at $T = 1.35$ it is solid-like at $T = 1.15$ (figure 4.10). One important point to emphasize here is that these pressures do not correspond to the equilibrium transition pressures for those given temperatures. They simply refer to pressures P_z where, at given temperatures, the fluid is frozen. For a detailed study of the equilibrium transition pressures and the phase diagram see the next chapter.

4.5 The influence of the wall-fluid interaction

4.5.1 Strong and weak walls

In order to examine the influence of the substrate on the freezing behaviour of the fluid I investigated three different wall-fluid potentials, i.e. I changed the ϵ^* parameter in equation (3.28) to have values of $\epsilon^* = 7.2375$, $\epsilon^* = 3.0$ and $\epsilon^* = 1.0$, all with the parameter $\alpha = 1.0$. Finally I also worked with purely repulsive walls, $\epsilon^* = 1.2771$ and $\alpha = 0.0$.

All these simulations were performed at constant temperature ($T = 1.15$) and the pressure was varied in each case. From these investigations some new features were observed in the formation of the crystal layers. a) For both the liquid-like or solid-like state the height of the first peak in the density profile (the first layer) is reduced as ϵ^* is reduced, i.e. as the wall is made less attractive (figure 4.11). Since the density profile gives us information about the number of particles per layer we assume that there are fewer particles in the first layer using weak walls than using strong ones. b) Moreover, for walls with $\epsilon^* = 7.2375$ and $\epsilon^* = 3.0$ we still see the first layer has a crystalline $g(r)$ structure (for both the liquid and solid-like states) but at $\epsilon^* = 1.0$ this crystalline structure is much less pronounced for the liquid-like state (figure 4.12). The peak height of $g(r)$ is > 3.5 but otherwise $g(r)$ is more characteristic of a liquid than solid.

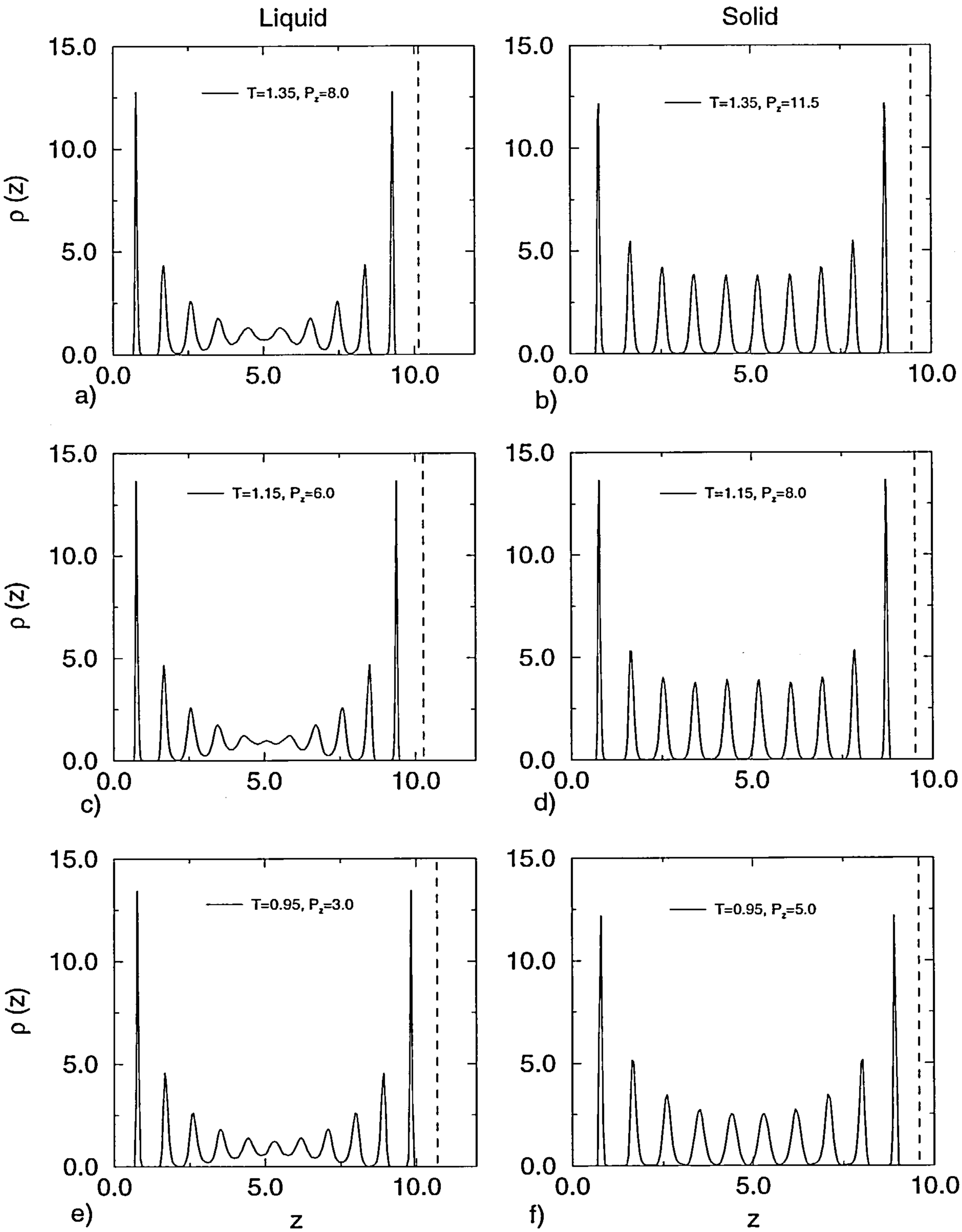

Figure 4.10: The density profiles for a 300-particle system for different thermodynamic conditions. The dashed line represents the position of the second wall.

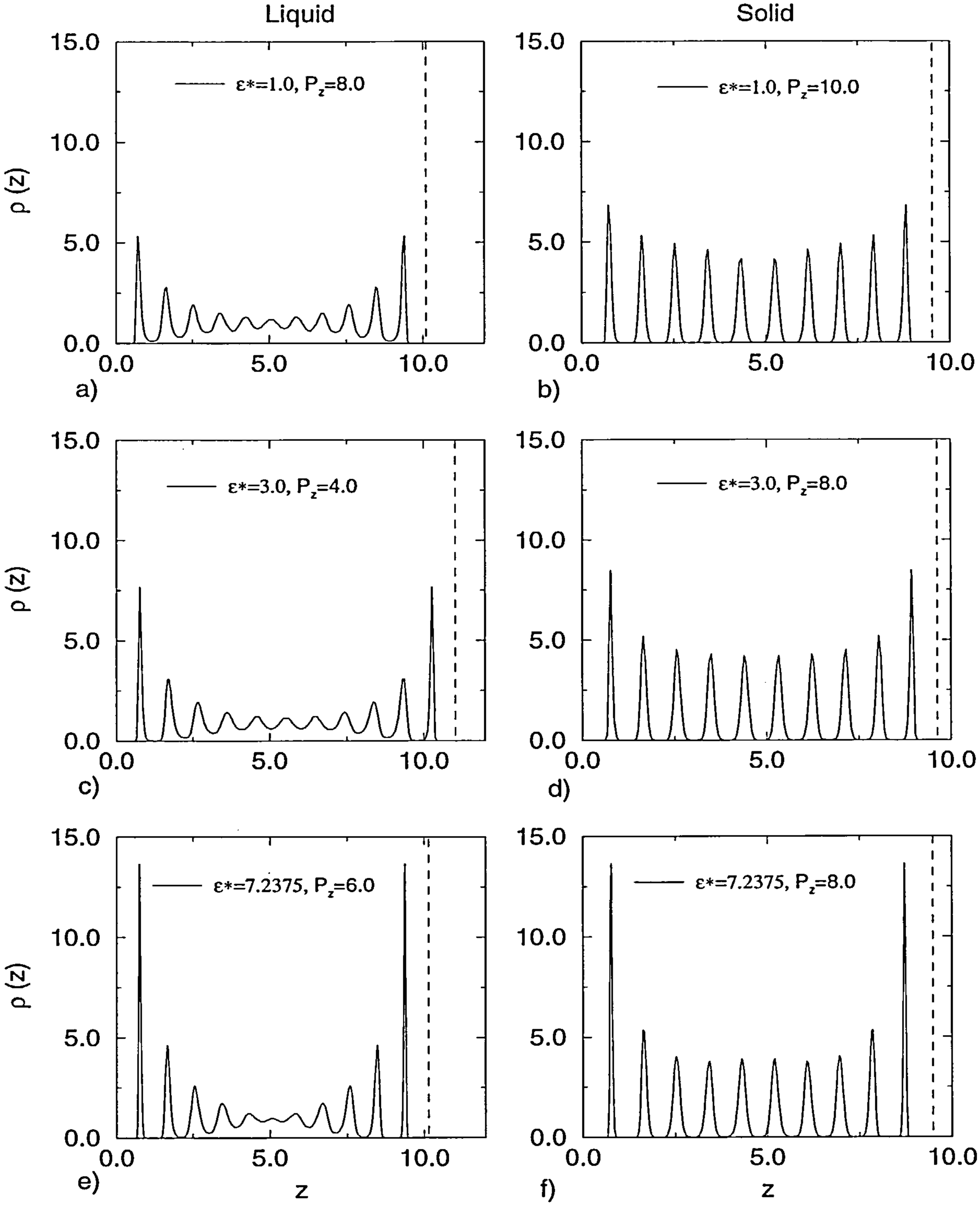

Figure 4.11: The density profiles for a 300-particle system for different values of ϵ^* the parameter which measures the strength of the attractive wall-fluid potential. The main effect is in the first contact layer. $T = 1.15$. The dashed line represents the position of the second wall.

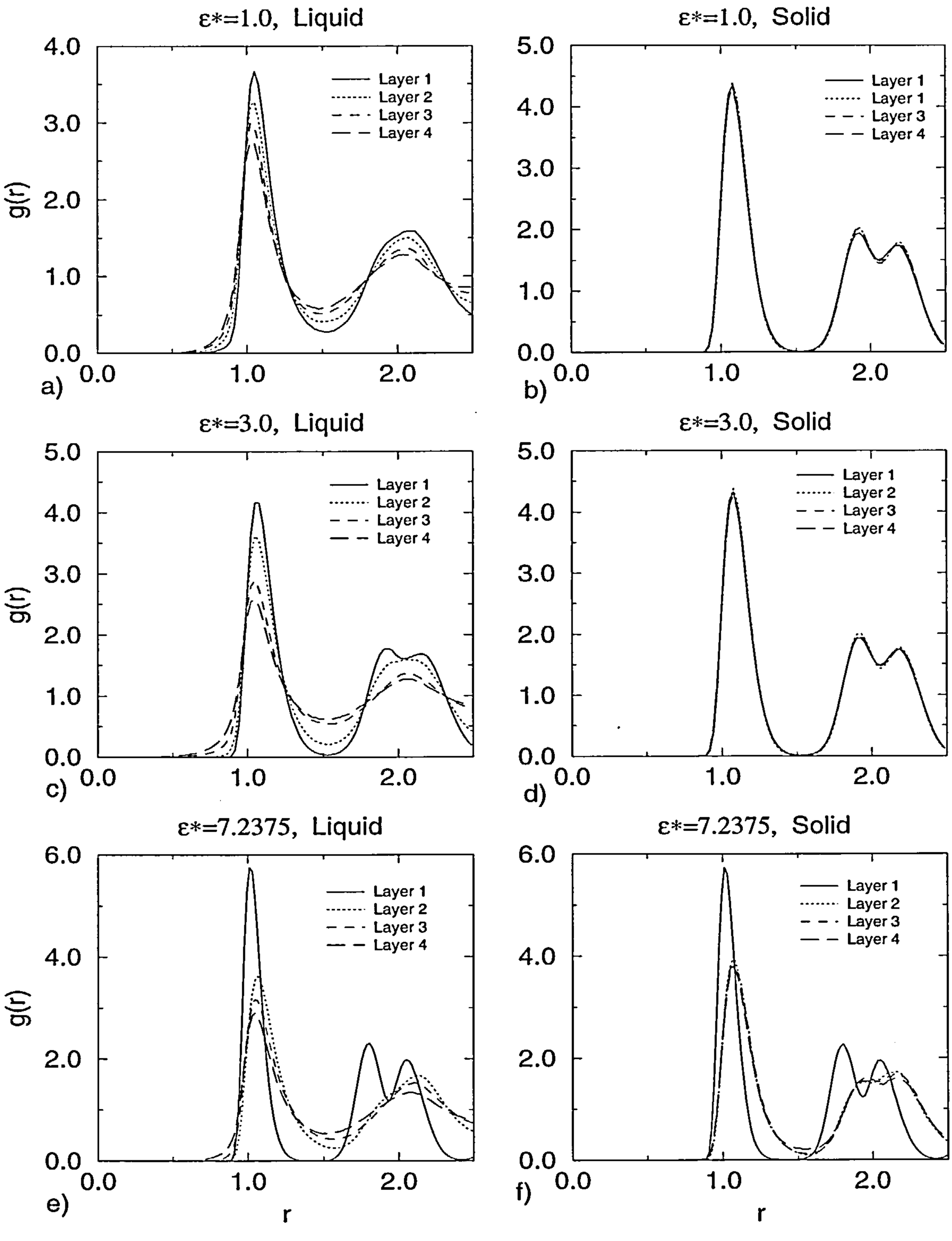

Figure 4.12: The $g(r)$ for the layers shown in figure 4.11. For ϵ^*=1.0 and 3.0 all layers in the solid have almost identical $g(r)$ (ICF).

Once the fluid freezes all the ten layers, for $\epsilon^* = 3.0$ and $\epsilon^* = 1.0$, have very similar structure (see especially $g(r)$ in figure (4.12)) with 30 particles in each one. However, in the formation of the crystal in the pore space an interesting feature occurs for $\epsilon^* = 1$. In this case, a stacking analysis of the layers was performed and I found that for layers 1-5 each plane points in the direction (01) and they are packed in a hcp crystal (abab...). Layers 6-10 also pack in a hcp crystal but they are oriented in the (10) direction. What appears to happen is that two crystals (with different orientations) begin to form from each wall touching each other in the middle of the pore. This effect is probably due to the symmetry of the square walls, since there is no preferred orientation to align the crystal. This phenomenon was also observed in other pore-systems, however for this particular one the effect was more pronounced. For $\epsilon^* = 3$ some layers point in the (01) direction others in the (10) but there is no evidence of any particular order in the stacking of the layers.

Finally, I employed the 9-3 wall potential (as described in equation (3.27)) with the parameter $\epsilon^* = 7.2375$, $\rho^* = 1.0$ and the same σ^* as the last simulations. For this case the minimum of the potential occurs at a lower value than for the 10-4-3 potential with the same ϵ^* and a higher value than for the 10-4-3 potential with $\epsilon^* = 1$. The freezing process is the same as for a 10-4-3 wall potential but in this case when the fluid freezes it adopts the hcp crystal array described above for the 10-4-3 potential with small ϵ^*, i.e. all the layers are similar.

4.5.2 Purely Repulsive walls

For a fluid confined by purely repulsive walls ($\epsilon^* = 1.2771$, $\alpha = 0.0$ and $\sigma^* = 1.0946$ in equation (3.28) similar features occur as when the fluid is confined by weakly attractive walls (small ϵ^*). Here the temperature is again $T = 1.15$. However, now there is definitely no formation of crystal layers close to the walls. For these particular simulations the wall area was taken to be, $S = S_x S_y = 5.5375 \times 5.7551$ which is selected to accommodate exactly the (111) layers of the fcc crystal. When

the system is in a liquid-like state the in-plane pair correlation function and its FT show that the contact layer is liquid-like, as are all the middle layers (figure 4.13). Since the walls exert no attraction at all, it is rather difficult for the fluid to nucleate an initial cluster (on the walls) which would start the freezing process (as occurs with attractive walls). In order to form the solid-like state in the pore requires increasing the pressure to much higher values. In fact, this increase in the pressure makes the average pore size smaller than when attractive walls are employed. Consequently the system forms (slightly) narrower crystal layers when it interacts with purely repulsive walls than when it interacts with attractive ones. The width of the layer (δ) is measured as the distance between two neighbouring minima in the density profile. Thus, $\delta \simeq 0.90$ for this repulsive case whereas for attractive walls $\delta \simeq 0.92$. Moreover, as for weakly attractive walls, when the fluid freezes all the layers are alike each having 30 particles and a stacking analysis of the layers again identifies two set of layers. Layers 1-3 point in the (01) direction and they pack in abab... sequence whereas layers 4-10, which are also stacking in abab... sequence, point in the (10) direction. Again, it seems that a frustrated crystal is formed over the whole space inside the pore.

4.5.3 Structured walls

The structured walls were constructed as described in chapter 3. The top and bottom walls were made of four layers (each) with 32 particles in each one, arranged in a fcc crystal with lattice parameter $a = 0.482$nm (this parameter is rather large compared with that used by other authors [96] where the lattice parameter is a=0.246nm). The walls were put exactly out of registry. In the frozen state we can see from the positions of the peaks in the ICF (and its FT, not shown here), each layer forms with the structure of the (100) face of the fcc crystal (figure 4.14) with the first contact layers in complete out of registry with the first wall layers. Actually, subsequent inner layers accommodate in adjacent layers of the (100) face of the fcc

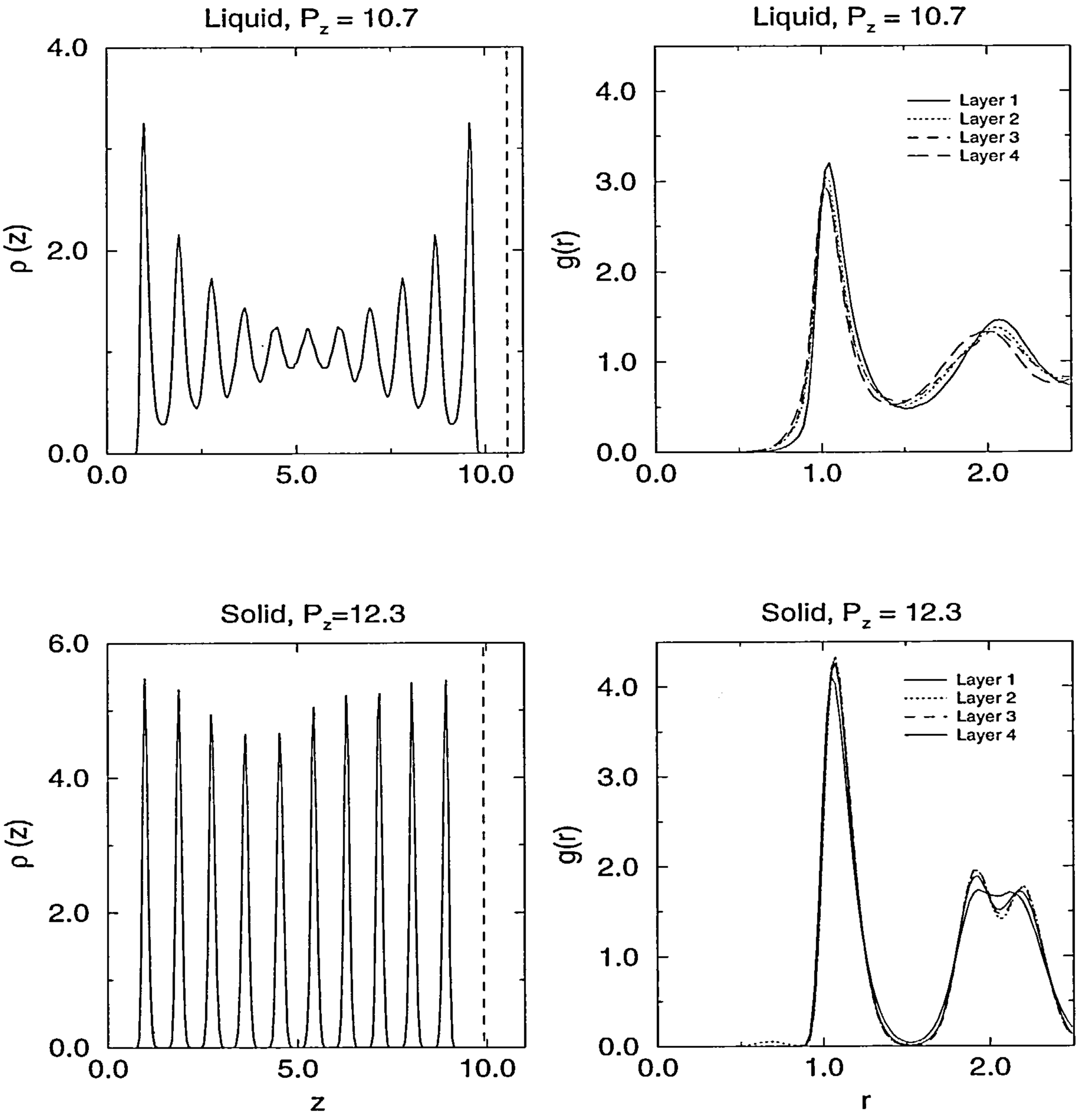

Figure 4.13: The density profile $\rho(z)$ and the $g(r)$ of each layer for a fluid confined by purely repulsive walls. $\epsilon^* = 1.2771$, $\alpha = 0.0$, $T = 1.15$ and $N = 300$. Note the lack of crystalline structure in the first layer when the system is in the liquid-like state. When the system freezes all layers have similar density profile and $g(r)$ (ICF). The dashed line represents the position of the second wall.

crystal (we observe the formation of 10 layers). Thus solid has a tendency to form a 3-D fcc crystal. A brief study of the structure factor for a confined and bulk fluid was performed by Ma et al. [35]. However, they did not compare the structure of the confined solid with the bulk solid. Other authors [96] reported no distinction in the structure of the layers when structured or structureless walls are used, i.e. they observed the same $g(r)$ for both types of walls. I attribute this difference to the different lattice parameter used for this work. For a small lattice parameter the degree of the atomic corrugation in the walls should be small. Recall that in the limit when a goes to zero we have a continuous surface. Thus the structure of the contact layer should not be too different for structured or structureless walls for small values of a.

Of course, the choice of wall-fluid interaction not only affects the structure of the confined fluid and of the solid but also has a strong influence in determining the phase diagram of the confined fluid and this will be discussed in the next chapter.

4.5.4 Bulk crystal structure versus that in the pore

Sokol et al. [100] in an experimental study of confined O_2 and D_2 in Vycor glass, using neutron scattering techniques, observed interesting features in the crystal structure when these liquids freeze. They discussed whether the solid that forms takes the bulk structure. In order to see if the pore fluid has a tendency to take the bulk crystal structure when it freezes, comparisons were made for the 3-D pair correlation function and its FT. For the slit-pore system, the 3-D ICF was measured in the middle of the pore avoiding the first contact layer. I focused on particles in a centre region of the pore. Then I counted the number of neighbours of these particles within a sphere of radius R. The pair correlation function was calculated in the same way as for bulk system (in 3-dimensions). We know that the structure of the bulk argon crystal (simulated with a LJ potential) is fcc [117] (some NPT runs with periodic boundary conditions were made to check this). The actual structure (either

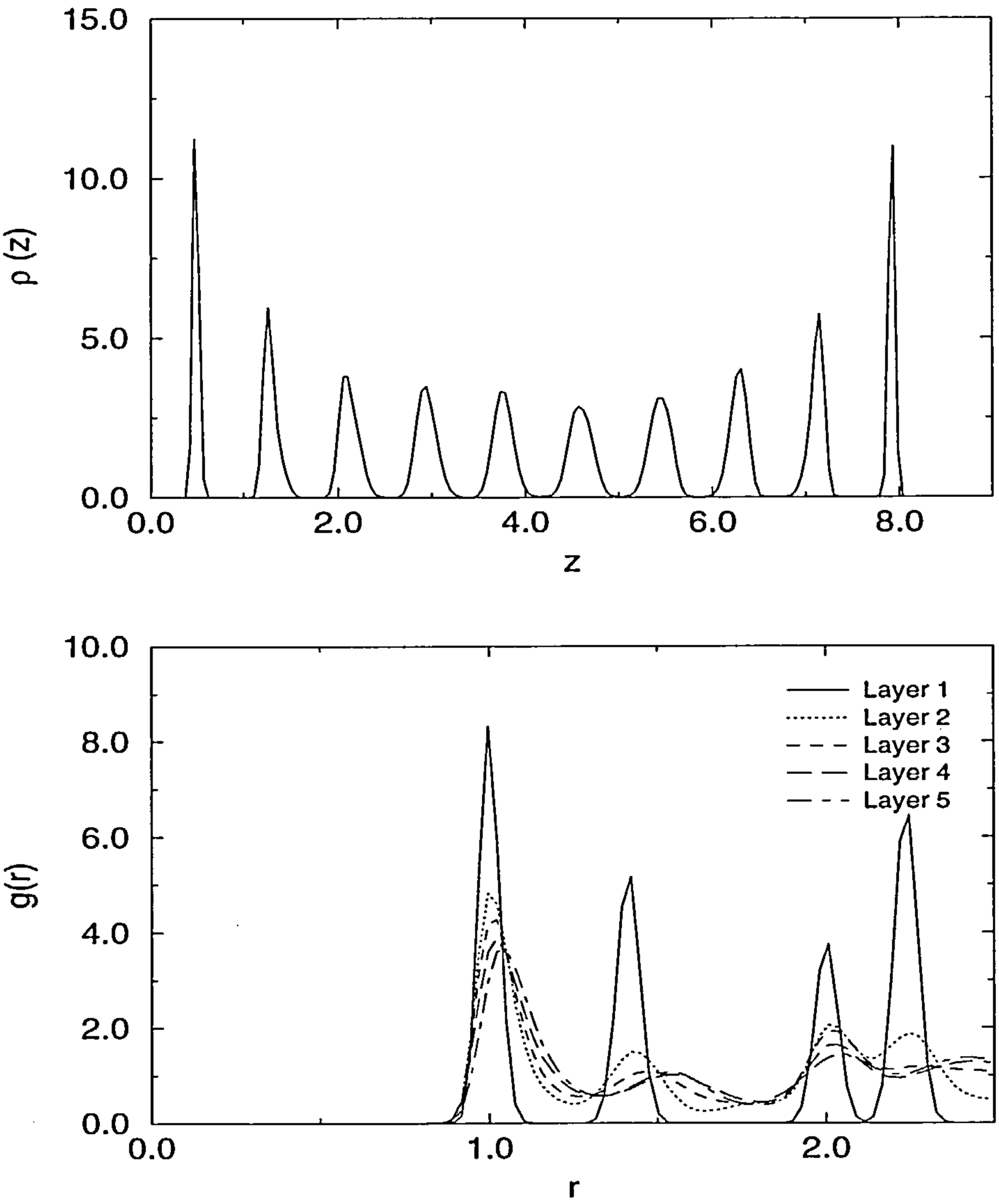

Figure 4.14: The density profile $\rho(z)$ and the $g(r)$ for a fluid confined by structured walls. The results refer to $P_z = 8.0$, $T = 1.15$ and $N = 300$ where the system is solid-like. Here, once the fluid freezes all the layers are in registry with the particles forming the structured walls, i.e. they take the structure of the (100) face of a fcc crystal.

fcc or hcp crystal) that the confined system adopts, was discussed in the paragraphs above.

Whether the fluid takes on the bulk structure depends on the pore size and the wall-fluid interaction, as is seen in figure 4.15. For a fluid confined by small pores ($l \simeq 10\sigma$) with attractive walls ($\epsilon^* = 7.2375$) with a 9-3 potential the agreement between its pair correlation function (and its structure factor) and that for a bulk fluid is poor. The peaks and shape of $g(r)$ ($S(k)$) are not similar. However, for a fluid confined by small pores ($l \simeq 10\sigma$) with weakly attractive walls interacting with a 10-4-3 potential ($\epsilon^* = 1.0$ and $\alpha = 1.0$) the agreement between its $g(r)$ ($S(k)$) and that in bulk seems to be better. For a large pore ($l \simeq 20\sigma$, N=600), as was expected, the pore fluid takes on a structure similar to bulk. We observe similar peaks in $g(r)$ ($S(k)$) with those in the bulk. Since there is no difference in the layers, we also observe a similar shape in the peaks of $g(r)$ ($S(k)$) for a fluid interacting with purely repulsive walls, i.e. the fluid pretends to take on the bulk structure. The wall fluid potential for the results of figure 4.15 is the 10-4-3 potential with $\epsilon^* = 7.2375$ and $\alpha = 1.0$ for the large pore. For the fluid interacting with purely repulsive walls $\epsilon^* = 1.2771$ and $\alpha = 0$. For a fluid confined by structured walls, even when the pore is small ($l \simeq 10\sigma$), the shape of the $g(r)$ and $S(k)$ suggest that the fluid would like to take on the bulk structure.

4.6 Hysteresis

By hysteresis we mean the phenomenon where freezing occurs at a different pressure P_z from melting. It is associated with a region of metastable thermodynamic states. The determination of the equilibrium transitions between the two branches of the hysteresis curve will be investigated in the next chapter. It was found that the extent of the hysteresis depends strongly on the choice of the wall-fluid interaction. Strongly-attractive walls lead to a small hysteresis whereas weakly-attractive walls, or purely repulsive walls produce large hysteresis.

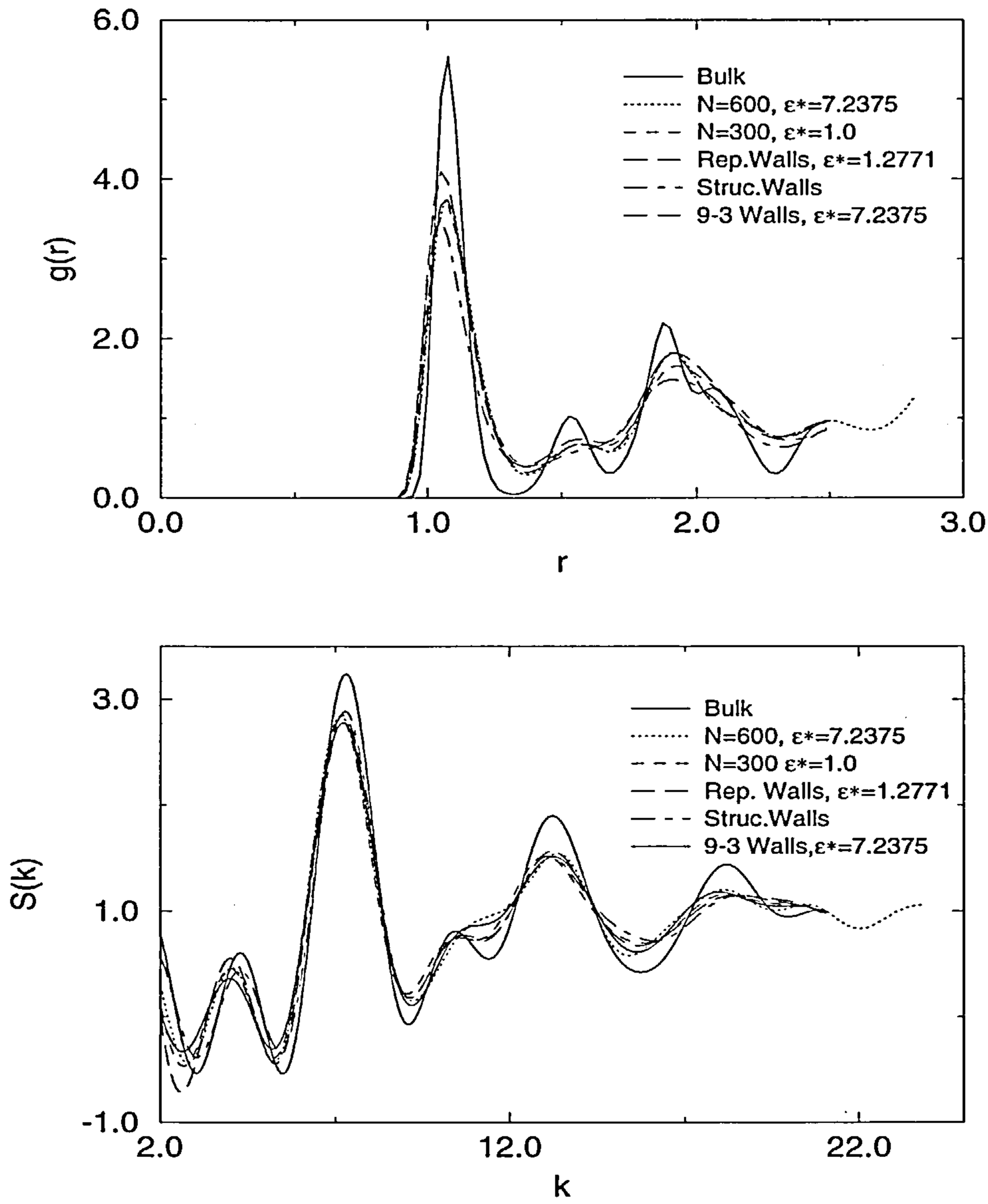

Figure 4.15: The 3 dimensional pair correlation function $g(r)$ and the structure factor $S(k)$ for bulk and confined solids for several pore conditions. All the confined fluids are at $T = 1.15$. $P_z(N = 600) = P_z(N = 300) = P_z(\text{struc.Walls}) = 8.0$, $P_z(\text{Rep.Walls}) = 12.3$, $P_z(\text{9-3 Walls}) = 9.0$. The bulk was simulated at $P(\text{Bulk}) = 5.68$ and $T = 0.5$ with $N = 300$.

It is known that in computer simulation is difficult to nucleate a bulk crystal from a liquid, and therefore large hysteresis is observed [118]. Thus, here we expect a similar situation. Freezing will start only when the crystal nucleates. Moreover in the NP_zT ensemble the system finds its equilibrium pore size (i.e. the volume changes until equilibrium is reached), so we expect to observe larger hysteresis than for the GCMC ensemble where the pore size is fixed [34,38,59,96]. In order to study the hysteresis I performed Monte Carlo runs for different wall-fluid interactions. For this particular analysis the pore-walls had a rectangular cross section, $S_x = 5.5378$ and $S_y = 5.7551$ and the temperature was again $T = 1.15$. For a fluid interacting with purely repulsive walls there was very large hysteresis, no matter whether it was a 300-particle or a 600-particle system, suggesting that the extent of hysteresis is not affected by the size of the pore. This is shown in d) and f) of figure 4.16 where the mean density in the pore is plotted versus P_z. As we will see in the next chapter, a useful parameter to characterize the freezing transitions is the pore width l (i.e. the mean density ρ if N and the wall area are fixed). However, it has been reported that for GCMC [96] the hysteresis is significantly affected by the precise way the layers are packed in the pore. By changing the pore width slightly, Miyahara and Gubbins [96] observed that the layers get wider or narrower and that this affects directly the extent of the hysteresis. Unfortunately it is not possible to confirm this effect in the present ensemble since I do not have control over the pore width, i.e. it is not fixed at the outset. For a 300-particle fluid interacting with repulsive walls plus a small attraction (α=0.5, $\epsilon^* = 1.2771$ and $\sigma^* = 1.0946$ in equation (3.28)) the extent of the hysteresis is smaller (see figure 4.16 b)) and when the fluid interacts with fully attractive walls ($\alpha = 1.0$) the hysteresis is even smaller. Now strong (ϵ^*=7.2375) and weak (ϵ^*=1.0) attractive potentials do not lead to any significant difference in the hysteresis (a) and (e) of figure 4.16 (for this particular wall-fluid interaction the wall area is $(5.66139)^2$). I also monitored the hysteresis for a purely repulsive fluid interacting with purely repulsive walls (equation (3.28) with ϵ^*=1.2771 and σ^*=1.0946) (figure 4.16 c) and for this case

the extent of the hysteresis is relatively small but it occurs at a higher range of pressures. The repulsive fluid was modelled by the WCA part of the Lennard Jones fluid potential discussed in chapter 1 (equation (1.7) with the ϵ and σ parameters of argon).

In general we can explain these observations with the following argument. For attractive walls, there is always a crystal layer near to the walls which quickly initiates the nucleation of the solid making the overall freezing easy to achieve. When there is no solid contact layer (as occurs for repulsive walls) the freezing is more difficult. Thus, it is necessary to apply higher pressures in order to freeze the fluid. Although in this case is not clear whether the fluid starts freezing from the walls or not, there is some evidence from other work to show that all the layers freeze at almost the same time [35].

4.7 Conclusions.

Freezing of a confined fluid appears to be a complex phenomenon which depends on several factors, even for simple geometries such as the slit pore. For instance, the structure of the fluid is governed by both the size of the pore and by the interaction of the fluid with the walls. In fact, the mere presence of the walls produces order normal to the walls (oscillations in the local density $\rho(z)$). Whether the fluid freezes from the walls towards the centre or vice versa seems to be determined by the type of wall potential that is employed. Fluids confined by attractive walls favour the creation of crystal layers near to the walls, even when the fluid is liquid-like in the centre of the pore and the fluid starts freezing from the walls. We can also observe new features in the formation of the layers once the fluid crystallizes. For fluids confined by purely repulsive walls there is no formation of crystal layers until the whole fluid freezes, suggesting that the layers freeze simultaneously. The extent of the hysteresis is also affected by the type of walls which confine the fluid. Larger hysteresis is observed for systems confined by purely repulsive walls than for those

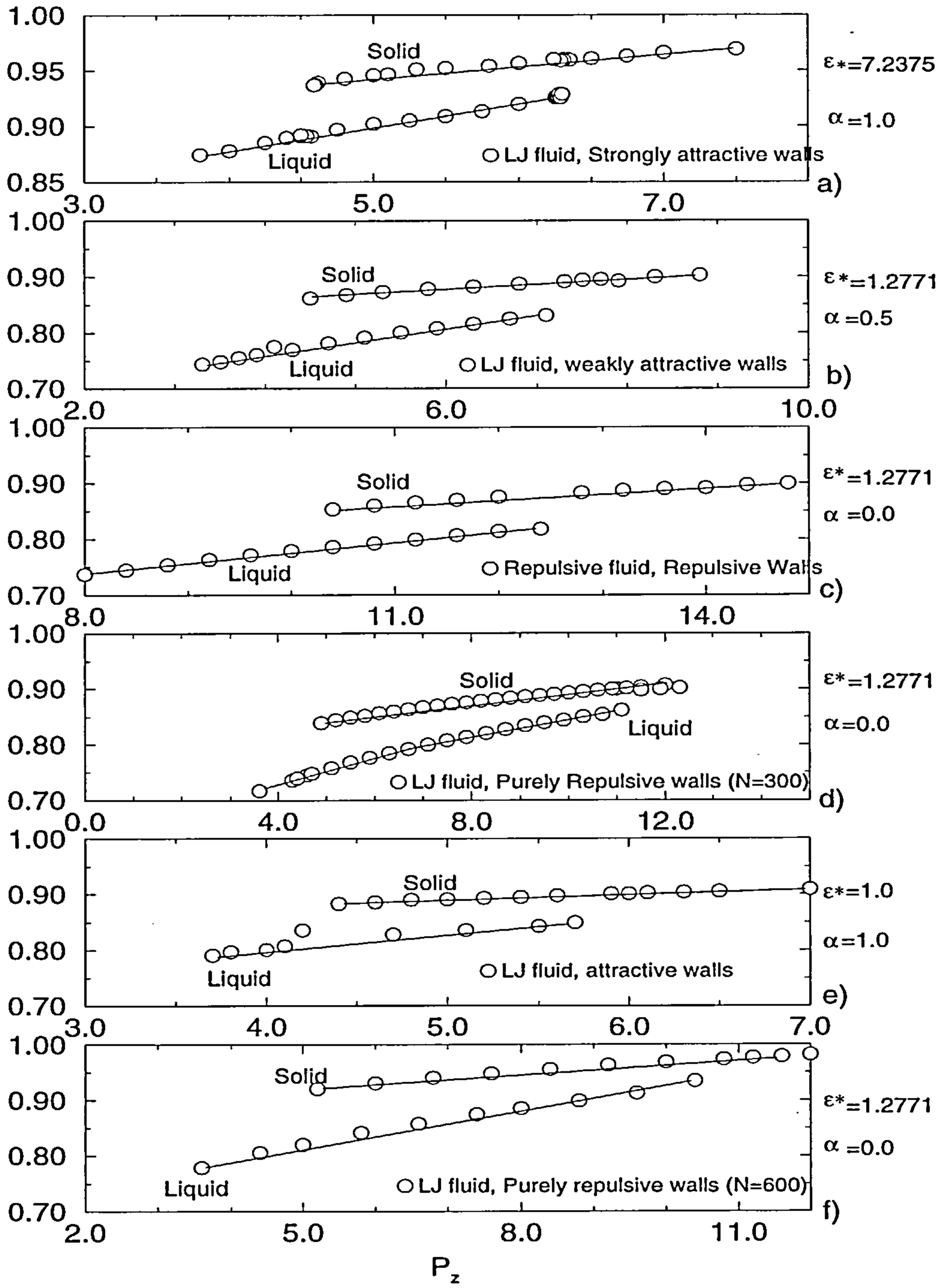

Figure 4.16: Mean density ρ (in reduced units) versus P_z for various wall-fluid potentials. The upper curve in each figure refers to solid and the lower to liquid. There is pronounced hysteresis in all cases. Note the different pressure scales. $N = 300$ for all figures except figure f) where $N = 600$. Error bars are of the size of the symbols.

confined by attractive walls.

Chapter 5

Phase Diagram

5.1 Introduction

As mentioned in the last chapter, on going from freezing to melting (increasing or decreasing the pressure) large hysteresis is observed. Thus, in order to locate the point of true coexistence it is necessary to calculate free energies for all the relevant thermodynamic states. Although several techniques have been developed to calculate free energies for bulk systems [111] (and references therein), for inhomogeneous systems such as confined fluids there are few. In spite of many investigations of the effects of confinement for fluids there are few reports of free energies. To the best of my knowledge only references [34, 38, 64] have attempted this task. However, those calculations were performed for a confined fluid at low density where the liquid-gas transition occurs.

In this section I present a novel technique to calculate free energies for the inhomogeneous fluid that is designed to work at high densities.

5.2 Thermodynamics for the slit-pore ensemble

Before any calculation of free energies it is useful to characterize the transition in the slit-pore from the thermodynamic point of view. The changes in internal energy

for the system in terms of the appropriate thermodynamic variables, described in chapter three (the slit-pore in the NP_zT ensemble), is:

$$dU = TdS + \mu dN + 2\xi dA - (AP_z)dl. \tag{5.1}$$

In this expression the first two terms are the same as those in bulk, the third one corresponds to the wall-fluid tension contribution (the factor 2 comes from the fact that there are two walls in the slit), the last term is due to the external force (AP_z) applied normal to the walls and A is the area of a single wall. Some authors (e.g. reference [68,119]) write $2\xi = (\partial U/\partial A)_{S,T,l} \equiv T_{||}l$ where the stress $T_{||}(= T_{xx} = T_{yy})$ is the negative of the transverse component of the pressure tensor, and write $P_z = -T_{zz}$ for the normal pressure.

From equation (5.1) I can define an expression for the Gibbs free energy of the confined system:

$$G = U - TS + (AP_z)l \tag{5.2}$$

and using equation (5.1) in equation (5.2) I can write the change in the Gibbs free energy as:

$$dG = -SdT + \mu dN + \zeta dA + lAdP_z \tag{5.3}$$

where

$$\zeta \equiv 2\xi + lP_z = \left(\frac{\partial G}{\partial A}\right)_{N,T,P_z}. \tag{5.4}$$

I refer to this term as the excess plate-fluid interfacial tension. The connection between this potential and other thermodynamic potentials can be expressed in terms of the grand potential. From the thermodynamics given by equation (5.1) we see that the interfacial tension is a function (at fixed area) of the intensive variables T, μ and the separation between the walls, l. Thus if we integrate equation (5.1) with T, μ and l fixed we obtain:

$$U = TS + \mu N + 2\xi A. \tag{5.5}$$

Then, the grand potential for this system is given by the expression:

$$\Omega = U - TS - \mu N = 2\xi A. \tag{5.6}$$

Recall that for bulk systems the grand potential is given by $\Omega = -PV$. Since our system experiences a external pressure normal to the walls (P_z), we define the excess quantity:

$$\Omega_{ex} \equiv \Omega + P_z l A \tag{5.7}$$

Then, from the last two equations we can write:

$$\Omega_{ex} = (2\xi + P_z l)A, \tag{5.8}$$

so that (recalling (5.4))

$$\frac{\Omega_{ex}}{A} = \zeta. \tag{5.9}$$

i.e. $\zeta = 2\xi + lP_z$ can be identified with an excess grand potential per unit area. This expression for the grand potential is analogous to that which would hold if the pore were in contact with a reservoir (see chapter 2, [44]). However, since in the present case we do not have any reservoir of fluid we do not expect the definition of the surface tension to be equivalent in both cases. Note that there is no bulk term $-PdV$ in equation (5.1)

Now, coming back to the Gibbs free energy, if we take second partial derivatives in equation (5.3), the following expression is found;

$$l = \left(\frac{\partial \zeta}{\partial P_z}\right)_{N,T}. \tag{5.10}$$

This tells us how the pore-length changes because of variations of the excess interfacial tension with respect to the normal pressure applied to the walls. Also, from equation (5.3) we have;

$$S = -\left(\frac{\partial G}{\partial T}\right)_{N,A,P_z}, \tag{5.11}$$

$$\mu = \left(\frac{\partial G}{\partial N}\right)_{T,A,P_z}, \tag{5.12}$$

$$lA = \left(\frac{\partial G}{\partial P_z}\right)_{T,N,A}. \tag{5.13}$$

From the statistical mechanics viewpoint, the thermodynamic potential given by equation (5.2) is related to the partition function of the NP_zT ensemble by the following expression:

$$G = -k_B T \ln Q_{NP_zT} \tag{5.14}$$

where Q is the partition function

$$Q_{NP_zT} = \sum_{\{\mathbf{r},\mathbf{p}\}} \sum_{V} \exp(-(H(\mathbf{r},\mathbf{p}) + P_z A l)/k_B T) \qquad (5.15)$$

$H(\mathbf{r},\mathbf{p})$ is the Hamiltonian of the system as a function of the positions $(\mathbf{r})$ and momenta $(\mathbf{p})$ of the particles, $V = Al$ is the volume and P_z is the normal pressure. The volume changes resulting from this scheme are characterized by a transition probability,

$$\exp(-\beta(P_z A l_{nm} + \delta\phi_{nm}) + N \ln(l_n/l_m)) \qquad (5.16)$$

(see chapter 3, equation (3.32)).

Coexistence of two different confined phases, α and β, is given when the Gibbs free energies are equal, i.e. $G_\alpha = G_\beta$, for given P_z, T, A and N. For fixed wall area, by performing an infinitesimal change in (P_z, N, T) in such way that α and β remain in equilibrium, I obtain

$$-(S_\alpha - S_\beta)dT + (\mu_\alpha - \mu_\beta)dN + (l_\alpha - l_\beta)A dP_z = 0. \qquad (5.17)$$

Thus, the coexistence of the two phases is given by the following Clapeyron equations,

$$\left(\frac{\partial P_z}{\partial T}\right)_N = \frac{(S_\alpha - S_\beta)}{A(l_\alpha - l_\beta)}, \qquad (5.18)$$

$$\left(\frac{\partial P_z}{\partial N}\right)_T = -\frac{(\mu_\alpha - \mu_\beta)}{A(l_\alpha - l_\beta)}, \qquad (5.19)$$

$$\left(\frac{\partial N}{\partial T}\right)_{P_z} = \frac{(S_\alpha - S_\beta)}{\mu_\alpha - \mu_\beta}. \qquad (5.20)$$

These equations are the analogues of equations (2.12)-(2.9) in chapter 2. They show that for a phase-change in the system, the change in pore width, l, or in the chemical potential, μ, are useful order parameters for the transition. Moreover the first order transition from one phase to another will be signalled by a discontinuous jump in these quantities. In fact, one of these criteria (the jump in the pore width) was used to indicate the freezing and the melting transition in the hysteresis curves shown in the last chapter.

5.3 Free Energy Calculations

In order to locate the equilibrium freezing transition of the pore-fluid system, the free energies of the liquid and the solid branches of the hysteresis curve should be calculated. Then the actual coexistence is determined when the Gibbs free energy of the liquid and the solid are equal.

For the solid branch, I did these computations using a standard technique. For the present case I worked with the Frenkel-Ladd method [120, 121] performing a thermodynamic integration. In this method the integration is performed by constructing a reversible path, taking the solid system of interest to a state where the free energy is known (a reference system). Here, the reference system is the Einstein solid under the same thermodynamic conditions as the confined solid.

To implement this method one modifies the original Hamiltonian of the system by the addition of an extra term. Then the new Hamiltonian is written as a function of a coupling parameter, λ (which takes values from 0 to 1):

$$H(\lambda) = K.E. + \lambda U_0 + (1-\lambda)U_R \tag{5.21}$$

$K.E.$ denotes the total kinetic energy of the N particles of the system i.e. $\sum |\mathbf{p}_i|^2/2m$, where $\mathbf{p}_i$ is the momentum of the atom i of mass m. U_0 and U_R are potential energies.

For $\lambda = 1$ ($H(\lambda = 1) = K.E. + U_0$) we recover the Hamiltonian of the system whose free energy we require, the solid within the slit-pore in this case. $H(\lambda = 1)$ contains the contributions of all the interactions in the system, i.e. fluid particle-fluid particle and wall-fluid terms. For $\lambda = 0$ ($H(\lambda = 0) = K.E. + U_R$) we have the reference system, a crystal whose atoms are vibrating independently about their equilibrium positions. This is the classical Einstein crystal with potential energy:

$$U_R = \sum_i^N \kappa \frac{|\mathbf{r}_i|^2}{2} \tag{5.22}$$

with $\mathbf{r}_i$ the position of the atom i and κ the spring constant [2]. The Helmholtz free energy for the system expressed by the Hamiltonian of equation (5.21) is:

$$F(\lambda) = -k_B T \ln Q(\lambda) \tag{5.23}$$

where $Q(\lambda)$ is the partition function,

$$Q(\lambda) = \frac{1}{N!\Lambda^{3N}} \int \exp(-\beta(\lambda U_0 + (1-\lambda)U_R))d\mathbf{r}. \tag{5.24}$$

Here $\mathbf{r}$ is a shorthand for the positions of the N particles. For $\lambda = 0$, the Helmholtz free energy is given by

$$F(\lambda = 0) = -Nk_B T \ln \frac{e}{N\Lambda^3} \int \exp(-\beta U_R)d\mathbf{r} \tag{5.25}$$

where Stirling's approximation was used. If we take for U_R the oscillator potential given by equation (5.22) we have (see e.g. reference [122]):

$$F(\lambda = 0) = -\frac{3}{2} N k_B T \ln \left(\frac{4m\pi^2}{\kappa h^2 \beta^2} \right). \tag{5.26}$$

From equations (5.23) and (5.24), I can write

$$\frac{\partial F(\lambda)}{\partial \lambda} = \langle U_0 - U_R \rangle_\lambda \tag{5.27}$$

where $\langle\rangle_\lambda$ denotes the ensemble average in the state with coupling λ . The Helmholtz free energy of the state of interest is obtained by integrating the last equation,

$$F(\lambda = 1) - F(\lambda = 0) = \int_0^1 \langle (U_0 - U_R) \rangle_\lambda d\lambda. \tag{5.28}$$

Thus, the calculations were performed as follow: For one single solid state point (at fixed N, T and P_z) I obtained the spring constant (from the width of a Gaussian given by the one-particle distribution [123]) of this system. Then for different values of the coupling parameter λ, I calculated $\langle U_0 - U_R \rangle_\lambda$. For such state points, simulations are performed for fixed T, N, and volume obtained from $\langle l \rangle$ in the (NP_zT) simulation. Then equation (5.28) is integrated numerically. The procedure is performed for several state points at different pressures, P_z.

One important point to keep in mind when doing this thermodynamic integration is that we have to avoid any phase transition [120, 123, 124]. The choice of spring constant helps to ensure this, and we saw no evidence of any phase transitions in the solid state in our integrations.

For the liquid branch, I did not find any useful methods in the literature to calculate free energies. Thus, I developed a new scheme to perform free energy calculations in the inhomogeneous fluid. Again the idea is to perform a path integration (as described above), taking the fluid under consideration to a state where

the free energy is known. I carried out this integration by slowly switching off the effects of the walls until the bulk fluid was reached. Then, I used that state as the reference state. In terms of the simulation, this means that the wall-fluid interaction is reduced as λ varies ($\rightarrow 0$) until it vanishes, which then allows periodic boundary conditions in all directions in the simulation box. The Hamiltonian which describes this system is the same as equation (5.21). However in this case U_0 is now the potential energy of the liquid system we seek ($\lambda = 1$), which includes the total potential energy of the pore-fluid, i.e. the fluid-fluid (equation (3.26)) and wall-fluid potential (equation (3.28)). For U_R we have the potential energy of the reference system ($\lambda = 0$), in this case the bulk fluid (a bulk Lennard-Jones fluid). However, since the wall potential is infinite for values of z at the walls, this brings a technical problem to the simulation. The potential (in equation (3.28)) can be infinitely large no matter what value the λ parameter takes (except at $\lambda = 0$). I solved this problem by introducing a large but finite value in the repulsive part of the potential. This means that when the potential is larger than certain value, then it takes a constant value. This value is chosen large enough to ensure that the main potential (the repulsive part) is not affected ($\phi = 15 - 20\epsilon$). Then, the potential was progressively reduced as λ changed.

The free energy calculation was carried out using equations (5.27) and (5.28) with U_0 the total potential energy of the pore-fluid including the walls and U_R that for a bulk.

The computation of the free energy (per particle) for the bulk fluid (reference system) was performed using the standard expression [81],

$$F(\lambda = 0) = F_{id} + \int_0^{\rho} \frac{P(\rho') - \rho' k_B T}{\rho'^2} d\rho' \tag{5.29}$$

where ρ is the fluid density, T the temperature, P the pressure given by the equation of state (calculated from my own bulk simulations) and F_{id} is the Helmholtz free energy per atom of the ideal gas:

$$F_{id} = k_B T(\ln(\rho\Lambda^3) - 1). \tag{5.30}$$

The procedure to calculate free energies was then similar of that for the solid phase. For one single liquid state I calculated $\langle U_0 - U_R \rangle_\lambda$ (at constant N, T and V, obtained from $\langle l \rangle$) for different values of λ. Then, with these results as input and using equation (5.29) I implemented equation (5.28). The procedure was performed for several state points.

Although this procedure is reliable for calculations of the free energies of inhomogeneous fluids, it has a practical limitation. We cannot employ this technique for fluids interacting with a strongly attractive wall potential. If the attraction is strong enough (e.g. $\alpha = 1$ and $\epsilon'/\epsilon = 1.2771$ in equation (3.28)), a well defined solid layer, in contact with the pore liquid, is formed close to the walls (see chapter 4). Thus, if I perform a thermodynamic integration on this system, my method could fail because the path encounters a surface phase transition. For purely repulsive walls ($\alpha = 0$) and for walls with weaker attraction ($\alpha = 0.5$) no solid layers appear when the state is liquid-like (the in-plane pair correlation functions are liquid-like in all the layers). The same is observed for repulsive fluids interacting with repulsive walls. My method should work correctly in all these situations.

A plot of the wall-fluid potential for different values of the α parameter is shown in figure 5.1.

It is important to note that all above results (the thermodynamic integrations) refer to the Helmholtz free energy. However, I use the Gibbs free energy G because this potential characterizes a phase transition more easily. The two free energies are connected by the following expression:

$$G = F + P_z A l \tag{5.31}$$

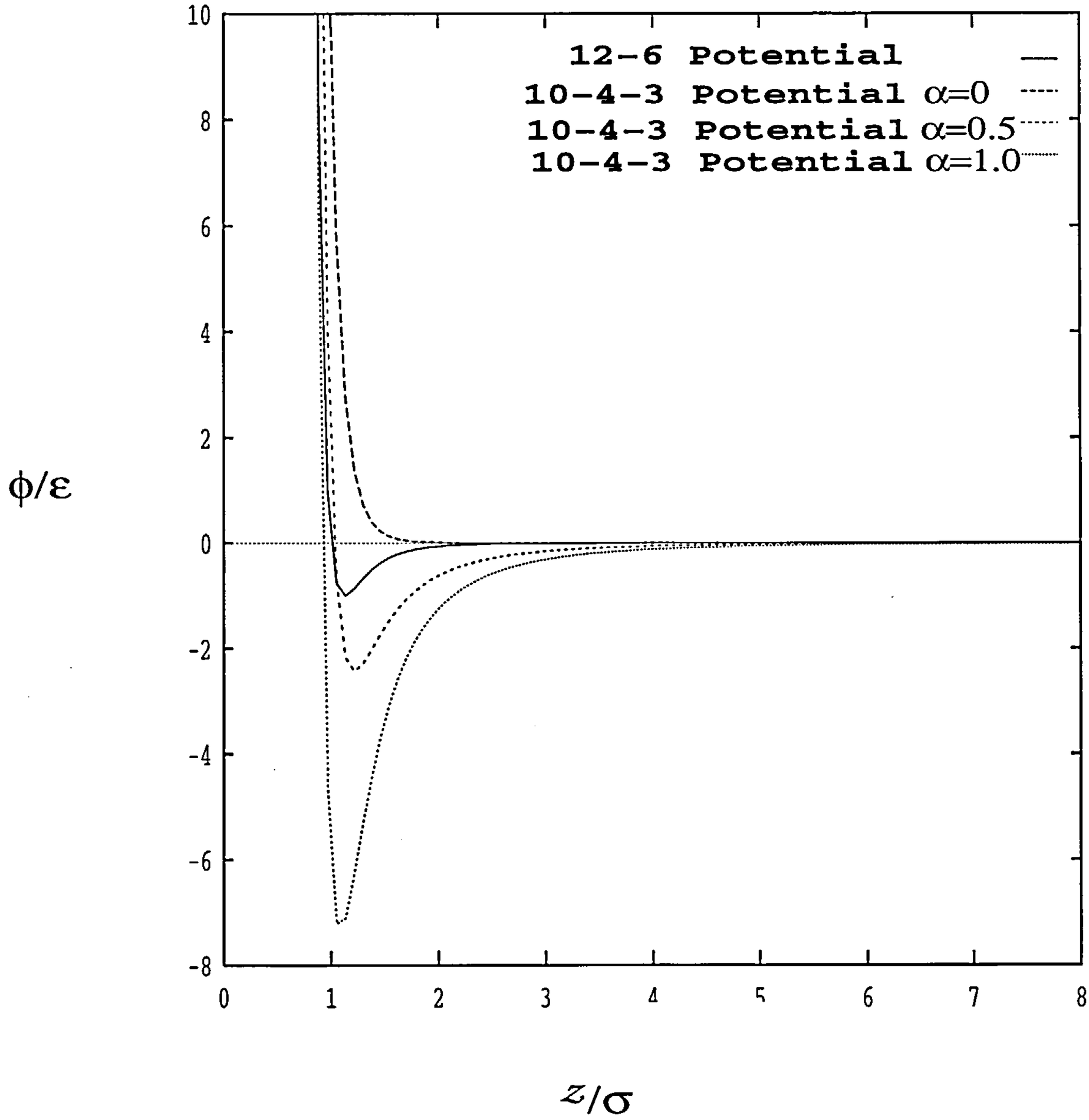

Figure 5.1: Different single wall-fluid potentials and the fluid-fluid (LJ) potential used in this work. The LJ (12-6) and the 10-4-3 potentials are given by equations (3.26) and (3.28). In all cases $\sigma' = 1.0946\sigma, \epsilon' = 1.2771\epsilon, \rho\sigma^3 = \sqrt{2}$ and $\Delta l = \sigma/\sqrt{2}$ with σ and ϵ the fluid-fluid LJ parameters. These parameters with $\alpha = 1$ mimic Argon fluid with CO_2 walls.

with

$$F = U - TS \tag{5.32}$$

which is simply equation (5.2)

5.4 Gibbs-Duhem Integration

With the scheme outlined above I can locate the liquid-solid transition in the confined fluid for one single thermodynamic state. Fortunately, once one transition pressure ($P_z = P_{z0}$) is known for a certain temperature, I can map out more points of the phase boundary using the approach of Kofke [84, 125–127]. The idea behind this method is the following; from one initial coexistence point, an increment in the temperature is attempted, then the pressure is predicted using the Clapeyron equation for the new temperature so as to maintain coexistence. The beauty of this method lies in the fact that in principle just one coexistence point is needed in order to trace out the whole coexistence boundary without further free energy calculation.

The appropriate Clapeyron equation used for this purpose is given by equation (5.18). Using some thermodynamic relations this can be rewritten in a more useful way [125]

$$\frac{d\ln(P_z)}{d\beta} = -\frac{\Delta h}{\beta P_z A \Delta l} = f(\beta, P_z) \tag{5.33}$$

where $\Delta h = h_\alpha - h_\beta$ is the difference in the molar enthalpies of the coexisting phases, $\Delta l = l_\alpha - l_\beta$ is the difference in the pore width and $A = S_x S_y$ is the area of the pore. Δh is calculated from the simulations using the expression $h = U + P_z A l$, which are known quantities in the simulation.

Sometimes it is more useful to work with an alternative version of the Clapeyron equation [127] (e.g. if the pressure drops drastically at low temperatures)

$$\frac{d\beta}{d\ln(P_z)} = -\frac{\beta P_z A \Delta l}{\Delta h}. \tag{5.34}$$

This equation is equivalent to equation (5.33) -we are simply changing the dependent variable (P_z) for the independent one (β or T).

Equation (5.33) (or (5.34)) is solved numerically using e.g. a predictor-corrector algorithm based on the trapezoid formula [128]:

$$P_z = P_{z0} \exp[b f_0]. \tag{5.35}$$

b is the difference in the reciprocal temperatures between the new and the initial state. P_{z0} and f_0 are initial conditions given by the original coexistence point, calculated previously using the methods described in the last section.

Then, the right hand side of equation (5.33) is calculated by simulating two independent and simultaneous boxes in the NP_zT ensemble, each one for each phase. During the simulation, data collection of energies and pore-widths are stored from time to time to compute $f(\beta, P_z)$ and Δh in order to update the pressure (at fixed temperature) with the corrector formula (e.g. again from the trapezoid rule):

$$P_z = P_{z0} \exp[b(f_0 + f_1)/2]. \tag{5.36}$$

f_1 is calculated from the current simulation. Then, the simulation continues with this new pressure. Finally, this process is subsequently applied taking the last temperature and pressure to calculate the next state point until the whole coexistence line is constructed.

This procedure (the Gibbs-Duhem integration) was applied successfully to map out the phase diagram of the bulk Lennard Jones fluid [125, 126]. The results are in good agreement with those calculated with other methods (e.g. simulations in the Gibbs ensemble [129]). Of course it is possible to have some inaccuracy in the method. One error can be due to the inaccuracy in the location of the initial point. If the system is not truly at equilibrium we can have errors in the location of the next coexisting thermodynamic state. Another error can be due to taking the step size too large.

5.5 Results and discussion

5.5.1 Bulk Phase Diagram

In order to investigate how the phase diagram is affected by confinement, first we need to have a good characterization of the bulk phase diagram -in this case of the bulk Lennard Jones system.

Although the Lennard Jones model has been the most used model for studying simple fluids by computer simulations, the complete phase diagram was characterized accurately just recently. For the liquid-gas coexistence line several investigations using various cut-off and shifted potentials have appeared in the literature, and nowadays we know this line quite accurately [125, 126, 129–131]. Moreover, some equations of state exist in the literature which describe quite well the thermodynamic properties of the fluid [106, 132] (and references therein).

For the liquid-solid transition, less work has been performed. Probably the first (detailed) investigation in this direction was conducted many years ago by Hansen and Verlet [81]. They calculated four points on the freezing line and they also estimated the position of the triple point. However, the full liquid-solid boundary line was determined only recently by Agrawal and Kofke [127]. Unfortunately data for different cut-off and shifted potentials were not reported. Since in this present

study all the results refer to a particular cut-off and shifted potential (r_c=2.5), I performed my own calculations to locate the liquid-solid coexistence line for this potential. I carried out the calculations using the NPT ensemble for a system of 400 particles. For this system, initially in a liquid state, I increased the pressure (at fixed temperature) until the fluid froze, then I decreased the pressure until it melted. A large degree of hysteresis was observed. The equilibrium transition was determined by calculating the necessary free energies on the liquid and solid branch of the hysteresis curve. For the solid phase I calculated the free energy using the Ladd-Frenkel method, described above. For the liquid phase I used equations (5.29) and (5.30) constructing the equation of state (P) for one isotherm to calculate the free energy. The equilibrium transition was located by equating the Gibbs free energy of both phases. Then, I mapped out the complete liquid-solid boundary line using the Gibbs-Duhem method. For this particular analysis the Gibbs-Duhem integration began at a reduced temperature of $T = 1.0$.

Data for the liquid-gas coexistence line were taken from reference [106] given by the equation of state. The triple point was estimated by intersection of the two coexistence lines. The results are shown in Figure 5.8 and Tables 5.1 and 5.2.

5.5.2 Phase Diagram of confined fluids

I started my calculations of free energies for a system of 300 LJ-particles at a reduced temperature of $T = 1.15$ and selected the area of the box to accommodate (once the fluid freezes) (111) layers of the fcc crystal: $S_x = 5.5375$ and $S_y = 5.5175$ (in reduced units). The ratio between S_x and S_y is exactly $\sqrt{3}$ times (3/5), i.e. they are constructed to accommodate a perfect hexagonal close packed plane. These dimensions were the same as those used by Lupkowski and van Swol in their simulations of hard spheres confined by hard walls [94]. For the wall-fluid interaction, I chose the potential given by equation (3.28). The wall parameters were chosen equal to those used by Peterson et al. [133], $\epsilon'/\epsilon = 1.2771$ and $\sigma'/\sigma = 1.0946$ (these

Temperature	Pressure(P)	Temperature	Pressure(P)
1.111	6.90(5)	0.682(6)	0.8993
1.053	6.01(4)	0.657(5)	0.6028
1.000	5.20(3)	0.640(5)	0.4041
0.952	4.50(3)	0.619(5)	0.1815
0.909	3.89(2)	0.609(5)	0.0816
0.869	3.35(2)	0.606(5)	0.0367
0.833	2.86(2)	0.604(6)	0.0165
0.799	2.42(2)	0.603(5)	0.0074
0.769	2.02(2)	0.6026(45)	0.0033
0.717(5)	1.3417	0.6025(45)	0.0015

Table 5.1: Values of pressures and temperatures at coexistence for the bulk liquid-solid boundary, $N = 400$. The numbers in parentheses denote the mean error estimated in the last decimal place, e.g. $6.90(5) = 6.90 \pm 0.05$. Errors in T or P depend on which Clapeyron equation was used (equation (5.33) or (5.34)).

parameters were selected to mimic argon confined by carbon dioxide plates, which is considered to be a very weakly adsorbing substrate). The wall density is $\rho\sigma^3 = \sqrt{2}$ and the separation between the lattice planes is $\Delta l = \sigma/\sqrt{2}$. The first calculations were performed for $\alpha = 0.0$, purely repulsive walls. For this choice I found that all layers are liquid-like for all pressures before the fluid freezes (Figure 5.2). Thus, the method described above to evaluate free energies for the liquid is reliable in this case. For pressures where the confined fluid is frozen, ten layers are formed, each with a crystal-like $g(r)$, corresponding to the (111) face of the fcc crystal (i.e. hexagonal order) and the procedure for the calculation of free energies in solids can be used.

As in the earlier simulations the system is initially equilibrated to be liquid-like

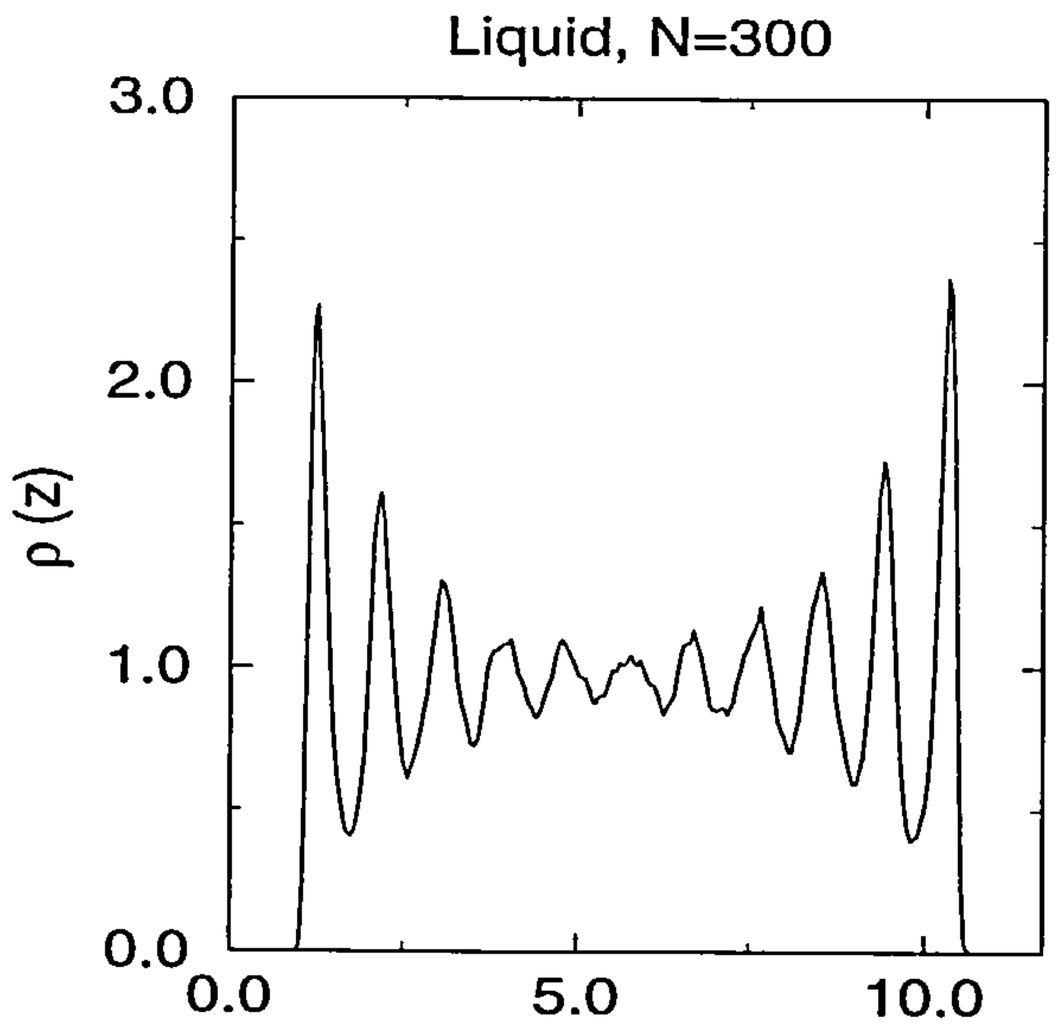

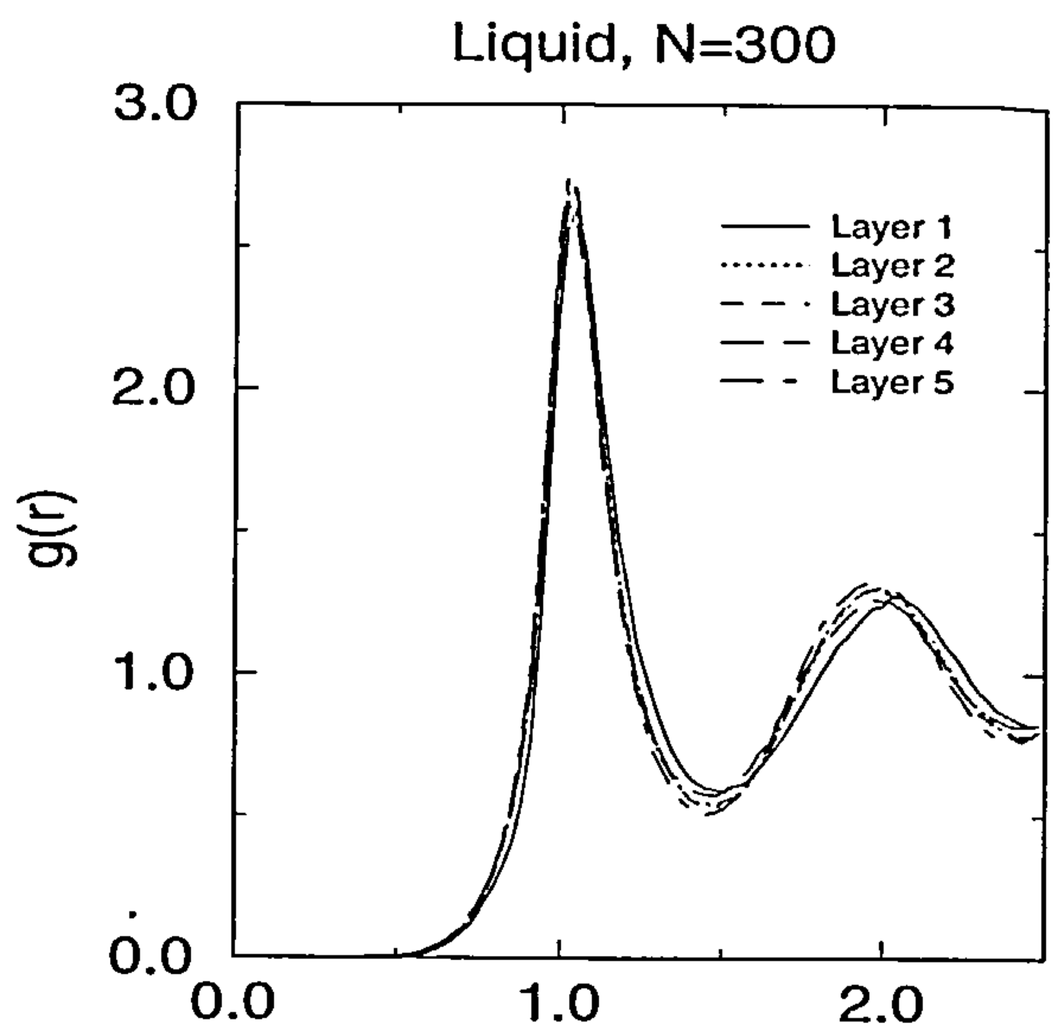

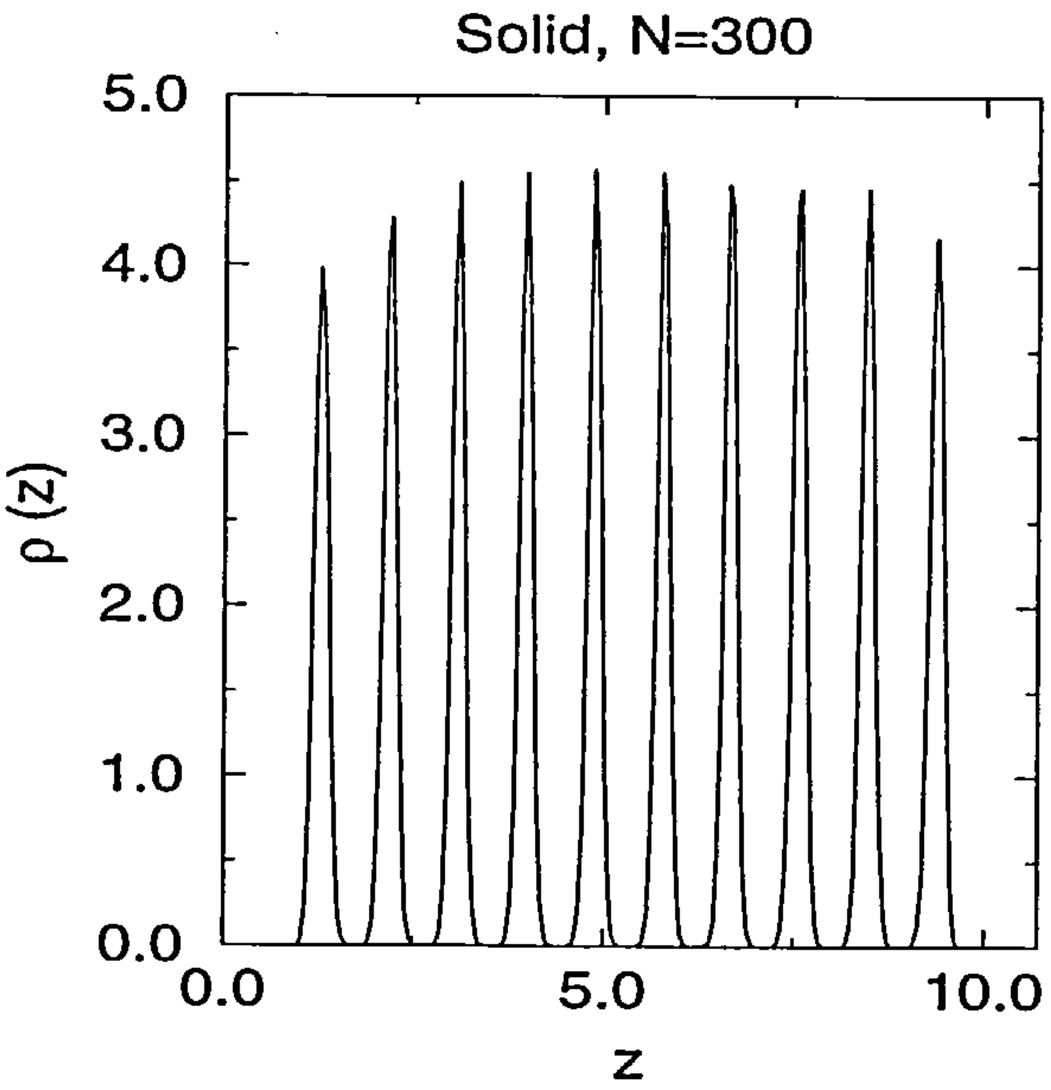

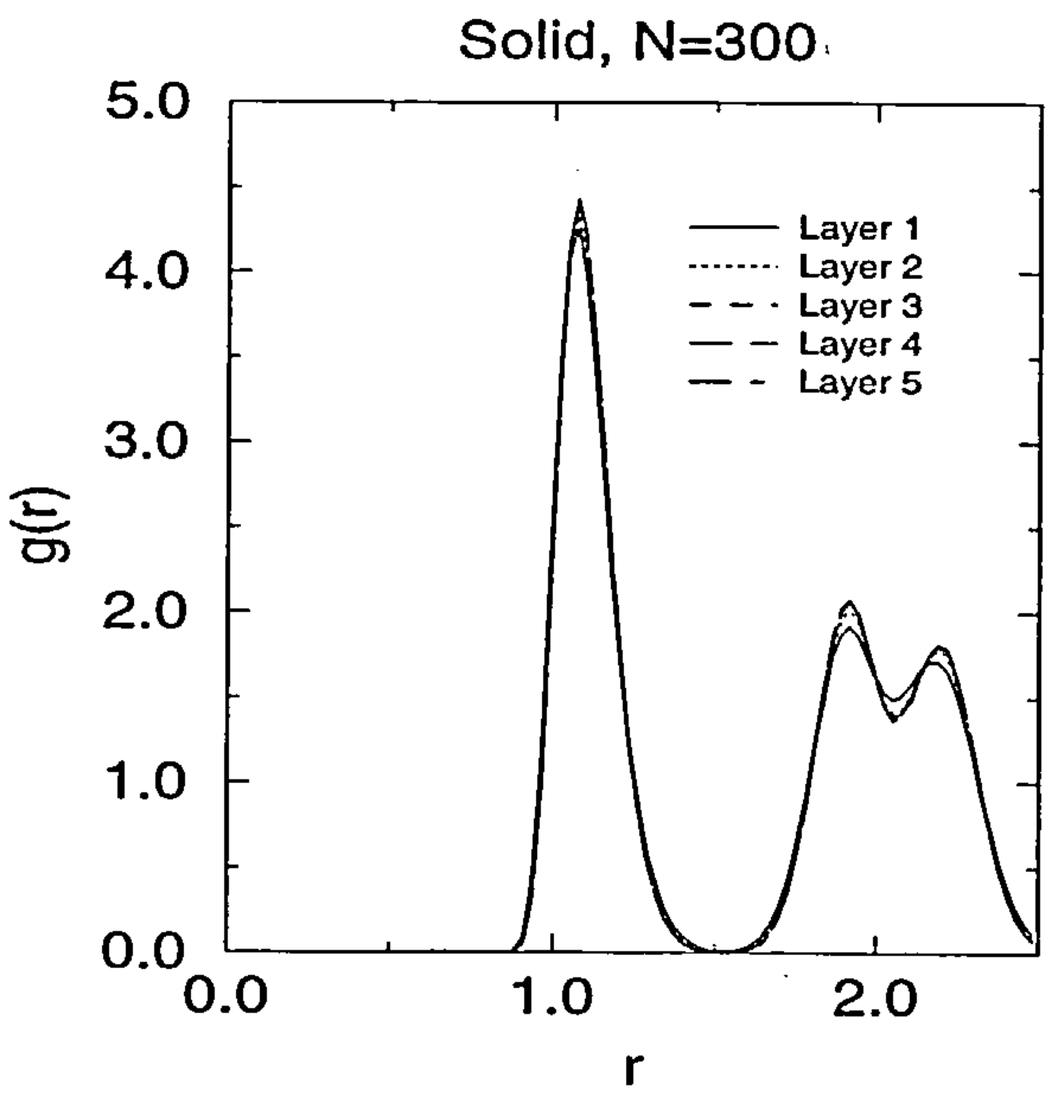

Figure 5.2: Liquid and solid density profiles at coexistence for purely repulsive walls $\alpha = 0.0$. The graphs are for temperature $T = 1.15$ and the coexistence pressure $P_z = 8.52$. The IFC, $g(r)$, of each layer is also plotted. Note that $\langle l \rangle$ is larger for the liquid than for the solid. $\langle l \rangle = 11.41$ for the liquid and $\langle l \rangle = 10.68$ for the solid.

Temperature	Pressure
1.00	0.0636
0.95	0.0454
0.90	0.0320
0.85	0.0224
0.80	0.0144
0.75	0.0082
0.70	0.0050
0.65	0.0025
0.60	0.0012

Table 5.2: Values of pressures and temperatures at coexistence for the bulk liquid-gas boundary. Data were taken from reference [106].

within the pore. Then the pressure is increased (at fixed temperature) until the fluid freezes. This is signalled by a jump in the fluid density or in the pore-width (one of the order parameters). Once the fluid is frozen, I gradually reduce the pressure until the fluid melts. For the solid, the formation of ten crystal layers is again observed for all pressures. As shown in figure 5.3, large hysteresis is observed.

I performed a series of calculations of the free energy for states on the two branches in the hysteresis curve. I found that coexistence occurred at the pressure of $P_z = 8.52 \pm 0.09$ (figure 5.3). This value was determined by fitting a line to the points of the free energies calculated on the liquid and the solid branches (see bottom of figure 5.3). Coexistence occurs when these two curves cross each other.

I also performed the same procedure for a larger pore, i.e. 600 particles under the same pore conditions. The transition pressure, for the same temperature of $T = 1.15$, was $P_z = 7.48 \pm 0.08$ (figure 5.4 and 5.5). Note that this pressure is

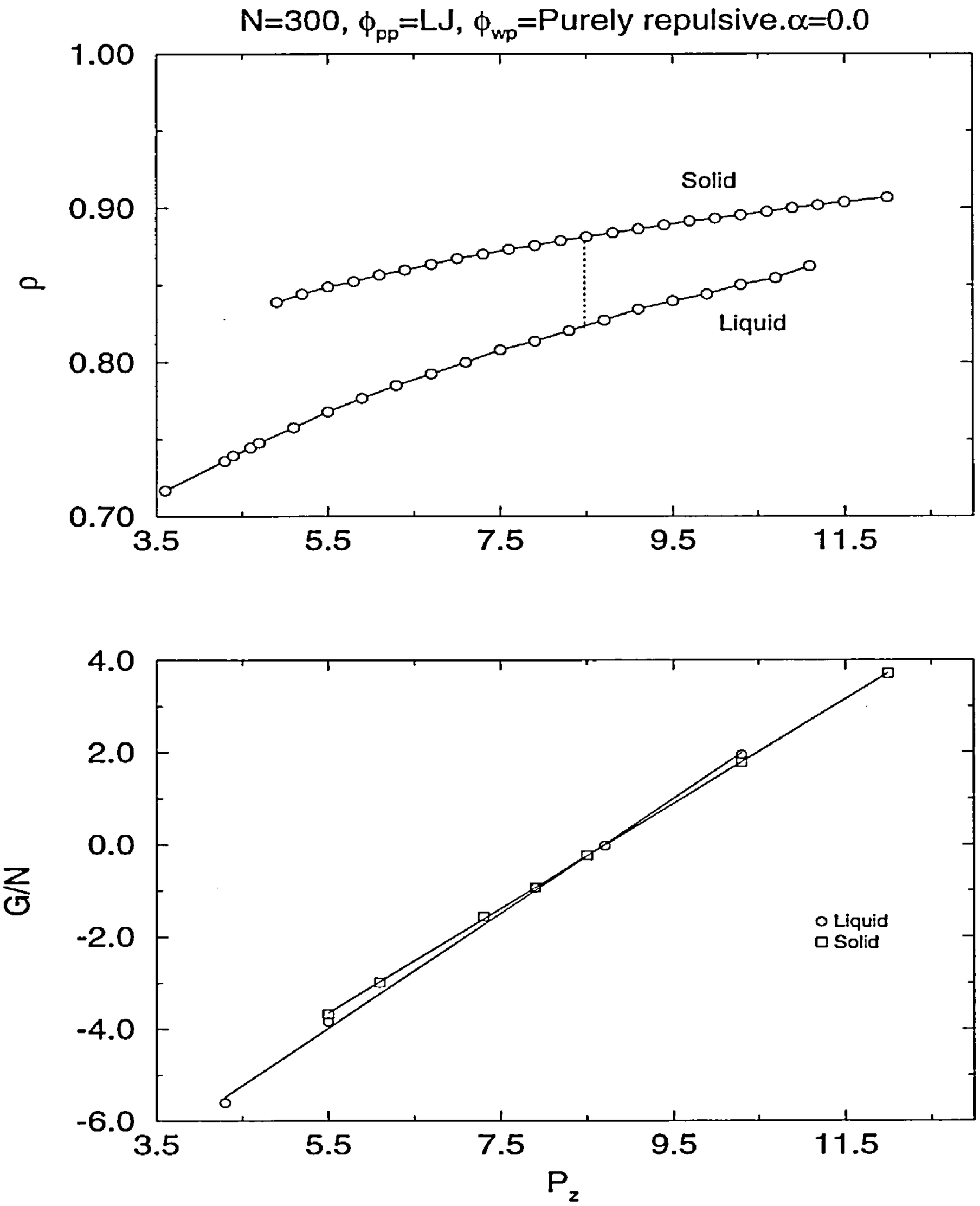

Figure 5.3: Plots of the mean density ρ and Gibbs free energy per particle (G/N) as a function of normal pressure P_z for the 300-particle system with repulsive walls $(\alpha = 0.0)$. The equilibrium transition is shown by the dashed vertical line in the top figure. $T = 1.15$. Error bars associated with the data are of the size of the symbols.

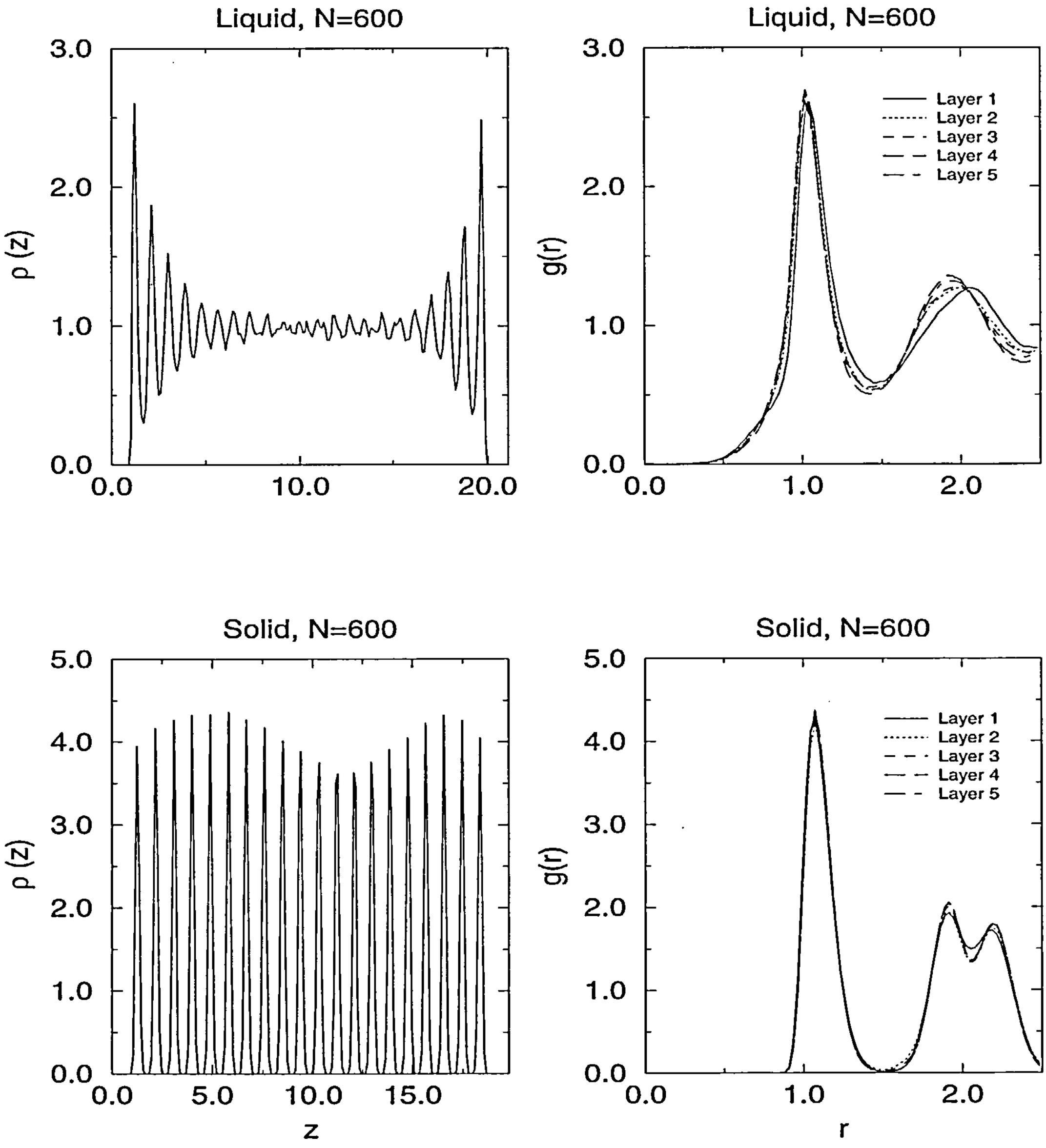

Figure 5.4: Liquid and solid density profiles at coexistence for purely repulsive walls $\alpha = 0.0$. for the 600-particle system. The graphs are for temperature $T = 1.15$ and coexistence pressure $P_z = 7.48$. The ICF, $g(r)$, of each layer is also plotted. $\langle l \rangle = 21.51$ for the liquid and $\langle l \rangle = 19.88$ for the solid.

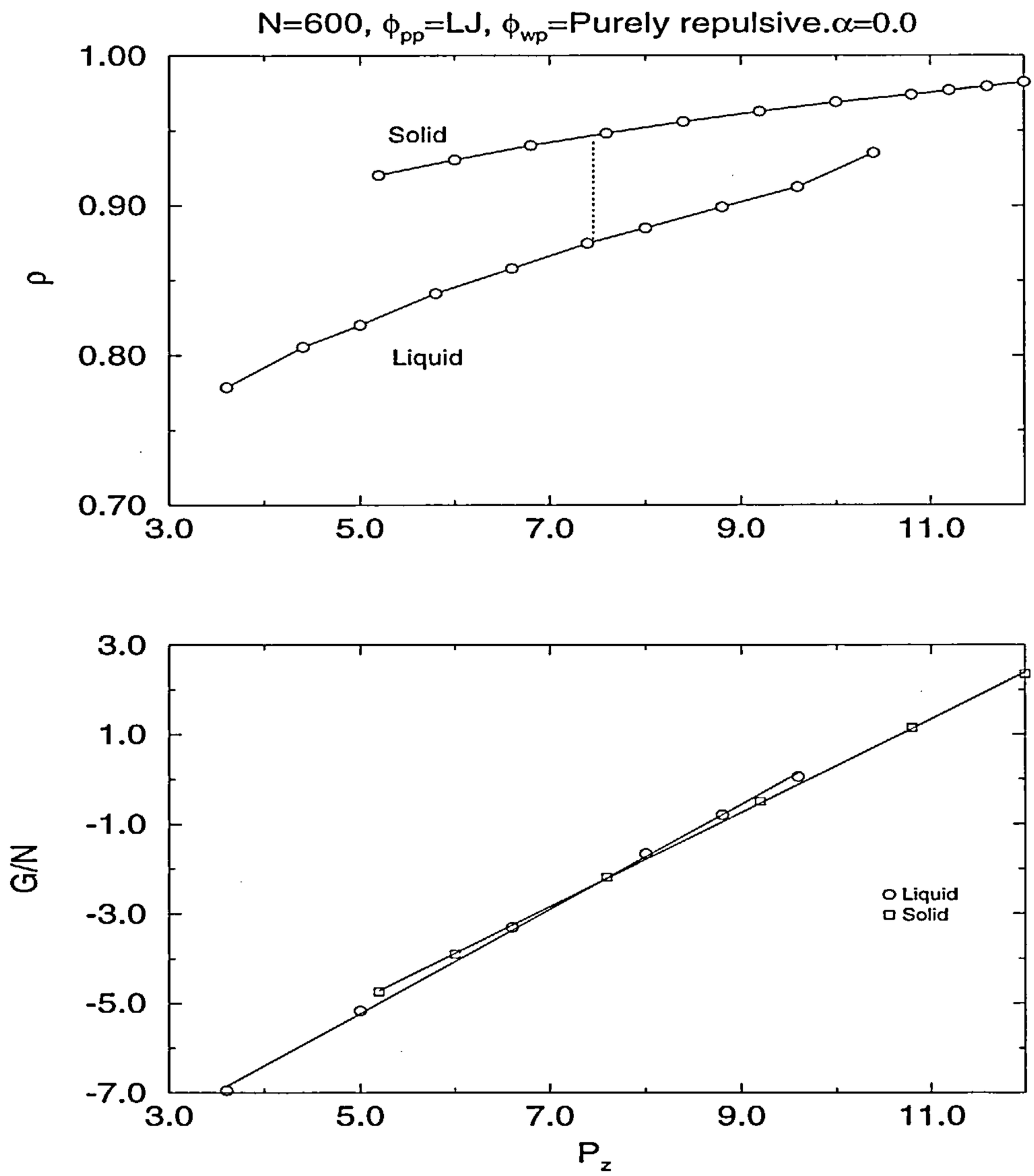

Figure 5.5: Plots of the mean density ρ and Gibbs free energy per particle (G/N) as a function of normal pressure P_z for the 600 particle system with repulsive walls $(\alpha = 0.0)$. The equilibrium transition is shown by the dashed vertical line in the top figure. $T = 1.15$. Error bars associated with the data are of the size of the symbols.

considerably lower than that of the transition in the 300-particle system. We can also observe that the first peak in the liquid density profile is higher for the 600-particle system than for the 300-particle system. This can be explained in terms of the overall density of the system. For the 600-particle system we have twice as many particles and number of layers as the 300-particle system in the same wall area. However this does not imply that the pore width is exactly twice as large. In fact from the figures we observe that the pore width for the larger system is a little less than twice the width of the 300-particle system. For the 300-particle system $\langle l \rangle$ = 11.41 for the liquid and $\langle l \rangle$ = 10.68 for the solid. For the 600-particle system $\langle l \rangle$ = 21.51 for the liquid and $\langle l \rangle$ = 19.88 for the solid. Consequently the total density for the 600-particle system is much higher (see figure 5.3 and 5.5). This information is reflected in the height of the peaks in the density profiles.

I also attempted to perform calculations for a fluid interacting with attractive walls. However, in this case I had to be cautious to avoid any formation of a crystal layer next to the walls which could make the calculations of the free energy of the fluid problematical. Thus, for this computation I deliberately imposed weak attraction to the walls by setting the parameter $\alpha = 0.5$ and $\epsilon'/\epsilon = 1.2771$ in equation (3.28). From figure 5.1 we can see that this potential is much more weakly attractive than the full 10-4-3 potential but it is stronger than the Lennard-Jones one (the fluid-fluid potential). Thus, the wall-fluid potential still exhibits sizeable attraction. The density profile and the in-plane pair correlation function in figure 5.6 show that no crystal layers appear in the liquid phase. On the liquid branch, although the first layer is more structured than those in the middle, $g(r)$ is still characteristic of a liquid (not a solid). This gave me confidence to use my free energy-method. I followed the same procedure as that for fluids interacting with purely repulsive walls and I found the transition pressure for this system at $P_z = 5.56 \pm 0.05$ for the temperature of $T = 1.15$ (figure 5.7). From this analysis and from the last ones (with purely repulsive walls) we observe that some of the density profiles in the solid phase are not perfectly symmetric about the midpoint. One possible reason for this effect

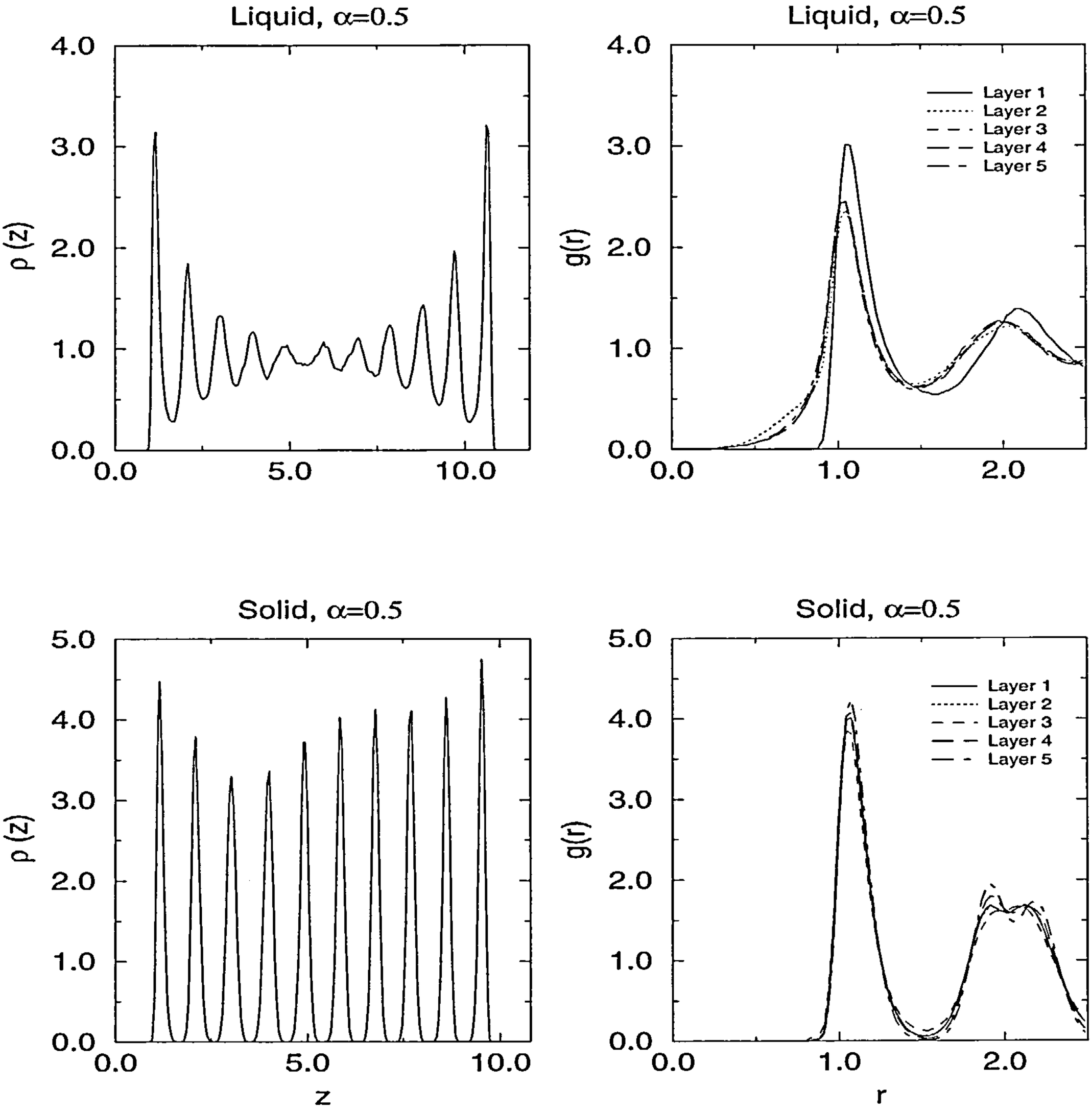

Figure 5.6: Liquid and solid density profiles at coexistence for weakly attractive walls $\alpha = 0.5$ for the 300-particle system. The graphs are for $T = 1.15$ and the coexistence pressure $P_z = 5.56$. The ICF, $g(r)$ of each layer is also plotted. Note that the first layer, for the liquid branch, is more highly structured than those in the middle but it is still liquid-like.

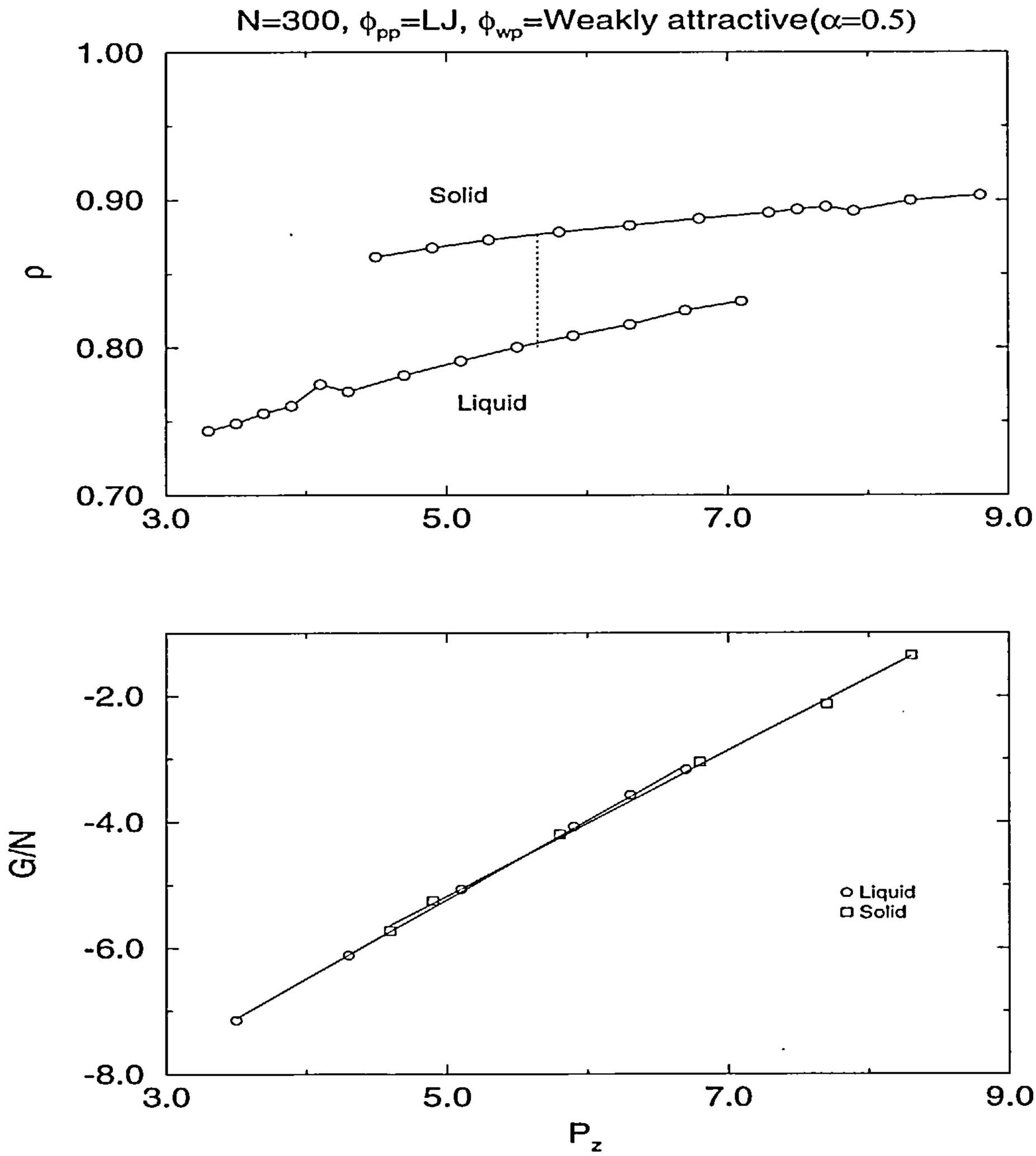

Figure 5.7: Plots of the mean density ρ and Gibbs free energy per particle (G/N) as a function of normal pressure P_z for the 300 particle system with weakly attractive walls ($\alpha = 0.5$). The equilibrium transition (at $T = 1.15$) is indicated by the dashed vertical line in the top figure. Error bars associated with the data are of the size of the symbols.

could be statistics (i.e. the length of the simulations). Another possible explanation could be the following: If we study each layer in the solid phase we find that each one has the same number of particles (30) in a hexagonal array (as was discussed above and in chapter 4). However, from chapter 4 we learned that the layers can align in the (10) or (01) direction. Moreover we saw that two groups of layers (with different orientations) can grow from the walls touching each other somewhere in the pore. When I analysed the layers in the solid state I observed this phenomenon. In fact the two set of layers touched each other in the layers where the density profile is extremely asymmetric. It seems that the mis-matching between the layers somehow affects the symmetry of the density profile.

Having completed the free energy calculations and located the coexistence point (for given wall-fluid conditions) the next step was to map out the phase boundaries for each model. Gibbs-Duhem integration was performed for the 300-particle and the 600-particle systems bounded by purely repulsive walls ($\alpha = 0.0$) and for the 300-particle system bounded by weakly attractive walls ($\alpha = 0.5$). The results for the phase diagram of the various models are shown in figure 5.8 and 5.9 and tables 5.3, 5.4 and 5.5.

One can observe that for the fluid interacting with purely repulsive walls the liquid-solid transition line is shifted towards lower temperatures (at constant pressure) than in bulk. Moreover, one can see that for the larger system the coexistence line is closer to the bulk one. This is not surprising in the sense that for wider pores the fluid should resemble more the bulk. For values of the normal pressure, P_z close to the bulk triple point, the depression in the freezing temperature for the large system is about $\Delta T \approx 0.07$ whereas for the small one it is $\Delta T \approx 0.15$. One interesting phenomenon which is observed for the liquid (at coexistence) at temperatures in the neighbourhood of the bulk triple point is that the density profile loses its oscillatory structure (figure 5.10 and 5.11). When the pressure and the temperature are reduced (at coexistence) the density profiles are similar of those for liquids approaching the liquid-gas transition (see top figure in figure 5.12).

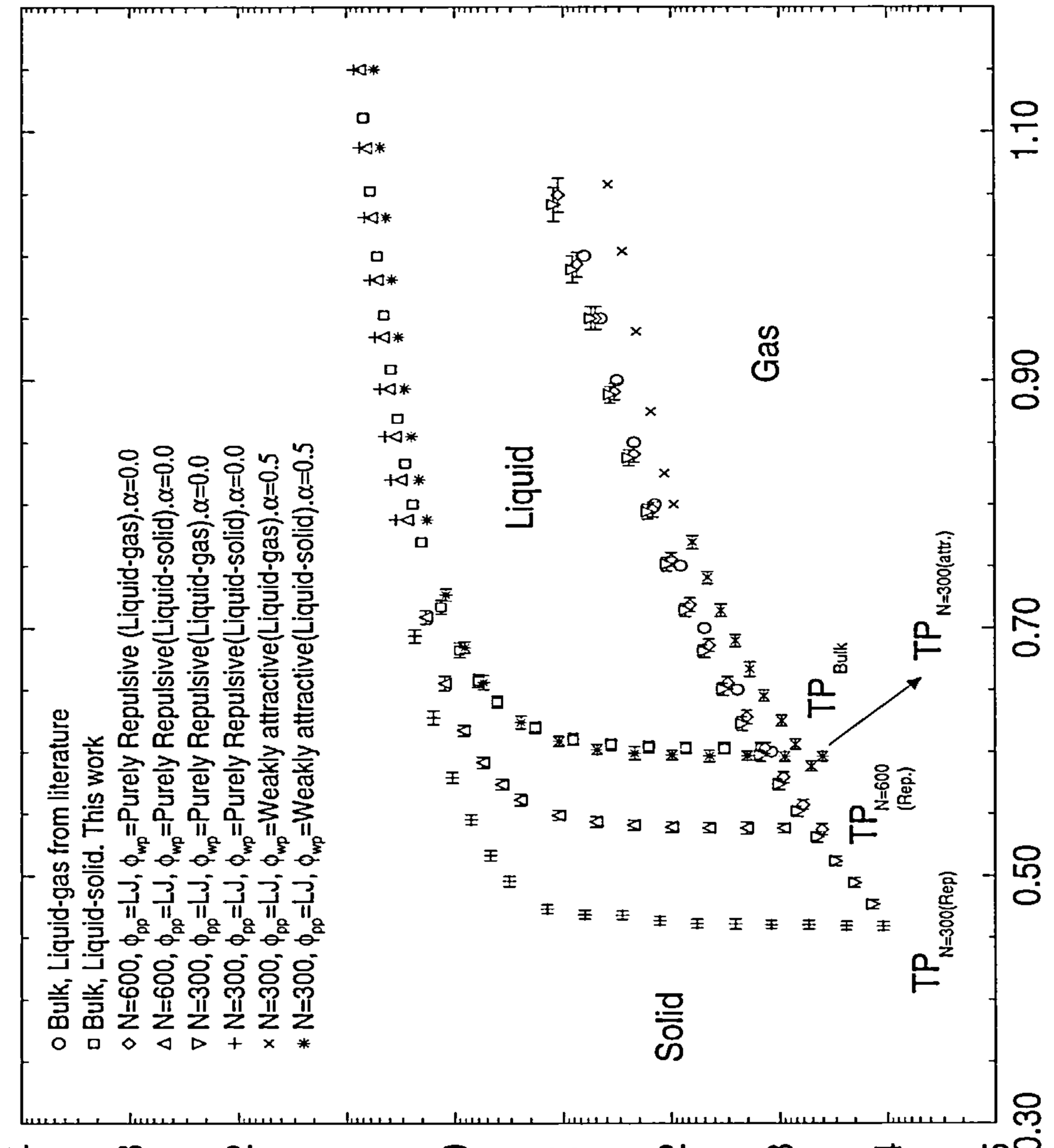

Figure 5.8: The phase boundaries for the confined fluids compared with those of bulk. Note that for the bulk system, P is the bulk pressure whereas for the confined fluid P is P_z, the normal pressure. TP means triple point. Error bars are indicated when they are bigger than the size of the symbols.

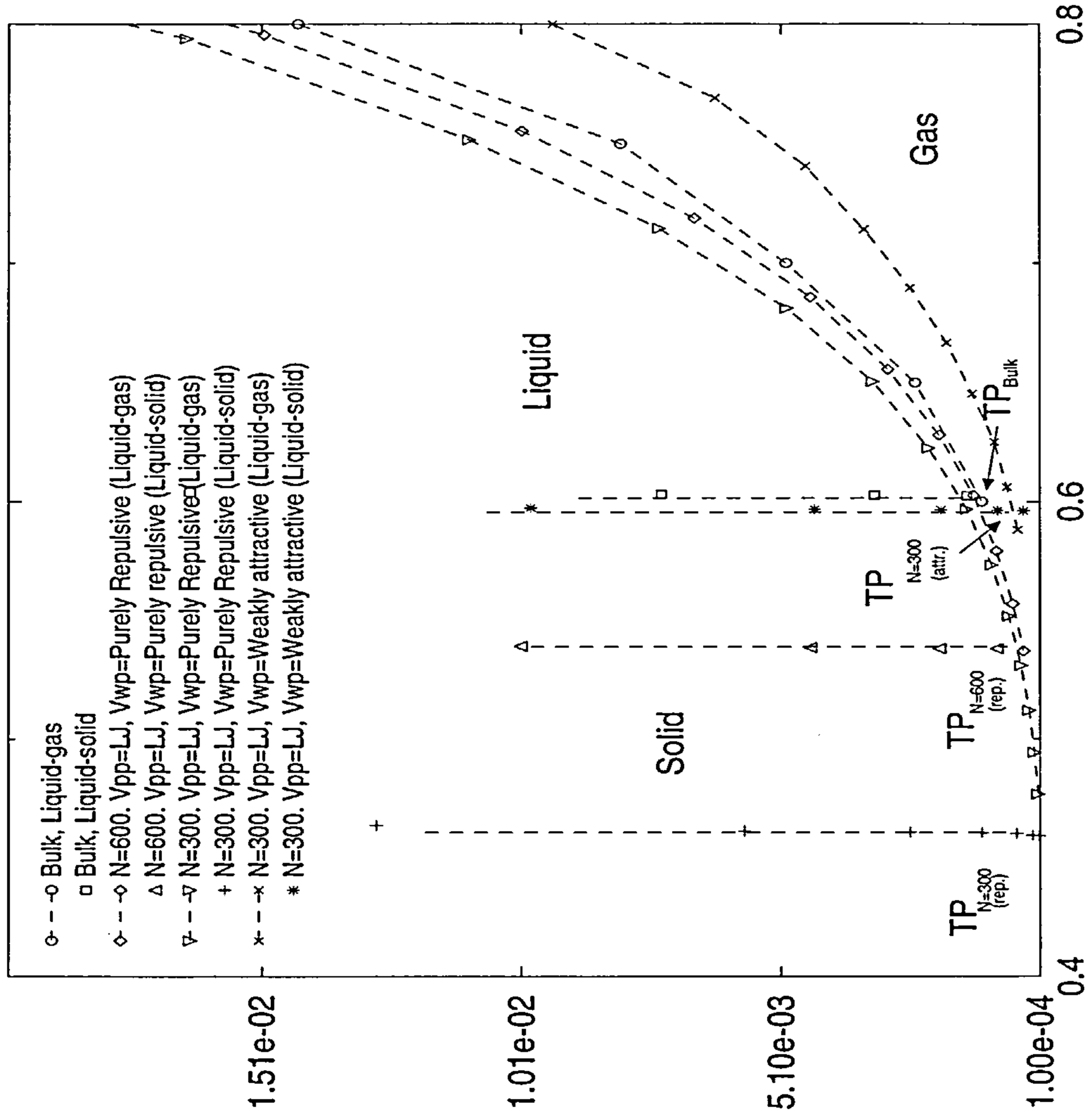

Figure 5.9: The phase boundaries for the confined fluids compared with those of bulk. The figure is plotted in normal scale for values of temperature and pressure close to the triple point. Compare this figure with figure 5.8. Note that for the bulk system, P is the bulk pressure whereas for the confined fluid P is P_z, the normal pressure. TP means triple point.

Temperature	Pressure(P_z)	Temperature	Pressure(P_z)
1.150	8.52(9)	0.516(4)	0.4711
1.088	7.55(6)	0.496(4)	0.3158
1.031	6.73(5)	0.473(3)	0.1419
0.981	6.01(5)	0.469(4)	0.0638
0.935	5.37(4)	0.468(4)	0.0286
0.893	4.82(4)	0.464(3)	0.0129
0.855	4.34(3)	0.461(3)	0.0058
0.819	3.88(3)	0.461(4)	0.0026
0.788	3.48(3)	0.4605(39)	0.0012
0.693(5)	2.3318	0.4602(34)	0.00054
0.628(5)	1.5639	0.4595(34)	0.00024
0.579(4)	1.0483	0.4591(34)	0.00011
0.545(4)	0.7027		

Table 5.3: Values of pressures and temperatures at coexistence for the liquid-solid boundary. Data are for the 300-particle system confined by purely repulsive walls (α=0.0). The numbers in parentheses denote the mean error estimated in the last decimal place, e.g. 8.52(9) = 8.52 $\pm$ 0.09. Errors in T or P_z depend on which Clapeyron equation was used (equation (5.33) or (5.34)).

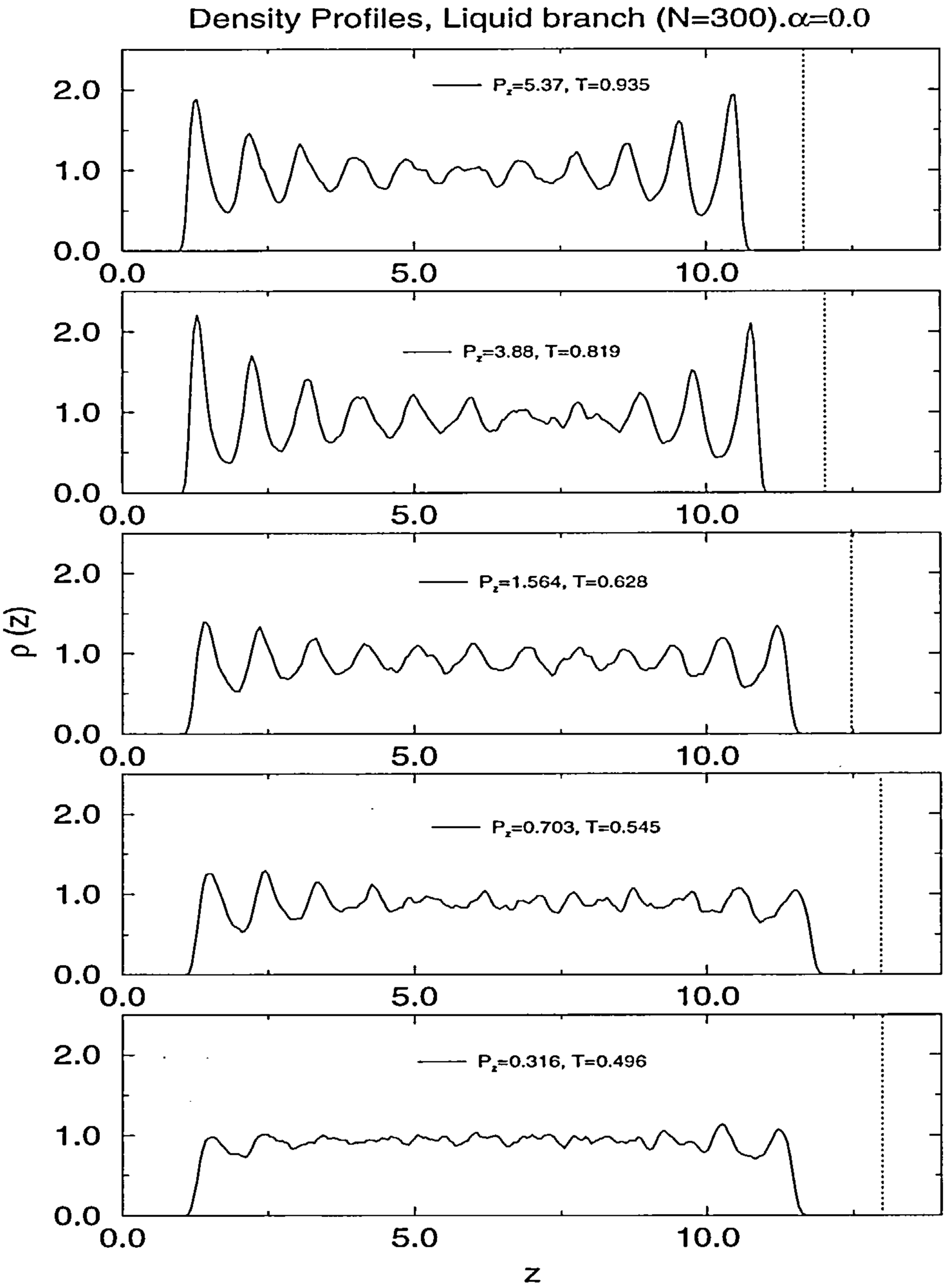

Figure 5.10: Density profiles for the liquid coexisting with the solid at different points on the coexistence line for the 300-particle system. The normal pressure P_z and the temperature are indicated. We can see how the fluid loses its oscillatory behaviour as the pressure decreases. Here the fluid is confined by purely repulsive walls ($\alpha = 0.0$). The dashed line indicates the position of the right hand wall.

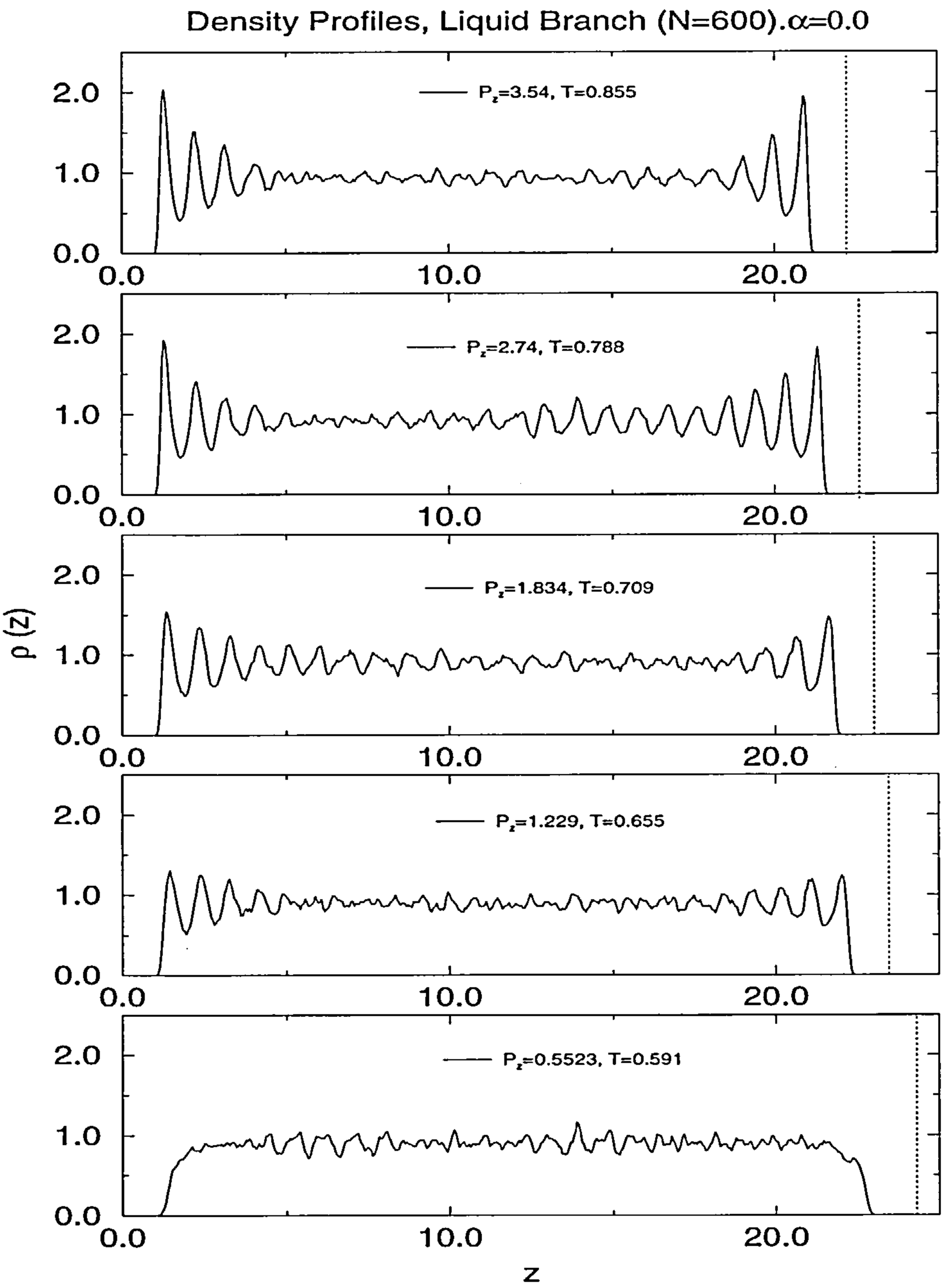

Figure 5.11: Density profiles for the liquid coexisting with the solid at different points on the coexistence line for the 600-particle system. The normal pressure P_z and the temperature are indicated. We can see how the fluid loses its oscillatory behaviour as the pressure decreases. Here the fluid is confined by purely repulsive walls ($\alpha = 0.0$). The dashed line indicates the position of the right hand wall.

Temperature	Pressure(P_z)	Temperature	Pressure(P_z)
1.150	7.48(8)	0.617(5)	0.8239
1.087	6.59(5)	0.591(4)	0.5523
1.031	5.82(4)	0.574(4)	0.3702
0.981	5.15(4)	0.561(5)	0.2482
0.935	4.56(3)	0.549(4)	0.1115
0.893	4.03(3)	0.543(4)	0.05010
0.855	3.54(3)	0.541(4)	0.02251
0.819	3.11(2)	0.539(4)	0.01011
0.788	2.74(3)	0.5384(40)	0.00454
0.709(5)	1.8335	0.5381(46)	0.00204
0.655(6)	1.2290	0.5380(36)	0.00092

Table 5.4: Values of pressures and temperatures at coexistence for the liquid-solid boundary. Data are for the 600-particle system confined by purely repulsive walls (α=0.0). The numbers in parentheses denote the mean error estimated in the last decimal place, e.g. $0.709(5) = 0.709 \pm 0.005$. Errors in T or P_z depend on which Clapeyron equation was used (equation (5.33) or (5.34)).

Using the Grand Canonical ensemble Miyahara and Gubbins observed a similar lowering of the freezing temperature for a LJ model of methane confined by hard walls [96]. However, their criterion to identify the phase transition did not involve free energy calculations and they did not map out the full coexistence line (see chapter 2).

For the fluid interacting with weakly attractive walls ($\alpha = 0.5$) the solid-liquid coexistence line moves to the right, i.e. to higher T, (at fixed pressure) with respect to the bulk at high pressures, whereas for low pressures, close to the triple point,

Temperature	Pressure(P_z)	Temperature	Pressure(P_z)
1.150	5.56(5)	0.656(6)	0.5415
1.088	4.88(3)	0.624(5)	0.2433
1.031	4.28(3)	0.608(4)	0.1093
0.981	3.78(2)	0.602(4)	0.0491
0.935	3.29(2)	0.599(5)	0.0221
0.893	2.88(2)	0.597(4)	0.00992
0.855	2.49(2)	0.597(5)	0.00446
0.819	2.13(1)	0.597(4)	0.00200
0.788	1.79(1)	0.596(4)	0.00089
0.727(5)	1.2052	0.596(4)	0.00040
0.684(4)	0.8078		

Table 5.5: Values of pressures and temperatures at coexistence for the liquid-solid boundary. Data are for the 300-particle system confined by weakly attractive walls (α=0.5). The numbers in parentheses denote the mean error estimated in the last decimal place, e.g. 5.56(5) = 5.56 $\pm$ 0.05. Errors in T or P_z depend on which Clapeyron equation was used (equation (5.33) or (5.34)).

this coexistence line moves to the left. However, throughout the pressure range we see that the shift from the bulk line is small. Recall for this model the well-depth of the wall-fluid potential is only a factor of two or so larger than that of fluid-fluid (figure 5.1). Thus, the situation is similar to that of Miyahara and Gubbins [96] modelling a LJ methane confined by methane walls (the same interaction strength as fluid-fluid). They see hardly any shift, or only a slight shift for the single case ($l = 7.5$) they consider. It appears the magnitude of the shift of the coexistence line with respect to the bulk is small when the fluid-fluid and the wall-fluid potential are

Temperature	Pressure(P_z)	Temperature	Pressure(P_z)
1.041(13)	0.12240	0.650(5)	0.00334
0.989(11)	0.08205	0.623(5)	0.00224
0.950(9)	0.05500	0.597(4)	0.00150
0.888(7)	0.03686	0.573(4)	0.00101
0.838(6)	0.02471	0.552(4)	0.00068
0.794(6)	0.01656	0.531(4)	0.00045
0.752(6)	0.01110	0.512(4)	0.00030
0.715(5)	0.00744	0.494(4)	0.00020
0.681(5)	0.00499	0.477(4)	0.00014

Table 5.6: Values of pressures and temperatures at coexistence for the liquid-gas boundary. Data are for the 300-particle system confined by purely repulsive walls (α=0.0). The numbers in parentheses denote the mean error estimated in the last decimal place, e.g. 1.041(13) = 1.041 $\pm$ 0.013.

of a similar strength.

In order to have a fuller description of the whole phase diagram of the confined fluid I calculated the liquid-gas phase boundary of each system and I plotted these on the same graph. I performed simulations for the 300-particle and 600-particle fluid interacting with the same type of walls mentioned above (purely repulsive and weakly attractive). In both cases the calculations to locate the coexistence lines were performed in the same way as described above for the liquid-solid transition. I performed a thermodynamic integration and I used the Gibbs-Duhem integration to map out the complete line.

The first simulations were carried out for the 300-particle system confined by weakly attractive walls. Although the wall-fluid interaction is not fully attractive

Temperature	Pressure(P_z)	Temperature	Pressure(P_z)
1.049(14)	0.1113	0.686(5)	0.0045
0.993(10)	0.0746	0.656(5)	0.0030
0.950(9)	0.0500	0.628(6)	0.0020
0.891(7)	0.0335	0.603(5)	0.0014
0.841(6)	0.0225	0.579(4)	0.0009
0.796(6)	0.0151	0.557(5)	0.0006
0.755(6)	0.0101	0.537(5)	0.0004
0.719(5)	0.0068		

Table 5.7: Values of pressures and temperatures at coexistence for the liquid-gas boundary. Data are for the 600-particle system confined by purely repulsive walls (α=0.0). The numbers in parentheses denote the mean error estimated in the last decimal place, e.g. 0.993(10) = 0.993 $\pm$ 0.010.

(figure 5.1), it is sufficiently attractive to observe capillary condensation [41]. Thus, as was expected, we observed the transition line of the confined fluid shifted towards higher temperatures (figure 5.8 and table 5.8). Here, the Gibbs-Duhem integration began at temperature of $T = 0.8$.

The fluid confined by purely repulsive walls exhibits capillary evaporation. From figure 5.12 we can see that the oscillations in the density profile, characteristic of the confined liquid, vanish at low pressures leading to a thick film of vapour intruding between the liquid and the walls before the fluid evaporates leaving only vapour in the pore. Figure 5.12 shows various density profiles at different pressures at temperature $T = 0.95$. Although coexistence for this system occurs at $P_z = 0.05$ we still observe density profiles of liquid-like at pressures of $P_z = 0.04$ and $P_z = 0.03$. However, these states are metastable. Probably the limit of stability is close

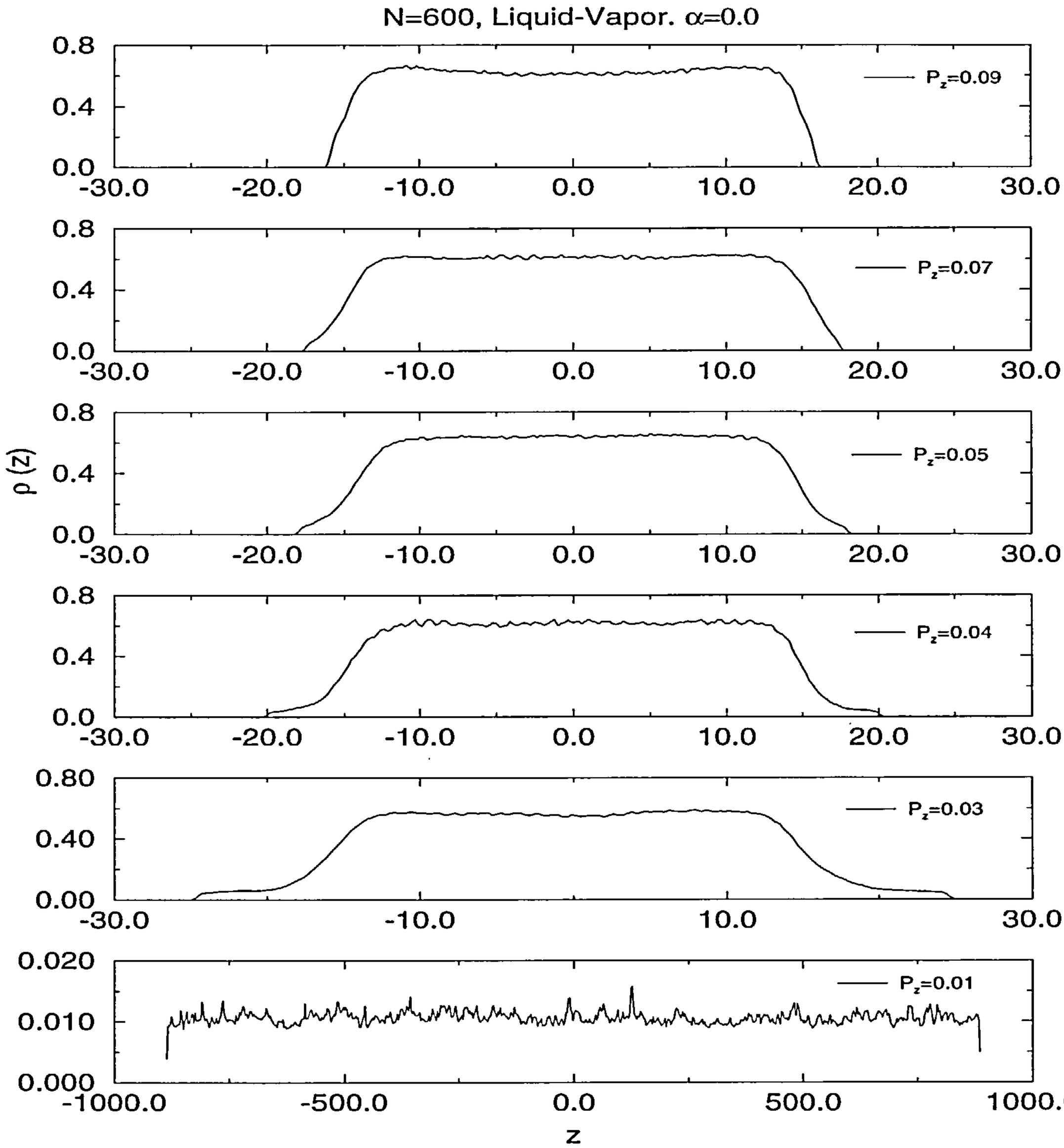

Figure 5.12: Density profiles for the confined fluid with repulsive walls ($\alpha = 0.0$) approaching the liquid-gas transition. $N = 600$. The system exhibits capillary evaporation. The graphs refer to a fixed temperature of T =0.95. For this temperature coexistence occurs for $P_z = 0.050$. The bulk coexistence pressure at this temperature is $P \approx 0.045$. Note that the results for P=0.04 and 0.03 refer to metastable states (see text). For P=0.01 we have a gas state.

Temperature	Pressure(P_z)	Temperature	Pressure(P_z)
1.058	0.0385(3)	0.714(5)	0.0035
1.004	0.0285(2)	0.689(5)	0.0026
0.939	0.0212(1)	0.667(6)	0.0019
0.875	0.0157(1)	0.645(4)	0.0014
0.825	0.0116(1)	0.625(4)	0.00096
0.800	0.0095(1)	0.606(4)	0.00071
0.769(5)	0.0064	0.588(4)	0.00051
0.740(5)	0.0046		

Table 5.8: Values of pressures and temperatures at coexistence for the liquid-gas boundary. Data are for the 300-particle system confined by weakly attractive walls (α=0.5). The numbers in parentheses denote the mean error estimated in the last decimal place, e.g. 0.769(5) = 0.769 $\pm$ 0.005. Errors in T or P_z depend on which Clapeyron equation was used (equation (5.33) or (5.34)).

to $P_z = 0.03$ since for the pressure of $P_z = 0.01$ the fluid turns to a gas state. This effect was observed for both 300-particle and 600-particle systems (see figure 5.8 and tables 5.6 and 5.7). To locate the liquid-gas transition of these systems, I began the Gibbs-Duhem integration at a temperature of $T = 0.95$ (see figure 5.13).

In performing the Gibbs-Duhem integration large extrapolations are required to determine the boundary lines and it is important to enquire if this leads to some intrinsic inaccuracies in the results [125,127]. I carried out independent calculations of the free energy to determine coexistence at lower temperatures for the 300-particle system in order to check the Gibbs-Duhem results, i.e. for the liquid-solid at temperature of $T = 0.693$ and for the liquid-gas at temperature of $T = 0.650$. In both cases the walls were purely repulsive ($\alpha = 0.0$). The results for the transition pressure

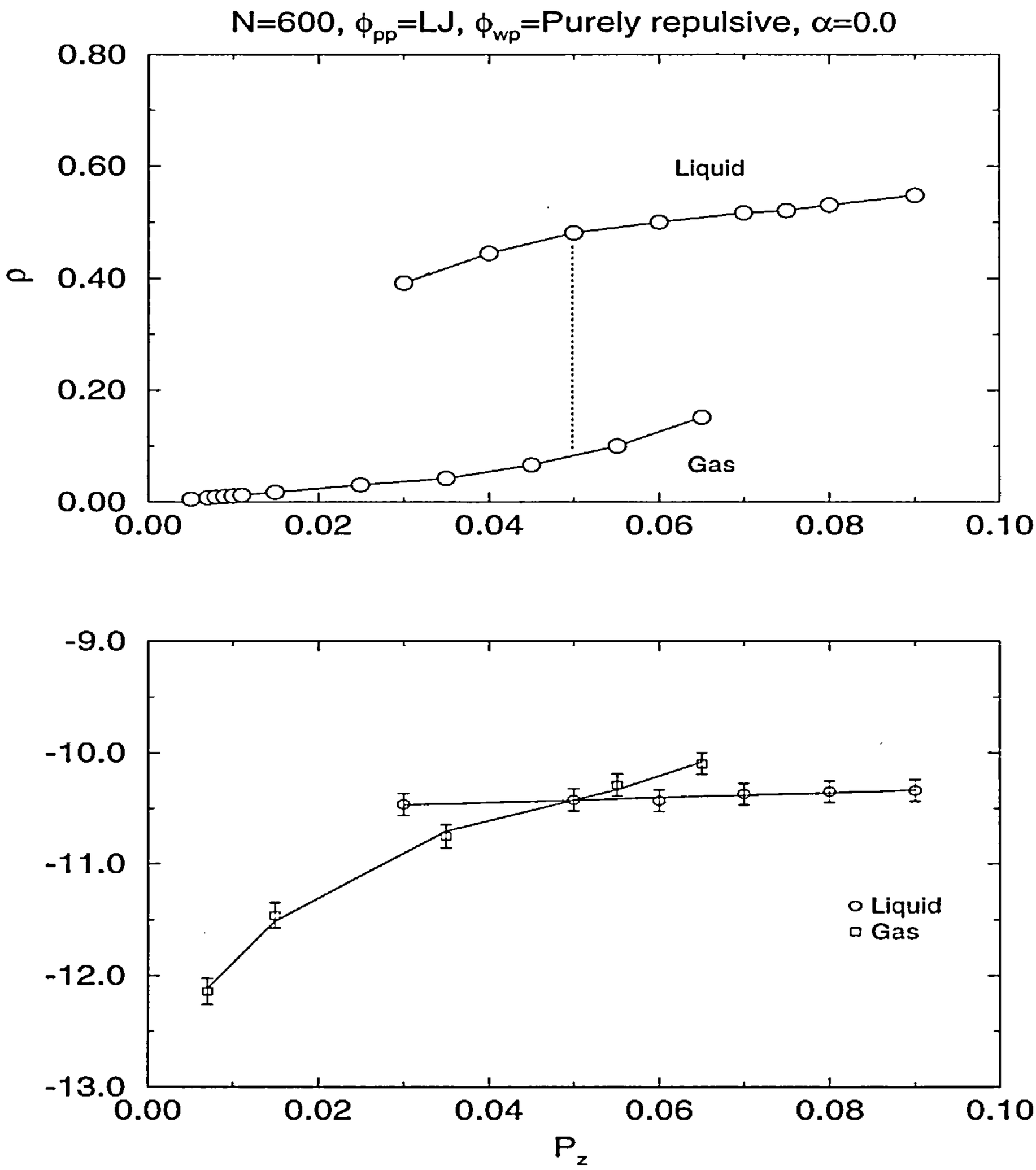

Figure 5.13: Plots of the mean density ρ and Gibbs free energy per particle (G/N) as a function of normal pressure P_z for the 600-particle system with purely repulsive walls ($\alpha = 0.0$). The temperature is fixed at $T = 0.95$ This plot is for the liquid-gas transition. The equilibrium transition is indicated by the dashed vertical line in the top figure. Error bars are indicated when they are bigger than the size of the symbols.

were $P_z = 0.00344(5)$ and $P_z = 2.39(2)$ for the liquid-gas and liquid-solid transition respectively. If we compare these results with those given in tables 5.6 and 5.3 we find good agreement between them. The differences are 2 or 3 percent in each case.

Once the liquid-solid and the liquid-gas transition lines are determined for a given system it is possible to obtain the triple point of the system. This point is located where the liquid-solid and liquid-gas coexistence lines cross each other. We can see from figure 5.8 that the triple point for the pore is shifted from that in bulk as a result of the confinement. For purely repulsive walls, the triple point shifts to lower pressures and temperatures. For a fluid confined by weakly attractive walls the triple point is at a lower pressure but the temperature is little changed.

For the liquid-gas transition, in all the systems, the coexistence lines were plotted until the gas and liquid density were similar. For the 300-particle and 600-particle system confined by purely repulsive walls (α=0.0) these temperatures are T=1.041 and T=1.049 respectively. For the 300-particle system confined by weakly attractive walls (α=0.5) this temperature in the coexistence line is T=1.058. For the shifted and truncated Lennard Jones system with $r_c = 2.5$ (used in this work) the bulk critical point occurs at temperature T=1.085 [131].

Finally, I performed simulations for a fluid confined within purely repulsive walls ($\alpha = 0.0$) where the fluid-fluid interaction is given by the Weeks- Chandler-Anderson (WCA) reference potential of the Lennard-Jones system [30] (see chapter 1, equation (1.7)). I followed the same procedure to map out the solid-liquid coexistence line. The pressure for the initial coexistence point was found to be $P_z = 11.51 \pm 0.13$ at temperature $T = 1.0$ (figure 5.14 and 5.15 also tables 5.9 and 5.10), and I started the Gibbs-Duhem integration with those values. From figure 5.16 we observe that for this system the coexistence line is shifted towards higher temperatures from that in the bulk at least for higher pressures. At lower pressures the shift is smaller and may even be towards lower temperatures. The bulk data was taken from de Kuijper et al. [134]. Previous work using a different simulation method for repulsive Yukawa fluids confined by repulsive Yukawa walls also showed a shift of the freezing curve

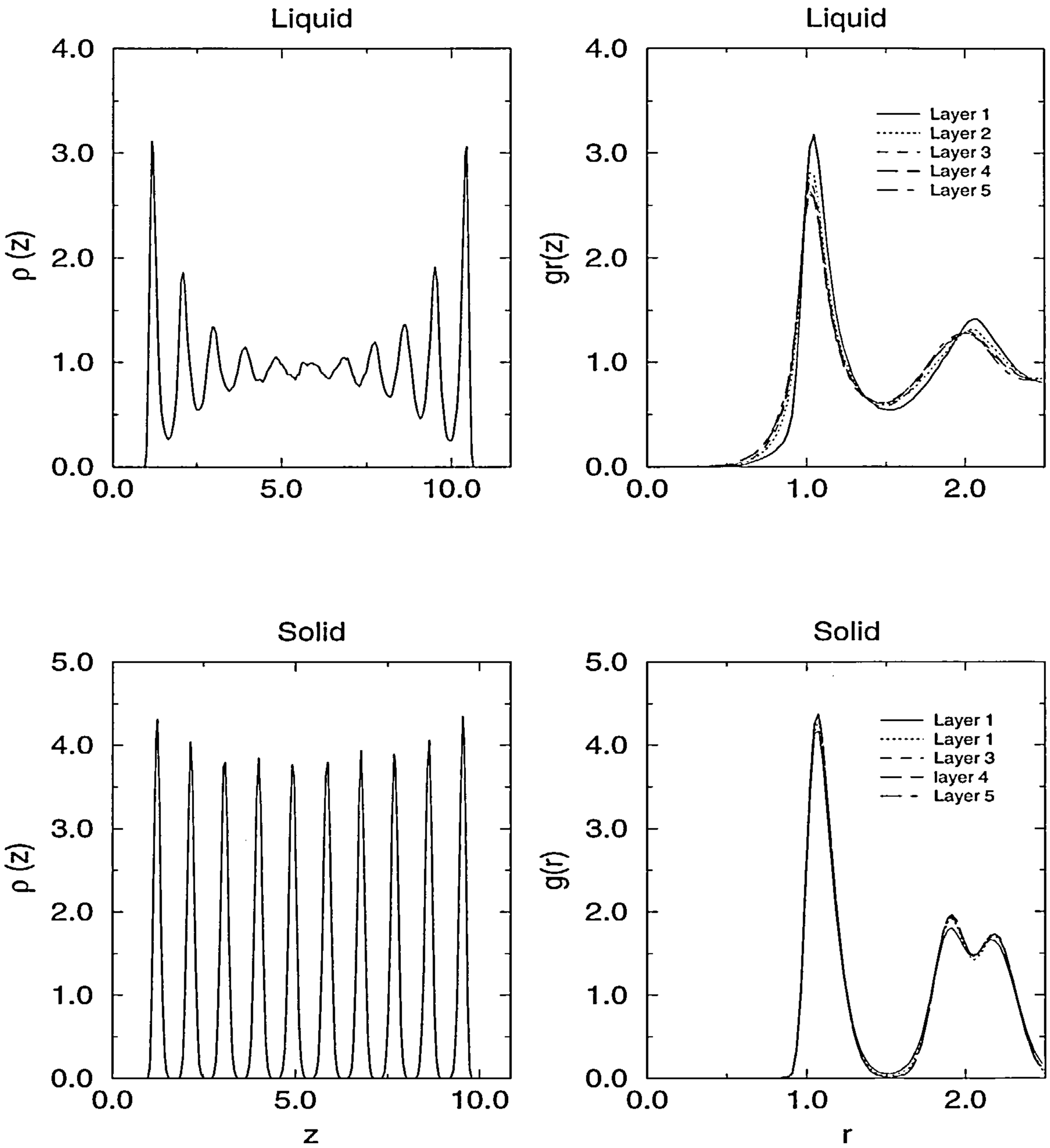

Figure 5.14: Liquid and solid density profiles ($\rho(z)$) at coexistence for a WCA fluid confined by purely repulsive walls. The figures refer to temperature $T = 1.0$ and pressure of $P_z = 11.51$ The ICF, $g(r)$ of each layer is also plotted. $N = 300$.

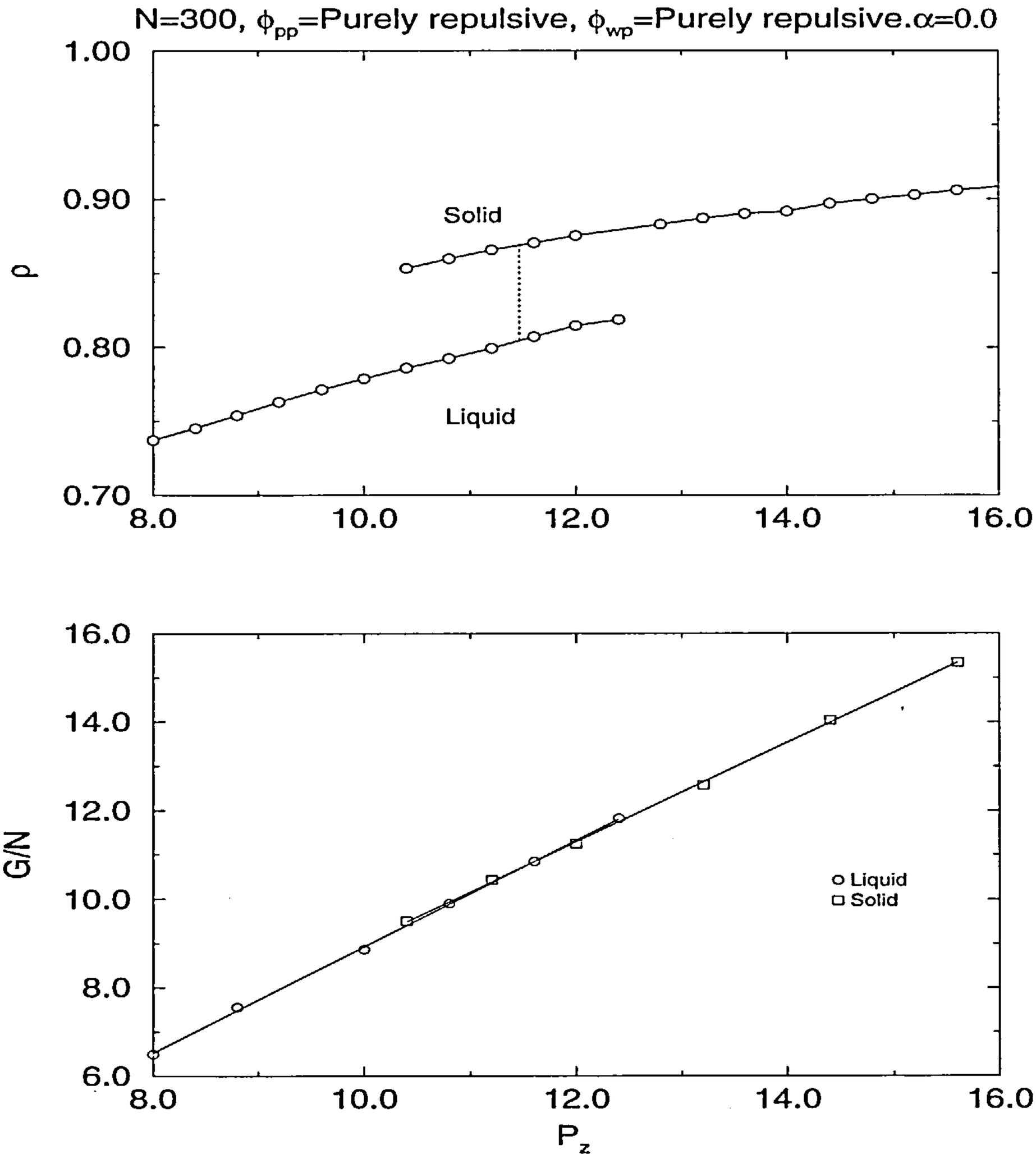

Figure 5.15: Plots of the mean density ρ and Gibbs free energy per particle (G/N) as a function of normal pressure P_z for the 300 particle repulsive system (the WCA fluid) confined by purely repulsive walls ($\alpha = 0.0$). $T = 1.0$. The equilibrium transition is indicated by the dashed vertical line in the upper figure. Error bars associated with the data are of the size of the symbols.

Temperature	Pressure(P_z)
1.000	11.51(13)
0.952	10.92(12)
0.909	10.39(11)
0.869	9.92(10)
0.833	9.48(10)
0.799	9.08(9)
0.531(6)	6.09
0.344(4)	4.08
0.196(2)	2.74

Table 5.9: Values of pressures and temperatures at coexistence for the liquid-solid boundary. Data are for the 300-particle system (WCA fluid) confined by purely repulsive walls (α=0.0). The numbers in parentheses denote the mean error estimated in the last decimal place, e.g. 11.51(13) = 11.51 $\pm$ 0.13. Errors in T or P_z depend on which Clapeyron equation was used (equation (5.33) or (5.34)).

to lower pressures (at constant temperature) [95]. Note that for purely repulsive fluid-fluid potentials there is no liquid-gas transition.

I also determined the latent heat of the liquid-solid transition as a function of the temperature for the slit-pore systems studied in this work. The latent heat is the difference in the enthalpies of the two phases (liquid and solid) at coexistence. These are plotted in reduced units per particle, $\Delta h/\epsilon N$ in figure 5.17. We see that the change in the enthalpy for the confined fluid is higher than that in bulk. For the 600-particle system interacting with purely repulsive walls these values are slightly higher than those for the 300-particle one. This result is a little surprising, since we expected the large system to be closer to bulk. However, this effect can be due

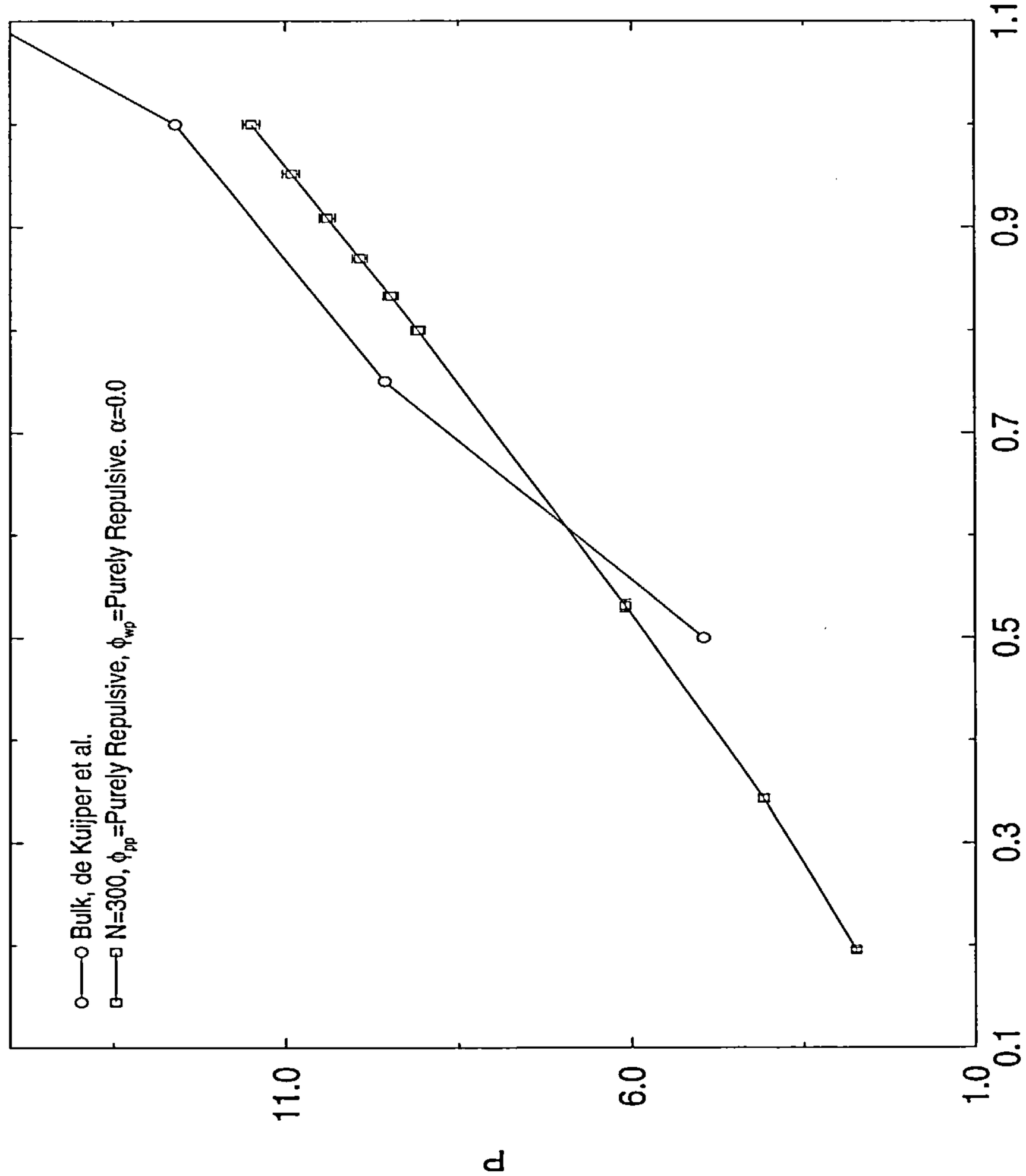

Figure 5.16: The freezing lines for the repulsive WCA fluid (with $N = 300$) confined by purely repulsive walls ($\alpha = 0.0$) compared with the bulk one (de Kuiper et al. [134]). The lines joining the points are drawn to guide the eye. For the confined fluid $P = P_z$ while for the bulk P is the bulk pressure.

Temperature	Pressure
1.25	16.0
1.00	12.6
0.75	9.57
0.50	4.95

Table 5.10: Values of pressures and temperatures at coexistence for the bulk liquid-solid boundary for the WCA system. Data were taken from reference [134].

to the difference in the mean density of the two systems. From previous results we saw that for the same pressure (P_z), the (mean) densities are much higher for the 600-particle system than for the 300-particles (see e.g. figure 5.3 and 5.5). Since the enthalpy depends strongly on the density, the higher densities in the large system may give rise to a larger latent heat (enthalpy). The entropy (in reduced units per particle), which gives us the same information, is also plotted in figure 5.17.

To conclude this chapter I must emphasize that these results refer to a fixed number of particles and the phase diagrams are plotted using the normal component of the pressure and not that of any reservoir. Nevertheless, I believe that these results show new insight into the liquid-solid transition for a single slit-pore.

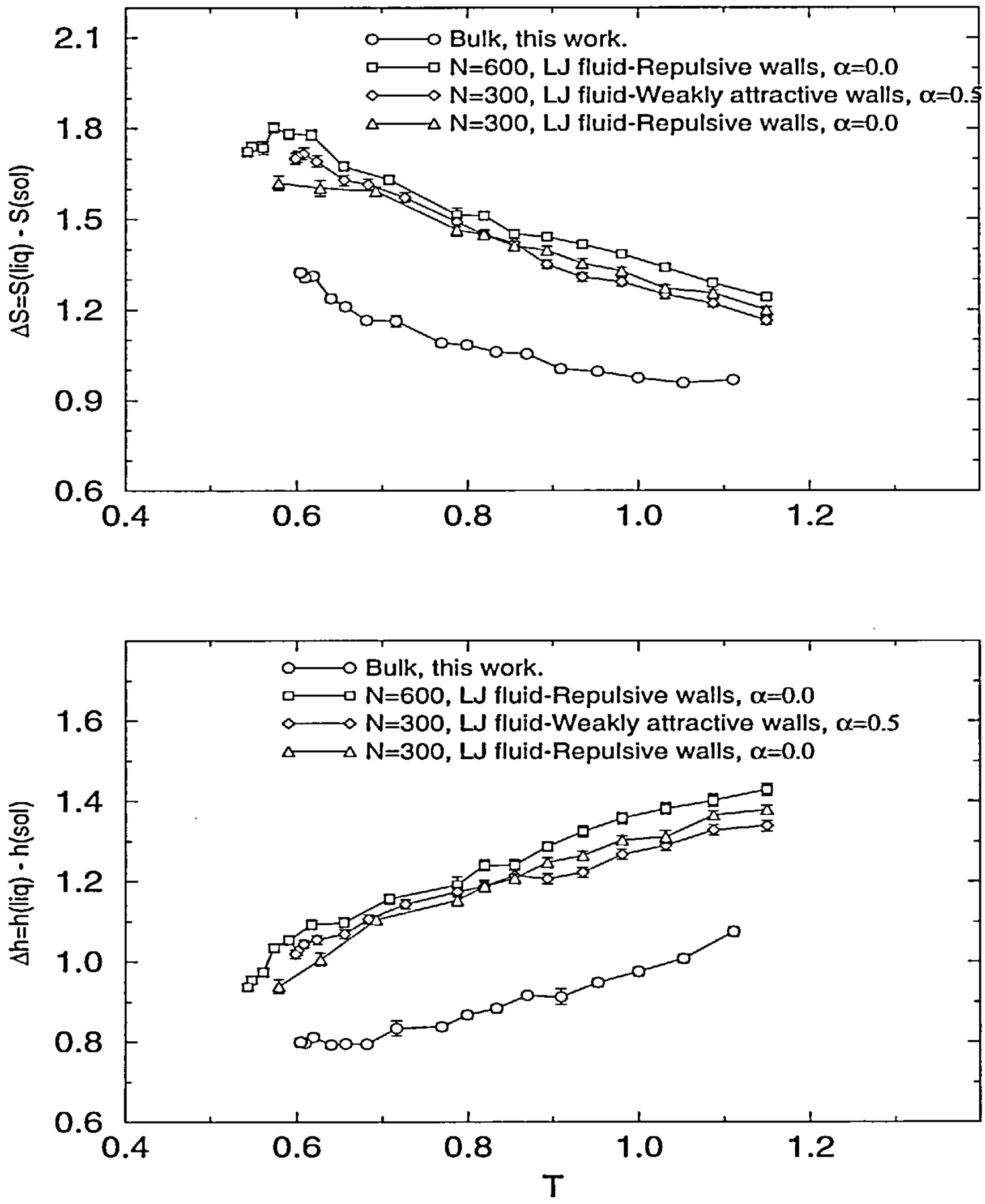

Figure 5.17: This figure shows the differences in entropy (top) and enthalpy (bottom) between the liquid and the solid at coexistence.

Chapter 6

A slit-pore in contact with a reservoir

6.1 Introduction

This chapter describes simulations performed in a slit pore immersed in a particle reservoir. As was stated in chapters 1 and 2, experiments on confined fluids are usually carried out under constant chemical potential (pressure) and temperature. Thus, I conducted simulations to mimic more closely these experimental conditions. The model and the simulation details are carried out as described in chapter 3. Two types of computation were used. In the first I performed simulations using the Molecular Dynamics technique and in the second simulations were performed using the Monte Carlo technique. For both I did mainly structural investigations of the confined and bulk fluid, rather than attempting to calculate the free energy as described in chapter five. Results for diffusion coefficients, obtained from Molecular Dynamics simulations, are also presented.

6.2 Molecular Dynamic Simulations

For this investigation I ran constant-pressure Molecular Dynamics simulations. i.e. the calculations are performed at fixed (bulk) pressure (P), temperature (T) and number of particles (N). As described in chapter 3, in the middle of the simulation box a slit pore is immersed with fixed wall separation (l) (see chapter 3). Thus, I have a slit pore surrounded by a fluid reservoir. Particles in the system can flow from the pore to the reservoir and vice versa, keeping the chemical potential constant between the pore and the reservoir. This series of simulations was performed at pressures close to the bulk triple point, for a slit-pore with the same wall area, A, as the system described in chapter five, $A = S_x S_y$; $S_x = 5.5378$ and $S_y = 5.7551$. The fluid-fluid interaction is a Lennard Jones potential given by equation (3.26) (using a cut-off of 2.5), and the wall-fluid interaction is a (10-4-3) potential given by equation (3.28). The wall parameters are $\rho\sigma^3 = \sqrt{2}$, $\Delta l = \sigma/\sqrt{2}$ and the parameter $\alpha = 1.0$, i.e. a fully attractive wall. The ϵ' and σ' parameters, in equation (3.28), were those employed in chapter 5, i.e. I simulated the argon-like fluid confined within carbon dioxide plates (see chapter 5).

The equations of motion of the particles were solved using a Gear 4th-order predictor-corrector method [105], using a time step of 0.005τ, where $\tau = (m\sigma^2/\epsilon)^{1/2}$, σ and ϵ are the argon parameters and m is the mass of the fluid molecule (argon). Runs were performed for up to 75000 time steps after an equilibration of 50000 time steps.

6.2.1 Freezing of the pore and reservoir fluid

The first investigations for this system were aimed at observing the freezing transition of the confined fluid. In order to induce freezing, I initially equilibrated the pore and the reservoir in a liquid-like state. Then, from high temperatures and fixed pressure, I decreased the temperature in increments of $\Delta T = 0.025$. At temperatures close to freezing these increments were made shorter ($\Delta T = 0.001$) until either

the pore or the reservoir fluid seemed to freeze. Each new simulation, for a new thermodynamic state, started from the final configuration of the previous state. The internal energy per particle of the whole system (pore and reservoir) was monitored for each temperature. A freezing 'transition' was observed in that a discontinuous jump occurred in the internal energy for some (low) temperature on cooling. We must emphasize that the freezing 'transition' is characterized by the 'jump' in the internal energy; this is certainly not the temperature of the equilibrium transition.

I performed simulations for several pore widths at different pressures (all of them at low pressures, close to the bulk triple point) and in all cases, I observed the transition at temperatures well below of those in bulk (see figure 5.8 in chapter 5), i.e. the system exhibits a high degree of supercooling (see e.g. figure 6.1) w.r.t the bulk transition temperature. Due to this supercooling effect, it is difficult to determine which fluid, the pore or the reservoir, freezes first. The snapshots of the pore and reservoir fluid seem to indicate that both freeze simultaneously (figure 6.2). Obviously, at this low temperature, the reservoir fluid is in a highly metastable state, and most probably the pore fluid is also metastable. Thus, any perturbation in the system could nucleate freezing in the pore and the reservoir liquid. Thus, I will refer to the freezing temperature as the limit of the metastability (this is T =0.425 for the system of figure 6.1). Clearly there is also an upper limit of metastability of the solid, this is T=0.70 for this system. I return to this melting transition later.

This supercooling behaviour was found for all the pore-sizes and thermodynamic conditions employed in this work. In order to determine whether this phenomenon was due to the finite size of the simulation, I carried out calculations for two different values of N. In the first series of simulations I used a total of 1250 particles and in the second 2000 particles. However, the problem remained, i.e. in both sets of simulations the pore and the bulk fluid froze simultaneously.

Looking at the literature, I found that the free energy barrier that separates the bulk solid phase from the supercooled liquid, for systems interacting with purely repulsive forces and for Lennard-Jones systems, is high compared with typical values

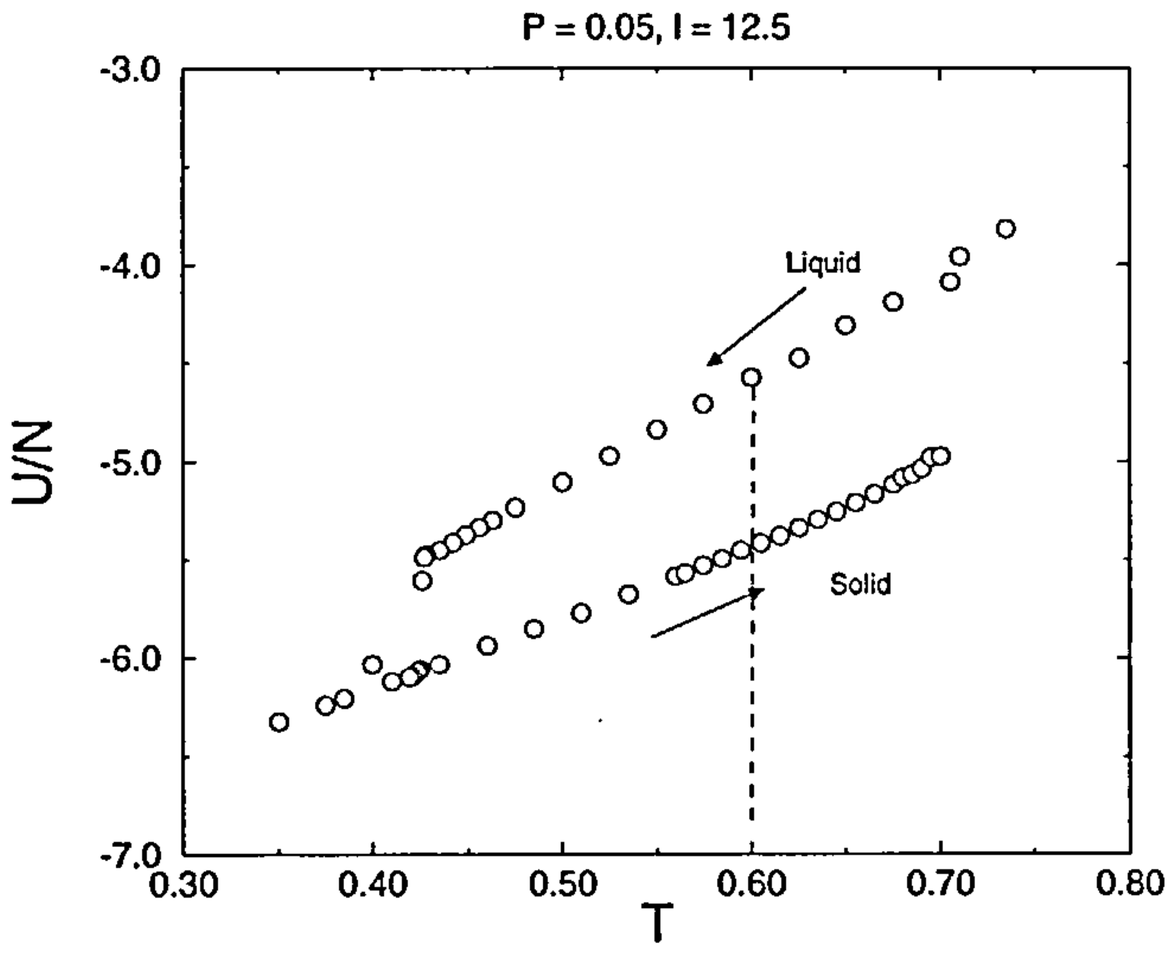

Figure 6.1: Internal energy of the system per particle as a function of the temperature. $P = 0.05$, pore width $l = 12.5$ and $N = 2000$ particles. Note the large hysteresis between heating and cooling. The bulk freezing transition, for the same pressure, occurs around $T \approx 0.6$ (indicated by the dashed line). Error bars are of the size of the symbols.

of the energy calculated in this work [135,136]. -The energy barrier is measured by defining and order parameter W (monitoring the degree of crystallinity) and writing the free energy in terms of this order parameter [135,136], i.e. using the Gibbs free energy: $G(W) = constant - k_B T \ln[P(W)]$. Here $P(W)$ is the probability per unit interval of finding the order parameter around a given value of W. At coexistence between the liquid and solid, $P(W)$ develops a double peaked structure. Then, from the free energy equation, the energy barrier is estimated from the minimum of $P(W)$ that occurs between the solid-like and liquid-like peak. Then, it is not

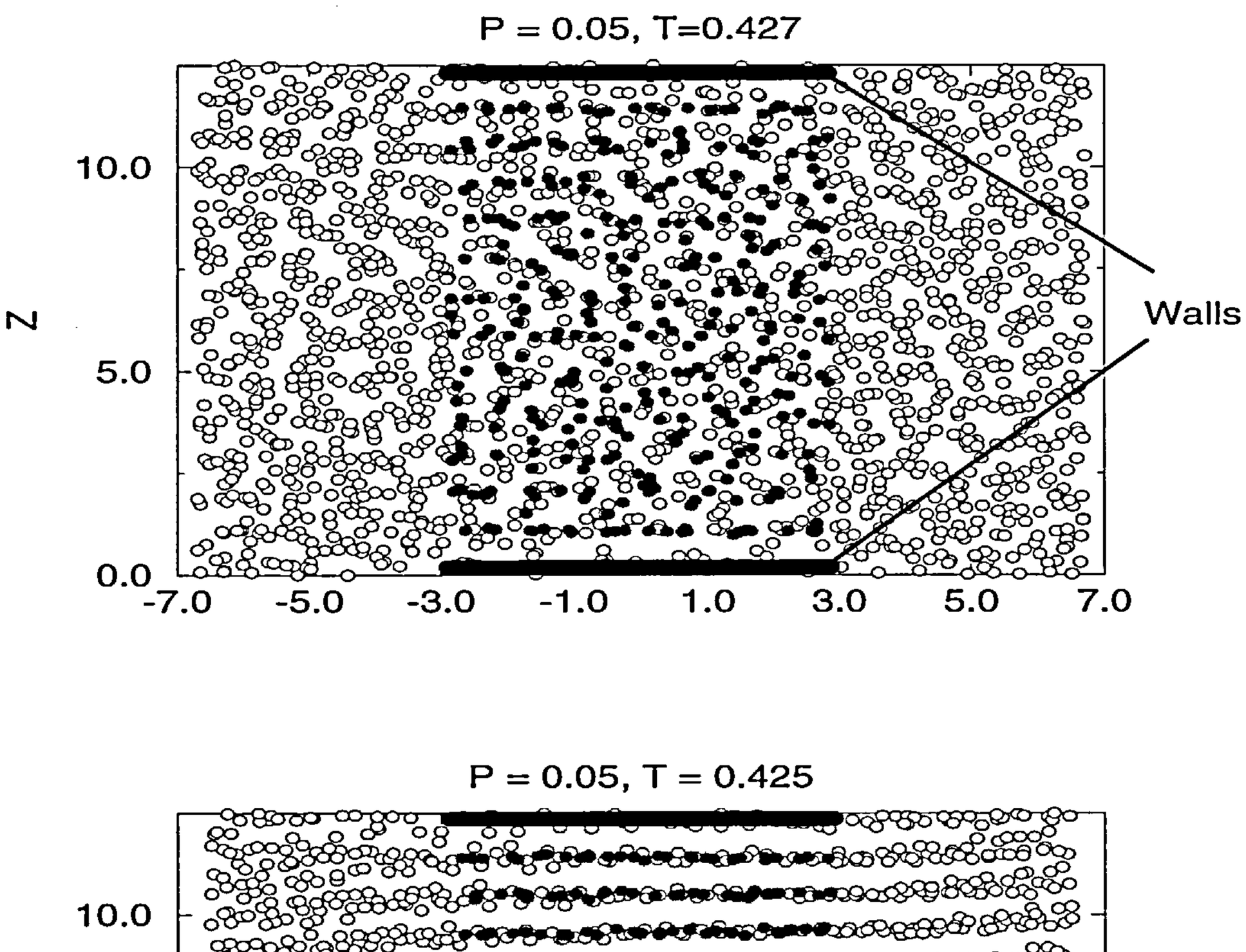

Figure 6.2: Snapshots of particles for a slit-pore in contact with a reservoir ($l = 12.5$ $N = 2000$) at temperatures slightly above and below the freezing transition. a) For $T = 0.427$ the pore and the reservoir fluid are liquid-like. b) For $T = 0.425$ both fluids, the pore and the reservoir, simultaneously freeze showing the same ordering of the particles. The black circles represent the particles in the pore whereas the open circles are the particles in the reservoir.

Pressure	Temperature
0.01	0.437
0.02	0.443
0.05	0.447
0.10	0.450
4.0	0.680

Table 6.1: The freezing temperature for a slit pore with $l = 10.0$ at various pressures.

surprising that I observe the phenomenon described above. Simulating a solid and a liquid phase coexisting in the same box could be rather difficult, especially for small systems where the size can have significant effects on the nucleation rate. Swope and Anderson [137] showed that for systems containing more than 10^4 particles do the system-size effects become unimportant. Obviously, simulations of these sizes are really expensive. Despite this difficulty, it still may be possible to extract some information about the freezing process from the results.

For one fixed pore size, $l = 10$, I also conducted simulations at different pressures ($P = 0.01, 0.02, 0.05, 0.10$ and 4.0). The transition temperature, as defined above, changes. At higher pressures it increases (Table 6.1).

6.2.1.1 Structure of the solid

I carried out the simulations at a pressure $P = 0.05$ for several pore widths: $l = 7.5$, 8.0, 9.0, 10.0, 11.0, 12.0 and 12.5. In all these systems a total of 2000 particles was used. For the largest pore width the ratio between the average number of particles in the pore and in the reservoir is 0.175 and for the smallest pore it is 0.09. Thus, I

assumed that there was enough reservoir fluid surrounding the pore. The structure of the frozen fluid (the pore and the reservoir fluid) was different for different pore widths. For pore width l=7.5 and 12.5, we can observe (from the density profile) how the pore fluid arranges itself in layers. When the fluids freeze, the layers are very well defined and lie parallel to the pore walls (figure 6.3). The freezing temperature for the l=12.5 pore is $T = 0.425$, and 12 crystal layers of approximately one molecular diameter thickness develop. For the l=7.5 pore 7 layers appear at a temperature of $T = 0.466$.

For the other pores, $l = 8.0, 9.0, 10.0, 11.0$ and 12.0, the first (contact) layer was well ordered and parallel to the walls. However, in the middle of the pore I never observed a fully layered structure when the pore fluid froze, i.e. after the jump in the internal energy (see e.g. figure 6.4). For these pore sizes, even at very low temperatures far below any freezing temperature, the confined solid does not seem to form completely well-ordered layers parallel to the walls in the middle of the pore (see e.g. figure 6.5). These observations are different from my previous results (earlier chapters). However, in my previous simulations I did not have any reservoir in contact with the slit-pore. These effects in the structure of the fluid emerge for the use of the thermal bath.

Snapshots for the various systems show that the pore and the reservoir fluid appear to freeze with the same type of ordering, however the ordering is different for each pore size. Sometimes this ordering is not parallel to the x-y plane, i.e. no parallel layer structure is present in the pore or the reservoir (see e.g. figure 6.2, 6.6 and 6.7). It is rather difficult to predict what type of ordering the pore fluid will take on freezing. For the system in the pore, these seems to be a competition between forming layers parallel to the walls and aligning layers with the bulk structure. However the results, from Molecular Dynamics and Monte Carlo simulations (see next section), suggest that for high pressures the ordering is always parallel to the pore-walls (a layered structure is observed). Since particles in the pore feel both the interaction with particles in the reservoir and with the walls of the pore, it seems

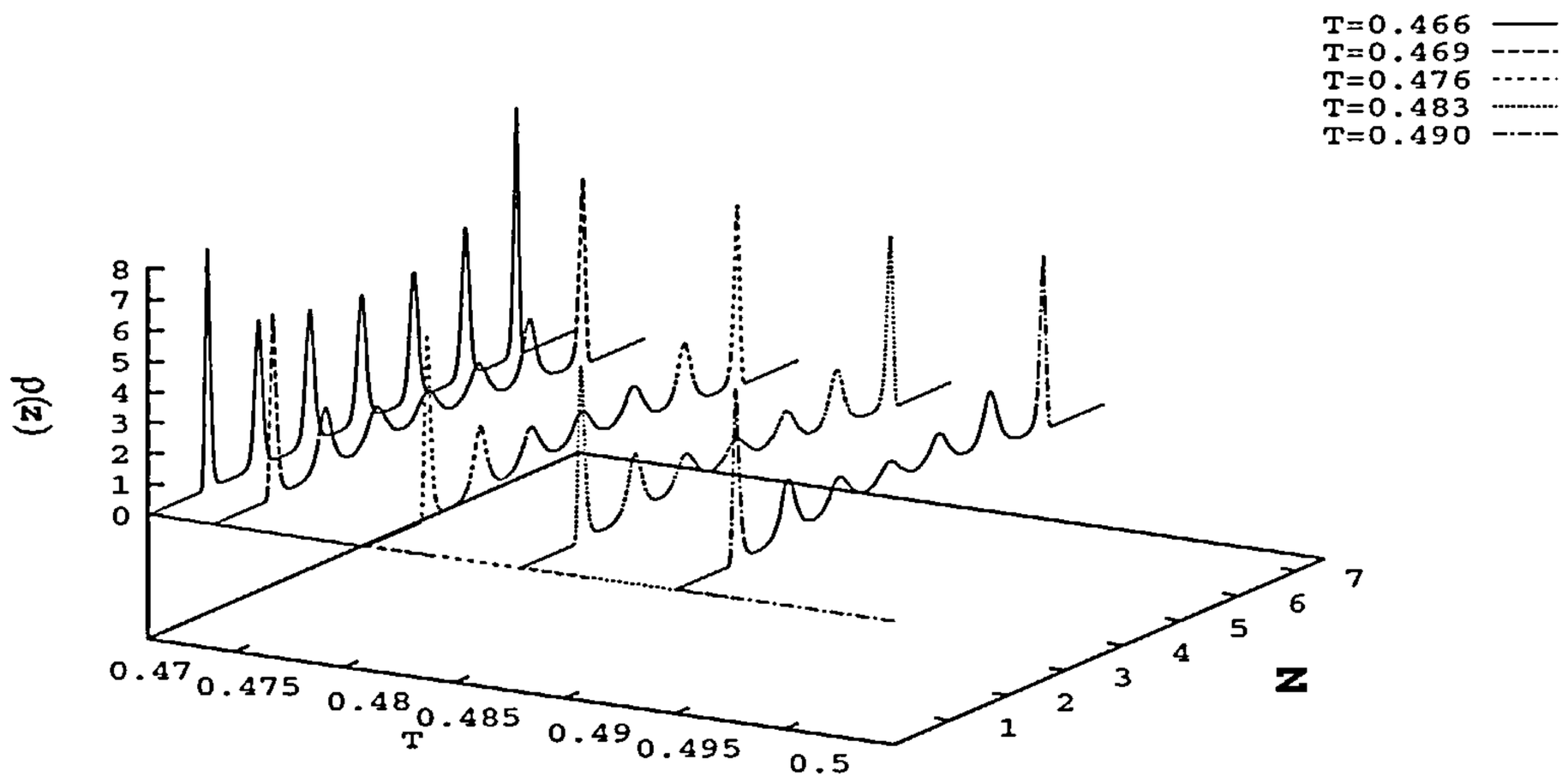

a)

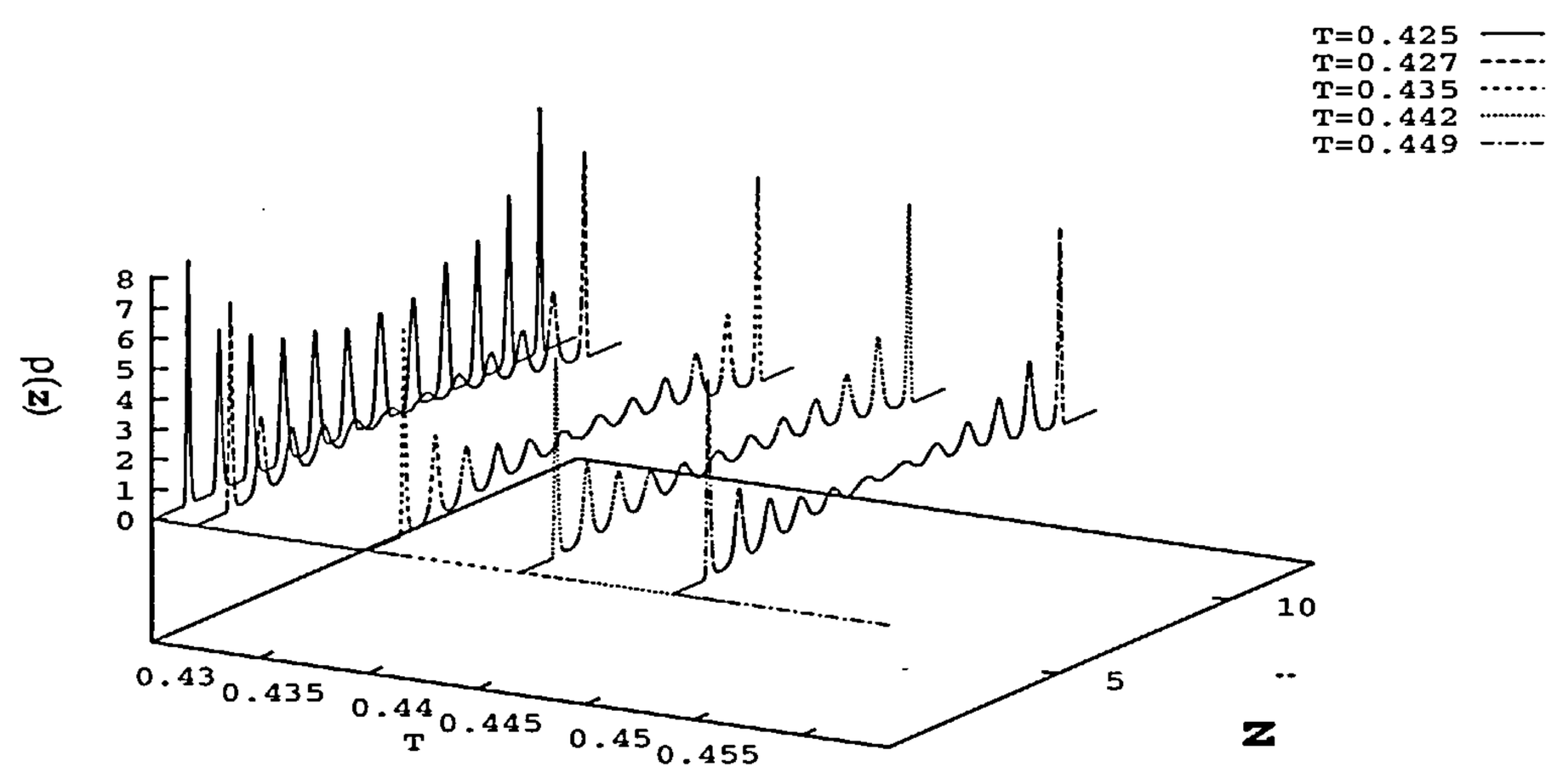

b)

Figure 6.3: The density profile of the confined fluid at different temperatures T for two pore widths. a) $l = 7.5$ and b) $l = 12.5$. For both cases $P = 0.05$ and $N = 2000$. We observe, once the freezing temperature is reached, the formation of layers parallel to the walls.

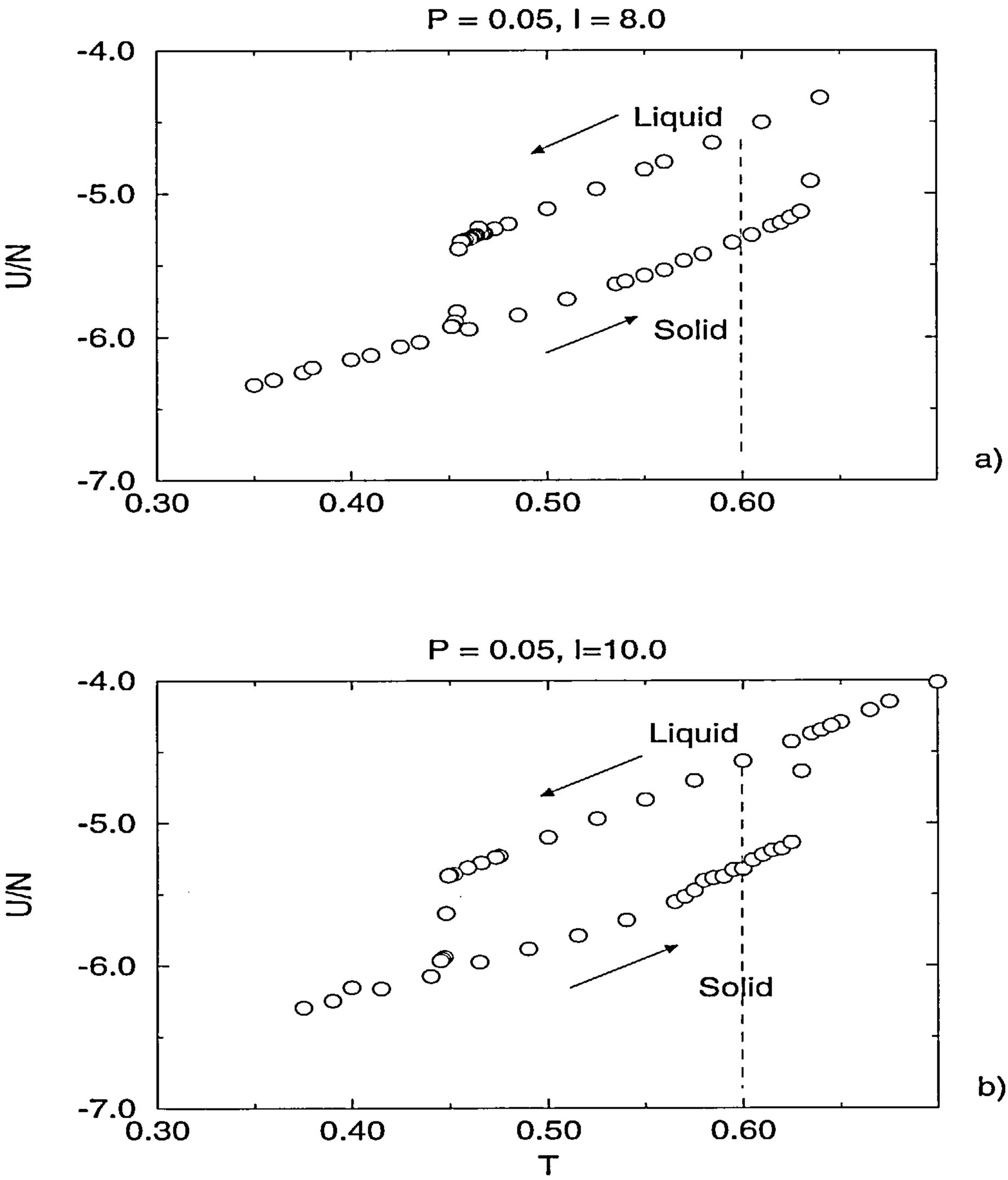

Figure 6.4: The internal energy as a function of the temperature for a slit-pore of width a) $l = 8.0$ and b) $l = 10.0$. The jumps at the left and the right of the curves indicate the freezing and the melting temperature respectively. $P = 0.05$ and $N = 2000$. The bulk transition temperature is indicated by the dashed line ($T \approx 0.6$). Error bars are of the size of the symbols.

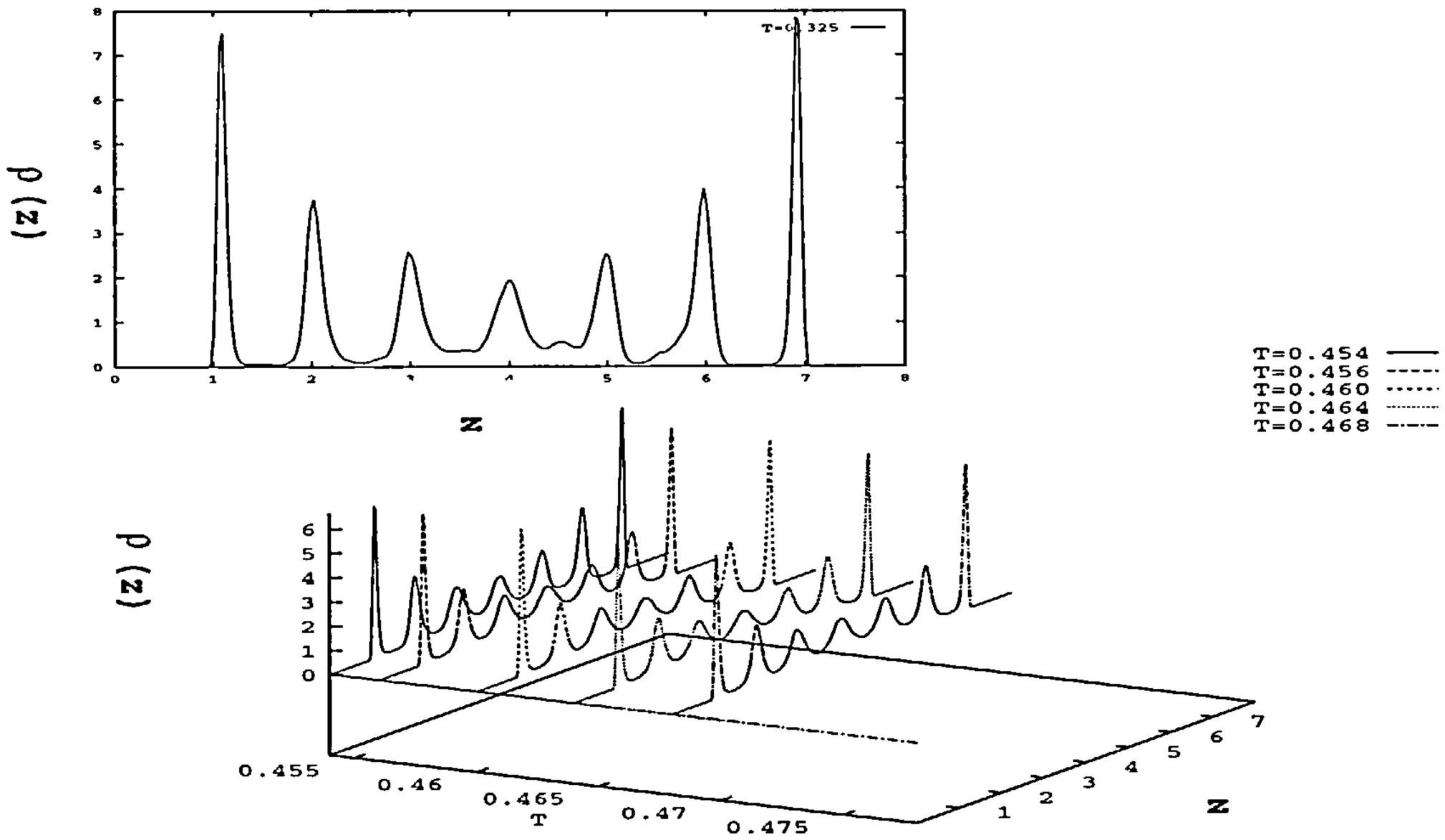

Figure 6.5: Density profiles for several of the temperatures in figure 6.4. a) $l = 8.0$ and b) $l = 10.0$. Note that at the temperature where the freezing transition occurs (the jumps in figure 6.4 at $T = 0.454$ and $T = 0.447$ for the pore of $l = 8.0$ and $l = 10.0$ respectively) the pore fluid does not form well-defined layers throughout the pore. The layering does not appear even for temperatures ($T = 0.325$ for $l = 8.0$) which are far below the freezing temperature ($T \approx 0.6$ for this pressure $P = 0.05$), see inset in figure a).

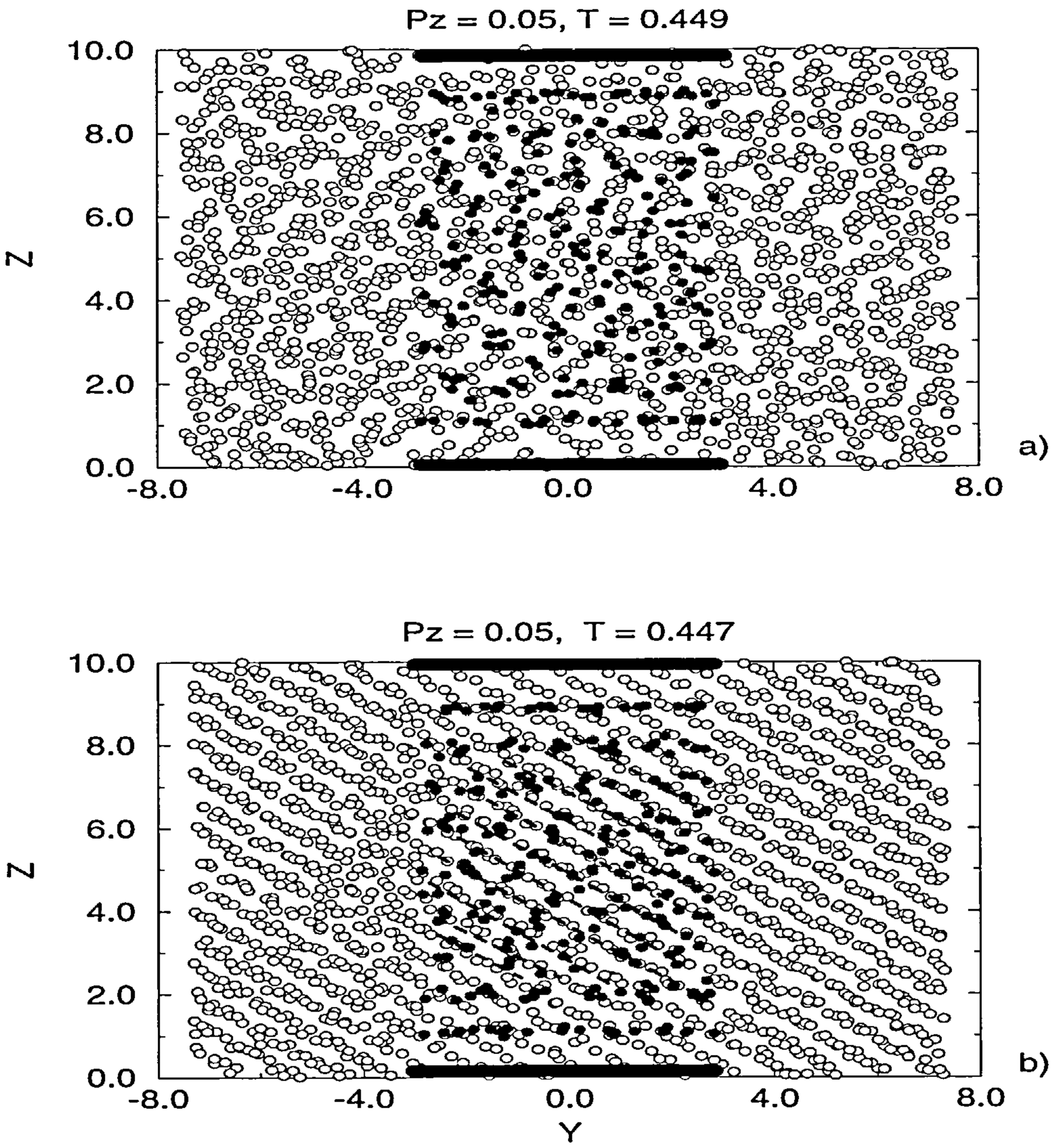

Figure 6.6: Snapshots of particle configurations for the pore system investigated in figures 6.4 b) and 6.5 b), i.e. $l = 10.0$ and $P = 0.05$. a) Prior to the jump (in the internal energy) both the pore and reservoir fluids are liquid-like. b) At the temperature where the jump occurs, $T = 0.447$, the pore and the reservoir fluid freeze simultaneously. Apart from the first (contact) layer next to the walls, the pore and the reservoir solid appear to adopt the same ordering. The black circles represent the particles in the pore whereas the open circles are the particles in the reservoir.

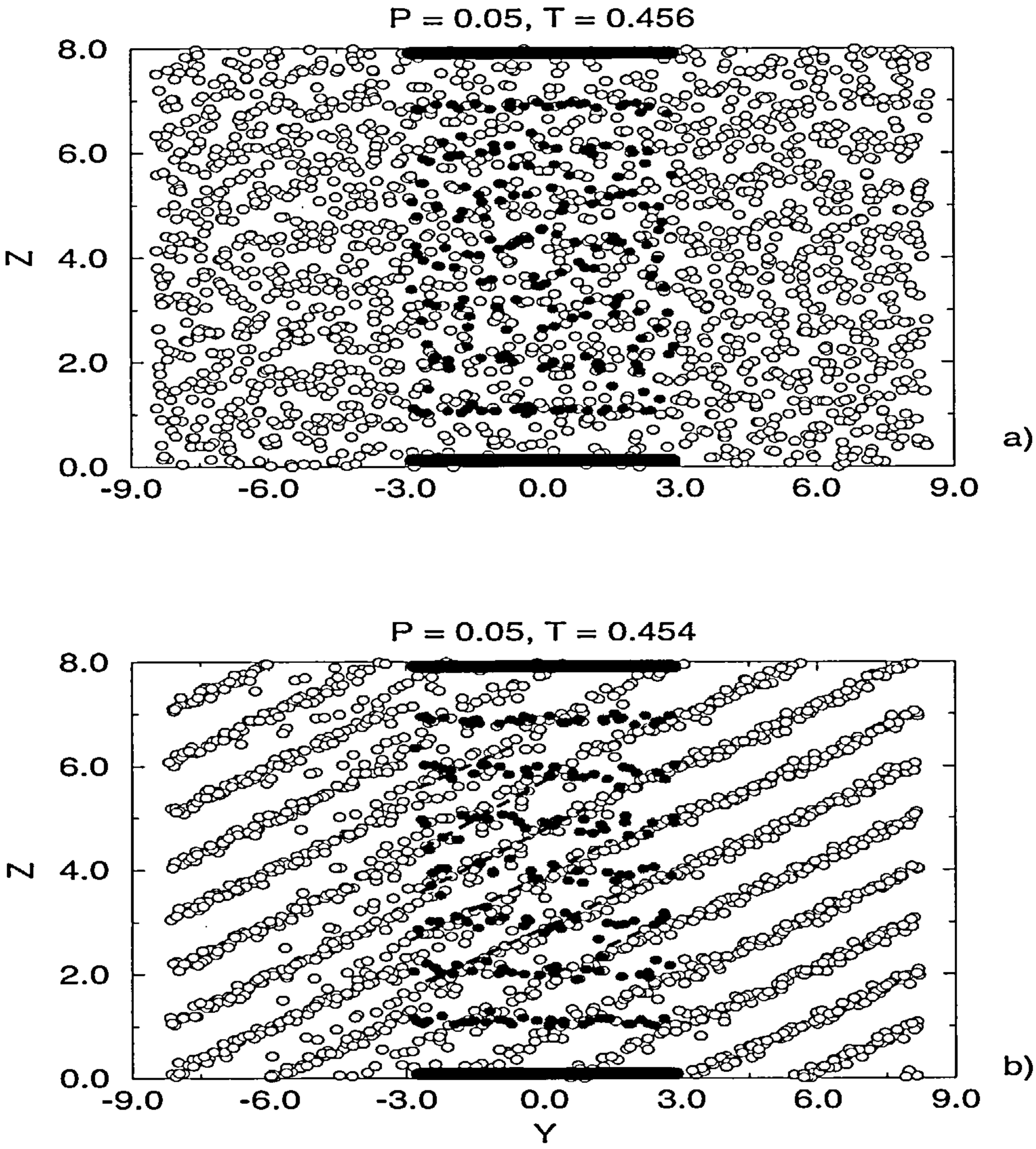

Figure 6.7: Snapshots of particles configurations for the pore system investigated in figures 6.4 a) and 6.5 a), i.e. $l = 8.0$ and $P = 0.05$. a) At temperature $T = 0.456$, both the pore and reservoir fluid are liquid-like. b) Once the freezing temperature is reached ($T = 0.454$) both fluids freeze simultaneously. The black circles represent the particles in the pore whereas the open circles are the particles in the reservoir.

l	T (freezing) from (ϵ/N)	T (freezing) from (Diffusion)
12.5	0.425	0.425
12.0	0.431	0.431
11.0	0.437	0.437
10.0	0.447	0.447
9.0	0.450	0.450
8.0	0.454	0.454
7.5	0.466	0.466

Table 6.2: The freezing temperature for different pore widths, l, for pressure $P = 0.05$ and $N = 2000$.

that for higher pressures the reservoir has less influence on the ordering of pore-particles. Thus, the dominant interaction would seem to be from the walls leading the formation of layers parallel to the walls (as seen in my previous simulations, chapter 4 and 5). If the interaction of the pore fluid with the reservoir and with the walls was similar (what might occur for low pressures), the structure of the pore fluid could arise from the competition between these two interactions. Another possible explanation can be stated in term of the fluctuations of the whole simulation box to maintain constant pressure. Sometimes the crystal becomes commensurate more easily in one particular direction (to fit with the box size). The freezing temperature for each pore width is shown in table 6.2.

Hug and van Swol [95], in a similar simulation of repulsive colloidal particles between repulsive Yukawa walls, did not observe this structural behaviour. They

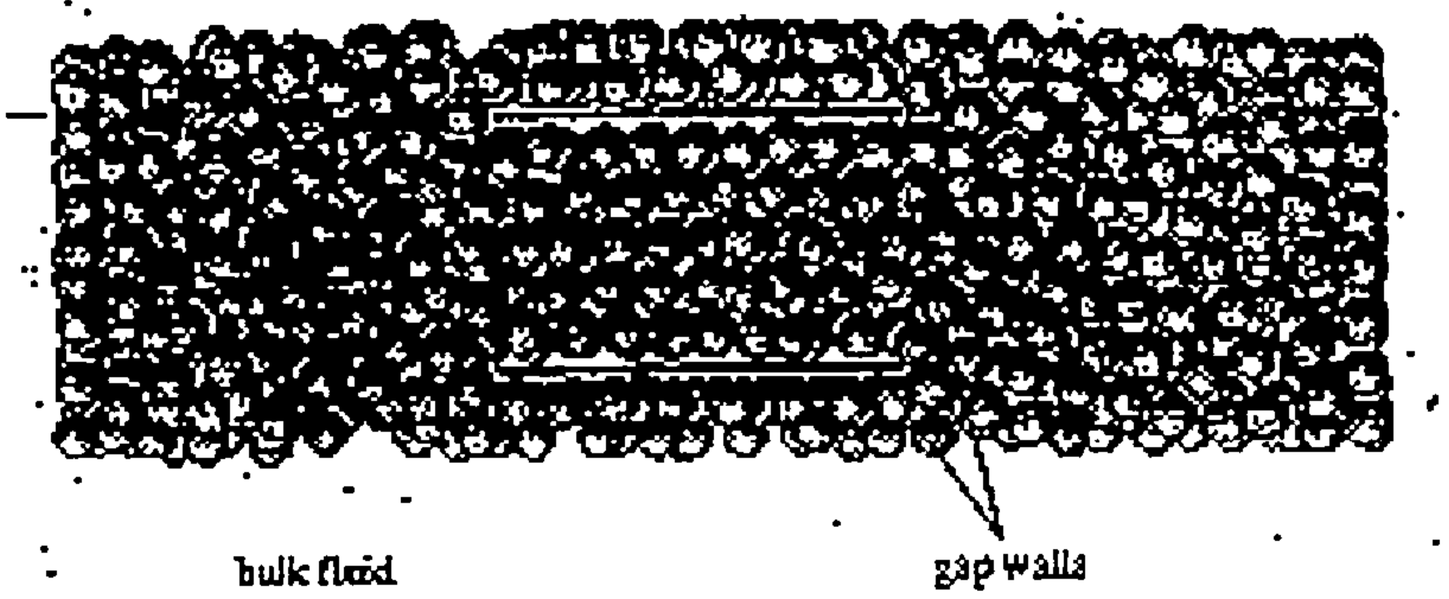

Figure 6.8: The bulk and the pore particle configuration for a Yukawa fluid confined by repulsive Yukawa walls. $l = 6.0$, the pressure $P = 0.016$, is well below the bulk freezing pressure ($P_{bulk} = 0.024$). The figure was taken from [95]. Note the formation of horizontal layers inside the slit parallel to the pore walls and of vertical layers at the end of the bulk fluid. The latter arise from interactions with the plates which are imposed at the ends of the simulation box.

found that the fluid in the slit-pore could freeze at pressures (or volume fraction) well-below that of the bulk transition (see figure 6.8). However, they attached fluctuating plates at the ends of their simulation box in one direction, i.e. periodic boundary conditions were not imposed in that direction. Although the authors claim that the plates are far enough away from the pore to avoid any interaction, from my own point of view, there seems to be some difficulty in distinguishing between the pore and bulk configurations. Once the bulk or the pore fluid freezes, the pore fluid forms layers parallel to the walls of the slit. However, layers also form at the plates at the end of the simulation box (figure 6.8). These two sets of layers grow in opposite planes and in the middle of the reservoir there is frustration. The system does not know what structure to take and it could appear to be liquid-like because

of this structural competition. In other words the whole system in the simulation box might prefer to be solid, even though the pressure is well-below that of the bulk transition.

6.2.1.2 Diffusion Coefficients

The dynamical properties of a confined fluid should be different from those in bulk. In order to observe whether or not the fluid has anisotropic transport properties, due to the presence of the walls, I performed measurements of diffusion coefficients.

The following analysis discusses the diffusion coefficients for particles in the pore only. For bulk (homogeneous) fluids we know that the self-diffusion process is governed by Fick's law:

$$\frac{\partial c}{\partial t} = D\nabla^2 c \tag{6.1}$$

where c is the particle concentration and D is the self-diffusion coefficient.

For large slit-pores ($l \to \infty$) the fluid in the pore will be homogeneous and we expect this expression to be valid. For finite l we assume that the fluid is isotropic in the x and y direction, and we can write the appropriate time correlation functions as for bulk systems. Thus, in terms of the velocity autocorrelation function in the x direction,

$$D_{xx} = \int_0^\infty \langle v_x(0)v_x(t)\rangle dt. \tag{6.2}$$

where D_{xx} is the diffusion coefficient along the x plane and v_x is the centre of mass velocity of the particle in the x direction. A similar equation can be written for the y component.

For times t, large compared with the correlation time, we can calculate D_{xx} from an Einstein relation [138],

$$2D_{xx} = \lim_{t\to\infty} \frac{\langle \Delta x^2(t) \rangle}{t} \tag{6.3}$$

where

$$\langle \Delta x^2(t) \rangle = \langle [x(0) - x(t)]^2 \rangle \tag{6.4}$$

is the mean square displacement in the x direction.

Again, there is a similar expression for the coordinate y. Moreover, if the fluid is isotropic in x and y, we have by symmetry,

$$D_{xx} = D_{yy}. \tag{6.5}$$

Then, I define the relation

$$D_{||} = (D_{xx} + D_{yy})/2, \tag{6.6}$$

where $D_{||}$ is the diffusion coefficient parallel to the plates.

Because of the walls, we do not expect equations 6.2 and 6.3 to apply directly to the diffusion coefficient in the z direction.

I do not attempt to give a detailed analysis of how to calculate diffusion coefficients for this situation, I just mention the relevant results given by other authors. Following the work of Hall and Ross [53, 139], who solved the diffusion equation for the boundary conditions appropriate to the restricted fluid, the mean square displacement in the z direction is given by the expression:

$$\langle \Delta z^2(t) \rangle = \frac{l^2}{6} - \frac{16l^2}{\pi^4} \sum_{j=1}^{\infty} (2j-1)^{-4} \times \exp[-(2j-1)^2 \pi^2 D_\perp t / l^2]. \qquad (6.7)$$

Here $D_\perp = D_{zz}$ is the diffusion coefficient perpendicular to the walls.

We can examine the behaviour of $\langle \Delta z^2(t) \rangle$ for wide pores taking the limit of $l \to \infty$. The Weierstrass M test shows that the series in equation (6.7) converges uniformly as $l \to \infty$. Then, in this limit, provided t constant but sufficiently large, the exponential can be expanded in Maclaurin series [140]. Then, using the identities $\sum_{j=1}^{\infty}(2j-1)^{-2} = \pi^2/8$ and $\sum_{j=1}^{\infty}(2j-1)^{-4} = \pi^4/96$ equation 6.7 is written by the following expression [53,139]

$$2D_\perp t = \lim_{l \to \infty} \langle \Delta z^2(t) \rangle \qquad (6.8)$$

For times large compared with the correlation time this expression defines the diffusion coefficient reasonable well. Moreover, in this limit (of $l \to \infty$) we expect that $D_\perp = D_{||}$. Schoen et al. [66] found that for pores wider that about 3σ the diffusion coefficient normal to the walls is reasonably well-described by the above large-pore limiting equation. Thus, I assume that for $l > 3$ (which is satisfied in all my simulations) equation (6.8) defines a sensible diffusion coefficient perpendicular to the walls.

Thus, diffusion coefficients were calculated (in a Molecular Dynamics simulation) with the mean square displacement (from the standard expression, equation (6.4)) of the particles and using equation (6.3) and equation (6.8) for the parallel and perpendicular coefficient diffusion respectively. Following the prescription of Schoen et al. [66,141], if we assume that particles are statistically independent, we write in cartesian coordinates for the z component:

$$\langle \Delta z^2(t_k) \rangle = (N_p L)^{-1} \sum_{j=1}^{L} \sum_{i=1}^{N_p} ([z_i(t_j) - z_i(t_j + t_k)]^2) \tag{6.9}$$

N_p is the number of particles in the system of interest and L is the total number of time origins used. Similar equations are used for the x and y directions for particles in each layer of the pore. The calculations of the mean square displacement were performed considering particles in the pore only (i.e. I followed particles which stayed in the pore). Moreover, since I calculated diffusion coefficients in each layer, equation (6.9) refers to one layer only, in this case N_p is the number of particles in the layer (from the particles in the pore I just analyzed particles in one layer). Since particles can flow from the pore to the reservoir and vice versa and particles in the pore can also flow from one layer to another we should define N_p in equation (6.9). First, we must define which particles are in the reservoir and which are in the pore. This classification was carried out following the particles in a large simulation time. If a particle spends more time out of the pore this particle is counted in the reservoir but if it spends more time in the pore region it is counted in the pore fluid. The same criterion was used to define particles in the layers; particles are counted in one layer only if they spend more time in that layer than in others (here we followed the particles in the pore only).

All of the above measurements refer to the particles within the pore (i.e. particles in the layers). In order to compare these values with those in the reservoir, I also calculated the diffusion coefficient for particles in the reservoir. For these calculations I considered particles outside the pore region only, i.e. I followed particles which are in the reservoir (not in the pore). The definition of the reservoir diffusion coefficient employed for this case is.

$$D = (D_{xx} + D_{yy} + D_{zz})/3, \tag{6.10}$$

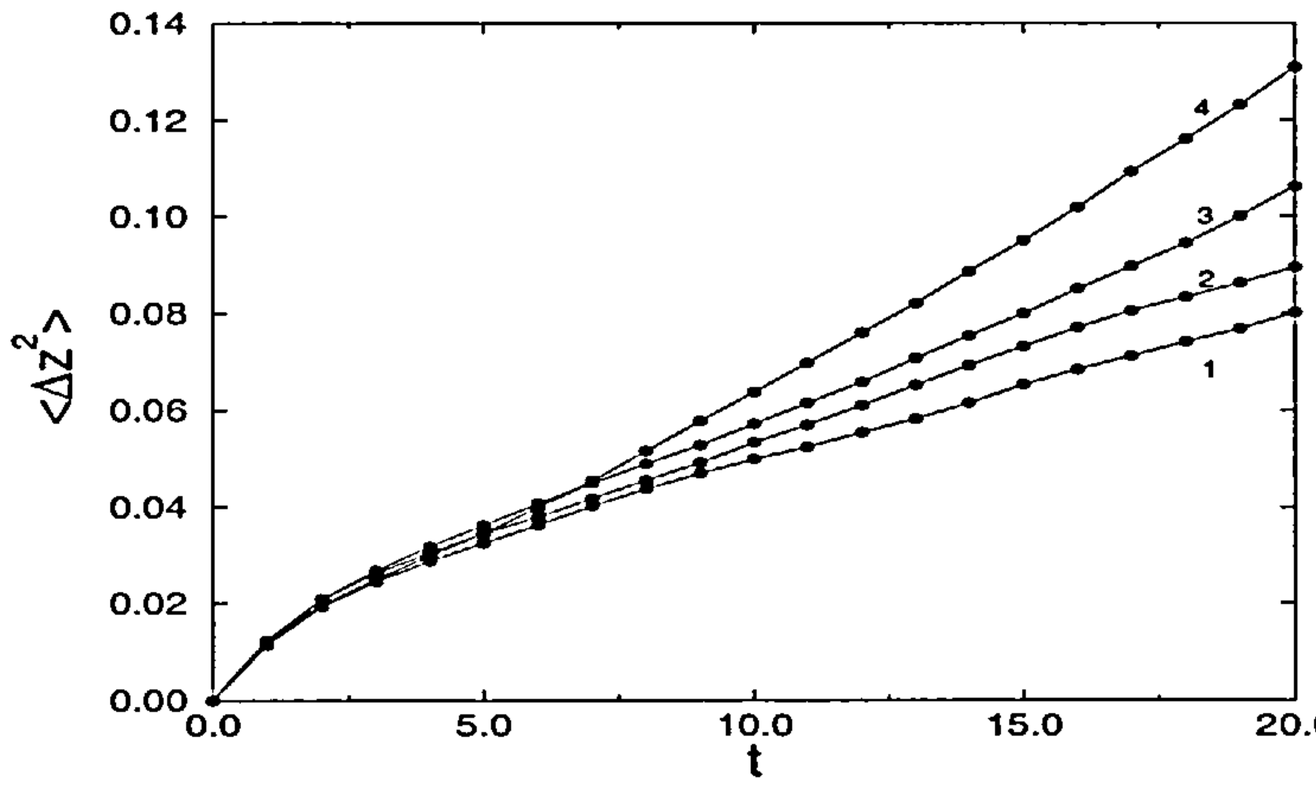

Figure 6.9: Mean square displacement, perpendicular to the walls, for different layers for a slit pore with $l = 12.5$, at pressure of $P = 0.05$ and $N = 2000$ and at temperature before freezing (T=0.427). The effective diffusion coefficient is obtained from the slope of each curve in the range of t=8-20. The number 1 refers to the first layer closest to the walls, 2 to the second inner layer, etc.

where the diffusion coefficient in each direction was defined in similar way as equation (6.3). The mean square displacement was calculated as in equation (6.9). However, as was stated, these bulk calculations were performed for particles outside the pore. In this case the number of particles N_p in equation (6.9) refer to those particles in the reservoir only, where the definition of reservoir-particles was described above for the classification of the particles.

In figure 6.9 we observed typical curves of mean square displacements. In this figure the mean square displacement in the z direction is plotted for different layers for the pore width of $l = 12.5$ at pressure $P = 0.05$ and very close to the freezing

temperature ($T = 0.427$). The diffusion coefficient corresponding to those curves is obtained from the slope of each curve at times, $t = 8 - 20$, where the slope does not seem to change. One feature that we observe is that the mean square displacement does not present the classical behaviour at very short times (i.e. it does not seem to go to t^2). A similar plot is observed for the mean square displacements parallel to the walls (not shown here). In figures 6.10, 6.11 and 6.12 I plot the coefficient diffusion in the layers and in the reservoir for different pore widths. The diffusion coefficient is given in reduced units (D=D*= $D/(\epsilon\sigma^2/\mathrm{m})^{1/2}$). We can observe that the layers next to the walls show less parallel diffusion than those in the middle. We can also observe that the transverse diffusion coefficient D_{zz} is lower for particles in the first layer. The diffusion coefficients in the layers were calculated as the average of the symmetric layers, e.g. for the pore width $l = 12.5$ we have 12 layers and the diffusion coefficient of the layer next to the walls was the average over layers 1 and 12.

As the temperature decreases diffusion in the layers also decreases but the coefficients take liquid-like values for all slit widths. We also observe the diffusion coefficient in the reservoir, for all temperatures, is always much higher than that in the pore. However, the diffusion coefficients in the reservoir seem to be different in each case i.e. they depend upon the pore width. For instance the freezing transition, as signalled by the rapid decrease in diffusion, occurs at different temperatures, whereas for a true bulk fluid it should be independent of pore size. Of course, this effect can be due to the finite size of the simulation box. i.e. the reservoir is not sufficiently large to simulate a bulk fluid in contact with the pore (as discussed above). However, once more, we have to remember that the reservoir at the limit of metastability and any perturbation can nucleate the system. Therefore we have to be cautious to say reservoir rather than bulk fluid. Recall that the reservoir-particles are those which spend more time outside the pore region. That is why I refer to the fluid surrounding the pore simply as the reservoir. Thus, in figures 6.10, 6.11 and 6.12 we observe that both the pore and the reservoir remain liquid-like down to the

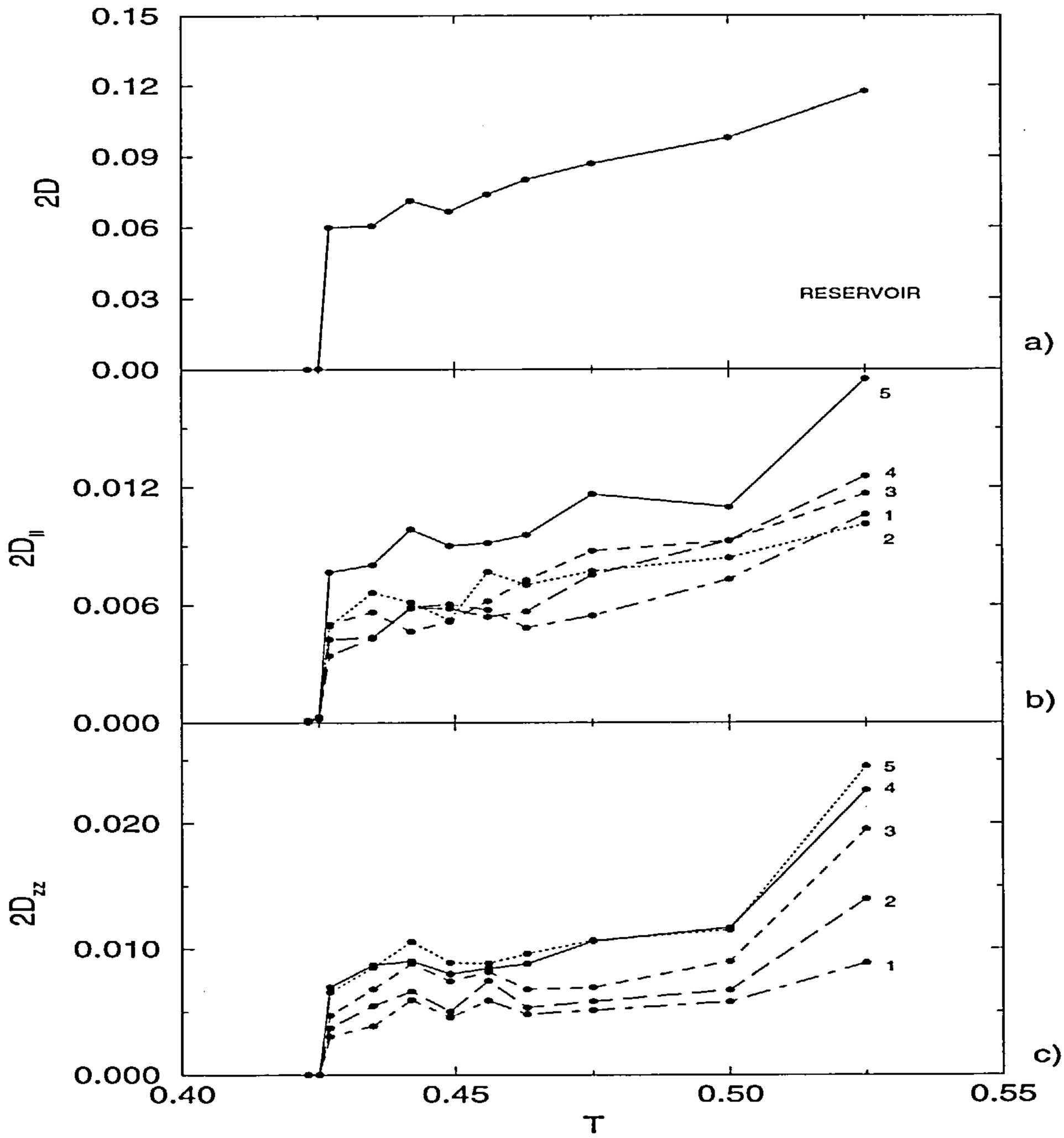

Figure 6.10: The self-diffusion coefficient (in each layer) as a function of the temperature for a slit-pore with $l = 12.5$, at pressure of $P = 0.05$ and with $N = 2000$. The diffusion coefficients b) parallel and c) transverse to the walls are smaller for the first contact layers than in the middle. The self-diffusion coefficient in the reservoir is also measured (plot a) for the same temperatures. These values are always much higher than those in the pore -note different scales. Note that at temperature $T = 0.425$ where the system freezes, both the pore and the bulk diffusion coefficients drop simultaneously. The number 1 refers to the first layer closest to the walls, 2 to the second inner layer, etc.

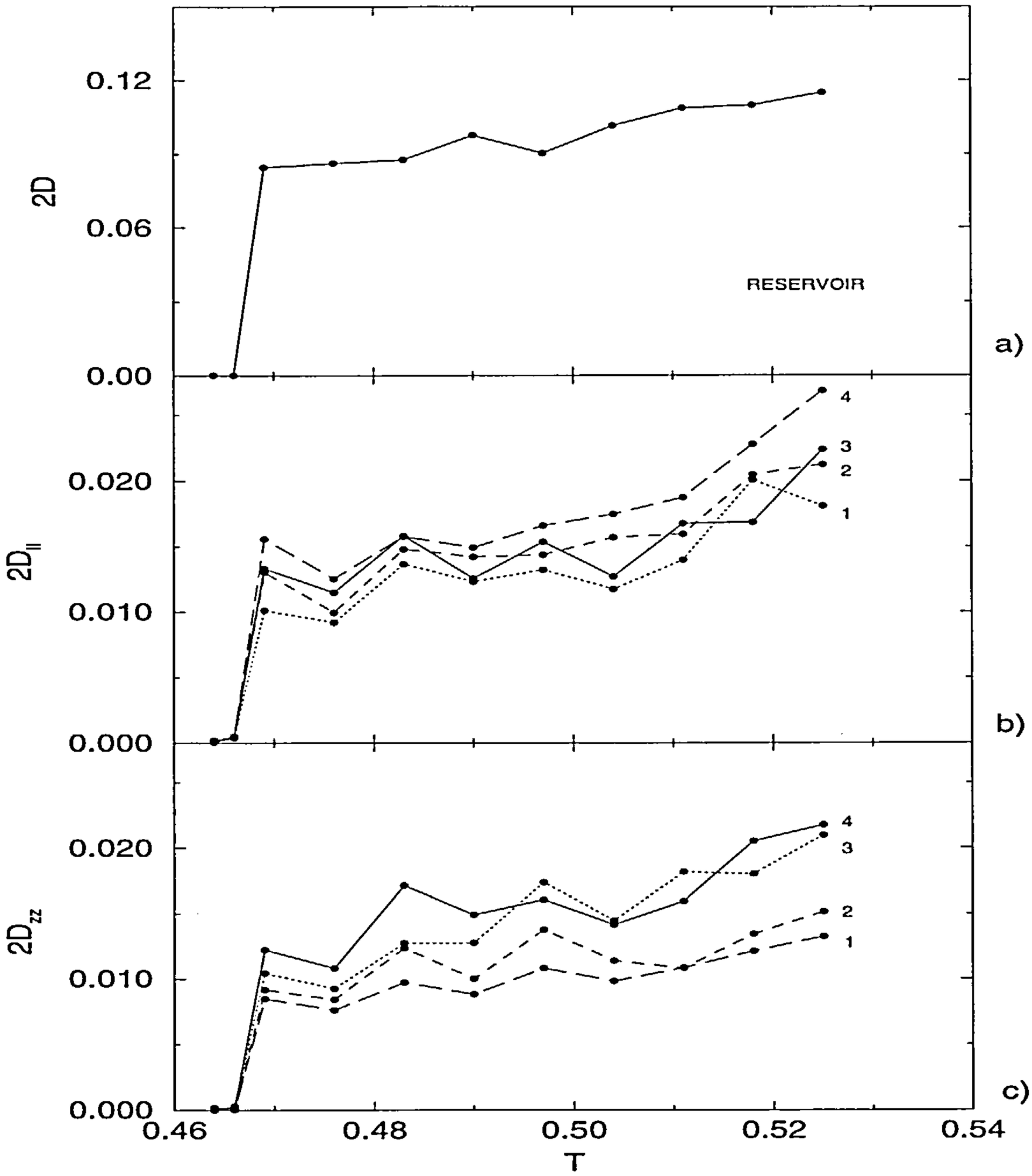

Figure 6.11: The self-diffusion coefficient (in each layer) as a function of the temperature for a small slit-pore, $l = 7.5$, at pressure of $P = 0.05$ and with $N = 2000$. Once again, we observe that the reservoir diffusion coefficient (plot in figure a)) is always much higher than those in the pore. However, all drop simultaneously at the freezing temperature (see text). The number 1 refers to the first layers closest to the walls, 2 to the second inner layer, etc.

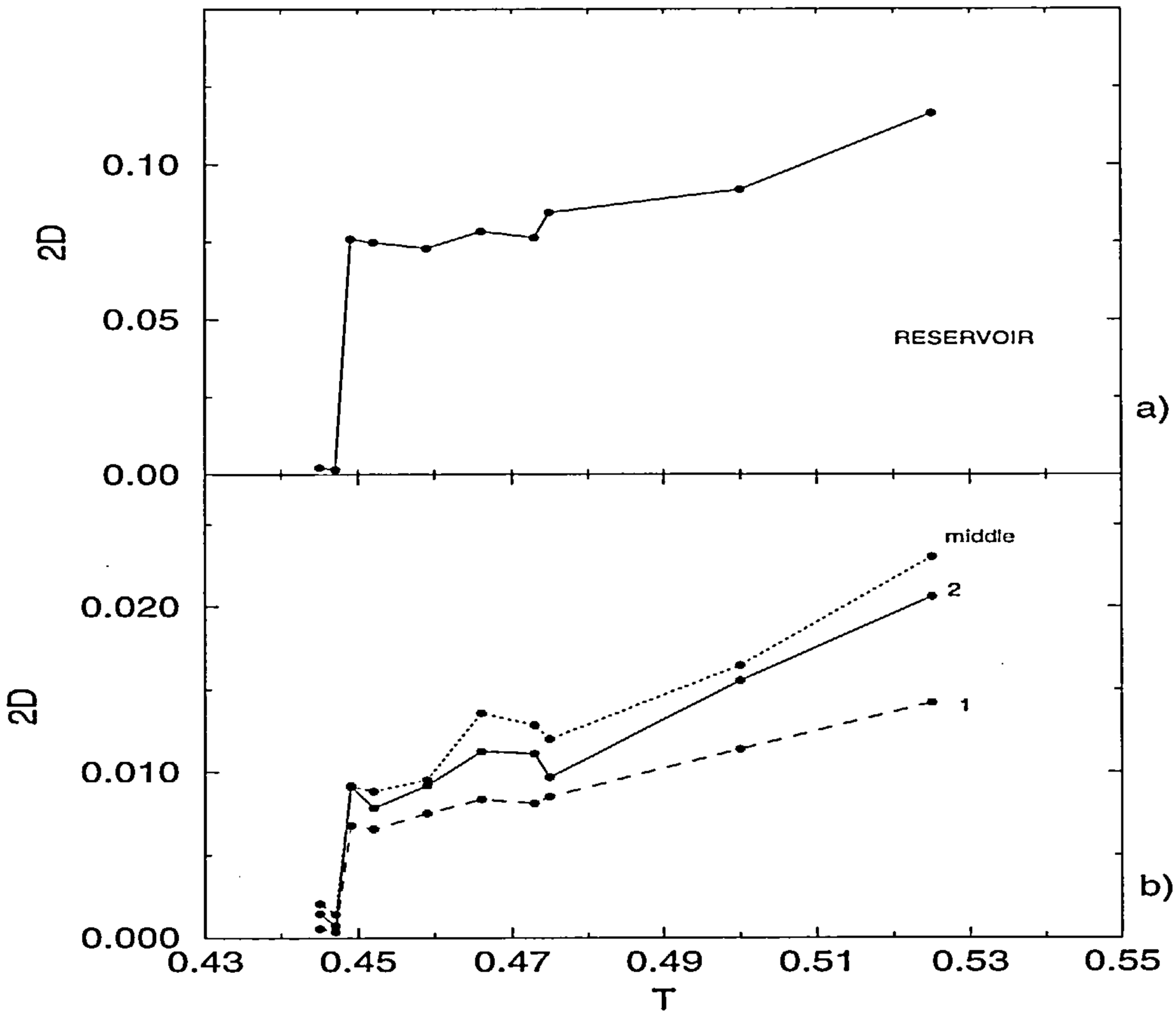

Figure 6.12: The self-diffusion coefficient for a pore width of $l = 10.0$ at pressure $P = 0.05$ and $N = 2000$. Because the layers are not well-developed parallel to the pore walls when the fluid freezes (see figures 6.5 b and 6.6), I plot the diffusion coefficient for the first and second layer and for the "middle" of the pore. The "middle" means the average of the diffusion coefficients in the inner layers. The reservoir diffusion coefficient is also plotted (figure a). Note once more, that the pore and reservoir diffusion coefficients drop simultaneously at the freezing temperature ($T = 0.447$.)

freezing temperature. Once this temperature is reached, however, diffusion in the pore and in the reservoir drop sharply, indicating freezing in the pore and in the reservoir occur both simultaneously. Again, it is not possible to discern which fluid freezes first. For given pore, the temperature at which the drop in diffusion occurs is the same as that at which the change in the internal energy occurs (see table 6.2).

6.2.2 Melting of the pore and reservoir system

Once the fluid was completely frozen I took a final configuration and began to heat up the system. I looked for melting, for the same pressure of $P = 0.05$, by increasing the temperature in increments of $\Delta T = 0.025$. As the solid-liquid transition approached the increment was reduced to $\Delta T = 0.005$. The simulation procedure was carried out in the same way as described for freezing, for a series of pore widths.

I observed a very large degree of hysteresis (see figure 6.1 for l=12.5). The melting transition, as defined by the rapid jump in the internal energy, occurs at a much higher temperature than freezing and is somewhat above the bulk melting temperature (see figure 5.8 in chapter 5). For most pores sizes a significantly larger part of the hysteresis curve lies below the bulk transition temperature, see e.g. figure 6.4 and figure 6.13. However, for the largest pore $l = 12.5$, where the hysteresis is enormous, the bulk transition is near the middle (figure 6.1). In my simulations for the bulk at the same pressure I also observed large hysteresis. In fact, the hysteresis in bulk has a similar extent to that for the pores of width $l = 8.0, 10$ (compare figure 6.4 and 6.14). Miyahara and Gubbins [96], simulating methane fluid with different wall-fluid interactions, found that the extent of the hysteresis seems to be very sensitive to the way that particles pack in the slit-pore. However, they conducted Grand Canonical Monte Carlo simulations in their investigations of freezing. Thus, the extent of the hysteresis also seems to depend on the method of simulation that is employed.

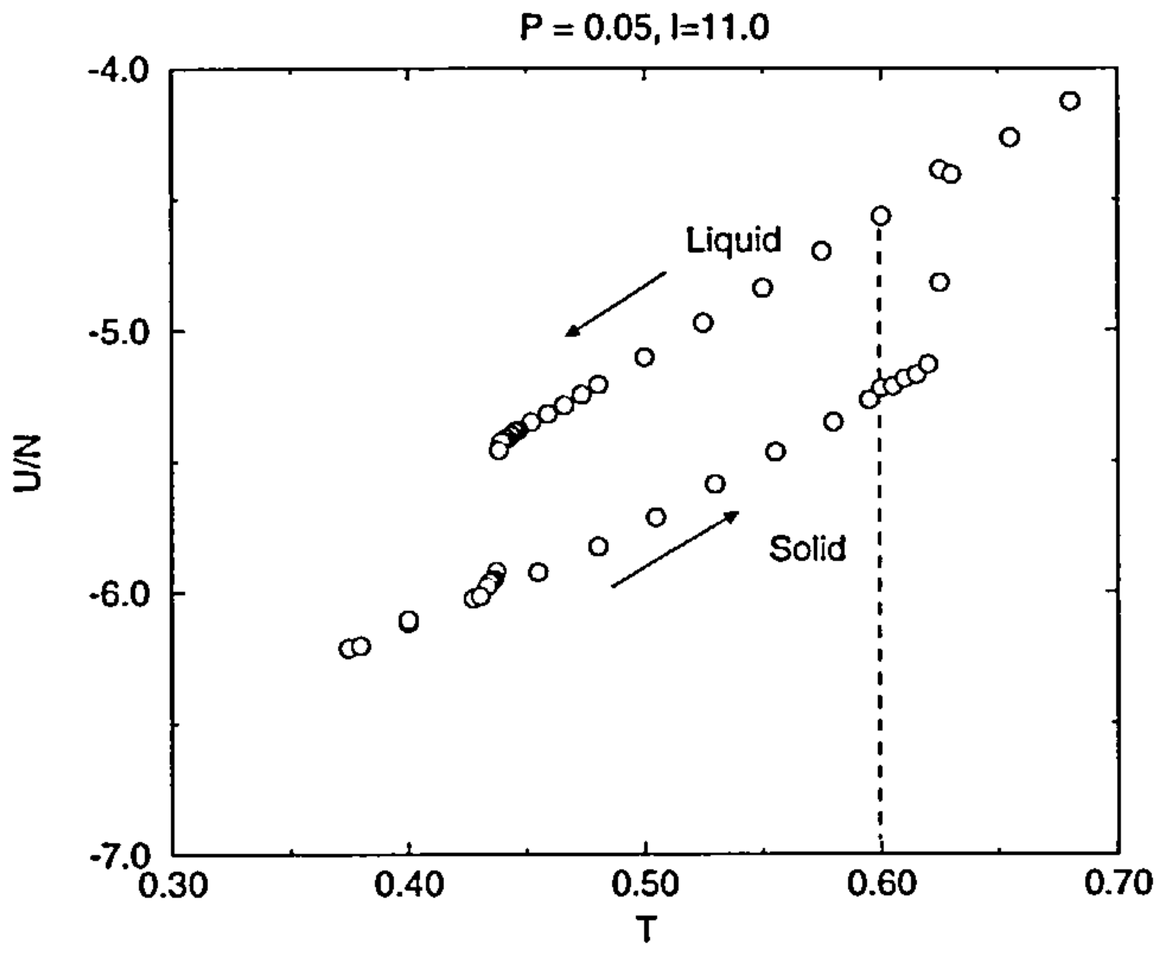

Figure 6.13: The internal energy as a function of the temperature for a pore of width $l = 11.0$. $P = 0.05$ and $N = 2000$. The freezing temperature occurs at $T = 0.437$ and the melting at $T = 0.625$ (jumps at the left and right respectively). Note that the hysteresis extends much further below the bulk freezing temperature ($T_{bulk} \approx$ 0.6, dashed line) than it does above.

6.2.2.1 Structure of the fluid at melting

As I stated in the last section it is rather difficult to distinguish whether the pore or the reservoir fluid freezes first. It is important to raise the same issue for the melting transition i.e. the high temperature limit of metastability. Thus, I investigated configurations of the whole system near to the melting point. Although the difficulty of having liquid and solid phases in the same simulation box is equally relevant here, I attempted to analyze the pore and reservoir fluid structure. From figures 6.15, 6.16 and 6.17 we observe that at temperatures close to the melting transition the pore

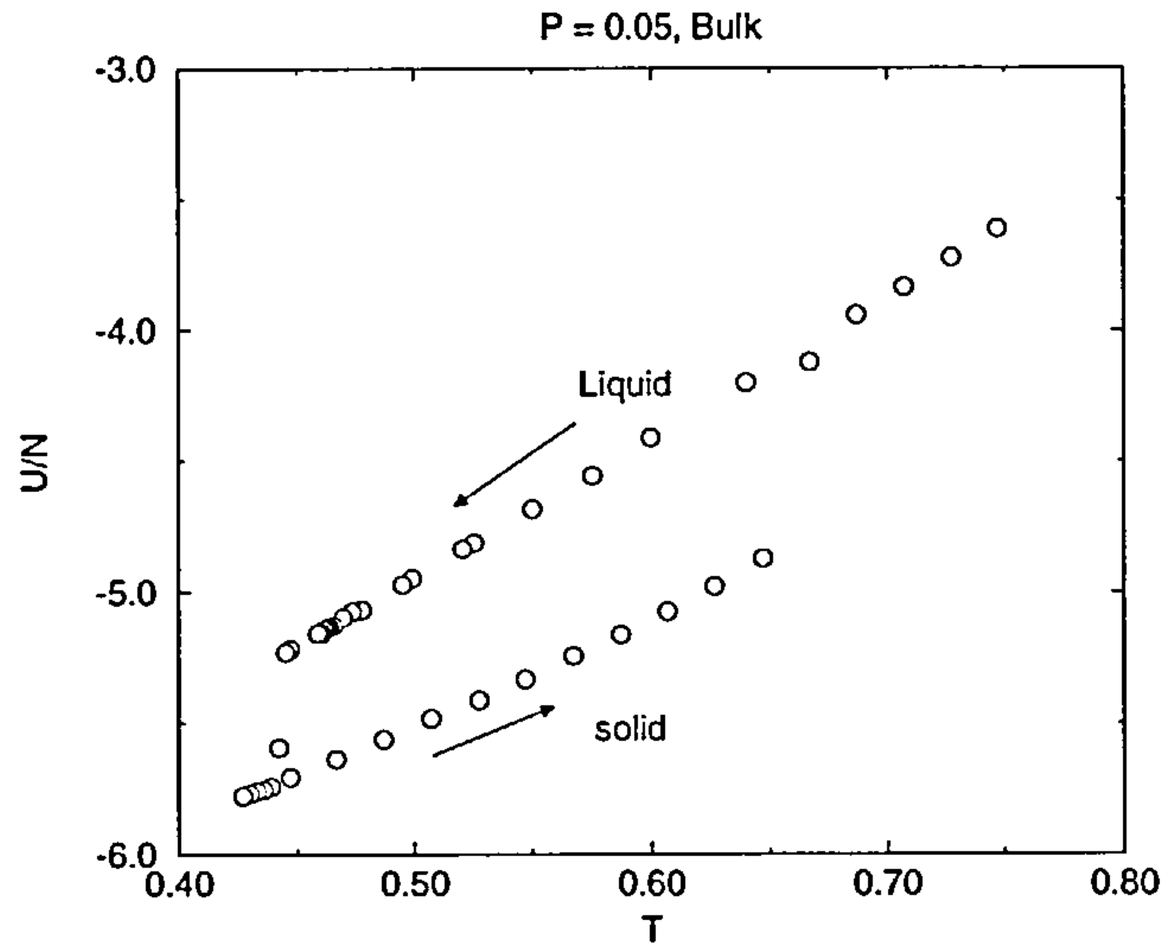

Figure 6.14: The internal energy as a function of temperature for a bulk system; $N = 2000$, $P = 0.05$. The equilibrium freezing transition occurs at $T \approx 0.60$. Compare this plot with those for the pore systems (figures 6.1, 6.4, 6.13). Error bars are of the size of the symbols.

fluid exhibits a different structure from that in the reservoir, i.e. in some regions (of the pore) the fluid begins to lose its solid structure. This new feature was not found in the freezing studies. Thus, for these investigations of melting I introduced an order parameter to characterize the degree of order in the pore and the reservoir fluid. Some authors, such as Ma et al. [35] in their studies of freezing in slit pores, defined an order parameter as the normalized peak of the structure factor. Moreover, since in their simulations the pore fluid always forms layers parallel to the walls (when the fluid freezes) they defined an in-plane order parameter, again as the normalized maximum of the structure factor in two dimensions. Other authors [95] also defined

the order parameter in each layer, measuring the two dimensional structure factor w.r.t the reciprocal lattice parameters appropriate to a two dimensional hexagonal lattice. However, in this work we have seen that layers are not always formed parallel to the pore-walls. Thus, in this case it is more useful to define an order parameter which characterizes the structure of the whole fluid, either in the pore or in the reservoir. For this purpose I defined a three dimensional order parameter as the normalized maximum of the 3D-structure factor

$$OP = \frac{\max[S(K_x, K_y, K_z)]}{S(0,0,0)} \tag{6.11}$$

where

$$S(K_x, K_y, K_z)] = \frac{1}{N_p} \left| \sum_{j=1}^{N_p} e^{i(K_x x_j + K_y y_j + K_z z_j)} \right|^2 \tag{6.12}$$

excluding the value for $K_x = K_y = K_z = 0$. The maximum possible value for the order parameter is 1 (i.e. for a well-defined crystal structure).

I performed calculations of the order parameter for the pore and the reservoir as the average over several configurations in the simulations. For the pore I followed particles which stayed in the pore only, then N_p in equation (6.12) refers to the particles in the pore. For the order parameter in the reservoir I used the same equation (6.12), however N_p refers to all particles outside the pore, i.e. I consider only particles which stay in the reservoir fluid. Once more, the classification of pore and reservoir particles is the same as described above (for the calculations of the diffusion coefficients).

It is rather difficult to say for which values of the order parameter the fluid (pore or reservoir) changes from liquid-like to solid-like. However I observed that when the fluid is liquid-like (it lies on the liquid branch of the energy-temperature curve) the order parameter is always low ($\approx$ 0.30-0.40 or less) and when the fluid is solid-like

(after the jump in the internal energy) the order parameter is relatively higher ($\approx$ 0.65-0.70 or more). Thus, I use this criterion for the values of the order parameter, to say whether the fluid is liquid-like or solid-like.

We can observe for the pore $l = 9.0$, at temperature of $T = 0.530$ (figure 6.15) both the pore and the reservoir are frozen (the state point lies at the solid branch in the energy-temperature curve), the order parameter is 0.751 and 0.715 respectively. However, at temperature $T = 0.610$ it seems that the reservoir remains solid-like (order parameter 0.662) whereas the fluid in the pore starts losing its solid structure (order parameter 0.348). We must emphasize that these results refer to temperatures very close to melting. Finally, at $T = 0.615$ both fluids are liquid-like (the jump in the internal energy occurs), the order parameter is (0.313) for the pore liquid and for the reservoir one is (0.322). We can see similar results for pores of width $l = 10.0, 12.0$ (see e.g. figure 6.16 and figure 6.17). For the largest pore, $l = 12.5$, is not possible to assert anything since both fluids (the pore and the bulk) seem to remain solid-like until they melt simultaneously (figure 6.18).

6.3 Monte Carlo simulations

In this brief sub-section I describe Monte Carlo simulations of the same slit-pore surrounded by a thermal bath.

This series of simulations was conducted at high pressures ($P = 0.7, 2.0, 6.0, 9.0$) for a single pore size ($l = 10.0$). The simulation procedure was exactly the same as described above, for the Molecular Dynamics results, with 1500 particles in total. For the pressures of $P = 0.7, 2.0, 9.0$ the wall area was the same as in the above section, and the same ϵ' and σ' parameters were used. For $P = 6.0$, however, the wall area was bigger ($A = (7.5)^2$) with a strong wall-fluid interaction: $\epsilon'/\epsilon = 7.2375$ and $\sigma'/\sigma = 0.7823$, i.e. modelling argon fluid between graphite walls. Despite the difference in the wall-area and the wall-parameters, we observe that freezing occurs in a similar way for all these (Monte Carlo) simulations at higher pressures, i.e. we

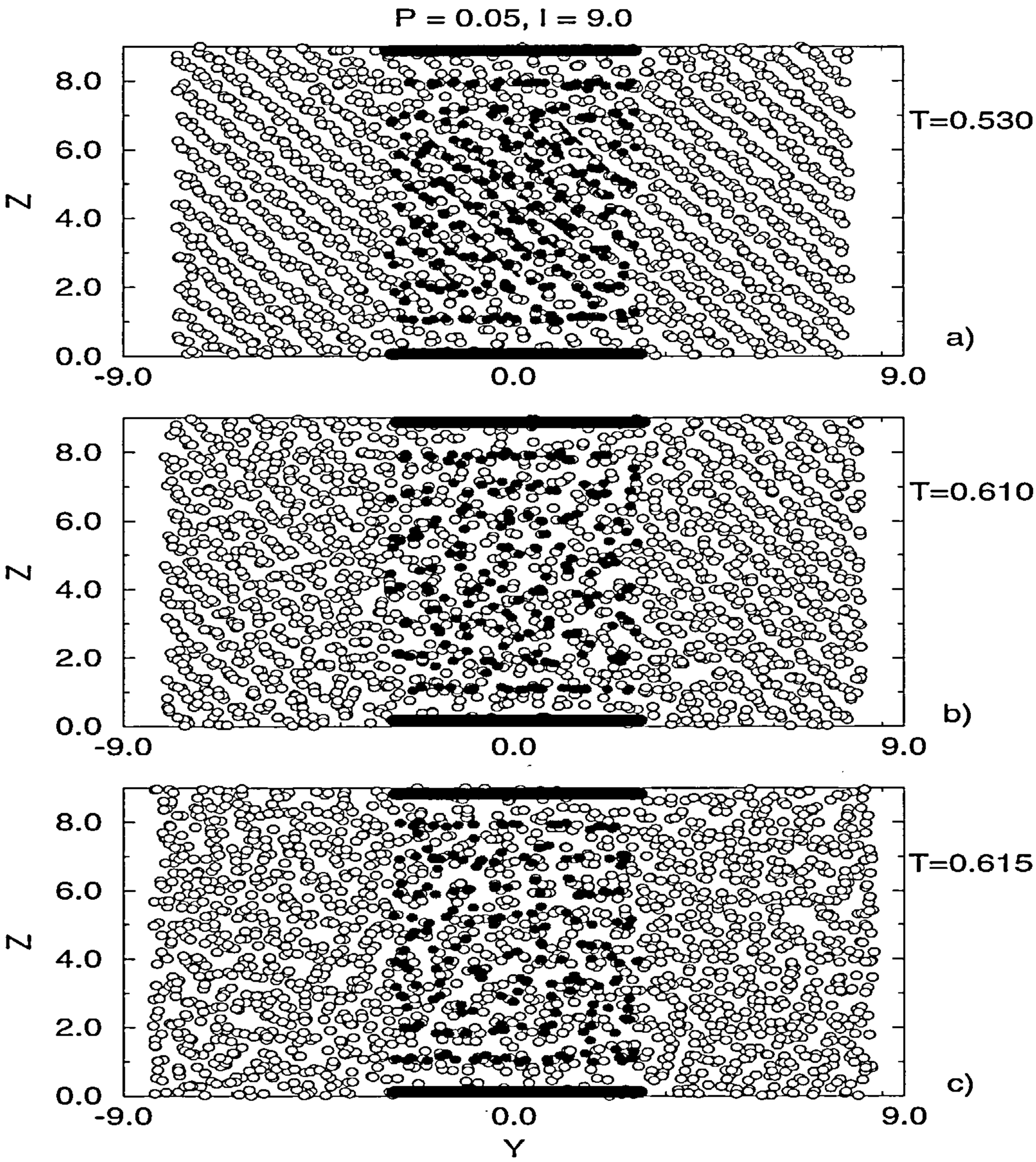

Figure 6.15: Snapshots of particles for a pore with $l = 9.0$, $P = 0.05$, $N = 2000$. a) At $T = 0.530$, both the pore and reservoir are solid-like. The OP are 0.715 and 0.751 respectively. b) Close to the melting temperature $T = 0.610$ the reservoir seems to be solid-like ($OP = 0.662$) whereas the pore fluid starts losing its solid structure ($OP = 0.348$). c) Finally at temperature $T = 0.615$, both the pore and reservoir fluid are liquid-like. The OP for the pore fluid is 0.313 and for the reservoir is 0.332. The black circles represent the particles in the pore whereas the open circles are the particles in the reservoir.

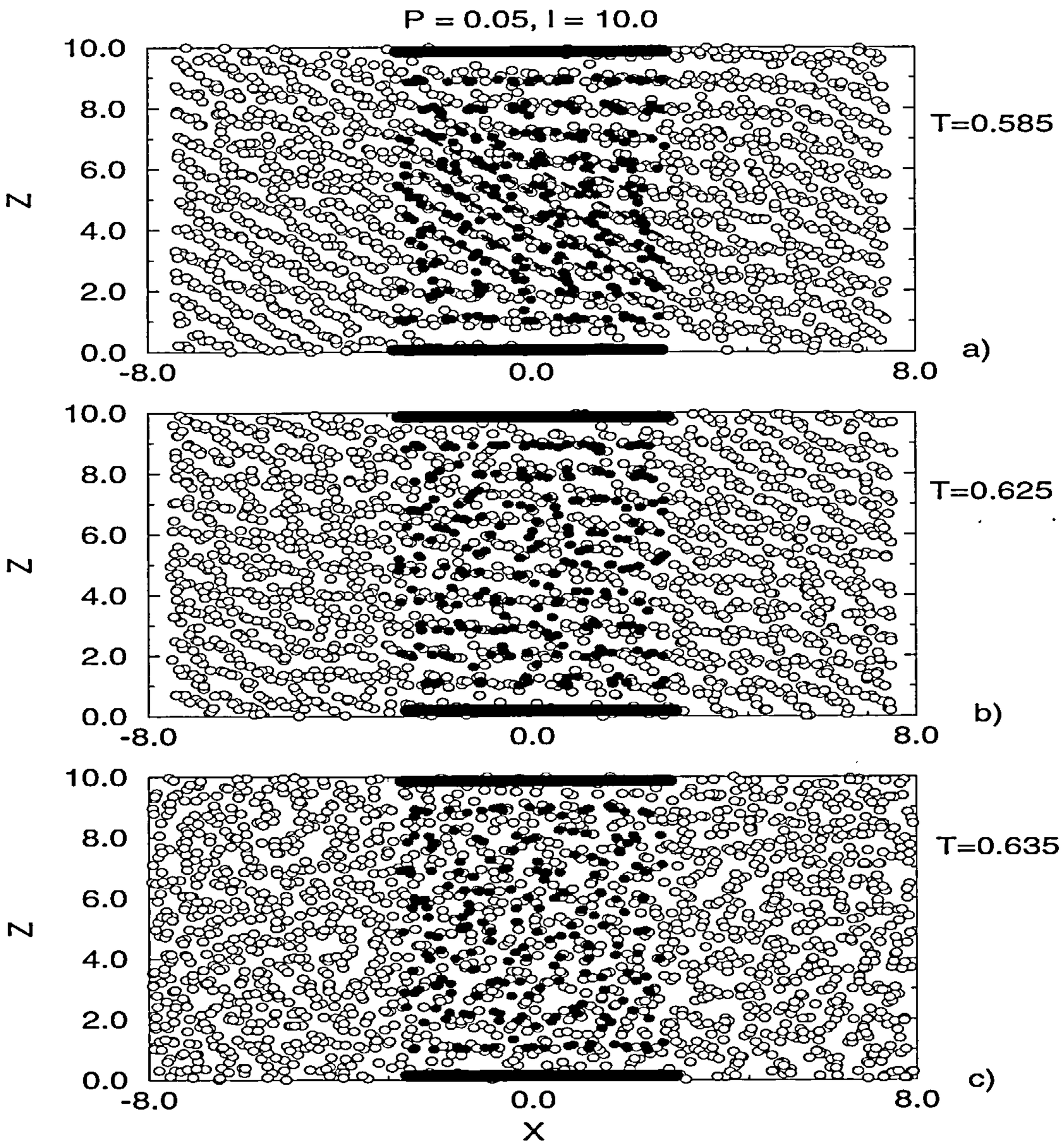

Figure 6.16: Snapshots of particles for a pore width with $l = 10.0$, $P = 0.05$, $N = 2000$. a) At $T = 0.585$, both the pore and reservoir are solid-like. The OP are 0.696 and 0.650 respectively. b) Close to the melting temperature $T = 0.625$ the reservoir seems to be solid-like ($OP = 0.590$) whereas the pore fluid starts losing its structure ($OP = 0.413$). c) Finally at temperature $T = 0.635$, both the pore and reservoir fluid are liquid-like. The OP for the pore fluid is 0.301 and for the reservoir is 0.282. The black circles represent the particles in the pore whereas the open circles are the particles in the reservoir.

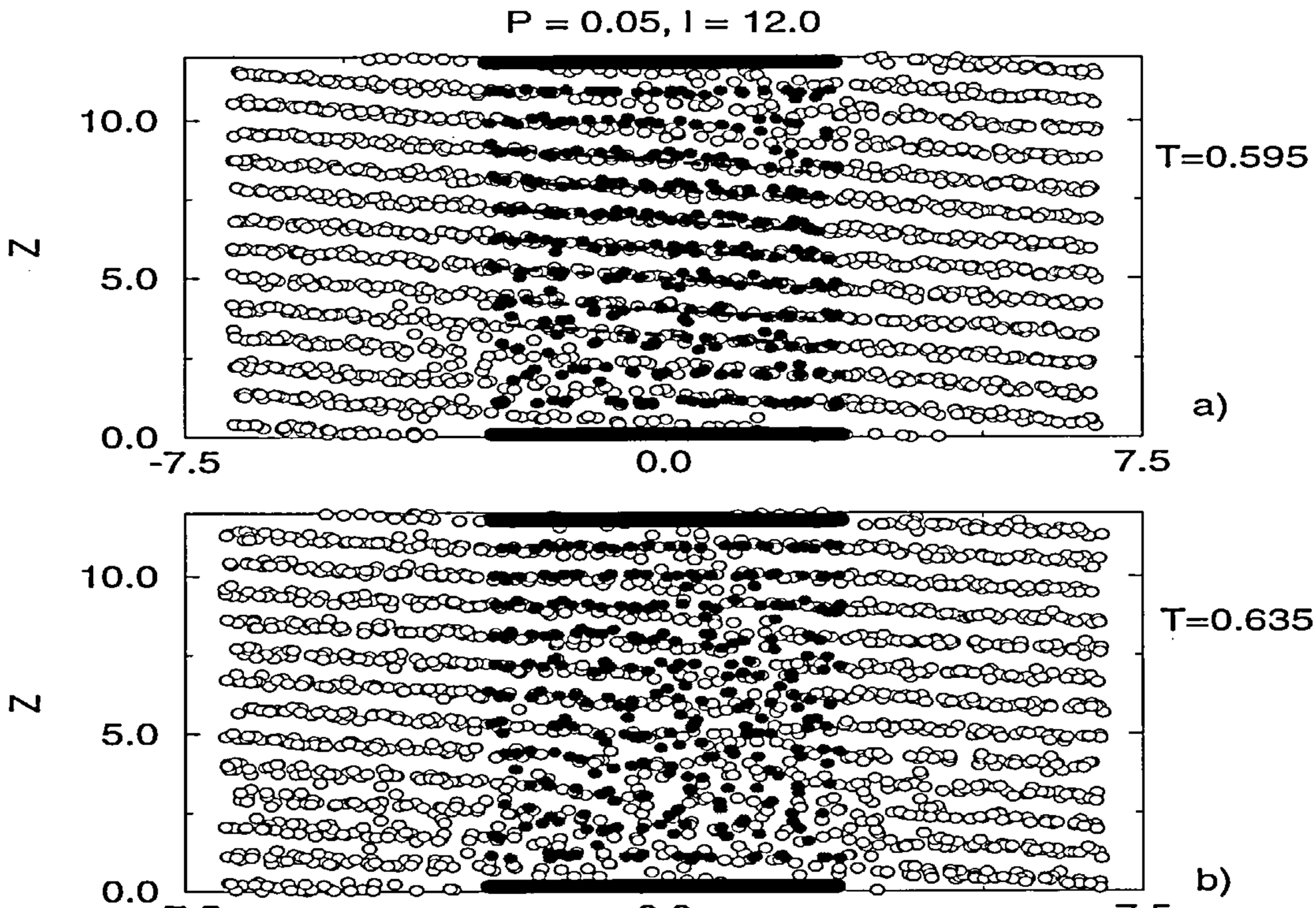

Figure 6.17: Snapshots of particles for a pore width with $l = 12.0$, $P = 0.05$, $N = 2000$. a) At $T = 0.595$, both the pore and reservoir are solid-like. The OP are 0.750 and 0.702 respectively. b) Close to the melting temperature $T = 0.635$ the reservoir seems to be solid-like ($OP = 0.736$) whereas the pore fluid starts losing its structure ($OP = 0.5320$). c) Finally at temperature $T = 0.640$, both the pore and reservoir are liquid-like. The order parameter for the pore fluid is 0.360 and for the reservoir one is 0.332. The black circles represent the particles in the pore whereas the open circles are the particles in the reservoir.

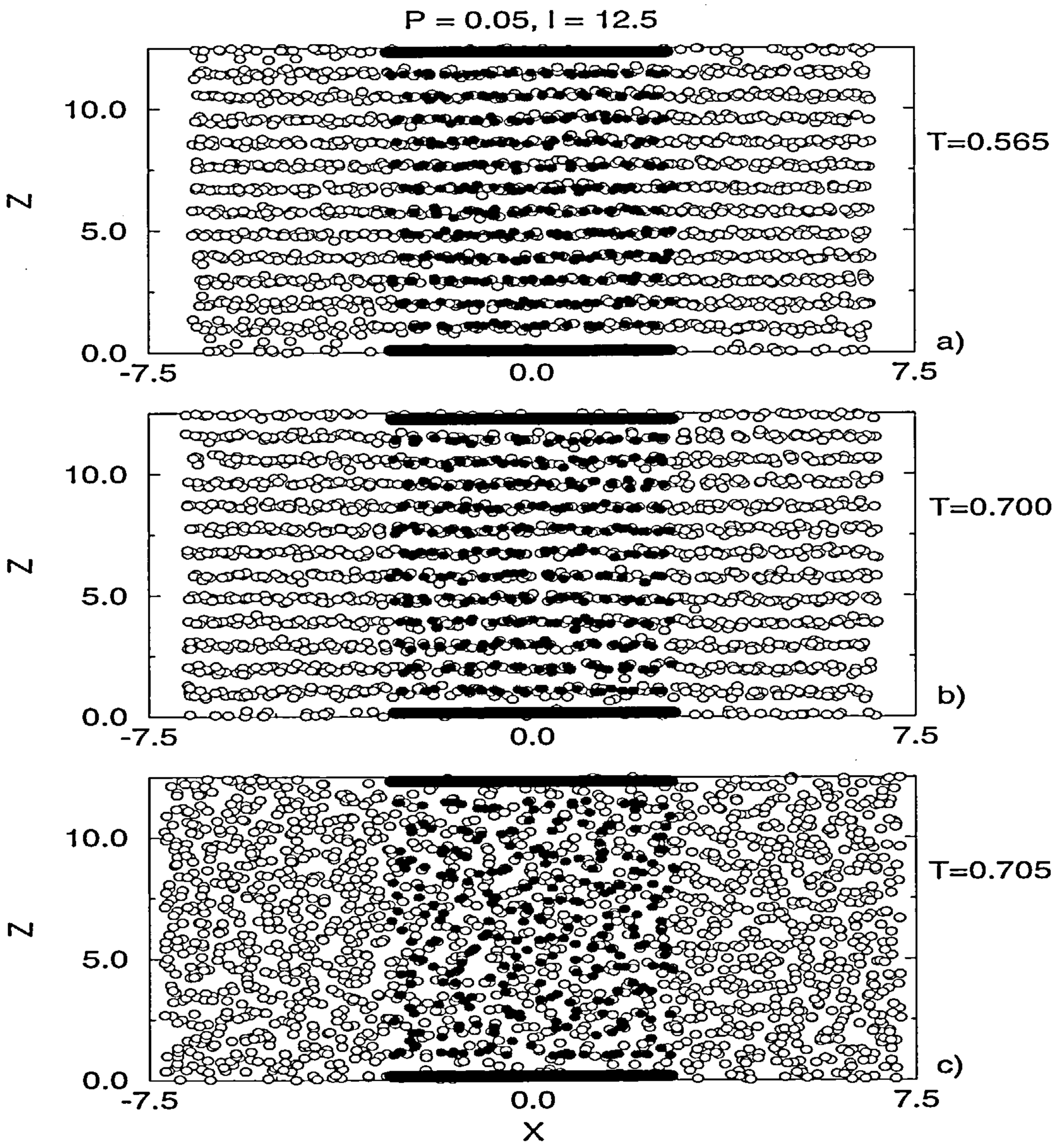

Figure 6.18: Snapshots of particles for a pore width with $l = 12.5$, $P = 0.05$, $N = 2000$. a) At $T = 0.565$, both the pore and reservoir are solid-like. The OP are 0.711 and 0.701 respectively. b) Close to the melting temperature $T = 0.700$, both the reservoir and the pore are solid-like. The OP are 0.698 and 0.689 respectively. c) Finally, at temperature $T = 0.705$, both the pore and reservoir are liquid-like. The OP for the pore fluid is 0.389 and for the bulk one is 0.387. The black circles represent the particles in the pore whereas the open circles are the particles in the reservoir.

observe hysteresis, and the same structure of the confined solid for all the pores investigated in this sub-section. Then, I discuss in detail only the results for the last system, i.e. a fluid confined by strongly attractive square walls at pressure of $P = 6.0$. The effects of the wall-fluid interaction were discussed in chapter 4.

6.3.1 Structure of the confined fluid: Strongly attractive walls

The structure of the fluid within the pore walls was studied for the freezing transition in the same spirit as the previous Molecular Dynamic simulations. As we found in chapter 4, even at temperatures where the fluid is liquid-like in the middle of the pore, we can observe the formation of well-defined structured layers close to the walls. This is clear from the density profile and from the in-plane correlation function measured in each layer (figure 6.19). Once the pore fluid freezes ($T = 0.92$) ten well defined crystal layers appear parallel to the walls. As was stated in a previous section of this chapter, for high pressures the fluid always forms layers parallel to the walls. The ordering in the pore and in the reservoir is again the same in the solid phases. From the in-plane correlation function in each layer (defined in chapter 4) one can observe that all layers take the structure of the (111) face of a fcc crystal. The positions of the peaks in $g(r)$ are at the distances of the first, second, etc. nearest neighbours of a (111) plane (i.e. a triangular lattice in two dimensions). This lattice structure is also observed for fluids interacting with weak walls, however the density profile is a little different now. As was discussed in chapter 4, for weak walls all the layers exhibit similar peaks in the density profile; this is not the case for strong walls (see chapter 4). Above we noted the pore and the reservoir fluid freeze simultaneously (by freezing temperature again I mean the lower limit of metastability). Most of the hysteresis seems to lie on the low temperature side of the bulk liquid-solid transition $T_{bulk} \approx 1.05$ (in agreement with the previous results in Molecular Dynamics). The melting temperature, i.e. the upper limit of

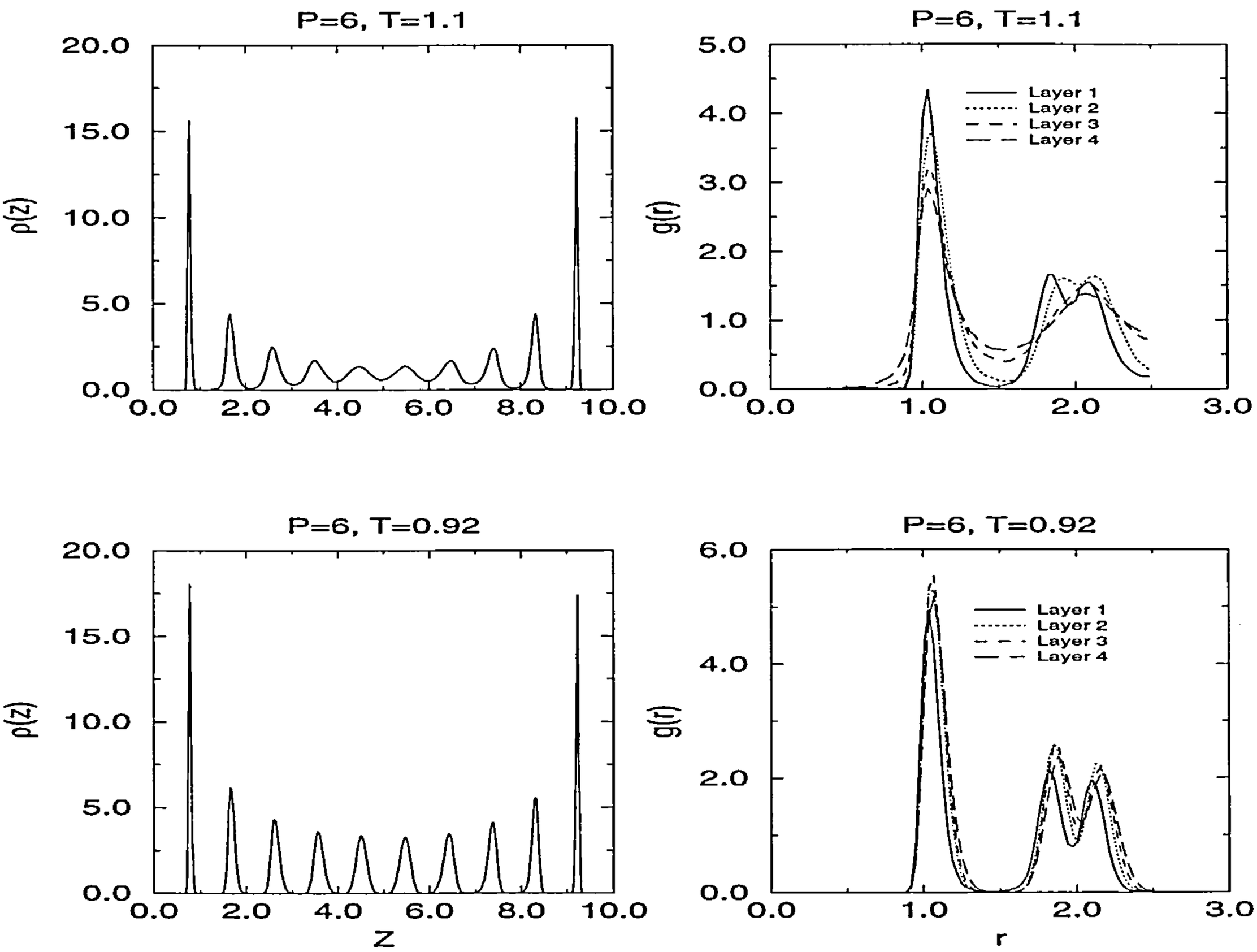

Figure 6.19: Results of Monte Carlo simulations for a pore of width $l = 10.0$ at a high pressure, $P = 6.0$. Here the wall area is $A = (7.5)^2$. The density profiles $\rho(z)$ and the corresponding in-plane correlation function $g(r)$ in each layer are plotted. The top figures refer to above the freezing temperature and the bottom ones are just below the freezing temperature. The wall fluid interaction mimics argon confined by graphite walls, $\epsilon' = 7.2375\epsilon$ and $\sigma' = 0.7823\sigma$. We observe two crystalline-like layers close to the walls for all temperatures (even when the fluid is liquid-like in the middle). Note that the bulk equilibrium freezing temperature is $T_{bulk} \approx 1.05$.

metastability, is $T = 1.13$ for this pore size at this pressure. The freezing and melting temperatures for the other (l=10) models (with weaker wall potential) are: $P = 0.7$, $T_{freeze} = 0.525$ and $T_{melt} = 0.665$, respectively ($T_{bulk} \approx 0.66$). For $P = 2.0$, these are $T_{freeze} = 0.625$ and $T_{melt} = 0.835$, respectively ($T_{bulk} \approx 0.76$) and finally, for $P = 9.0$, $T_{freeze} = 1.10$ and $T_{melt} = 1.365$ (for this case I do not have the value of the bulk transition temperature in figure 5.8). The relevant hysteresis curves for the internal energy of these systems are plotted in figure 6.20.

6.4 Conclusion

Although it is difficult to simulate a liquid and a solid phase in the same simulation box, interesting observations about the behaviour of the freezing and melting transitions of confined fluids can be made. A special feature is the large hysteresis observed in these systems. As we can observe from figures 6.1, 6.4, 6.13 and 6.20, the extent of the hysteresis can be altered by the pressure and the pore width. At constant pressure we observe that the extent of the hysteresis appears to depend on the pore width. Whereas the freezing branch remains practically unaltered (in all the hysteresis curves), the melting branch, in some cases, seems to be extended. For the largest pore (l=12.5) the melting point goes to higher temperatures than that for smaller pore widths. For a single pore size ($l = 10.0$), the extent of the hysteresis also changes with pressure. At high pressures the hysteresis is larger than at low pressures. However, in all cases the freezing transition always occurs at a temperature well-below that of the equilibrium bulk transition. Unfortunately it was not possible to conclude if the reservoir freezes before or after the pore. However, from the melting studies it was possible to conclude, in some cases, that the pore fluid melts before the reservoir. Finally, we observed that the diffusion coefficient of fluids is also affected by the confinement. The diffusion coefficient in the contact layers next to the walls is lower than in the middle layers. Moreover, the diffusion coefficient in the reservoir is always much higher than that in the pore for temperatures

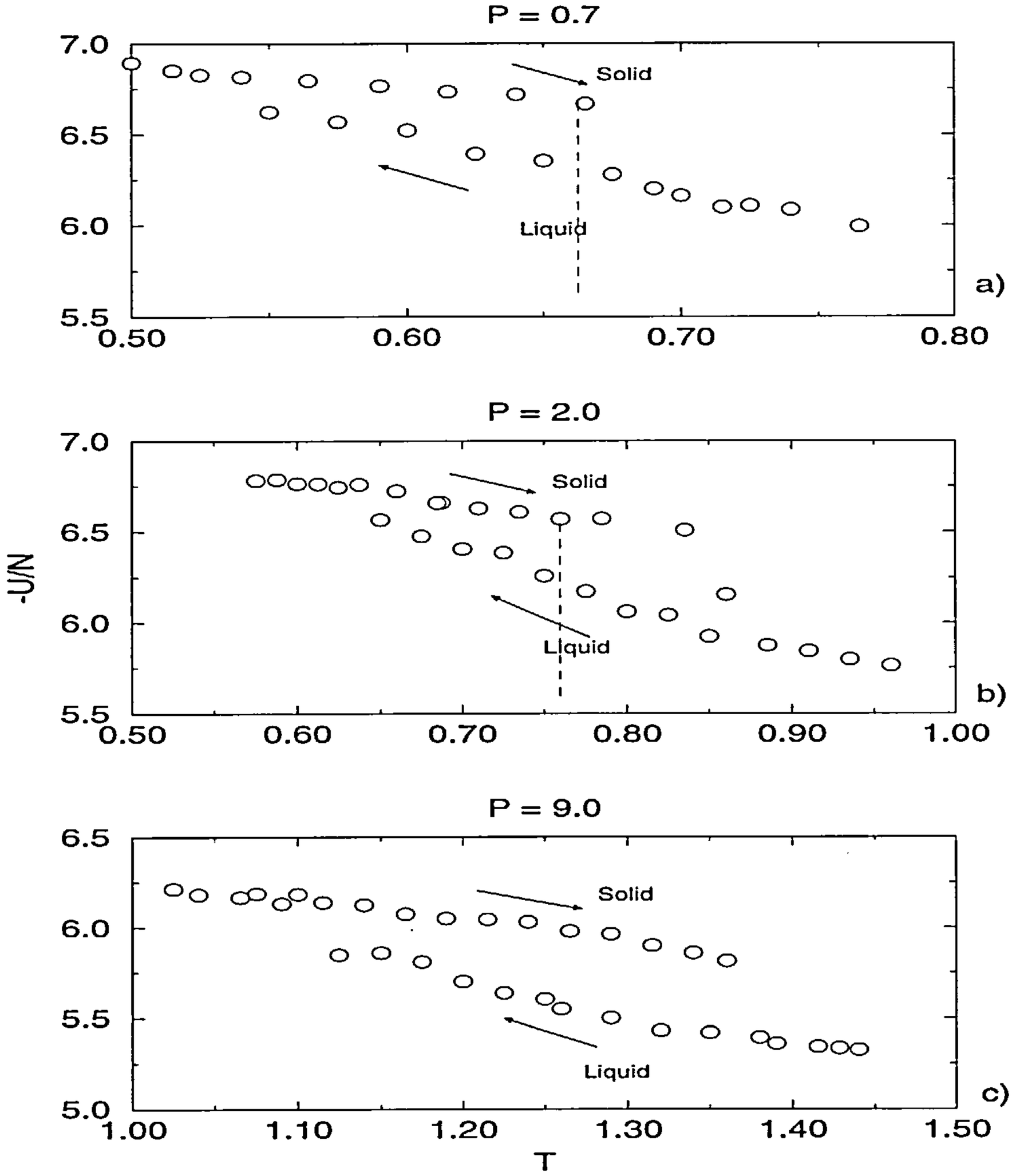

Figure 6.20: The internal energy per atom as a function of the temperature for a slit pore of width $l = 10.0$. Each plot refers to a different pressure, P. In all cases, most of the hysteresis lies to the left of the corresponding bulk equilibrium transition, T_{bulk}. The bulk transition temperature is indicated by the vertical dashed line in figures a) and b). These results refer to weak wall-fluid potential: $\epsilon' = 1.2771\epsilon$ and $\sigma' = 1.0946\sigma$.

prior to freezing. However, all diffusion coefficients drop simultaneously when the freezing temperature is reached.

Chapter 7

Summary and conclusion

In this thesis I have presented results of a computer simulation investigation of the behaviour of confined fluids. Although attention was focused primarily on the liquid-solid transition, results for the liquid-gas transition were also discussed. Unlike the liquid-gas transition in pores, the liquid-solid transition appears to depend sensitively on the nature of fluid-fluid and wall-fluid potential functions. For instance, the structure of the frozen fluid, and the form of the phase diagram for freezing, show more interesting features than those for condensation. The first investigations employed the NP_zT ensemble in slit-pore geometry, and Lennard-Jones particles. In this simulation I fixed the normal pressure on the walls of the slit, rather than fixing the bulk pressure. Simulations were performed with parameters to mimic argon fluid confined by carbon dioxide walls.

Whether the structure of the confined solid is the same as that in bulk was the first topic of investigation. Although some experimental evidence has shown that fluids confined in porous solids can take different crystal structures on freezing [100], no systematic studies have been performed to find out what produces this effect. Is this a consequence of the type of substrate employed, or is it simply the effect of the confinement? Alternatively, does it reflect the complexity of the real porous solid?. In this thesis some results which may contribute to a better understanding of this phenomenon were discussed. As stated by several authors [32, 35], the mere

presence of walls produces order across the pore, i.e. we observe a layered structure. However, once the fluid freezes, we observe that it can also develop different crystal layer structures which depend on the type of walls employed. For continuous walls, using a 10-4-3 or a 9-3 potential, where the potential depends only on the normal distance from the walls, the structure in each layer is always that of the (111) face of the fcc crystal, i.e. a triangular lattice in two dimensions. However, for corrugated walls (e.g. constructed by fixed particles in the (100) face of the fcc crystal) the particles in the layers may order to fit to those of the walls. However, this feature seems to depend on the lattice parameter employed in the construction of the pore-walls. For a large lattice parameter the solid layers adopt the same lattice structure as that in the walls whereas for a small lattice parameter the structure in the layers seems to be always the (111) face of the fcc crystal, as for the case of continuous walls [96]. The system size and the wall-fluid interaction also influence the details of the 3D structure of the confined solids. This can be observed from the 3D pair correlation function and the 3D structure factor of the confined solid (see chapter 4). Recall that the structure for a 3D bulk Lennard Jones solid is a fcc crystal. Whereas for large systems, as expected; the solid tends to take the bulk structure, for small pores the structure is influenced by the wall-fluid interaction. The confined solid seems to take the 3D bulk structure more easily for corrugated walls, than for planar walls.

A phenomenon which is usually observed in simulations of phase transitions in confined fluids is that of hysteresis. However, the precise nature of this hysteresis is still the cause of several debates. In this present case hysteresis was observed between freezing and melting as the pressure or temperature was varied. We know that in computer simulations it is difficult to nucleate a solid from a liquid. For simulations of confined fluids we expect that walls assist nucleation. Nevertheless, I found a large degree of hysteresis between freezing and melting, which is dependent on the type of wall-fluid interaction employed. For fluids confined by fully attractive walls, there is always the formation of well-defined crystal layers close to the walls

which help nucleation; then the hysteresis is small. For fluids confined by purely repulsive or weakly attractive walls, there is no formation of crystal layers next to the walls, and the extent of the hysteresis is large. Because of this large hysteresis, free energy calculations were required to locate thermodynamic coexistence. Some effort was made to make comparisons between the phase diagram of bulk and confined fluids.

Earlier attempts to determine the shift of the liquid-solid boundary from that in bulk have investigated only single state points on the coexistence line, and did not perform any calculations of free energies to support their results. In this thesis, I present a detailed analysis, based on free energy calculations, mapping out the liquid-solid and the liquid-gas coexistence curves for a Lennard Jones argon fluid confined by model CO_2 walls. The investigations were performed for several pore-sizes (systems confined by two walls separated by 10 or 20 molecular diameters approximately) and for different wall-fluid interactions. As stated above, the liquid-solid transition is significantly affected by the choice of wall-fluid potential. For purely repulsive walls, the liquid-solid boundary line lies at much lower temperatures than in bulk. For weakly attractive walls this freezing line lies at lower temperatures than in bulk, for temperatures close to the bulk triple point. However, at high temperatures and pressures, the freezing line may cross that of the bulk. The liquid-gas coexistence line was also determined for the same systems. The phenomena of capillary condensation (using weakly attractive walls) and capillary evaporation (using purely repulsive walls) were observed. Given the location of both coexistence lines, liquid-gas and liquid-solid, the triple point of each system was determined, which is also shifted from the bulk value due to the confinement. For purely repulsive fluids confined by purely repulsive walls, the coexistence line is shifted to higher temperatures with respect to those in bulk at high pressures, but at low pressures it may shift to lower temperatures from those in bulk.

These results are consistent with those suggested by other authors [95,96]. What occurs for the freezing line of a fluid confined by strongly attractive walls, is an open

question, which is not possible to answer from this study. This is because of the limitation of my method to calculate free energies for the inhomogeneous liquid, which is restricted to weak wall-fluid attraction. However, we should remember that most of the experiments in real porous solids are conducted in glasses of silica type where the wall-fluid interaction is weak. I must emphasize that my results refer to a fixed number of particles, and the phase diagrams are plotted using the normal component of the pressure. I should also say that the system may be under a special strain, since the system in the x and y directions is fixed whereas in the z direction is free to fluctuate.

Comparisons of the present results with any real experiment, e.g. on real porous solids containing a complex network of interconnected pores of different sizes, are not straightforward. Although hysteresis is also observed in the experiments (see e.g. [21,22]), its nature should be different from that observed in my computer simulations. Whether the hysteresis observed in real porous solids is due to the existence of metastable states or to consequences of network effects, is still an unresolved question. Certainly, a shift in the liquid-solid (and liquid-gas) boundary line from that in bulk is observed (see e.g. [21,22]). However, because of the complexity of the porous solid, it is difficult to interpret the results or to identify precisely what physical effect produces the shifts in these experiments. Thus, some authors have performed experiments in simpler geometries. For instance, Christenson [27] and Klein and Kumacheva [28], carried out experiments using the surface forces apparatus. The first author studied depression in the freezing temperature and the second authors studied freezing by monitoring the viscosity of confined fluids.

Computer simulations which mimic (in some sense) these experimental conditions were also carried out (see chapter 6). Constant pressure molecular dynamics simulations of a Lennard-Jones fluid confined by two parallel attractive walls (again modelling argon between CO_2 walls) showed that the freezing temperature is always lower than that in bulk. Here, we must make clear that freezing temperature means the limit of the metastability of the liquid. This observation always occurred for

all the pore widths studied (l=7.5, 8.0, 9.0, 10.0, 11.0, 12.0, 12.5) at pressures close to the bulk triple point, and for high pressures in a single pore width (l=10.0 using Monte Carlo simulations). For these simulations the slit-pore was immersed in a thermal bath, using a reservoir surrounding the pore. Although there was direct contact between the pore and the reservoir, it was not easy to distinguish which fluid freezes first. However, complementary investigations of melting indicated that, for some pore widths, the confined fluid seems to melt before the reservoir. In all cases melting occurred at a significantly higher temperature than freezing, i.e. significant hysteresis was observed. Measurements of diffusion coefficients in the slit and in the reservoir were also performed. The diffusion coefficient for the fluid in the reservoir is higher than that in the pore. Moreover, studies of individual layers of the pore fluid showed that the diffusion coefficients in layers next to the walls are lower than in the middle layers. However, all diffusion coefficients, in the reservoir and in all the layers of the fluid in the slit, drop simultaneously at the freezing temperature (i.e. the limit of metastability of the liquid).

While the present results show some new insight into the understanding of freezing in confined fluids, there is still more work to be carried out, especially if we are interested in direct comparisons with experimental investigations. For instance, it is desirable to have control of the bulk pressure (or chemical potential) instead of the normal pressure, as used in my first simulations. In this context we must remember that this ensemble was chosen as an alternative to the grand canonical ensemble which fails at high densities, where the liquid-solid transition occurs. Thus, new simulation techniques are probably needed to investigate freezing of confined fluid where the bulk (reservoir) parameters are specified. Of special consideration is the need for clever simulation methods to calculate free energies for inhomogeneous fluids. One should consider once more simulations of pores in contact with a thermal bath, as this mimics better an experimental situation. However, in order to get meaningful results we need a huge reservoir. This could help us to see a liquid and a solid phase coexisting in the same box. In addition we still need calculations of

free energies in order to locate thermodynamic coexistence. We can also envisage simulations of more complicated geometries to mimic experimental conditions. For instance, we can construct a porous matrix (e.g. a series of slit pores) and study the effects of fluids within this structure. These possibilities go beyond what could be attempted in the current study. These kind of studies, however, have been attempted, for the liquid-gas transition, by Page and Monson simulating a Lennard Jones fluid confined in a rigid matrix of big spheres [142].

Bibliography

[1] H. B. Callen. (1960) Thermodynamics., John Wiley and Sons, inc. New York.

[2] K. Huang. (1987) Statistical Mechanics., John Wiley and Sons., New York.

[3] R. J. Baxter. (1982) Exactly Solved Models in Statistical mechanics. Academic Press, London.

[4] Percus, J. K., J. Stat. Phys., **15**,505 (1976).

[5] Robledo, A., J. Chem. Phys., **72**,1701 (1980).

[6] S. R De Groot and P. Mazur. (1994) Non-Equilibrium Thermodynamics, Dover Publication, New York.

[7] J. H. Ferziger and G. H. Kaper. (1972) Mathematical Theory of Transport Process in Gases. North Holland, Amsterdam.

[8] A. W. Adamson. (1976) Physical Chemistry of surfaces 3rd. ed. Wiley, New York and London.

[9] S. Dietrich, in: Phase Transitions and Critical Phenomena, eds. C. Domb and J. Lebowitz (Academic Press, London, 1988) Vol. 12.

[10] Shick. M., (1988) Les Houches, Session XLVIII-Liquides aux interfaces (Liquids at interfaces). J. Charvolin, J. F. Joanny and J. Zinn- Justin, eds. Course 9, Introduction to wetting phenomena.

[11] Israelachvili, J. N. and McGuiggan, P. M., Science., **241**, 795 (1988).

[12] Israelachvili, J. N., McGuiggan, P. M., and Homola, A. M., Science, **240**, 189 (1988).

[13] J. N. Israelachvili. (1992) Intermolecular and Surfaces Forces, 2nd ed. Academic Press, London. The SFA was developed for fluids in 1978. Israelachvili, J. N. and Adams, G. E., J. Chem. Soc. Faraday II,,**74**,975(1978).

[14] Derjaguin, B. V., Kolloid Zeits., **69**,155 (1934).

[15] Horn, R. G. and Israelachvili, J. N., J. Physique.,**42**,39(1981).

[16] Horn, R. G. and Israelachvili, J. N., J. Chem. Phys.,**75**,1400(1981).

[17] Gee, M. L., McGuiggan, P. M., Israelachvili, J. N., and Homola, A. M., J. Chem. Phys.,**93**,1895(1990).

[18] Levitz, P., Ehret, G., Sinha, S. K., Drake, J. M., J. Chem. Phys.,**95**, 6151(1991).

[19] Levitz, P., Ehret, G. and Drake, J. M., Private communication with J. M. Drake

[20] Wilkinson, N. J., Alam, M. A., Clayton, J. M., Evans, R., Fretwell, H. M. and Usmar, S. G., Phys. Rev. Lett.,**69**,3535(1992).

[21] Duffy, J. A., Wilkinson, N. J., Fretwell, H. M. and Alam, M. A., J. Phys.: Condens. Matter,**7**,L27(1995).

[22] Molz, E. Wong, A. P. Y., Chan, M. H. W. and Beamish, J. R., Phys. Rev. B.,**48**,5741(1993).

[23] Awschalom, D. D., Warnock, J. Phys. Rev. B.,**35**,6779(1987).

[24] Beamish, J. R., Hikata, A., Tell, L. and Elbaum, C. Phys. Rev. Lett., **50**,425(1983).

[25] Torii, R. H., Maris, H. J. and Seidel, G. M., Phys. Rev. B.,**41**,7167 (1990).

[26] Ritter, M. B., Awschalom, D. D. and Shafer, M. W. Phys. Rev. Lett., **61**,966(1988).

[27] Christenson, H. K., Phys. Rev. Lett.,**74**,4675(1995).

[28] Klein, J. and Kumacheva, E., Science.,**269**,816(1995).

[29] J. P. Hansen and I. R. McDonald (1986). Theory of simple liquids. (2nd ed.) Academic Press, New York.

[30] Weeks, D. J., Chandler, D. and Anderson, H., J.chem.Phys.,**54**,5237 (1971).

[31] Magda, J. J., Tirrell, M. and Davis, H. T., J. Chem. Phys.,**83**,1888(1985).

[32] Schoen, M., Diestler, D. J. and Cushman, J. H., J. Chem. Phys., **87**, 5464(1987).

[33] Lane, J. E., and Spurling, T.H., Chem. Phys. Lett.,**67**,107(1979).

[34] Jiang, S. Rhykerd, C. L. and Gubbins, K. E., Mol. Phys.,**79**,373(1993).

[35] Ma, W. J. and Banavar, J. R. and Koplik, J., J. Chem. Phys.,**97**,485(1992).

[36] Woods G, B., Panagiotopoulos, A, Z., and Rowlinson, J, S. Mol. Phys, 63, 49, (1988).

[37] Peterson, B. K., Heffelfinger, G. S., Gubbins, K. E., and van Swol, F., J. Chem.Phys., **93**,679 (1990).

[38] Papadopoulou, A., van Swol, F. and Marconi, U. M. B., J. Chem. Phys., **97**,6942(1992).

[39] Heffelfinger, G. S., van Swol, F. and Gubbins, K. E., Mol. Phys.**61**,1381 (1987).

[40] Kozak, E. and Sokolowski, S., J. Chem. Soc. Faraday trans.,**87**,3415(1991).

[41] Evans, R. J. Phys: Condens. Matter.,**2**,8989(1990).

[42] Low, P. F., Langmuir.,**3**,181 (1987).

[43] Belak, J. F., MRS Bulletin.,**18**,15 (1993).

[44] Evans, R. and Marconi, U. M. B., J. Chem. Phys.,**86**,7138(1987).

[45] Evans, R., Marconi, U. M. B. and Tarazona, P., J. Chem. Phys.,**84**,2376(1986).

[46] Thompson, W. T. Phil. Mag.,**42**,448(1871).

[47] Evans, R. Microscopic Theories of Simple Fluids and their Interfaces. Liquids at interfaces (Les Houches Session XVIII). ed. J.Charvolin, J.F. Joanny and J. Zinn-Justin. Elsevier, 1989.

[48] Sullivan, D. E. and Weiss, J. J., J. Chem. Phys.,**72**,1170(1980).

[49] Henderson, J. R. and van Swol, F. Mol. Phys.,**56**,1313(1985).

[50] Sullivan, D. E. and Telo da Gama, M. M., Fluid Interfacial Phenomena. ed C A Croxton, New York. Wiley. 1986.

[51] Lane, J. E., and Spurling, T.H., Aust. J. Chem.,**33**,231(1980).

[52] Lane, J. E., and Spurling, T.H., Aust. J. Chem.,**34**,1529(1981).

[53] M. Schoen. Computer Simulation of Condensed Phases in Complex Geometries. New Series m: Monographs. Lecture Notes in Physics. Springer-Verlag.

[54] Curry, J. E., Cushman, J. H., Schoen, M. and Diestler, D. J., Mol. Phys.,**81**, 1059(1994).

[55] Van Megen, W. and Snook, I. K., Mol. Phys.,**54**,741(1985).

[56] Snook, I. K and Van Megen, W., Mol. Phys.,**47**,1417(1982).

[57] Quirke, N., Fluid Phase Equilib.,**29**,283(1986).

[58] Peterson, B. K. and Gubbins, K. E.,Mol. Phys.,**62**,215(1987).

[59] Schoen, M., Rhykerd, Jr. C. L. and Diestler, D. J., Mol. Phys.,**66**,1171(1989).

[60] Finn, J. E. and Monson, P. A., Mol. Phys.**65**,1345,(1988).

[61] Robledo, A. and Rowlinson, J. S., Mol. Phys.**58**,711,(1986).

[62] Heffelfinger, G. S., van Swol, F. and Gubbins, K. E., J. Chem. Phys.,**8**91, 5202(1988).

[63] Peterson, B. K., Gubbins, K. E, Heffelfinger, G. S., Marconi, U. B. M. and van Swol, F., J. Chem. Phys.,**88**,6487(1988).

[64] Heffelfinger, G. S., van Swol, F. and Gubbins, K. E., Mol. Phys.,**61**,1381(1987).

[65] Binder, K. and Landau, D. P.,J. Chem. Phys.,**96**,1444(1992).

[66] Schoen, M., Cushman, J. H., Diestler, D. J. and Rhykerd, Jr. C. L., J. Chem. Phys.,**88**,1394(1988).

[67] Diestler, D. J., Schoen, M., Hertzner, A. W. and Cushman, J. H., J. Chem. Phys.,**95**,5432(1991).

[68] Schoen, M., Diestler, D. J. and Cushman, J. H., Phys. Rev. B., **47**,5603(1993).

[69] Svensson, B. and Woodward, C. E., J. Chem. Phys.,**100**,4575(1994).

[70] Schoen, M., Diestler, D. J. and Cushman, J. H., J. Chem. Phys.,**100**, 7707(1994).

[71] Awschalom, D. D., Warnock, J. and Shafer, M. W., Phys. Rev. Lett.,**57**, 1607(1986).

[72] Duffy, J. A., Wilkinson, N. J., Fretwell, H. M., Alam, M. A. and Evans, R., J. Phys.: Condens. Matter,**7**,L713(1995).

[73] Tarazona, P. Marconi, U. M. B. and Evans, R., Mol. Phys.,**60**,573(1987).

[74] Ball, P. C. and Evans, R., J. Chem. Phys.,**89**,573(1988).

[75] Evans, R. and Ball, P. C., Phys. Rev A.,**32**,3817(1985).

[76] see e.g. R. Evans. "Density Functionals in the theory of Nonuniform Fluids" in fundamentals of Inhomogeneous Fluids edited by D. Henderson. Dekker, 1992.

[77] Metropolis, N., Rosenbluth, A. W., Rosenbluth, M. N., Teller, A. H. and Teller, E., J. Chem. Phys.,**21**,1087(1953).

[78] Alder, B. J. and Wainwright, T. E., Phys. Rev., **127**,359(1962).

[79] Hoover, W. G. and Ree, F. H., J. Chem. Phys.,**49**,3609(1968).

[80] Strandburg, K. J., Rev. Mod. Phys.,**60**,161(1988).

[81] Hansen, J. P., and Verlet, L., Phys. Rev.,**184**,151 (1969).

[82] Ladd, A. J. C. and Woodcock, L. V., Chem. Phys. Lett.,**51**,155(1977).

[83] Ladd, A. J. C. and Woodcock, L. V., Mol. Phys.,**36**,611(1978).

[84] Agrawal, R. and Kofke, D., Mol. Phys.,**85**,23(1995).

[85] See e.g. M. P. Allen and Tildesley, D. J., (1987) Computer Simulation of Liquids., Oxford University Press. and J. P. Hansen and I. R. McDonald (1976). Theory of simple liquids. (1st ed.) Academic Press, New York.

[86] Wendt, H. R. and Abraham, F. F., Phys. Rev. Lett.,**41**,1244(1978).

[87] Lindeman, F. A., Z. Physik.,**11**,609(1910).

[88] Caillol, J. M., Levesque, D., Weis, J. J. and Hansen, J. P., J. Stat. Phys.,**28**,315(1982).

[89] Broughton, J. Q., Gilmer, G. H. and Weeks, J. D., Phys. Rev. B.,**25**, 4651(1982).

[90] Ranganathan, S. and Pathak, K. N., Phys. Rev. A.,**45**,5789(1992).

[91] Cape, N. J., J. Chem. Soc., Faraday Trans.2,**78**,317(1982).

[92] Courtemanche, D. J. and van Swol, F., Phys. Rev. Lett.,**69**,2078(1992).

[93] Courtemanche, D. J., Pasmore, T. A. and van Swol, F., Mol. Phys.,**80**, 861(1993).

[94] Lupkowski, M. and van Swol, F., J. Chem. Phys.,**93**,737(1990).

[95] Hug, J. E., van Swol, F. and Zukoski, C. F., Langmuir.,**11**,111(1995).

[96] Miyahara, M. and Gubbins, K. E. J. Chem. Phys.,**106**,2865(1997).

[97] Diestler, D. J., Schoen, M. and Cushman, J. H., Science.,**262**,545(1993).

[98] Schmidt, M. and Löwen, H., Phys. Rev. Lett.,**24**,4552(1996).

[99] Unruh, K. M., Huber, T. E. and Huber, C. A., Phys. Rev. B.,**48**,9021(1993).

[100] Sokol, P. E., Ma, W. J., Herwig, K. M., Snow, W. M., Wang, Y. Koplik, J. and Banavar, J. R., Appl. Phys. Lett.,**61**,777(1992).

[101] Grier, D. G. and Murray, C. A., J. Chem. Phys.,**100**,9088(1994).

[102] Churaev, N. V., Barbasov, S. A. and Sobolev, V. D., Colloids and Surfaces A:Physicochemical and Engineering Aspects., **79**,11(1993).

[103] Barbasov, S. A., Sobolev, V. D. and Churaev, N. V., Colloid J. of the Russian Academy of Science.,**55**,512(1993).

[104] Ramsay, J. D. F. and Poinsignon, C. Langmuir.,**3**,320(1987).

[105] M. P. Allen and Tildesley, D. J., (1987) Computer Simulation of Liquids., Oxford University Press.

[106] Johnson, J. K., Zollweg, J. A. and Gubbins, K. E. Mol. Phys.**78**,591 (1993).

[107] H. Goldstein (1980) Classical Mechanics (2nd edn.) Addison-Wesley.

[108] Alder, B. J. and Wainwright, T. E., J. Chem. Phys.,**31**,459 (1959).

[109] Verlet, L. Phys. Rev.**159**,98 (1967).

[110] Evans, D. J. and Morris, G. P., Chem. Phys.**77**,63 (1983).

[111] D. Frenkel and B. Smit. (1996) Understanding Molecular Simulations. Academic Press.

[112] Steele, W. A., Surf. Sci.,**36**,317 (1973).

[113] W. A. Steele, (1974) The Interaction of Gases with Solid Surfaces. Pergamon Press, Oxford

[114] Snook, I. J and van Megen, W., J. Chem.Phys.,**72**,2907 (1981).

[115] Widom, B. J. Chem. Phys.,**39**,2808(1963).

[116] Verhaegh, N. A. M. van Duijneveldt, J. S., van Blaaderen, A and Lekkerkerker, H. N. W., J.Chem.Phys.,**102**,1416 (1995).

[117] Pollack, G. L., Rev. Mod. Phys.,**36**,748 (1964).

[118] See e.g. D. Frenkel. Advanced Monte Carlo Techniques. Computer Simulation in Chemical Physics edited by M. P. Allen and D. J. Tildesley. NATO ASI Series (1993).

[119] Diestler, D. J., Schoen, M., Curry, J. E. and Cushman, J. H., J.chem.Phys., **100**,9140(1994).

[120] Frenkel, D. and Ladd, A. J. C., J.chem.Phys.,**81**,3188 (1984).

[121] Lutsko, J. F., Wolf, D. and Yip, S., J.chem.Phys.,**88**,8525 (1988).

[122] R. K. Pathria. (1985). Statistical Mechanics. Pergamon Press.

[123] R. Lovett, in Observations, prediction and simulation of phase transition in complex fluids, vol. 460 of NATO ASI series C. By M. Baus, L. F. Rull and J. P. Ryckaert (Kluwer Academic publisher, Dordrecht 1995). Proceeding of NATO advanced study institute on "Observation, prediction and simulation of phase transitions in complex fluids", Varenna, Italy July-August1994.

[124] Sheu, S. Y., Mou, C. Y. and Lovett, R. Phys. Rev. E., **51**,R3795 (1995).

[125] Kofke, D. A. J.chem.Phys.,**98**,4149 (1993).

[126] Kofke, D. A. Mol. Phys.,**78**,1331 (1993).

[127] Agrawal, R. and Kofke, D., Mol. Phys.,**85**,43(1995).

[128] B. A. Finlayson, Nonlinear Analysis in Chemical Engineering (MacGraw-Hill, New York, 1980).

[129] Panagiotopoulos, A. Z., Quirke, N. Stapleton, M. and Tildesley., Mol. Phys.,**63**, 527(1988).

[130] B. Smit, Ph.D. thesis, University of Utrecht, The Netherlands (1990).

[131] Smit, B. J. Chem. Phys.,**96**,8639 (1992).

[132] Nicolas, J. J., Gubbins, K. E., Streett, W. B. and Tildesley, D. J., Mol. Phys.,**37**,1429(1979).

[133] Peterson, B. K., Walton, J. P. R. B. and Gubbins, K. E., J.chem.Soc. Faraday Trans. II**82**,1789 (1986).

[134] de Kuijper, A., Shouten, J. A. and Michels, J. P., J.chem.Phys.,**93**,3515 (1990).

[135] ten Wolde, P. R., Ruiz-Montero, M. J. and Frenkel, D., J. Chem. Phys., **104**,9932 (1996).

[136] van Duijneveldt, J. S. and Frenkel, D., J. Chem. Phys.,**96**,4655 (1992).

[137] Swope, W. C. and Andersen, H. C., Phys. Rev. B.,**41**,7042 (1990).

[138] D. A. McQuarrie. Statistical Mechanics, Harper and Row. New York, 1976.

[139] Hall, P. L. and Ross, D. K., Mol. Phys.,**36**,1549 (1978).

[140] G. Arfken, Mathematical methods for Physicists, Academic Press. London, 1985.

[141] Hoheisel, C., Schoen, M. and Vogelsang, R., Comp. Phys. Commun.,**34**, 9(1984).

[142] Page, K. S. and Monson, P. A., Phys. Rev. E.,**54**,6557(1996).